

# **Minimally invasive therapies for the brain using magnetic particles**

Chris Payne

Centre for Advanced Biomedical Imaging (CABI)

Division of Medicine

UCL

A degree submitted for the degree of

*Doctor of Philosophy*

October 2019

I, Chris Payne, confirm that the work presented in this thesis is my own. Where information has been derived from other sources, I confirm this has been indicated in the thesis.



# Abstract

Delivering a therapy with precision, while reducing off target effects is key to the success of any novel therapeutic intervention. This is of most relevance in the brain, where the preservation of surrounding healthy tissue is crucial in reducing the risk of cognitive impairment and improving patient prognosis. Our scientific understanding of the brain would also benefit from minimally invasive investigations of specific cell types so that they may be observed in their most natural physiological environment.

Magnetic particles based techniques have the potential to deliver cellular precision in a minimally invasive manner. When inside the body, Magnetic particles can be actuated remotely using externally applied magnetic fields while their position can be detected non-invasively using MRI. The magnetic forces applied to the particles however, rapidly decline with increasing distance from the magnetic source. It is therefore critical to understand the amount of force needed for a particular application. The properties of the magnetic particle such as the size, shape and magnetic content, as well as the properties of the applied magnetic field, can then be tailored to that application.

The aim of this thesis was to develop magnetic particle based techniques for precise manipulation of cells in the brain. Two different approaches were explored, utilising the versatile nature of magnetic actuation for two different applications. The first approach uses magnetic nanoparticles to mechanically stimulate a specific cell type. Magnetic particles conjugated with the antibody ACSA-1 would selectively bind to astrocytes to evoke the controlled release of ATP and induce a calcium flux which are used for communication with neighbouring cells. This approach allows for the investigation into the role of astrocytes in localised brain regions using a naturally occurring actuation process (mechanical force) without effecting their natural environment.

The second approach uses a millimetre sized magnetic particle which can be navigated through the brain and ablate localised regions of cells using a magnetic resonance imaging system. The magnetic particle causes a distinct contrast in MRI images, allowing for precise detection of its location so that it may be iteratively guided along a pre-determined path to avoid eloquent brain regions. Once at the desired location, an alternating magnetic field can be applied causing the magnetic particle to heat and deliver controllable, well defined regions of cell death.

The forces needed for cell stimulation are orders of magnitude less than the forces needed to guide particles through the brain. Chapters 4 and 5 use external magnets to deliver forces in the piconewton range. While stimulation was demonstrated in small animals, scaling up this technique

to human proportions remains a challenge. Chapters 6 and 7 use a preclinical MRI system to generate forces in the millinewton range, allowing the particle to be moved several centimetres through the brain within a typical surgical timescale. When inside the scanner, an alternating magnetic field causes the particle to heat rapidly, enabling the potential for multiple ablations within a single surgery. For clinical translation of this technique, MRI scanners would require a dedicated propulsion gradient set and heating coil.



# Impact Statement

Your brain, as we know it, is irreplaceable. If a part of it is damaged, or altered over time, for better or worse the person can change. With the ever increasing prevalence of dementia in an aging population, increased awareness and levels of mental health problems, along with the devastating effects of cancer in the brain; the impact and burden these have on the subject, their family, their friends and society as a whole has never been greater.

As such, it has never been more important to understand how the brain changes, and to have the ability to treat or even prevent these conditions so that they do not become detrimental to our quality of life. This thesis is therefore dedicated to the development of two potential therapies within the brain that minimise damage to surrounding healthy tissue but still deliver the necessary precision to be effective. Magnetic particles were used for this purpose because once placed inside the body they can be actuated remotely using externally applied magnetic fields.

The work proposed has the potential to move magnetic targeting therapies closer to more widespread basic and clinical application. The novel techniques developed in this thesis will have a direct benefit for academic centres (both nationally and internationally) that are working on the clinical diagnosis and basic mechanisms of disease. The ability to non-invasively manipulate astrocytes represents a valuable basic science research tool for whole brain, repeated, longitudinal measurements in the same cohort of animals without invasive surgery that is required for optogenetics.

Furthermore, the novel technologies outlined in this proposal allow a magnetic particle to be navigated through the brain and ablate localised regions of cells using a magnetic resonance imaging system. The successful clinical translation of the novel MR sequences would form a valuable tool for academic centres focused on novel therapy and imaging biomarker development, such as the new McMillian Cancer Hospital at UCL.

Minimally invasive therapies have the potential to treat a myriad of conditions that affect our wellbeing including diseases such as cancer, as well as diseases and tissue degeneration associated with an aging population, such as neurodegenerative diseases, heart and respiratory ailments. Our commercial partners bring product development expertise to the current study, as well as the skills required to take magnetic targeting into hospitals and clinics in the future. Existing collaborations include *Chemicell* and *Micromod*, magnetic particle manufacturers, which specialise in biofunctionalisation for diagnostics. *Bayer-Schering Pharma* is a major pharma corporation and the

manufacturer of *Resovist*, whose contrast media division sees magnetic targetting as opening up new product streams. *Philips and Tesla Engineering* are international medical imaging/devices companies and a potential manufacturing and/or distribution partner.

Reaching out we will use our public partners which include patient advocacy, engagement forums and support groups. These include the *Cheltenham Science Festival*, *Cancer Research UK*, *The British Lung Foundation*, and engaged end-user groups within our hospitals. Industry-academic partnerships (Philips, Tesla Engineering) in minimally invasive work will increase in the coming years, and public understanding and support will be needed to maximise chances of success. Therefore, we will prioritise approaches to improve the public perception of the value of novel technologies such as magnetic nanoparticles in drug discovery and development.

# Acknowledgements

I used to think nothing was impossible, but this thesis simply would not have happened without the help of so many people.

To my primary supervisor Mark Lythgoe I will simply say thank you. Thank you for going beyond the call of duty when it was needed. I am also immensely grateful for the wisdom and insight of my secondary supervisor Quentin Pankhurst, for enlightening me in all things to do with magnetic particles.

A huge thank you must also go towards my colleagues that made a direct contribution to this thesis. I thank Yichao Yu for his sheer will power and dedication, Matin Mohseni for his companionship, John Connell for keeping a smile on my face and Rebecca Baker for her diligence. Thanks also to the folks over at the Royal Institution: to Fangyu Lin during heating experiments, Paul Southern for SQUID measurements and George Frodsham for introducing me to finite element modelling.

Thanks must also go to my friends and colleagues in CABI, Jack Wells for putting up with sitting next to me for so many years, Stephen Patrick and Bernard Siow for your ever insightful conversations and to everyone else for making the lab as good a place to work as I could have hoped for.

Finally, I thank mum, dad and Mike for being there when needed. And you were needed.

# Table of Contents

Declaration .....	2
Abstract .....	3
Impact Statement .....	5
Acknowledgements .....	7
Table of Contents .....	8
List of Figures .....	13
List of Tables .....	15
1 Magnetic particles: potential uses for cellular control and therapeutic delivery in the brain .....	16
1.1 Brain stimulation .....	17
1.1.1 Electrodes .....	19
1.1.2 Optogenetics .....	21
1.1.3 Magnetic nanoparticle techniques for cell stimulation .....	24
1.2 Brain cancer .....	32
1.2.1 Surgery and standard practice .....	34
1.2.2 Focal ablation techniques .....	36
1.2.3 Magnetic thermoseeds .....	45
2 Magnetic particles in medicine .....	48
2.1 Definitions and basic principles .....	49
2.1.1 Magnetic fields .....	49
2.1.2 Magnetic materials .....	51
2.1.3 Magnetisation curves .....	52
2.1.4 Magnetic force .....	53
2.2 Applications of magnetic particles in medicine .....	55
2.2.1 Magnetic separation .....	55
2.2.2 Magnetic cell and drug delivery .....	57

2.2.3	Magnetic hyperthermia/thermal ablation .....	59
2.2.4	Particle and cell tracking .....	62
3	Magnetic Resonance Imaging and targeting.....	64
3.1	Basic principles of MRI .....	65
3.1.1	Nuclear magnetic resonance .....	65
3.1.2	Relaxation.....	66
3.2	Magnetic resonance targeting .....	70
3.3.1	Basic components of an MRI scanner .....	71
3.3.2	Magnetic propulsion using MRI gradient coils .....	73
3.3	Imaging magnetic particles using MRI.....	75
3.3.1	Positive contrast imaging .....	76
3.3.2	Susceptibility artefacts .....	78
3.3.2	MRI tracking of steel spheres .....	80
3.4	Existing magnetic resonance targeting work .....	83
4	Characterisation of forces for <i>in vitro</i> stimulation of astrocytes using magnetic particles .....	87
4.1	Introduction .....	87
4.2	Methods .....	89
4.2.1	Iron oxide particles used .....	89
4.2.2	Ligand coupling.....	89
4.2.3	Astrocyte cell culture.....	90
4.2.4	Calcium imaging .....	90
4.2.5	Yoke electromagnet design .....	91
4.2.6	Force Calculation .....	92
4.3	Results .....	94
4.3.1	Characterisation of electromagnet and magnetic particles used .....	94
4.3.2	<i>In vitro</i> force threshold quantification .....	98
4.3.3	Targeted stimulation of astrocytes with ACSA-1 coupled magnetic particles.....	101
4.4	Discussion.....	104

4.5	Conclusion .....	107
5	In vivo stimulation of astrocytes using magnetic nanoparticles .....	108
5.1	Introduction .....	108
5.2	Methods .....	109
5.2.1	Mixed cortical cell cultures.....	109
5.2.2	Design and simulation of a magnetic mangle.....	109
5.2.3	Detection of ATP release .....	110
5.2.4	Stereotaxic injection of magnetic particles .....	111
5.2.5	MRI for particle retention .....	111
5.2.6	Immunofluorescence.....	112
5.2.7	In vivo stimulation .....	113
5.3	Results .....	114
5.3.1	Magnetic Mangle simulations and validation .....	114
5.3.2	ATP release using Fe <sub>3</sub> O <sub>4</sub> particles .....	117
5.3.3	ATP release using SiMAG particles .....	119
5.3.4	MRI and immunofluorescence of particle fate in vivo .....	123
5.3.5	In vivo magnetic stimulation .....	125
5.4	Discussion.....	127
5.5	Conclusion .....	130
6	Navigation of magnetic beads through the brain using MRI.....	131
6.1	Introduction .....	131
6.2	Methods .....	133
6.2.1	Propulsion gradients .....	133
6.2.2	Movement measurements in 0.125% agar .....	133
6.2.3	Localisation using signature selective excitation and validation.....	133
6.2.4	Movement detection of 2mm seeds .....	134
6.2.5	<i>Ex vivo</i> brain tissue movement detection .....	135

6.2.6	Navigation of magnetic seeds through brain tissue using bespoke propulsion gradient set	135
6.3	Results .....	136
6.3.1	Characterisation of distance moved by magnetic beads in viscoelastic medium .....	136
6.3.2	Initial movements in <i>ex vivo</i> brain tissue .....	138
6.3.3	Development of localisation method and validation .....	140
6.3.4	Assessment of movement control using 2 mm magnetic beads.....	143
6.3.5	Movement of 2 mm beads through <i>ex vivo</i> brain tissue using preclinical imaging gradients	145
6.3.6	<i>Ex vivo</i> navigation of magnetic beads using dedicated imaging/propulsion gradient coil	148
6.4	Discussion.....	152
6.5	Conclusion .....	156
7	Thermal ablation using magnetic beads for MINIMA, an MRI based minimally invasive, image-guided ablation technique .....	157
7.1	Introduction .....	157
7.2	Materials and Methods .....	159
7.2.1	Initial heating attempts with MRI radiofrequency coil.....	159
7.2.2	Heating coil specification .....	159
7.2.3	Heating of bead in air and water.....	160
7.2.4	Temperature distribution in agar phantom .....	160
7.2.5	Development of TTC staining of 3D cell culture .....	160
7.2.6	Cell death via heating of bead.....	161
7.2.7	<i>In vivo</i> ablation .....	161
7.3	Results .....	163
7.3.1	Temperature of spherical beads dependent on bead diameter .....	163
7.3.2	Characterisation of 2 mm bead heating in different media .....	164
7.3.3	Development of TTC staining of 3D cell culture .....	166
7.3.4	<i>In vitro</i> cell death via bead heating .....	168

7.3.5	<i>In vivo</i> ablation with MRI compatible hyperthermia coil .....	170
7.4	Discussion .....	172
7.5	Conclusion .....	175
8	General conclusions and future direction .....	176
	References .....	179



# List of Figures

- 1.1** Penfield and Boldreys diagram of cortical organisation of the post central gyrus
- 1.2** Comparison of electrical and optogenetic stimulation
- 1.3** Diagram for thermogenetic stimulation
- 1.4** Diagram of various mechanical stimulation methods
- 1.5** Stereotactic radiosurgery diagram
- 1.6** Interstitial laser ablation
- 1.7** Example of MRI-HIFU
- 1.8** Example of different RF ablation systems
- 1.9** Ice ball formation during cryoablation
- 1.10** Magnetic stereotaxis concept
  
- 2.1** Magnetisation curves for paramagnetic, diamagnetic, ferromagnetic and superparamagnetic materials
- 2.2** Magnetic separation diagram
- 2.3** Linear and cylindrical Halbach arrays
  
- 3.1** Magnetic moment and relaxation diagrams
- 3.2** Spin echo and gradient echo pulse sequence diagrams
- 3.3** Schematic of an MRI scanner
- 3.4** GRASP sequence diagram
- 3.5** Off resonant excitation signal from magnetic particles
- 3.6** Gradient echo, white marker and IRON images of phantom containing iron oxide labelled glioma cells
- 3.7** MRI susceptibility artefacts of steel balls
- 3.8** Cross section of MRI powered “Gauss gun”
  
- 4.1** Yoke magnet simulations
- 4.2** Yoke magnet simulation validation
- 4.3** Magnetisation curves of the magnetic particles used
- 4.4** Astrocyte stimulation using collagen coated  $\text{Fe}_3\text{O}_4$  particles
- 4.5** Particle cluster volume calculation
- 4.6** Force and stress threshold for astrocyte stimulation

- 4.7 Stress calculations for biocompatible magnetic particles
- 4.8 Targeted magnetic stimulation of astrocytes with antibody coated magnetic particles
  
- 5.1 Photo of magnetic mangle
- 5.2 Design and characterisation of magnetic mangle
- 5.3 Measuring ATP release of astrocytes using collagen coated  $\text{Fe}_3\text{O}_4$  particles
- 5.4 ACSA-1 coupled SiMAG particles selectively bind to astrocytes
- 5.5 Measuring ATP release of astrocytes using SiMAG particles
- 5.6 MRI for localisation and fate of SiMAG particles after injection into rat brainstem
- 5.7 Immunostaining of particles in brainstem
- 5.8 Measured sympathoexcitation response after stimulation using ACSA-1 coupled SiMAG particles
- 5.9 *In vivo* stimulation using lower concentrations of ACSA-1 coupled SiMAG particles
  
- 6.1 Demonstrating movement of magnetic beads in three dimensions using MRI gradients
- 6.2 Distance moved can be controlled with gradient strength and seed size
- 6.3 Movement of 2 mm seed in *ex vivo* brain tissue
- 6.4 Localisation of ferromagnetic beads using modified signature excitation method
- 6.5 Localisation validation phantom
- 6.6 Movement characterisation of 2 mm beads using two new localisation methods
- 6.7 Movement of 2 mm beads through *ex vivo* brain tissue
- 6.8 Examples of path taken by 2 mm beads through 0.4% agarose phantom
- 6.9 Navigation of 3 mm beads through brain tissue using bespoke propulsion gradient coil
- 6.10 Comparison of movement of 3 mm beads 400 mT/m at clinically relevant duty cycle and 300 mT/m continuously.
  
- 7.1 Photo of MACH system and MRI compatible hyperthermia coil
- 7.2 Recorded thermal camera temperatures of different sized beads
- 7.3 Fibre optic temperature readings of 2 mm beads in air, water and agar
- 7.4 TTC staining of cell pellets (mesenchymal stem cells and 4T1 tumour cells) and 3D cell culture
- 7.5 Development TTC staining protocol of 3D cell cultures
- 7.6 TTC staining of 3D cell cultures indicate clear perimeter of cell death after AMF application
- 7.7 Thermal camera temperature readings of beads in 3D cell culture

## **7.8** In vivo cell death using MRI compatible heating coil

# List of Tables

## **1** Comparison of measurements between magnetic and plastic seeds

# 1 Magnetic particles: potential uses for cellular control and therapeutic delivery in the brain

The goal of any novel therapeutic intervention must be to target the specific pathology or cell in question while leaving all other cells and surrounding healthy tissue unaffected. This criteria is of most relevance in the brain, where perturbation or damage of healthy tissue can lead to cognitive impairment and a reduction in quality of life. To effectively treat a pathology, the underlying mechanisms and principles of it must be understood which in turn can be guided by a comprehensive understanding of a perfectly healthy brain. The opposite is also true. By observing an absence or impairment of cognition as a result of localised damage, pathology or stimulation, we can infer the functional role of that particular region. It could be said that the earliest studies into the brain relied on the latter, while in the present day the seemingly endless advancement in technologies have allowed us to investigate the brain closer, and with more control than ever before. This thesis looks to improve on the techniques currently available for brain cell manipulation by developing novel techniques using magnetic particles (ranging from nm-mm) that deliver the precision necessary to reduce disruption of healthy tissue while delivering outright control of the particle and it's manipulation of the cells in question.

This chapter broadly covers two areas: tools for manipulating normal brain cells and tools for treating abnormally proliferating cells, cancer. An overview of minimally invasive techniques is given in each case. The impact, advantage and disadvantage of each technique is discussed, concluding that there is scope for less invasive alternative methods than those we currently possess.

## 1.1 Brain stimulation

The ability to selectively stimulate brain cells and measure their response will give us a greater understanding of brain function, connectivity and cellular responses to neurological pathology. This knowledge would in turn benefit the development of new therapeutic techniques for neurological disorders and cancer therapies. When we talk about brain stimulation we mean fast transient changes in brain activity; a voluntary movement, speech or perception of an event takes from around 50 milliseconds to a few seconds. Being awake, asleep or unconscious are states of the brain, but it is the fast changes in brain activity that are of most interest and to this day remains an incredibly active and exciting area of research. Rapid biochemical or biophysical changes in neurons and glial cells are what trigger our voluntary and involuntary movements, thoughts and perceptions. To assess the role and function of these cells it is essential to investigate each cell type separately to determine their characteristics and how they interact with other cells to determine how brain function is affected by these processes. This can be summed up by a quote from Sir Francis Crick who stated that it is essential to be able to manipulate and control one specific cell type within the brain, leaving others unaltered to further our knowledge and assemble a theory of the mind<sup>1</sup>.

Our present understanding of the brain is indebted to the many behavioural and psychophysical experiments that have provided us a solid understanding of cortical organisation. In absence of stimulation technologies the earliest experiments used behaviour observations on brain injury patients, which allowed them to identify regions of the brain associated with certain tasks. An early example of this is the work by Paul Broca, who by assessing loss of speech and motor movement identified that the third gyrus of the left temporal lobe was responsible for speech production<sup>2</sup>. In early primate studies, Hermann Munk rather barbarically found that a monkey was unable to see one half of its visual field when one side of its occipital lobe was removed, while removal of both sides resulted in total blindness<sup>3</sup>. While these methods allowed them to associate fairly large regions of the brain with certain tasks, it was the advent of electrical stimulation that allowed us to really probe discrete regions of the brain. In 1870, Fritsch and Hitzig found that electrical stimulation of the somatosensory cortex of the frontal lobe resulted in the movement of a limb or body part on the opposite side of the body, which led to the famous study by Penfield and Boldrey<sup>4</sup>. By stimulating discrete regions along the somatosensory cortex they were able to map out the body part associated with that location.

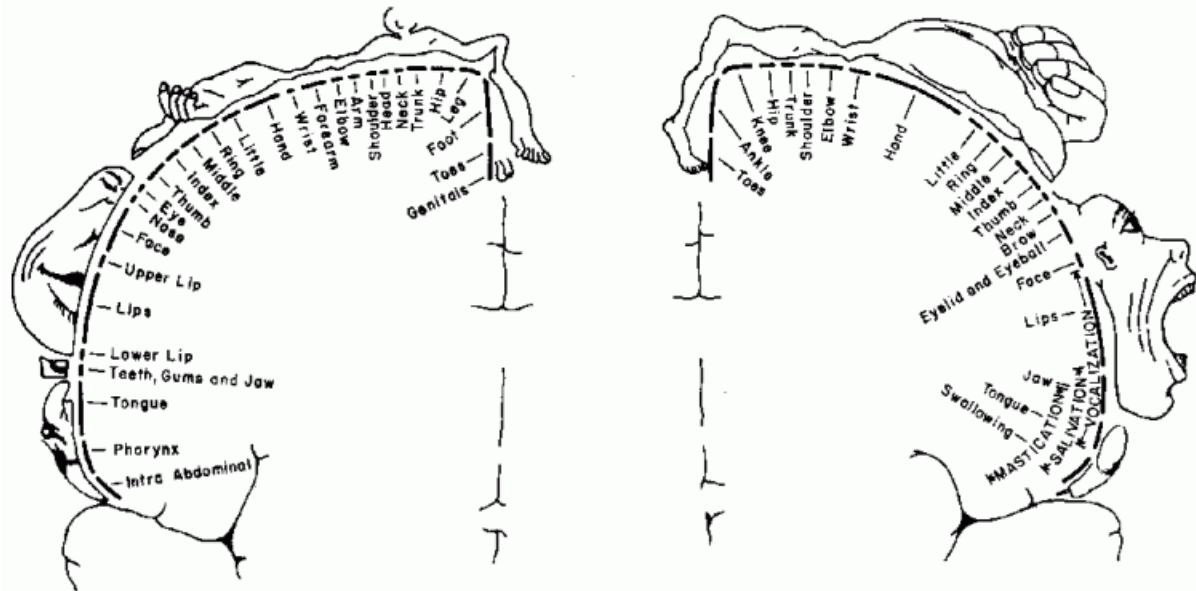


**Figure 1.1.** Taken from Penfield and Boldrey<sup>4</sup>. Diagram showing cortical organisation of the postcentral gyrus and the corresponding body parts associated with that area.

This combination of electrical stimulation and behaviour studies, particularly with the development of sophisticated imaging technologies such as EEG, MEG and fMRI and DTI, has provided us with a comprehensive map of the cortical organisation of the brain and its major connections. But to delve deeper into the intricacies of the mind, novel minimally invasive and targeted stimulation techniques need to be adopted. The ideal technique would be stimulation of a single cell type, with minimal or no disturbance of other cells and their surrounding environment, facilitating investigations into the function of highly localised regions of cells in their natural physiological environment. The following section will therefore outline the existing techniques available, their impact on the field and their advantages and disadvantages.

### 1.1.1 Electrodes

Gustav Fritsch and Edvard Hitzig are generally considered to be the first to demonstrate electrical stimulation of the human brain<sup>5</sup> however credit also goes to Roberts Bartholow<sup>6</sup>. Using platinum wires connected to a battery they could electrically stimulate more discrete regions of the brain than lesion studies. The effects of stimulation were reversible too, i.e. the brain was still intact and would resume to normal function after stimulation. In terms of significance, Wilder Graves Penfield was one of the first neurosurgeons to utilise both stimulation and ablation by electrical means to construct the early maps of the human brain while also developing a surgical treatment for epilepsy<sup>7</sup>.

Particular focus has been given to the visual cortex due to the value of its importance over the other senses. It has been said that the value of vision to an animal is the value of its intelligence<sup>8</sup>. Simply seeing the shape and properties of an object means nothing without recognising, interpreting and understanding it. Humans appear to have a more developed visual cortex than other mammals who instead often have a well developed olfactory system. The relative simplicity of the sense of smell (a specific odor will correspond to specific thing) means that, in some corners, it is acknowledged as the bestial sense<sup>8</sup>. Modern electrical stimulation uses microelectrodes which can be implanted and have been widely used for studying neural circuits in vivo. Microstimulation in the primary visual cortex (V1) cause patients to report the visualisation of a small dot of white light which they termed a phosphene. The mapping of the location of these dots in the visual field between different stimulation sites on V1 agreed with findings from patients with war wounds<sup>9</sup>. In the middle temporal visual area on the other hand, neurons were found to be sensitive to direction and speed of motion. Rhesus monkeys were used to test whether microstimulation would affect the perceptual judgement of the motion of a collection of dots in a near threshold stochastic motion display<sup>10</sup>. These studies along with many others in the visual cortex and other regions have been invaluable in furthering our understanding of the brain<sup>11</sup>.

Electrical stimulation is also used as a treatment. Deep brain stimulation (DBS) is now used in the clinic as a therapy for Parkinsons disease<sup>12</sup>, essential tremor<sup>13</sup>, obsessive compulsive disorder<sup>14</sup>, dystonia<sup>15</sup>, epilepsy<sup>16</sup> and chronic pain<sup>17</sup>. Implanted electrodes work by exciting or inhibiting brain cells using low or high frequency currents respectively<sup>18</sup>. However there are of course some obvious risks and limitations in using electrodes in the brain. The invasive nature of implanting them into the brain will cause damage and inflammation to surrounding and intervening healthy tissue<sup>19</sup>. Infection is the most common reported complication of DBS<sup>20</sup>, while battery packs only last up to 3 years for treatment of dystonia and 5 years for Parkinsons disease. Migration of the electrode and haemorrhages have also been reported<sup>21</sup>. Another drawback is the mechanism of electrical

stimulation itself, which stimulates all electrically active cells within close proximity to the electrode. Electrical stimulation therefore falls short if a particular cell type needs to be interrogated.



### 1.1.2 Optogenetics

Optogenetics uses a combination of optical and genetic approaches to selectively excite or inhibit a particular cell type. The cell type of choice is genetically altered to express exogenous light responsive transmembrane proteins so that a specific cellular response can be controlled by the delivery of light<sup>1</sup>. The emergence of this technique caused quite a stir within the community because, for the first time, the activity of a single cell type can be controlled with remarkably high cell specificity and temporal precision, operating on a millisecond time scale. In recognition of the impact optogenetics has made in the community, in 2010 it was named method of the year by the Nature Methods journal<sup>22</sup>. Since the first seminal paper by Zemelman et al in 2002<sup>23</sup> there has been an explosion of optogenetics research since with over 5000 articles to date.

The light sensitive proteins that are typically used for optogenetics are called opsins. To stimulate cells, the most popular forms of microbial opsins are the Channelrhodopsins. In particular ChR2, a non specific cation channel that depolarises a neuron when opening, was used in the early work by Boyden et al<sup>24</sup>. On the other hand Halorhodopsins like NpHR conduct chloride ions which hyperpolarises neurons when illuminated<sup>25</sup>, demonstrating that neurons can be both stimulated and inhibited using optogenetics. Figure 1.2 shows the cellular specificity that optogenetics has over electrical stimulation, which emits a current radially and affects all cells. Common methods for introducing the opsin gene into the cell include the use of viral vectors such as the lentivirus or adeno-associated virus (AAV), via transgenesis or knock-in technologies<sup>26</sup>. Limitations for viral vectors are the relatively low genetic payload length in viral expression systems and while a number of ChR2 expressing transgenic lines<sup>27,28</sup> and knock-in lines<sup>29</sup> have been established the cost, time and effort for creating and maintaining these mouse lines are considerable.

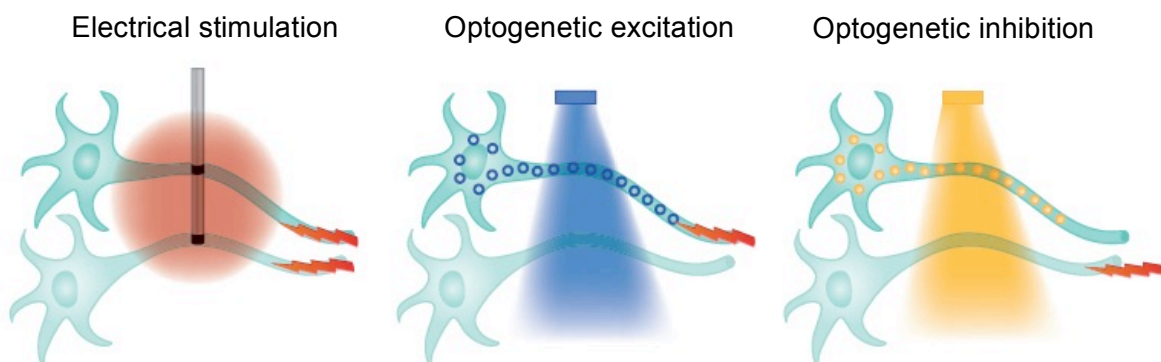


**Figure 1.2.** Taken from Deisseroth, 2011<sup>1</sup>. Diagram demonstrating the superior cellular and projection specificity of the light used in optogenetics compared to electrical stimulation.

To deliver light *in vitro* the light source can range from mercury arc lamps, LEDs and lasers<sup>30</sup>. For *in vivo* investigations, due to the poor penetration of light through tissue optical fibres are often implanted to deliver light to the transduced tissue<sup>28</sup>. Several wireless systems have been developed but are not widely used due to their power inefficiency and bulkiness<sup>31–33</sup>, however efforts to develop smaller wireless devices will continue with improving technology. Fibre optic systems have also been combined with electrodes for electrophysiological recording of optical control of neural activity<sup>25,26,34</sup>, allowing for comparison to more traditional techniques.

The use of optogenetics has not been restricted to investigating neuronal activity. With this new ability to stimulate specific cell types, optogenetics has also been used to investigate the functional role of astrocytes, the most abundant glial cell in the brain. Star like in shape, their endfeet are often wrapped around blood vessels leading to the historical belief that they are merely there for structural support for neurons and to control cerebral blood flow<sup>35</sup>. However optogenetic investigations have revealed closer communication between astrocytes and neurons than previously thought, showing that they play an important role in breathing<sup>36</sup>, pain and sleep<sup>37,38</sup>, while they are also involved in pain processing<sup>39</sup> and can suppress food intake<sup>40</sup>. As the field of optogenetic stimulation of astrocytes is relatively new, it is exciting to wonder what other functions of astrocytes are yet to be discovered.

As with electrical stimulation, optogenetics has therapeutic potentials too with a clinical trial currently underway for the optogenetic treatment of blindness<sup>41,42</sup>. Cardiac optogenetics is an emerging field to control cardiac pacing and prevent arrhythmia<sup>43–45</sup>. It has also been shown that optogenetic control of the parasympathetic vagal drive can in fact enhance cardiac contractility and exercise endurance<sup>46</sup>. There is also the potential for optogenetic treatment of epilepsy<sup>47</sup>, hearing loss<sup>48</sup> and restoration of motor function post stroke<sup>49</sup>. Clearly there is a demand for cell specific stimulation techniques for a whole range of applications, whether therapeutic or purely scientific, which begs the question. Is optogenetics the answer?

Despite the incredible impact optogenetics has already made on the field of neuroscience it still has its limitations. The implantation of an optical fibre means it is still a very invasive technique which, along with genetic modification of cells perturbs the natural environment of the cells being investigated. Efforts to develop opsins sensitive to red-shifted light, which can penetrate up to 3 mm below the surface of the brain, have resulted in the development of a cruxhalorhodopsin named Jaws<sup>50</sup>. While this provides non-invasive *in vivo* inhibition of cells, researchers have yet to find an equivalent excitatory opsin. Even so, with a penetration of 3 mm deep, deeper brain structures cannot be reached, restricting it to applications on the cortical surface of the brain. As such there is

scope for the development of targeted stimulation of cells by other means which can provide the same cell specificity but in a less invasive manner.

### 1.1.3 Magnetic nanoparticle techniques for cell stimulation

Magnetic nanoparticle techniques have the potential to improve on some of the limitations of optogenetics. Their use as a mechanism for targeted stimulation is attractive because they can be actuated remotely using an externally applied magnetic field. As magnetic fields pass harmlessly through the body, these techniques are less invasive than stimulation by optical or electrical means. This section covers the current status of cell stimulation via magnetic particles; a more detailed description of magnetic particles, covering definitions, principals and further applications in medicine are provided in chapter 2.

The idea for using magnetic nanoparticles to investigate the properties of cells originates back to the 1950's. Crick and Hughes used small ferrite particles which could be phagocytosed by cultured fibroblasts to investigate the rheological properties of cytoplasm by using an external magnetic field to drag and twist the particles inside the cell. The realisation that magnetic nanoparticles could be used for the control of cellular activity occurred in the 1990's. Early work by Wang et al used magnetic microbeads coated with a peptide that would bind to integrin receptors in the cell membrane<sup>51</sup>. Integrins are what connects the extracellular matrix with the cytoskeleton of the cell. By magnetically twisting the magnetic beads they found that the cytoskeleton stiffened, showing that integrins are responsive to mechanical stimulation. A number of studies have occurred since using magnetic nanoparticles to control the cellular activity of a whole range of cell types where two main mechanisms have arose: Stimulation via heat and stimulation via force. An overview of the work carried out using these two mechanisms is provided in this section.

#### 1.3.3.1 Stimulation via heat transfer/thermogenetics

The concept of thermogenetics is very similar to optogenetics. Cells are genetically modified to express a certain protein or ion channel except in this case, the protein is sensitive to temperature change as opposed to light. ThermoTRP's, non-specific cation channels that can directly alter the membrane potential of neurons, emerged as prime candidates for this technique that can either be heat activated or cold activated<sup>52</sup>. Initial experiments were carried out to investigate the courtship acts of drosophila where the ambient temperature could be changed to activate TRPA1 channels<sup>53,54</sup>. Since then infrared light has been utilised as a heat source to deliver stimulation down to cellular resolution *in vivo*<sup>55</sup> and sub cellular resolution *in vitro*<sup>56</sup>.

To demonstrate the efficacy of thermogenetics in mammals, a targeted heat delivery system is required. For this purpose magnetic particles can be targeted to these ion channels. Once attached, an alternating magnetic field (AMF) can be applied which causes the particle to heat as a result of

hysteresis power loss (described in detail in chapter 2). This was first demonstrated *in vitro* where HEK293 cells were transduced with the TRPV1 channel and were also made to express biotin<sup>57</sup>. These cells were then cultured with manganese ferrite nanoparticles conjugated with streptavidin, which binds to biotin. When an AMF was applied, cells labelled with magnetic nanoparticles experienced an increase in calcium concentration whereas no response was observed for non-labelled cells.

The efficacy of this technique was then demonstrated *in vivo* by regulating plasma glucose levels in mice<sup>58</sup>. HEK293T cells were made to express a TRPV1 channel engineered with an extracellular His epitope tag (TRPV<sup>HIS</sup>). Rather than biotin, the cells were made to express a calcium dependent human insulin construct. For *in vitro* testing the cells were then incubated with magnetic nanoparticles conjugated with the antibody anti-His to directly target the TRPV1<sup>HIS</sup> channel. After application of an RF field (465 kHz, 5 mT) an increase in proinsulin release and insulin gene expression was observed. A PC12 cell line expressing the same TRPV<sup>HIS</sup> and insulin construct was then created and subcutaneously injected into the flanks of mice to form tumours. The tumours were subsequently injected with either PBS or a magnetic nanoparticle solution and found that RF application caused a significant increase in plasma insulin and decrease in blood glucose when nanoparticles were injected. This was taken a step further a few years later in elegant fashion<sup>59</sup>. An adenovirus of expression GFP-TRPV1/GFP-ferritin, was injected into the ventromedial hypothalamus of glucokinase-Cre mice, causing the neurons to express TRPV1 channels engineered with GFP whereby a ferritin nanoparticle was attached. This meant that magnetic nanoparticles were already present requiring no more injections. This part of the hypothalamus contains glucose sensing neurons, so when an RF field was applied an increase in blood glucose was observed, showing that thermogenetics can be a powerful investigative and therapeutic tool.

The main limitation of optogenetics is the inaccessibility of deep brain regions. Taking advantage of the non-invasive nature of thermogenetics, stimulation of the hippocampus was demonstrated<sup>60</sup>. Cells were again made to express TRPV1 channels but the particles were not targeted specifically to the channels but merely injected at the same site four weeks after viral transduction of the ventral tegmental area. They found that applying an AMF in successive 10 second bursts in 60 second intervals was enough to trigger trains of action potentials.

While it has been demonstrated that thermogenetics can be used in deep brain regions, there are still a few drawbacks. First the time scale of stimulation is slower than optogenetics. Light can be pulsed down to the millisecond timescale matching the action potential of neurons, whereas thermogenetic stimulation is in the order of seconds as it is dependent on the rate of change of

temperature. It has also been shown that optogenetics can also be combined with fMRI to investigate neural networks<sup>61,62</sup> which would not be possible with magnetic nanoparticle techniques as the reduction in signal caused by the particles is much larger than the signal change due to blood flow (the BOLD signal). Importantly for the work carried out in this thesis, thermogenetics also suffers from the other limitation of optogenetics, genetic modification of cells. There is a risk that expression of these exogenous proteins at high levels can lead to non-physiological activity and adverse effects on the cells. As such, an alternative stimulation mechanism that does not rely on genetic modification would be preferable.

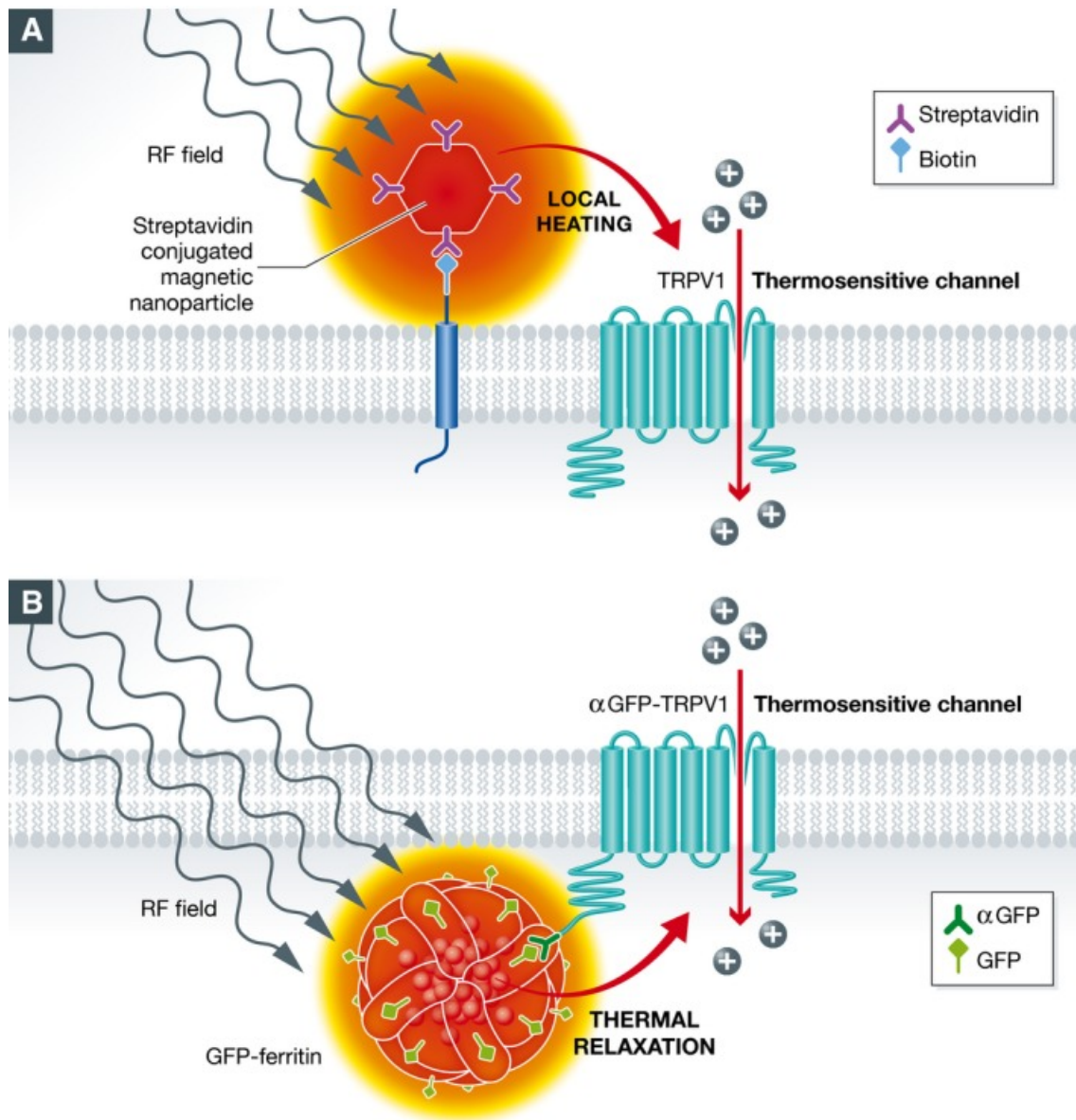


**Figure 1.3.** Edited from Nimpf and Keays<sup>63</sup>. **A)** Magnetic particles conjugated to streptavidin or **B)** a GFP-ferritin particle can be heated by applying radiowaves to cause the thermosensitive channel TRPV1 to open.

### 1.3.3.2 Mechanical stimulation

The majority of cells are in some way mechanosensitive so that they can adapt to changes in pressure of the local environment. There are then naturally occurring receptors within a cell that are sensitive to mechanical stimulation. Integrin appears to play a key part in sensing changes in pressure and has therefore been the target for most magnetic particle techniques using mechanical stimulation. Integrin is also present in most cell types. As a result magnetic particles have been used to stimulate a whole range of cells *in vitro* including: Fibroblasts<sup>64</sup>, Mesenchymal stem cells<sup>65</sup>, endothelial cells<sup>66,67</sup>, smooth muscle cells<sup>68</sup>, astrocytes<sup>66</sup> and neurons<sup>69</sup>. Force is applied to the cell using a static external magnetic field which can either twist the particle (apply torque) or apply a translational force which then deforms the membrane and forces ion channels to open. Particles were then coated either with collagen<sup>64,66,70</sup>, a peptide ligand<sup>71</sup> or an antibody<sup>72</sup> to attach to the cell. Upon mechanical stimulation, changes in calcium concentration, potassium and membrane potentials were reported.

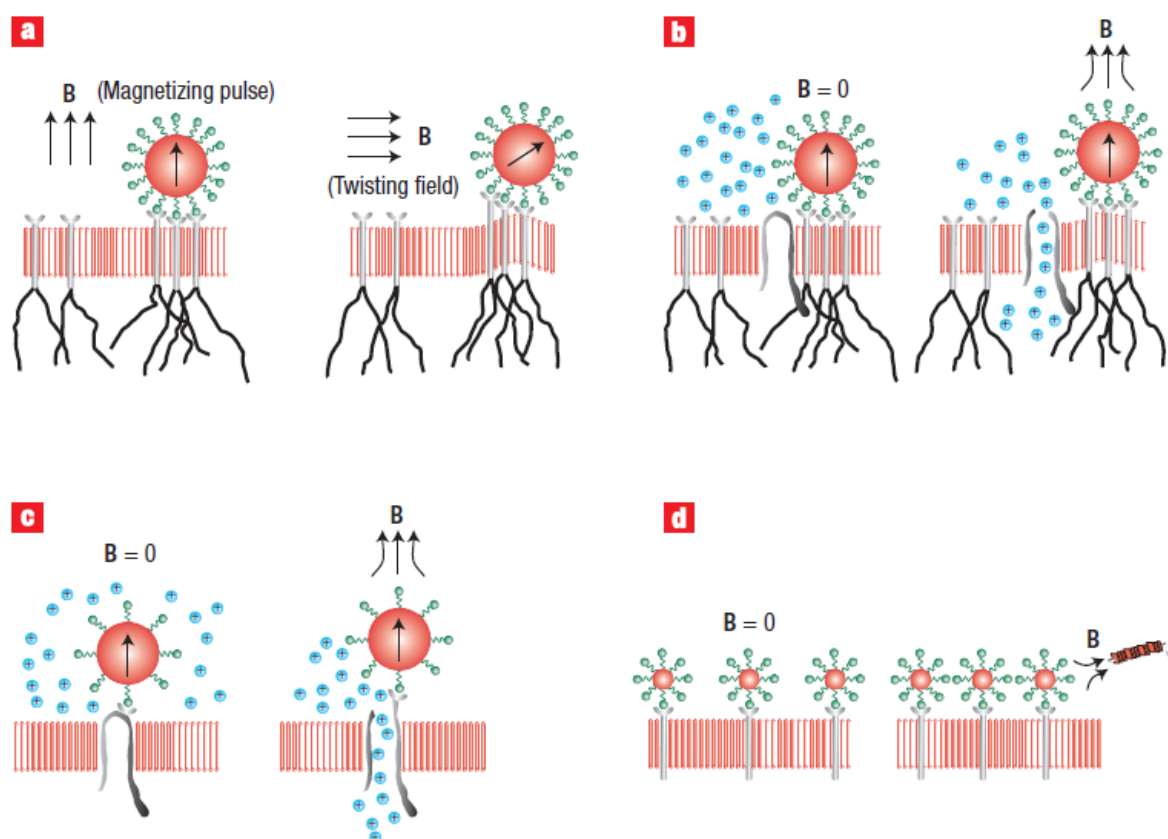


**Figure 1.4.** Taken from Dobson 2008. Schematic showing four different magnetic particle actuation processes: **A)** Magnetic particles bound to a cell surface receptor can be rotated by first orientating with an initial magnetising pulse followed by a twisting field to deform the cell membrane. **B)** A translational force can be applied to magnetic particles attached to proteins on the cell membrane to open nearby ion channels. **C)** an ion channel can be opened when a translational force is applied to a magnetic particle directly attached to that channel. **D)** Magnetic particles can aggregate in the presence of a magnetic field to increase receptor or protein proximity on the cell surface.

Early studies during the 1990's demonstrated the efficacy of mechanical stimulation using particles that were bound to integrins, transmembrane receptors that form links with the cytoskeleton, play important roles in extracellular signalling and are known mechanoreceptors<sup>51,73</sup>. Mechanical stimulation has been shown to trigger signalling events such as rises in intracellular  $\text{Ca}^{2+}$  concentration<sup>64,66,74,75</sup>, cyclic AMP signalling cascade<sup>76</sup> and activation of tyrosine kinase Src<sup>77</sup>. Particles were typically micron sized, coated with integrin targeting proteins such as collagen and actuated by a magnet that could generate a strong magnetic field gradient across cells, resulting in forces in the nanonewton<sup>78</sup> or piconewton range<sup>74,75</sup> and stresses of a few pascals<sup>75,76</sup> to tens of pascals<sup>64,77</sup>. These forces deform the cytoskeleton which activates the signalling event. More recent studies have investigated the forces needed to remotely control calcium influx of neurons with particles coated with either starch, chitosan or thiol<sup>79,80</sup>. They found that force had a sigmoidal relationship on calcium influx, suggesting that forces of 200-350 pN would be sufficient to stimulate a 20% increase in peak fluorescent signal. Fluorescent imaging of calcium flux is a well-established method for investigating cell excitability and as such is used in chapter 4 in determining the forces needed for the stimulation of astrocytes.

While this demonstrates a cellular response to mechanical stimulation, integrins are present in nearly all cells. To achieve cell specific stimulation, like both optogenetics and thermogenetics, endogenous mechanosensitive channels have been transduced. TREK-1, a TWIK-related potassium channel highly expressed in the brain has accrued particular interest for mechanical actuation<sup>81</sup>. This began with a study similar to the thermogenetic approach by Stanley et al, where modified TREK-1 channels were transduced expressing a His repeat in an extracellular loop<sup>82</sup>. Magnetic nanoparticles conjugated with the anti-His antibody targeted the TREK-1 channels which when a magnetic field of 80 mT was applied with a gradient of roughly 5.5 T/m, transient currents were recorded across the activated cells. Later studies have stimulated unmodified TREK-1 channels to promote differentiation of bone marrow stromal cells and human MSC's. As bone relies on mechanical stimuli to form and maintain functional tissue, mechanical stimulation of human MSC's transduced with TREK-1 implanted into an *ex vivo* chick fetal femur appears to promote mineralisation for bone regeneration. Controlling the differentiation of stem cells once at their target site is an exciting possibility in improving reparative medicine. Mechanical stimulation of targeted modified human



bone marrow stromal cells injected subcutaneously into rats appeared to show signs of differentiation<sup>83</sup>. Other various signalling proteins have also been targeted that are not known for their mechanosensitivity to induce clustering of membrane receptors and aggregation or translocation of intracellular proteins.

The TRPV1 channel has also been utilised for mechanical stimulation. Stanley et al, alongside thermal stimulation used the same GFP-TRPV1/GFP-ferritin to investigate mechanical stimulation in HEK cells<sup>84</sup>. An electromagnetic needle was used to generate a static magnetic field gradient to produce a force >10 pN on the ferritin to elicit a rise in  $[Ca^{2+}]_i$ . A permanent magnet was then used to apply a force for 5 s every 2 minutes for 1 hour to stimulate the release of proinsulin from the transfected cells. A later study by the same group also showed an increase in  $[Ca^{2+}]_i$  and induced an inward current in transfected neurons when a magnetic field was applied for 5 seconds<sup>59</sup>. Neuronal inhibition was also demonstrated using a mutated anti-GFP-TRPV1/GFP-ferritin. Brain slices were then used containing neurons transfected with either anti-GFP-TRPV1/GFP-ferritin or anti-GFP-TRPV1<sup>mutant</sup>/GFP-ferritin where increased firing rates and increased or decreased membrane potentials were observed respectively when a magnetic field was applied. Stimulation or inhibition occurred within 2 seconds after the onset of field application. This same study culminated with *in vivo* behavioural tests, whereby the fringe field of an MRI machine was used to generate the magnetic force. After 20 minutes in the fringe field (0.5 – 1T), mice expressing anti-GFP-TRPV1/GFP-ferritin or the mutant form in their glucose sensing neurons experienced a significant increase or decrease in their food intake.

ISCA1, an iron sulphur cluster assembly protein identified as a sensor for geomagnetic navigation in animals<sup>85</sup> has also been tested for mechanical stimulation, albeit controversially. As the name suggests, this protein has within it naturally forming iron sulphur clusters on which a magnetic force can act. Much like the TRPV1 studies, Long et al observed increases in  $[Ca^{2+}]_i$  in HEK293 cells and action potentials could be triggered in cultured neurons when a relatively small magnetic field (< 2.5 mT) was applied<sup>86</sup>. When taken *in vivo* using *C. elegans* (roundworm), they found that transduced muscle cells would contract simultaneously upon magnetic field application resulting in reduction in body length. Stimulation of transfected neurons also appeared to elicit withdrawal behaviour. This paper however was found to violate an apparent research agreement with the group who first identified the protein as a magnetosensor<sup>87</sup> who later reported that despite testing the same cell types, two different calcium imaging methods and different magnetic application regimes, magnetic stimulation was not possible with ISCA1 (MagR) alone<sup>88</sup>, directly contradicting Long et al.

#### 1.3.3.3 Called into question – Impossible physics?

In a rather damning report titled “Physical limits of magnetogenetics”, Meister goes as far as debunking the whole concept of genetically encoded magnetic stimulation via both heat and force using transduced proteins containing either a single ferritin or iron sulphur cluster<sup>89</sup>. While the papers themselves make little to no attempt to measure the force or heat on the particle, Meister reveals that both mechanisms generate values multiple log units lower than those stated in the literature. The force on a single ferritin particle for example is around  $7 \times 10^{-23}$  N, which is at least 9 orders of magnitude lower than the piconewtons that have been stated in previous studies. While the maximum theoretical temperature increase is around  $1.5 \times 10^{-10}$  K, 9 orders of magnitude lower than the required 5 K that has been reported to activate the TRPV1 channel<sup>90</sup>. Meister concludes that if the reported phenomena do in fact occur, they must have completely different causes than the forces or heat generated from the particle. Considering the journals these studies have been published in are relatively high impact factor (Nature/Science etc), the importance of quantifying the mechanism by which a cell is stimulated must be emphasised. As such the focus of chapter 4 is almost entirely on the quantification of the minimum force threshold for the mechanical stimulation of astrocytes using magnetic particles. This threshold is then used in chapter 5 to demonstrate our magnetic particle stimulation technique *in vivo*. Chapter 6 also focus on the forces applied to larger particles and how they can be maximised in order to be moved through tissue. The heating characteristics of these larger particles are then explored in chapter 7, measuring the absolute temperature changes of the particle to ensure it delivers enough heat to cause cell death.

The advantage of mechanical stimulation over the thermogenetic approach is it's faster action. An AMF application of 5 seconds was needed for a rise in  $[Ca^{2+}]$  in cells transfected with TRPV1 channels<sup>59,60,84</sup> while some studies have shown an almost immediate response to mechanical stimulation<sup>64,66,78</sup>. While magnetic particles have been utilised for exploring the mechanical properties of cells, their application in neuroscience has been limited. The few existing studies demonstrating remote brain cell control have shown its potential but either hold the same drawback as optogenetics in that foreign proteins need to be introduced into the cells, or they lack cellular

specificity. We therefore look to address these issues in chapters 4 and 5 by developing a technique for remote mechanical stimulation using antibody coated magnetic particles that bind selectively to astrocytes, the most abundant form of glial cell in the brain. Using the antibody ACSA1, the particles will target the endogenous GLAST protein naturally expressed by astrocytes, negating the need for viral introduction of foreign proteins to enable investigations into astrocyte function in their most natural physiological state. By determining the forces needed for controlling calcium flux (chapter 4) and the release of ATP (chapter 5) the stimulation mechanisms can be better understood, culminating in delivering a physiological response equivalent to that possible with optogenetics.

## 1.2 Brain cancer

So what tools do we possess for manipulating abnormal brain cells? While many of the techniques introduced in this chapter have been tested for a variety of pathologies including Parkinsons, epilepsy, tremor and obsessive compulsive disorder, this section focuses on a pathology that suffers the highest mortality rates of the lot and would benefit the most from a novel minimally invasive technology; brain cancer.

Brain tumours are one of the 10 most common forms of cancer with over 11000 patients diagnosed every year in the UK<sup>91</sup> and a 10 year survival rate of around 14%. Factors that affect the individual's survival rate include: age, tumour type, tumour grade, sex, type of treatment and level of fitness. Taking the most common form of brain tumour astrocytomas, which make up over 80% of brain tumours, more than 90% will survive up to 5 years for grade 1 astrocytomas but for grade 4 (Glioblastoma multiforme, GBM), which make up 75% of astrocytoma cases, the survival is around 5%. Considering the average 10 year survival rate for all types of cancer is 50%<sup>92</sup>, there is clearly a need for improvement.

Astrocytomas, the most common primary brain tumour is within the group of tumours called gliomas, which are graded from 1 - 4 according to their histology and as such define their behaviour. For slow growing low grade tumours, immediate treatment is not necessarily needed as surgeons may choose to use MRI to monitor its growth. Nevertheless around 50% of patients with low grade tumours have surgery within 2-3 years of monitoring. When surgery is needed, the goal of the surgeon is to remove as much of the tumour as possible while preserving the surrounding healthy tissue. In some cases patients are asked to take Gliolan, a fluorescent dye taken up by gliomas to aid visualisation of the tumour boundary during surgery using a fluorescent microscope which has been shown to improve complete resection rate and progression free survival at 6 months<sup>93,94</sup>. To determine whether complete resection was achieved, post-operative MRI is normally performed within 72 hours. Total resection rates range from 20-30% to 50-70% depending on the study and inclusion criteria. Surgery is then followed by radiotherapy and chemotherapy.

Grade 4 astrocytomas are usually called glioblastoma or GBM. The standard treatment for GBM at present is maximal surgical resection followed by radiotherapy plus concomitant and maintenance

temozolomide (TMZ) chemotherapy, despite TMZ only improving 5 year survival by 20%<sup>95</sup>. Most patients experience tumour progression and near universal mortality with a median survival rate of less than 15 months<sup>96</sup>. No standard of care has been established for recurrent or progressive GBM. Routine MRI is used to image the tumour during treatment and is recommended every 2-4 months<sup>97</sup>. Part of the difficulty comes in defining the tumour boundaries as gliomas can infiltrate diffusely through the brain and white matter<sup>98</sup>. Volumetric measurements of the tumour are typically performed on contrast enhancing regions on MRI, however regions where tumour infiltration is diffuse does not enhance the signal resulting in an underestimation of the full extent of tumour burden<sup>99</sup>. Even if the postoperative image shows complete resection, it is likely that microscopic residuals will remain, necessitating the combined radiotherapy/chemotherapy approach. It is generally accepted that at least 70-80% tumour resection provides measureable survival benefits, with increasing benefits with higher levels of resection<sup>100,101</sup>. The heterogeneity of the tumours make them incredibly difficult to predict therapeutic resistance, which combined with their aggressive development, difficulties in complete resection and drug delivery all add to the considerable complexity in treating this nemesis of a disease<sup>102</sup>. As such, emphasis has swung towards palliative care and focusing on improving patient's quality of life.

### 1.2.1 Surgery and standard practice

For the majority of patients with brain tumours, surgery will be the first line of treatment unless the patient is deemed not fit enough to undergo such an invasive surgical procedure. The surgeon must then decide whether the need to resect the tumour right up to the tumour boundaries outweighs the risk of damaging the surrounding tissue and the impact on the patient's quality of life. It is this need for precision, which in turn reduces the damage to healthy tissue, that has spurred the development of new neurosurgical and neuroablative technologies. As these technologies develop, so do their accuracies and the control available to the surgeon, in the hope that eventually mortality rate can be changed. In addition, considering the relentless complexity of treating GBM and other advanced and aggressively malignant tumours, development of minimally invasive techniques could allow for treatment at an earlier stage where tumours have more discrete boundaries, enabling the surgeon in removing a higher percentage of the tumour without increasing the risk of damage to eloquent tissue.

At present the most common form of surgery is a craniotomy, where part of the skull is removed so that the surgeon can operate on the brain. Image guided tumour and craniotomy localisation greatly increases the accuracy of the surgery, with reported localisation errors of over 10 mm without image guidance<sup>103</sup>. Sometimes awake craniotomy's are performed when the tumour is in close proximity to important eloquent brain regions<sup>104</sup>. A microscopic lens can be used, as well as fluorescent dyes to help the surgeon delineate between healthy and tumour tissue. For deep lying tumours such as in the ventricles, neuroendoscopy can be performed. An endoscope (either rigid or bendy) made up of a long tube, camera and eyepiece is inserted through a burr hole with tiny forceps and scissors at the end to cut away the tumour. For pituitary tumours the surgeon may enter through the nose (transphenoidal surgery) instead of through the skull as the pituitary gland is located at the front of the skull beneath the brain. The main risks of this route is damage to the optic nerve and higher risk of leakage of cerebral spinal fluid (CSF).

While neuroendoscopy reduces damage to eloquent healthy tissue, it reduces the precision of the surgery by increasing the burden on the surgeons own ability. Additionally, even if the post-operative MRI indicates complete resection, the standard of practise is still for the patient to undergo radiotherapy plus concomitant and maintenance chemotherapy in order to kill the microscopic residuals of the tumour left after surgery. Fractionated conformal radiotherapy is normally performed, delivering around 2 Gy 5 days a week for 6 weeks to the gross tumour volume

with a 2-3 cm margin for the clinical target volume<sup>95,96,105</sup>. The benefit of conformal radiotherapy over conventional external beam radiotherapy is the improved drop off in dose from the tumour margins. TMZ is taken alongside radiotherapy, typically around 75 mg/m<sup>2</sup> a day for 6 weeks, and often followed by 6 maintenance cycles (150-200 mg/m<sup>2</sup> daily for the first five days of a 28 day cycle), resulting in a 2 year survival rate increase from 10.4% with radiotherapy alone to 26.5% with combined RT and TMZ<sup>95</sup>. The duration of the maintenance cycles remains a topic for debate, while dose dense TMZ which results in prolonged depletion of MGMT in blood mononuclear cells and the tumour does not significantly affect overall survival (OS)<sup>106</sup> but did confirm the prognostic significance of MGMT methylation (OS = 21.2 vs 14 months). Any chemotherapeutic or cellular therapy for the brain also has an additional obstacle to overcome, the blood-brain-barrier, a layer of endothelial cells along the walls of the blood vessels which separates the blood from the cerebral spinal fluid (CSF)<sup>107</sup>.

Image guidance, particularly intraoperative MRI has led to an improvement in tumour localisation and higher resection rates<sup>108</sup>. Nimsky et al also found that residual tumour volume was significantly lower after additional resection using iMRI compared to the first iMRI scan and of the 17 patients where complete resection was achieved, 7 of them were attributed to additional resections with iMRI<sup>109,110</sup>. Given the impact of intraoperative imaging for increasing tumour resection up to and above 90% of the tumour volume, could the surgeon use alternative image guided techniques for destroying the tumour tissue other than surgical removal to increase that percentage further?

## 1.2.2 Focal ablation techniques

It is generally accepted that total resection of the tumour is the best approach for improving prognosis for brain tumours. However, conventional surgical techniques are limited by the need to preserve the function of surrounding healthy tissue which often results in incomplete resections. While keyhole surgery or neuroendoscopy is less invasive, it dramatically increases the difficulty of performing the resection, placing even more demand on the surgeon's abilities. As a result a number of different focal ablation techniques have been tested for the treatment of brain tumours as well as other pathologies, in an attempt to aid the surgeon in delivering precise regions of cell death in a less invasive manner. These techniques destroy tissue via three main processes: ionising radiation, thermal ablation or cryoablation (freezing). For thermal ablation, tissue heated above 60°C for 1 second will be irreparably damaged while temperatures above 50°C will do so within a matter of minutes. Tissue damage is normally estimated using models such as the cumulative equivalent minutes spent at 43°C (CEM43)<sup>111,112</sup>. For cryoablation, it is generally accepted that irreversible damage is caused at temperatures below -40°C. This section provides an overview of the existing techniques available in some clinics along with a selection of promising emerging techniques that aim to eradicate brain tumours in a less invasive manner than a conventional craniotomy and with less off target effects than chemotherapy and radiotherapy. After this section I will introduce magnetic thermoseeds (1.4.3.6), which is the basis for the particles used in our new method for minimally invasive tumour therapy using MRI.

### 1.4.2.1 Stereotactic radiosurgery

As opposed to whole brain radiotherapy, stereotactic radiosurgery uses a focused dose of ionising radiation in combination with medical imaging techniques such as fluoroscopy in the efforts to deliver a lethal dose to the affected tissue while minimising the dose to surrounding healthy areas. This is the most clinically established focal ablation technique and is normally used as a secondary treatment to chemotherapy and radiotherapy. The oldest running system is Gamma knife™, a non-invasive intracranial technique invented and developed by the Swedish neurosurgeon Lars Leksell. The first Gamma knife system was installed all the way back in 1968 consisting of two collimators which collimated a beam of photons from a cobalt source, with a secondary collimator attached to the treatment couch. At the time the ellipsoid in which 50% of the dose fell was 3 x 3 x 7 mm<sup>113</sup>,



while the full width half maximum of modern day systems have a precision of around  $6 \times 6 \times 5 \text{ mm}$ <sup>114</sup> claiming an actual spherical ablation volume as small as 0.3 mm.

Other stereotactic radiosurgery systems including Cyber knife<sup>115</sup> and LINAC (linear accelerator) systems have comparable focal ellipsoids. Recent developments of the LINAC system has been driven towards a combined MRI-LINAC systems due to the superior soft tissue contrast provided by MRI<sup>116,117</sup>, however issues with the divergence of the concentrated dose persist due to the strong magnetic fields in the MRI bore. These systems have been used to treat a range of pathologies including brain tumours<sup>118,119</sup>, trigeminal neuralgia<sup>120</sup>, arteriovenous malformations<sup>121,122</sup> and have been tested for treating epilepsy<sup>123</sup> and essential tremor<sup>124</sup>. With around 370 Gamma knife treatment centres across the world Gamma knife is used on approximately 70,000 patients every year.

The benefits of using Gamma knife or equivalent systems is that they are non-invasive, allowing for the treatment of tumours inaccessible with conventional surgery. It can also ablate submillimetre regions of tissue and ablate multiple locations in one sitting<sup>125</sup>. The main drawback to these systems is their cost and availability. Whole treatment centres need to be installed and maintained involving substantial costs which can be a limiting factor for hospitals around the world.

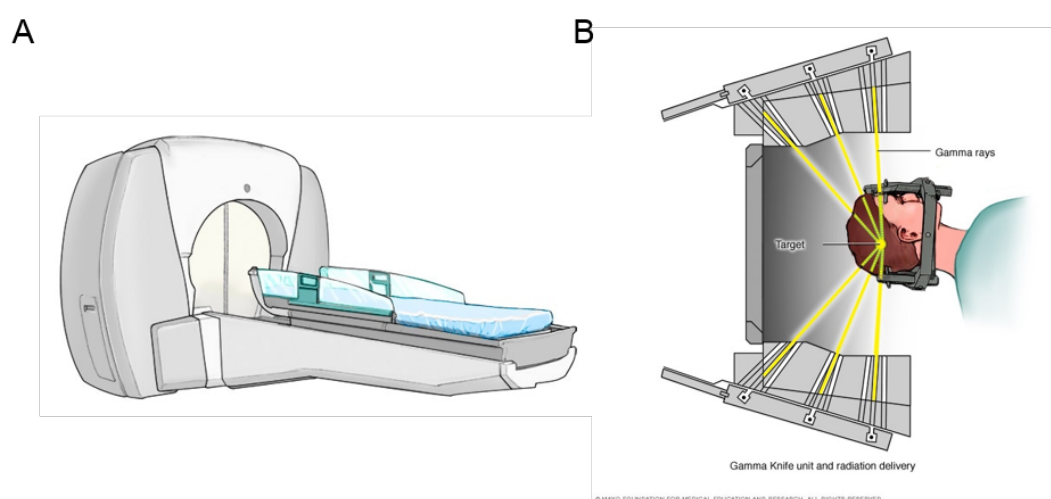


**Figure 1.5.** A) Image of the Gamma Knife system and B) diagram of the collimated beams of radiation to deliver focal ablation to a target region inside the patients head<sup>126</sup>.

#### *1.4.2.2 Interstitial laser ablation*

Interstitial laser ablation involves the implantation of optical fibres into the brain to ablate localised regions of tissue using high intensity laser light. One system Visualase has been introduced into specialised centres across the UK, its workstation shown in figure 1.5 . It consists of a 1-2 mm diameter catheter which is inserted stereotactically through a small burr hole using a robotic arm. Light energy is delivered to the surrounding tissue via an infrared diode laser which generates heat to cause coagulative necrosis<sup>127</sup>. This whole system is MRI compatible so that the insertion of the catheter can be guided in real-time with MRI, and the temperature monitored using MR-thermometry. Compared to conventional craniotomy, this technique is much less invasive leading to quicker post procedure recovery times for patients<sup>127,128</sup>. Patients considered for this treatment are those with deep seated tumours where standard craniotomy is difficult and risky. The ellipsoid of thermal ablation about the catheter tip is between 1 – 2.5 cm<sup>129</sup> and with MRI guidance can be delivered with submillimetre accuracy<sup>130</sup>.

Interstitial laser ablation has been primarily used for tumour surgery<sup>127,131</sup> however in the past few years there has been an emergence of its use in epilepsy surgery too<sup>131–134</sup>. Limitations of this system include the requirement for the insertion of multiple lasers to treat lesions with abnormal or non-spherical shapes where the entry point needs separating by  $\approx 3$  cm, increasing the risk of complications and invasiveness of this technique. This limitation is shared with any ablative technique that requires insertion of a tethered probe. Complications that have been reported include inaccurate catheter placement, haemorrhage and neurological deficits as a result of thermal injury<sup>135</sup>. While this technique holds promise in terms of the recovery times for the patient, inaccurate placement of the probe tip appears to be the main limiting factor at present.



**Figure 1.6.** Taken from LaRiviere and Gross, 2016<sup>134</sup>. **A)** Entire workstation of the Visualase system with computer, two monitors, a 15 W, 960 nm diode laser and peristaltic pump for saline coolant. **B)** Top monitor is shown and magnified in **C)** showing axial imaging plane. Four types of information can be shown at once: Phase image, thermal map, magnitude image and a rapidly acquired low resolution anatomical image which produces the phase image and an estimate for the irreversibly damaged zone.

#### *1.4.2.3 High Intensity Focused Ultrasound (HIFU)*

As a concept high intensity focused ultrasound is even older than stereotactic radiosurgery, being introduced in the 1940's as an approach for thermal ablation of various tissues. HIFU typically consists of a piezoelectric transducer that delivers ultrasound waves into tissue. Rather than being used for diagnostic imaging, ultrasound waves are concentrated to a focal point. The energy from the ultrasound waves get absorbed by the tissue, depositing heat to thermally destroy the tissue<sup>136</sup>. In terms of benefits this technique can be considered completely non-invasive as the transducer can be placed outside the head and unlike stereotaxic radiosurgery, does not use ionising radiation. Recent advances in ultrasound technology, software and real time monitoring have resulted in ultrasound induced thermal ablation being adopted for the treatment of essential tremor<sup>137</sup>, Parkinson's disease<sup>138</sup>, depression<sup>139</sup> and neuropathic pain<sup>140</sup>.

In terms of ablation volumes and accuracy for transcranial systems, one clinical study estimated a submillimetre mean targeting accuracy of 0.72 mm<sup>141</sup> with systems generally ablating an ellipsoid with diameters of 3-4 mm and lengths 4-5 mm. Another study states that, in general, hitting peak temperatures of 54-64°C creates a region of coagulative necrosis around 3-5 mm in diameter with a targeting accuracy of less than 1 mm<sup>142</sup>. The time taken for the focal zone to heat is in the order of seconds, however multiple sonication's are normally performed with the whole duration of the therapy lasting up to 5-6 hours<sup>137</sup>. This time scale, along with the size of the ablated ellipsoids are the main limiting factor of this technique, with intracranial systems capable of an ablation region of only a few millimetres in size<sup>142</sup>. However the fact that it is completely non-invasive means this technique still remains a promising technique and an active research field, constantly improving the technology as it currently stands.

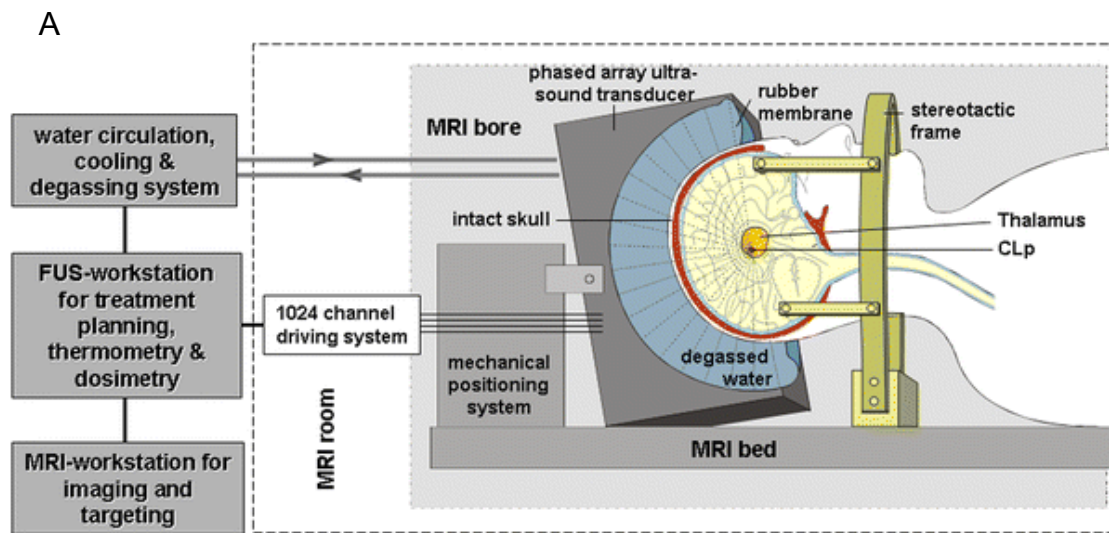


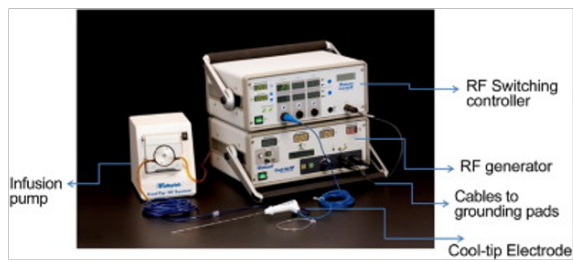
**Figure 1.7.** Taken from Martin and Werner, 2013<sup>142</sup>. **A)** Diagram showing patients head inside a half-spherical multielement phased array ultrasound transducer placed inside an MRI scanner. **B)** Photo of the ExAblate 4000 transcranial MRI-guided ultrasound surgery system (tcMRIGUS).

#### *1.4.2.4 Radiofrequency/microwave ablation*

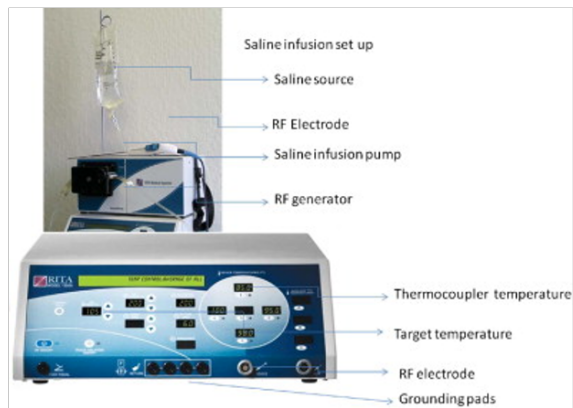
Radiofrequency ablation works by implanting an electrode into the target tissue connected to an RF-generator which induces a flow of RF current along the connecting cables to the electrode. The RF ablation probe acts as a cathode of an electrical circuit which is closed by placing dispersing pads on the patient's body (often the thighs)<sup>143</sup>. The small cross sectional area of the probe creates high energy flux around it while the larger area of the pads disperse the energy, concentrating the heat generation and tissue damage to the probe tip. The RF-current and voltage, and therefore heating, can be controlled by measuring the amount of electrical energy consumed and the temperature can be measured at the tip of the probe allowing for close real-time monitoring. The RF probe can also be used for electrical stimulation, which is useful for confirming the correct anatomical location or avoiding eloquent brain areas<sup>144</sup>.

The most popular use for RF ablation has been for liver tumour ablation<sup>145–147</sup> however it has also been used extensively for epilepsy<sup>144</sup>. It is considered relatively cheaper than other focal ablation techniques, with examples of different systems shown in figure 1.7, some of which are MRI compatible. Its main limitation again is delivering large homogenous ablation of tissue for volumes > 3 cm<sup>3</sup>, spurring the development of different electrode designs from monopolar to bipolar<sup>145,146</sup> to multi-tined expandable arrays<sup>147</sup> as opposed to implanting multiple electrodes. While the electrode itself heats rapidly, it still takes a long time for volumes > 3 cm<sup>3</sup> to be ablated, and often leads to carbonisation of the tissue closest to the electrode when it reaches around 100 °C which in turn limits the ablation volume<sup>143</sup>.

A



C



B

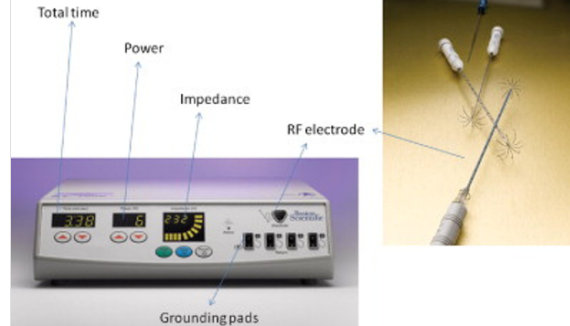


**Figure 1.8.** Examples of different RF ablation systems taken from Hong and Georgiades, 2010<sup>143</sup>. Photos of the **A)** Covidien Cool-Tip RF ablation system, **B)** Boston Scientific 'LeVeen' RF ablation system and **C)** Angiodynamics RITA RF ablation system.



#### 1.4.2.5 Cryoablation

Much like RF ablation, a probe is inserted into the target tissue except in cryotherapy, cell death is achieved by alternate cycles of freezing and thawing. It is generally accepted that a temperature of  $-40^{\circ}\text{C}$  is needed to achieve cell death<sup>148</sup>. Initially extracellular ice crystals form, along with dehydration and shrinkage of cells due to the passage of water down osmotic gradients. At colder temperatures intracellular ice crystals form leading to organelle and cell disruption. Mitochondria are also damaged, resulting in apoptosis. Vascular infrastructure can also be disrupted along with endothelial damage and intravascular thrombus formation, leading to tissue ischemia<sup>149</sup>. Maintaining freezing temperatures for  $> 1$  minute leads to more complete cell destruction. A slow thawing cycle should then be employed, causing a necrotic cascade as cells expand<sup>150</sup>.

During freezing an ice ball forms with a temperature gradient around the probe tip. A typical ellipsoid where temperatures of  $-40^{\circ}\text{C}$  are achieved is around  $10 \times 10 \times 20$  mm about the tip, decreasing to  $0^{\circ}\text{C}$  over a volume approximately  $30 \times 30 \times 40$  mm with freeze-thaw cycles lasting around 10 minutes. MRI guidance has been explored for interstitial cryotherapy of the brain as the location of the ice ball can be clearly delineated due to a complete drop out in signal of frozen tissue<sup>151</sup>. Again the main limitation of this technique is placement of the probe, while the need for multiple freeze-thaw cycles means that surgery will take multiple hours to complete.

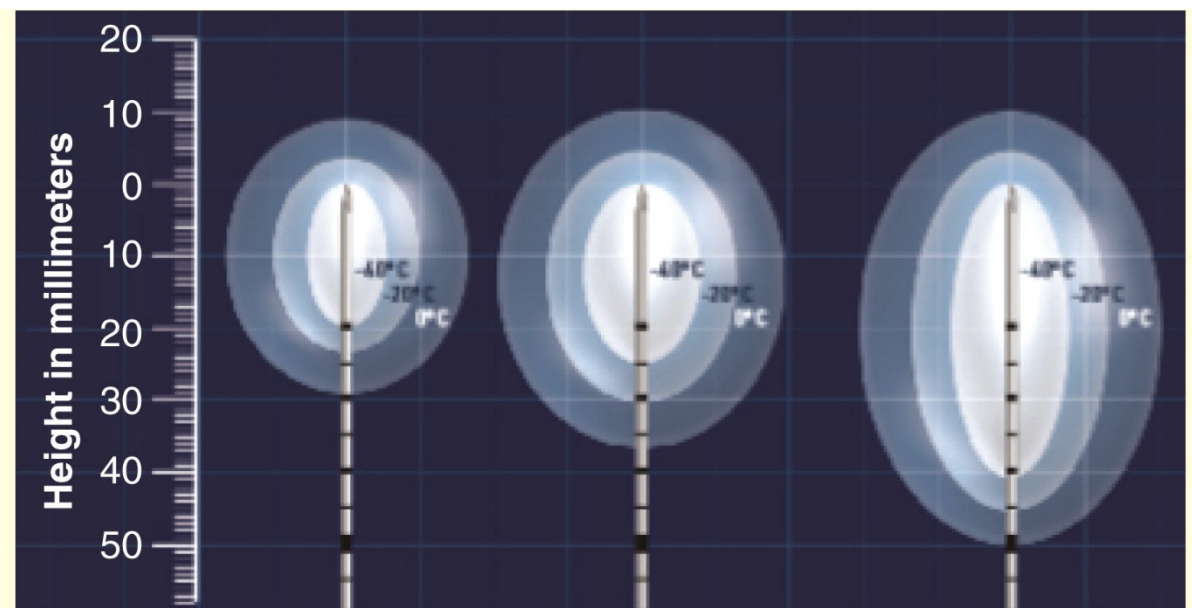


**Figure 1.9.** Taken from Shah et al, 2014<sup>148</sup>. Diagram showing ice ball formation and temperature at varying distances from the probe.



### 1.2.3 Magnetic thermoseeds

The idea of using magnetic thermoseeds grew in the 1990's. Rather than inserting a probe into the tumour, millimetre sized untethered seeds could be implanted into the affected tissue. The seeds would then be heated remotely by applying an alternating magnetic field (AMF) to either cause localised cell death or induce hyperthermia around the seed<sup>152</sup>. The main mechanism for the heating of the seeds is via induced eddy currents on the seed surface, however depending on the material a proportion of heating will also occur from hysteresis losses. These mechanisms are discussed in more detail in chapter 2. The size, material, shape and orientation of the seed with respect to the AMF will affect the heating capabilities of the seed. Any non-spherical seed needs to be aligned parallel to the AMF for optimal heating<sup>153</sup>. The majority of the work focused on thermos-regulatory materials that when their curie temperature is reached, the alignment of domains is lost and do not heat further, negating the need for real-time temperature measurements<sup>154–157</sup>. To achieve high and uniform temperatures over a whole region of tissue many studies used arrays of seeds or rods. A number of preclinical studies have investigated the use of needle shaped thermoseeds for focal ablation in the liver<sup>158,159</sup>, prostate<sup>157</sup>, brain<sup>156</sup>, mammary tumours<sup>160</sup>, abdominal tumours<sup>161</sup> and the eye<sup>162</sup>, to name a few.

The benefits of implanted seeds is their untethered nature, which reduces risk of infection and allows their position to be changed after implantation to ensure ablation is delivered to the correct region. The main difficulty in accurate ablation comes from accurate placements of the seeds themselves. Only a small number of clinical trials have used thermoseeds for the treatment of prostate cancer<sup>163</sup> and brain metastases<sup>164</sup> in combination with radiotherapy. The prostate study resulted in average PSA (prostate specific antigen) levels, a biomarker for prostate cancer, decreasing from 11.6 ng/mL to 2.4 ng/mL (4 ng/mL or below is considered normal) 3 months after a treatment of 6 weekly sessions. The brain metastases study resulted in 2 complete responses, 1 minor response and 3 progressions. Both trials however reported issues with seed migration after implantation. To overcome migration issues thermoseeds must either be removed from the body after treatment or they must have the ability to be manipulated and manoeuvred after implantation. The idea of magnetic stereotaxis was therefore tested. Static magnetic field gradients could be used to move the seed towards a target location while an AMF is applied to cause hyperthermia<sup>165</sup>. A propulsion and heating coil was built to be used alongside X-ray fluoroscopy to track the location of 3 mm and 5 mm NdFeB cylinders as it was manoeuvred *in vivo* through dog brain<sup>166</sup>. The seeds could be inserted through a burr hole into the occipital lobe, moved towards a pre-determined destination and then removed at another location. Remarkably, histological analysis revealed little to no haemorrhaging as a result of moving the thermoseeds with only a small track visible<sup>165</sup>.

While each component of movement, detection and heating was demonstrated this technique was never taken further in the brain. Instead this work led to the company stereotaxis, which uses external magnets to guide a magnetically tipped catheter for cardiac ablation for arrhythmias<sup>167</sup>. The most likely reason for this is the lack of soft tissue contrast from fluoroscopic or CT images, which is imperative for navigation of the seeds through the brain. While the dog brain studies used pre-acquired MRI images and fiducial markers to register with fluoroscopic images, there are inherent registration errors which would reduce the overall accuracy of the technique. All the focal ablation therapies introduced in this chapter use image guidance for accurate placement of the ablation device, often with MRI as the imaging modality of choice because of its good soft tissue contrast compared to other modalities.

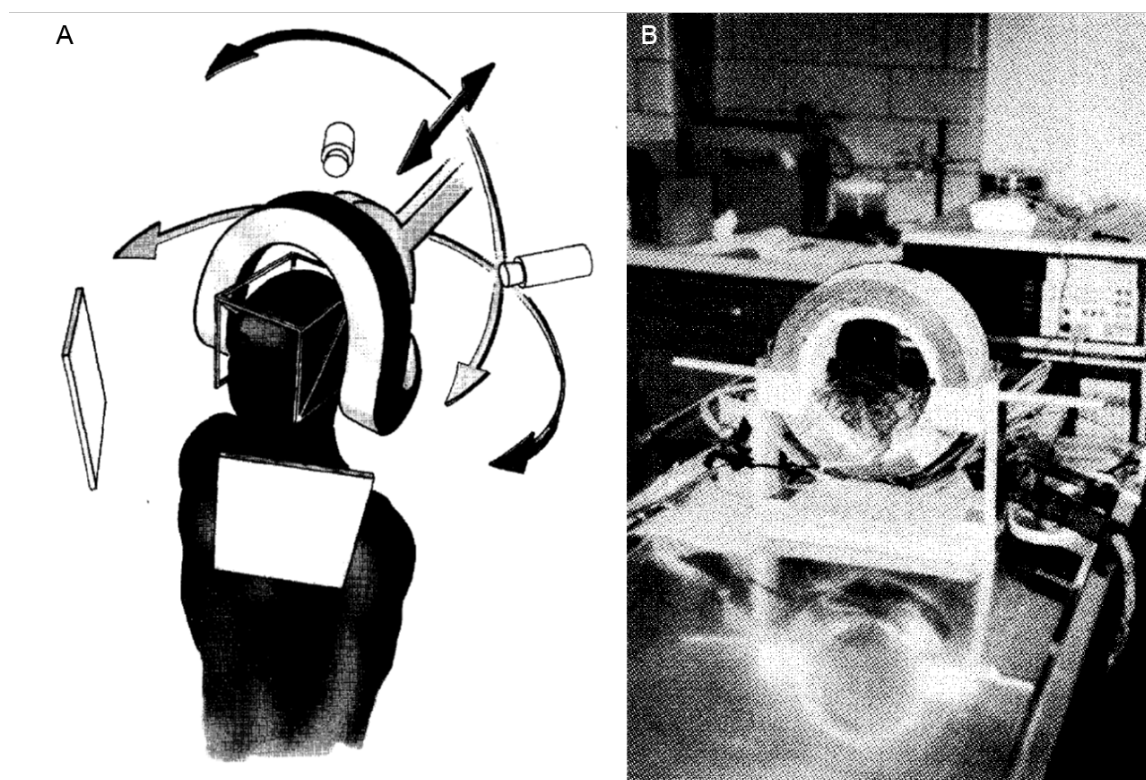


**Figure 1.10.** Magnetic Stereotaxis concept taken from Grady et al, 1989. **A)** Graphic of how the goniometric motions of the magnetic manipulation coils would be guided by stereotactic fluoroscopy. With a stereotaxic frame positioned about the head, the coils outside have 3 degrees of freedom as indicated by the arrows and the position of the thermoseed is tracked with the fluoroscopes. **B)** Photo of the manipulation coils on the operating table.

The idea that magnetic thermoseeds can be controlled remotely using magnetic field gradients to move them through the brain and deliver focal ablation forms the basis of chapters 6 and 7. In chapter 6, rather than use water cooled electromagnets I explore the possibility of using the imaging gradients of an MR system to both image and propel millimetre sized particles through the brain. The combination of pre-acquired anatomical MRI images and real-time localisation methods allow the particle to be tracked and guided towards a target location. In chapter 7 the ability to heat the particle using alternating magnetic fields to deliver localised cell death is explored. The main benefits of this untethered approach is that by using MRI, the position of the seed can be controlled with a greater degree of precision than existing tethered methods. Rapid heating would also allow for ablation at multiple locations which would enable not only greater ablation volumes, but also non spherical tumours, negating the need for multiple probes to be inserted.

In order to develop new magnetic particles techniques for cell manipulation, the underlying physics involved must be fully understood. The next chapter therefore introduces the main physical principles to both generate a magnetic force on a particle and to cause them to heat with magnetic fields. Other applications of magnetic particles in medicine are also introduced.

## 2 Magnetic particles in medicine

The ability to manipulate brain cells in a minimally invasive manner would be of huge benefit to the neuroscience, neurology and neurosurgery communities. Magnetic particles have potential in this regard as their actuation can be controlled remotely via external magnetic fields that pass harmlessly through the body. This chapter will therefore give a general overview of the concepts of magnetism that are used throughout this thesis, followed by a selection of their most popular medical applications.

## 2.1 Definitions and basic principles

### 2.1.1 Magnetic fields

Magnetic fields are generated by moving electrical charges, be it a current carrying wire, or the orbital moment of electrons or the spin of atomic nuclei. Here, the basic principles of magnetism will be presented in their classical explanation in that, an electron orbit acts as a current loop which generates a magnetic field. The magnetic field induced by a moving electrical current is described by the Biot-Savart law:

$$\mathbf{B} = \int \frac{\mu_0}{4\pi} \frac{I d\mathbf{l} \times \hat{\mathbf{r}}}{r^2} \quad 2.1$$

Where  $\mu_0$  is the permeability of free space,  $I$  is the current in amperes,  $\mathbf{l}$  is the vector of the current carrying conductor, and  $\hat{\mathbf{r}}$  and  $r$  are the unit vector and distance between the current element and the point in space at which the field is evaluated respectively.

No explanation of magnetism would be complete without Maxwells equations. These four famous equations demonstrated that electricity and magnetism are intertwined phenomena, and have formed the basis of our understanding of electromagnetic radiation. These equations are commonly represented as:

$$\text{Gauss's law of electric fields:} \quad \nabla \cdot \mathbf{E} = \frac{\rho}{\epsilon_0} \quad 2.2$$

$$\text{Gauss's law of magnetic fields:} \quad \nabla \cdot \mathbf{B} = 0 \quad 2.3$$

$$\text{Faraday's law:} \quad \nabla \times \mathbf{E} = -\frac{d\mathbf{B}}{dt} \quad 2.4$$

$$\text{Ampere-Maxell law:} \quad \nabla \times \mathbf{B} = \mu_0 \left( \mathbf{J} + \epsilon_0 \frac{d\mathbf{E}}{dt} \right) \quad 2.5$$

Where  $\nabla$  is the gradient operator,  $\mathbf{E}$  is the electric field in volts per metre,  $\rho$  is the charge density in coulombs per metre cubed,  $\epsilon_0$  is the electric permittivity of free space and  $\mathbf{J}$  is the electric current density in Amps per metre squared.

In the context of this thesis, equations 2.3 and 2.5 are of most relevance for chapters 4, 5 and 6, while equation 2.4 is utilised in chapter 7. Gauss's law indicates that the divergence of a magnetic field in space is always zero. Magnetic field lines will always form closed loops, resulting in a net magnetic flux through any surface of zero, implying that magnetic monopoles cannot naturally occur. Faradays law indicates that an electric field can be created perpendicular to a time varying

magnetic field. The dynamo, an early electrical generator, is a prime example of Faradays' law at work. Coils of wire are rotated around a magnetic field source which causes the magnetic field experienced by the wire to vary with time. This change in magnetic flux generates an electrical current through the wire. The Ampere-Maxwell law is effectively the reverse of Faraday's law, in that a magnetic field can be produced by an electrical current and time varying electric fields.

Arguably the easiest way to examine a magnetic field is to measure the force a moving charge experiences when a magnetic field is present. A popular example of this phenomena is a compass needle orientating itself with the earth's magnetic field. The force experienced by the needle, or any magnetic material is given by the Lorentz force equation:

$$\mathbf{F}_B = q\mathbf{v} \times \mathbf{B} \quad 2.6$$

Where  $q$  is the charge in Coulombs,  $\mathbf{v}$  is the velocity in metres per second and  $\mathbf{B}$  is the magnetic flux density in Tesla.

### 2.1.2 Magnetic materials

All materials have a degree of magnetism and respond to a magnetic field according to its atomic structure and temperature. If a material is placed in a magnetic field of strength  $\mathbf{H}$ , it is each individual magnetic moment within the material that contributes to its overall response, with a magnetic induction:

$$\mathbf{B} = \mu_0(\mathbf{H} + \mathbf{M}) \quad 2.7$$

Where  $\mu_0$  is the permeability of free space and  $\mathbf{M} = \mathbf{m}/V$  is the magnetisation of the material which is described as the magnetic moment  $\mathbf{m}$  per unit volume  $V$ . The response of a particular material can then be classified by its volumetric susceptibility  $\chi$ , where:

$$\mathbf{M} = \chi\mathbf{H} \quad 2.8$$

Which describes the magnetisation  $\mathbf{M}$  induced in a material by an external magnetic field  $\mathbf{B}$ . Most materials can be placed into three categories of magnetic materials. In general most materials respond weakly to magnetic fields as each magnetic moment within the material tends to cancel each other out. However, in paramagnetic materials there is an imbalance in the orientation of magnetic moments contributing to a magnetisation which is proportional to the external magnetic field. In diamagnetic materials, this slight imbalance of magnetic moments orient themselves against the magnetic field. This is effectively Lenz's law on an atomic scale as it is the electron spin of an atom which contributes to the magnetic moment and acts as a current loop. The scale of magnetisation in diamagnetic materials is orders of magnitude lower than paramagnetism at around  $10^{-6}$ - $10^{-3}$  compared to  $10^{-6}$ - $10^{-1}$ . In some metals, the magnetic moments become much more ordered when an external magnetic field is applied and are considered ferromagnetic. In the absence of an external magnetic field, regions or domains of magnetic moments tend to align with each other but get cancelled out by other domains within the material. When a magnetic field is applied, these domains align creating a magnetisation  $\mathbf{M}$  of the material in and up to the order of  $10^4$  higher than other materials. Interestingly, when an external magnetic field is removed some of these domains remain aligned with each other giving the material a remnant magnetisation. The differences between these materials can be clearly delineated from their M-H curves.

### 2.1.3 Magnetisation curves

In ordered materials the susceptibility of the material depends on the external magnetic field  $H$  as well as the temperature. In diamagnetic and paramagnetic materials, this relationship remains relatively linear (figure 2.1), but for ferromagnetic materials the magnetisation may reach a saturation point where all of the domains are fully aligned. This produces a characteristic sigmoidal shape in the materials M-H curve. When the magnetic field is removed, ferromagnetic material does not return to zero magnetisation. Permanent magnets are therefore made of ferromagnetic material. To return to zero magnetisation, an opposing magnetic field is necessary as extra energy is needed to re-orientate the domains within the material. If an alternating magnetic field is applied, the magnetisation then follows a loop known as a hysteresis loop.

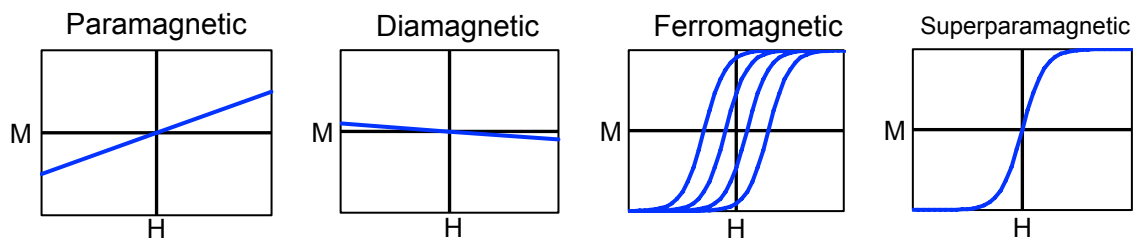


**Figure 2.1** Magnetisation (M-H) curves for paramagnetic, diamagnetic, ferromagnetic and superparamagnetic materials. Magnetisation of paramagnetic materials increases while diamagnetic materials oppose the applied magnetic field. Ferromagnetic materials exhibit hysteresis curves while superparamagnetic materials retain no magnetisation when the field is removed.

For magnetic particles, the size, shape and magnetic content will affect its M-H curve. Magnetic particles down to the micron size range will possess multi-domain cores and act in a ferromagnetic manner. However smaller particles in the nanoscale range will act as a single domain core and exhibit what is termed superparamagnetism. In this case the particles will become strongly magnetised when a magnetic field is present but has no residual magnetisation when the field is removed.



#### 2.1.4 Magnetic force

When a magnetic field is applied to a magnetic particle it acts as a magnetic dipole. The magnetic moment of the particle then experiences two forces: a torque or rotational force to align its dipole to the main magnetic field and a translational force which is always towards the region with the highest flux density (except for diamagnetic materials). For this to happen a magnetic field gradient must be present. The torque on the particle is given as:

$$\tau = \mathbf{m} \times \mathbf{B} \quad 2.9$$

And the translational force is<sup>168</sup>:

$$\mathbf{F}_m = (\mathbf{m} \cdot \nabla) \mathbf{B} \quad 2.10$$

Knowing that  $\mathbf{m} = V_m \mathbf{M}$  and using equations 2.7 and 2.8, this can be rewritten as:

$$\mathbf{F}_m = \frac{V_m \chi}{\mu_0} (\mathbf{B} \cdot \nabla) \mathbf{B} \quad 2.11$$

Equation 2.11 applies when the magnetic field strength is relatively low where the M-H curve is linear. In this case the amount of force applied to a particle is dependent on its size, magnetic content, the strength and the gradient of the external magnetic field. In the case where many particles are present in a small volume, they will agglomerate to form chains or clusters. When this occurs equation 2.11 still holds true because the cluster or chain acts as a single particle with its own magnetic moment. In the case where there is a higher magnetic field, such as inside the MRI bore, the particle will become magnetically saturated. In this case the force can be simplified in terms of the saturation magnetisation of the particle<sup>169</sup>:

$$\mathbf{F}_m = V_m (\mathbf{M}_{sat} \cdot \nabla) \mathbf{B} \quad 2.12$$

In this instance, only the magnetic field gradient and the saturation magnetisation will affect the force on a particle.

From equations 2.11 and 2.12 it is clear that the size of the particle is an important factor when it comes to applying force on a particle. Translational magnetic force is the essential component for the experiments conducted in this thesis. In chapters 4 and 5 which are concerned with developing a cell specific stimulation technique, the size of the particle must be within the same range, if not smaller (nanometres to microns), than the cell type investigated, in order that the particle does not dwarf the single cell. As multiple particles are likely to attach to a single cell it is also important that the total volume of those particles contribute to a magnetic force high enough to stimulate but not damage the interrogated cell. In chapters 6 and 7 where the goal is to penetrate tissue with magnetic particles, the forces needed far exceed that needed for cell stimulation (millinewtons

compared to femtonewtons). In this case the particle needs to be made of a magnetic material with very high magnetic saturation and of a size equivalent to the diameter of a biopsy needle (millimetres).

The shape of the particle is also important. Spherical particles are ideal for both situations because the surface area to volume ratio maximises the total force for that given volume. For cell stimulation, there is a trade off in the contact area between the cell and the particle. It must be sufficiently large for the particle to bind to the cell but also apply enough stress on the cell, which decreases for larger areas. For tissue penetration, giving the particle pointed edges would allow the particle to penetrate tissue easier but may reduce its total volume, and therefore total force. There is also an increased risk of haemorrhage if pointed particles are used whereas penetration with a spherical particle would be considered a blunt incision, moving most of the tissue out of the way rather than cut through it<sup>165,170</sup>. This re-iterates the need to tailor the magnetic particle to the particular application it is used for. The following section will therefore outline a number of different magnetic particle applications that are currently used and explain the ideal magnetic particle for each of them.

## 2.2 Applications of magnetic particles in medicine

Magnetic particles have been found to be incredibly useful in a range of applications in medicine<sup>168,171,172</sup>. In biomedical research the majority of magnetic particles used are in the nanometre size range and almost exclusively made of iron oxide due to its biocompatibility, strong magnetic susceptibility and biodegradability<sup>173</sup>. Particles less than a few hundred nanometres in size act as a single domain structure and exhibit superparamagnetic properties. The advantage of this trait is that they become strongly magnetic when a magnetic field is applied, but retain no magnetisation when the field is removed which improves the particles colloidal stability and avoids agglomeration<sup>174</sup>. These particles are then coated with polymers such as dextran, cellulose and alginate for the conjugation of drug molecules, high affinity ligands such as antibodies and other organic molecules<sup>175–177</sup>. In addition to cell stimulation, this section outlines the most popular applications of magnetic particles in medicine.

### 2.2.1 Magnetic separation

Separation of biological entities from their native surroundings can be advantageous in biomedicine whether it's to prepare concentrated samples for analysis<sup>178</sup> or as a filtration system<sup>179</sup>. Magnetic separation is the use of magnetic particles to separate a specific entity from its surrounding medium using an externally applied magnetic field. Only a few biological entities have magnetic properties strong enough for an external magnet to separate it from its medium, such as red blood cells<sup>180</sup> and magnetotactic bacteria<sup>181</sup>. All other biological entities therefore need to be labelled with magnetic particles. Most particles consist of a magnetic core and a biocompatible coating which range from polymers such as polyvinyl ethanol (PVA), polyethylene glycol (PEG) and small organic molecules such as gelatin, starch and carboxylates<sup>182</sup>. These particles are functionalised using high affinity ligands such as antibodies, peptides and other organic molecules which are attached to magnetic particles via adsorption, covalent binding or electrostatic means<sup>178,183</sup>. These ligands give the magnetic particle high specificity to the cell or entity that is being separated.

Magnetic separation has been used for cells<sup>179,184,185</sup>, proteins<sup>186</sup>, nucleic acids<sup>187</sup>, drugs<sup>188,189</sup> as well as other bioactive compounds<sup>178</sup>. Its popularity in life and medical sciences has led to a number of commercial companies providing a range of separation products. Entities can be separated in batch by simply placing a permanent magnet next to the sample (Figure 2.2). More sophisticated magnet configurations such as continuous<sup>190</sup> and quantitative systems<sup>191</sup> have also been developed<sup>184</sup>. Once separated a detachment process may need to be performed depending on the type of binding. The

advantages of magnetic separation is it's fairly cheap, fast acting and can be used in complex media such as blood and food as well as dilute media. Particles ideally have diameters in the order of microns so that their functional groups can easily bind to a single cell and experience larger forces than nanoparticles to ensure the process is rapid.

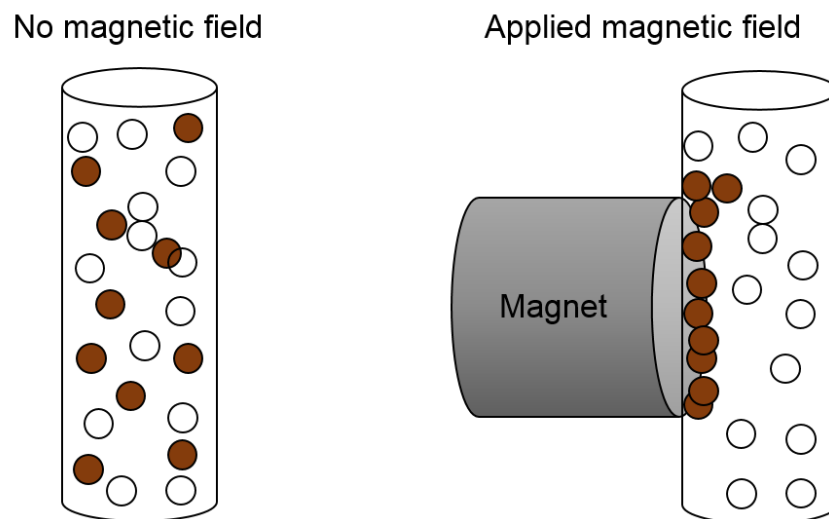


**Figure 2.2.** Diagram showing how magnetically labelled entities (brown) can be separated from surrounding medium (white). Magnetic entities are gathered by the magnet allowing for the supernatant to be removed.

### 2.2.2 Magnetic cell and drug delivery

Drugs are most often administered globally. Whether it's by oral means such as swallowing a tablet or intravenously injected, if the drug has an effect on non-diseased cells it can result in unwanted side effects. For example, chemotherapeutic cancer drugs aimed at fast growing cancer cells will also kill non-cancerous fast growing cells such as hair follicle cells and epithelial cells. There is therefore a drive for developing targeted therapies which would both increase drug payload to the disease while reducing systemic dosing to reduce off target effects. This could be achieved by changing the drug itself either by molecular recognition, i.e. drugs coupled with an antibody or protein that corresponds only to the disease, or the development of prodrugs which only activate in a specific environment<sup>192</sup>. An alternative approach is to apply physical forces to the drug to spatially localise the delivery.

Similar to magnetic separation, cells or drugs can be loaded with magnetic particles, administered systemically and then guided to, or captured at, a target site by applying an external magnetic field (Figure 2.3). Targeting of cells<sup>193,194</sup> and unencapsulated nanoparticles<sup>195,196</sup> have been demonstrated *in vivo* pre-clinically using a range of different permanent and electromagnet designs. The main limitation for translating magnetic targeting into a clinical setting is the exponential decrease in magnetic field with distance from the magnet. With this, efficient targeting is only possible for distances less than 1 cm into the body, limiting its use to superficial tissues<sup>197–199</sup>. A clinical trial has been carried out for magnetic targeting of superficial tumours however successful magnetic targeting was only achieved in about one half of the patients<sup>200</sup>. For magnetic targeting of drugs to the brain there is the additional obstacle of transporting the particles across the blood-brain-barrier, with magnetic force being proposed as a potential mechanism for the delivery of macromolecules<sup>201</sup>. To achieve magnetic targeting in a clinical scenario there are two options for improvement: one is optimising the design of the magnet to generate stronger magnetic forces deeper into the body, the other is to optimise the magnetic particles themselves so that they exhibit a greater response at lower fields.

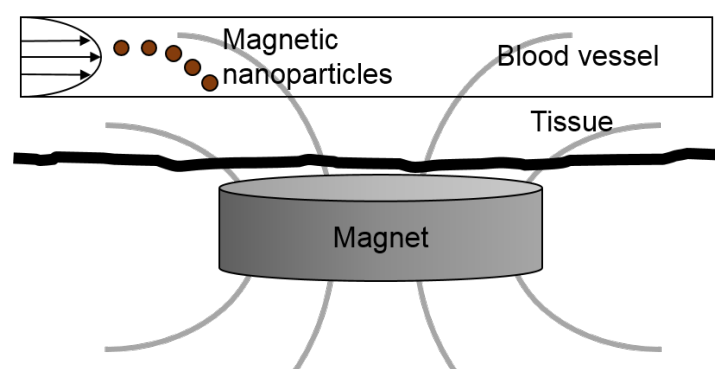


**Figure 2.3.** A Diagram of a simple drug delivery system. A magnet can be placed outside the body so that a magnetic field gradient can capture magnetic particles in a blood vessel. In terms of magnet design, halbach arrays consisting of a set of magnets orientated in a rotating pattern of magnetisation to increase the magnetic field have been adopted<sup>194,202</sup>, with efforts of designing scalable magnets that can be increased in size while retaining similar field strengths<sup>203</sup> (Figure 2.4). Magnetic field concentrators or magnetic stents<sup>204,205</sup> have also been tested, however this approach negates the non-invasive aspect of magnetic targeting. Another strategy is to use existing medical imaging devices such as MRI and Magnetic particle imaging (MPI) and adapting them to navigate and target magnetic particles<sup>169,206–208</sup>. Whereas MPI is a relatively new imaging modality, work undergone using MRI to target magnetic particles to a target site within the body appears to hold promise in overcoming the hurdle of clinical translation and is discussed in more detail in chapter 3.

To optimise cell delivery, particles must be chosen which introduce the greatest amount of iron content into the cell without affecting cell viability. For particles conjugated directly with a drug, larger diameters would lead to a greater force, however this must be balanced with the risk of agglomeration and vascular occlusion. Increasing particle size will also remove their superparamagnetic trait, while passing obstacles such as the blood-brain-barrier also becomes more difficult with larger particles. Researchers are still yet to find the optimum trade-off between maximising magnetic force and biocompatibility demands.

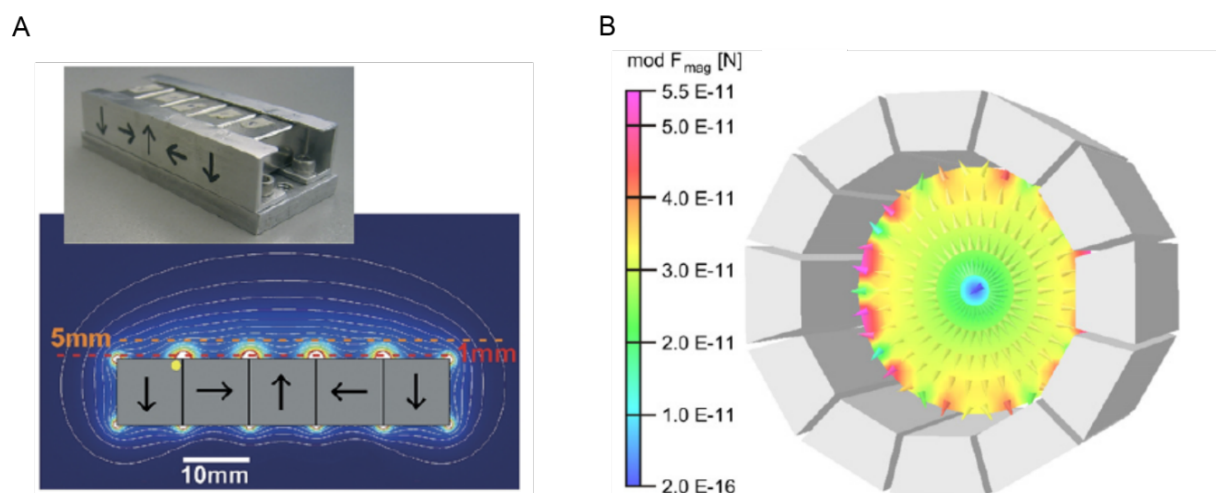


**Figure 2.4.** Examples of different halbach array designs to increase the magnetic force applied magnetic particles to improve targeting efficiency including a linear halbach array used in Kyratatos et al.<sup>194</sup> (A) and the scalable cylindrical halbach array used in Riegler et al.<sup>193</sup> (B).

### 2.2.3 Magnetic hyperthermia/thermal ablation

Magnetic hyperthermia is the use of magnetic particles in combination with an alternating magnetic field (AMF) to induce localised heating. The temperature range for hyperthermia is  $>42^{\circ}\text{C}$  in order to denature cells and induce apoptosis. Thermal ablation is differentiated from hyperthermia when temperatures above  $50^{\circ}\text{C}$  are used to destroy cells or tissue. These temperatures can yield necrosis, coagulation, carbonisation, fibrosis and inflammation<sup>209</sup>. The heating of magnetic particles can also be used as a method for the controlled release of drugs<sup>210</sup>. The size and shape of the magnetic particles will affect not only the rate of heating but also the underlying mechanisms involved.

Magnetic particles generate heat via three main mechanisms:

$$P_{tot} = P_{eddy} + P_{hyst} + P_{an} \quad 2.1$$

And is generally described as the specific power loss in  $\text{Wg}^{-1}$ . The first term is a result of eddy current losses. When a time varying magnetic field is applied to a magnetic particle it will generate a current on the surface of the particle which dissipates energy via resistive heating. These eddy currents also create their own magnetic flux against the main AMF which limits the penetration of the magnetic field into the particle to a skin depth  $\delta$ :

$$\delta = \sqrt{\frac{\rho}{\pi\mu_r\mu_0\omega}} \quad 2.2$$

Where  $\rho$  is the resistivity of the magnetic particle and  $\omega$  is the frequency of the AMF. For a spherical particle the eddy current losses are<sup>211</sup>:

$$P_{eddy} \cong 3\sqrt{2}\pi r^2 (\omega\mu/\sigma)^{1/2} H_0^2 \quad 2.3$$

Where  $\mu$  is the magnetic permeability of the particle and  $\sigma$  is its conductivity. The power loss due to eddy current heating is therefore proportional to the square of the magnetic field and square root of the frequency.

The second term is a result of hysteresis loss. The amount of heating per unit volume is given by the frequency multiplied by the area of the hysteresis loop<sup>168</sup>:

$$P_{hyst} = \omega\mu_0 \int_{loop} \mathbf{H}' d\mathbf{M} \quad 2.4$$

The hysteretic power losses are proportional to the frequency and strength of the magnetic field.

The third term is the anomalous losses of whatever power loss remains after eddy current and hysteresis losses are taken into account. These can be due to additional current losses due to sample inhomogeneity, non-uniform magnetisation and other effects<sup>212</sup>.

For magnetic particles a few millimetres in size, such as the thermoseeds introduced in chapter 1, both eddy current losses and hysteresis losses occur. For magnetic nanoparticles however, their small size negate most if not all eddy current losses. Associated with hysteresis losses, magnetic particles generate heat via two additional mechanisms: Neel relaxation and Brownian relaxation. Neel relaxation is a result of a time delay between the magnetisation of the particles and the AMF, whereas Brownian losses are due to particle rotation and collision when suspended in media. Neel's relaxation will depend on the particle characteristics such as size, shape and magnetic content whereas Brownian relaxation depends on the viscosity of the surrounding media and can be ignored for bound particles. The power loss of monodisperse magnetic particles in an AMF can be described as<sup>213</sup>:

$$P_{SPM} = \mu_0 \pi \chi'' \omega H_0^2 \quad 2.5$$

Where  $\chi''$  is the imaginary part of the particles complex magnetic susceptibility which is dependent on the frequency of the AMF:

$$\chi'' = \frac{\omega \tau}{1 + (\omega \tau)^2} \chi_0 \quad 2.6$$

Where  $\chi_0$  is the DC magnetic susceptibility and  $\tau$  is a combination of the Neel and Brownian relaxation time:

$$\frac{1}{\tau} = \frac{1}{\tau_N} + \frac{1}{\tau_B} \quad 2.7$$

Where  $\tau_N$  and  $\tau_B$  are defined as:

$$\tau_N = \frac{\sqrt{\pi}}{2} \tau_0 \frac{\exp\left(\frac{KV_m}{k_B T}\right)}{\sqrt{\frac{KV_m}{k_B T}}} \quad 2.8$$

And:

$$\tau_B = \frac{3\eta V_H}{k_B T} \quad 2.9$$

Where  $\eta$  is the viscosity of the fluid,  $V_m$  and  $V_H$  are the magnetic and hydrodynamic volumes of the particle,  $k_B$  is the boltzman constant,  $T$  is the absolute temperature,  $\tau_0 = 10^{-9}$  s and  $K$  is an anisotropy constant.



In both cases, heating of the particle can be increased with higher frequencies and field strengths. However an AMF will also cause non-specific eddy current heating of tissue with an approximate limit for  $H_0 \cdot \omega$  of  $5 \times 10^8 \text{ Am}^{-1}\text{s}^{-1}$ . Clinical trials for the treatment of Glioblastoma multiforme<sup>214</sup> state that strengths of up to 9 kA/m at 100 kHz were well tolerated by patients with minimal off target heating<sup>215</sup>.

The main limiting factor for nanoparticle mediated hyperthermia treatments is delivering high concentrations of particles needed for sufficient heating<sup>216</sup>. The success of thermoseed ablation depends on accurate placement of the seeds to ensure the whole tumour region is ablated without damaging healthy tissue. As the seeds need to be removed after treatment to avoid migration, the ability to move a single seed in situ would facilitate multiple ablations with a single seed<sup>165</sup>. Hyperthermia therapies using either nanoparticles or thermoseeds are yet to be shown as an effective stand-alone treatment. However, hyperthermia does enhance the effects of radiotherapy and chemotherapy and as a result are normally combined with either or both<sup>215,217</sup>.

#### 2.2.4 Particle and cell tracking

To better understand magnetic particle and cell based therapies, non-invasive imaging techniques are needed to assess whether particles have been delivered to the region of interest, whether they have migrated to other regions of the body or in finding the best delivery route. The success of emerging cell based therapies depend on the route and accuracy of cell transplantation, the fate of the cells after transplantation and the interaction between the cells and the host microenvironment. For the brain in particular a number of different imaging modalities including MRI, PET, SPECT, and in the preclinical setting bioluminescence, have been used to assess cellular therapies for neurological regenerative medicine and ischaemic injury<sup>218,219</sup>. Each of these modalities have their own distinct advantages and disadvantages and as such no single modality has been earmarked as the gold standard for cell tracking, with some taking a multimodal approach<sup>220–222</sup>.

Considering commercially available magnetic nanoparticles have already been developed as specific MRI contrast agents, MRI has a distinct advantage over other imaging modalities in locating magnetic particles and labelled cells in the body. The presence of magnetic particles results in a reduction of spin-spin relaxation times  $T_2$  and  $T_2^*$ <sup>223</sup> which is discussed in further detail in chapter 3. The shortening of these relaxation times results in hypointense regions, leading to particles or cells appearing dark on an image<sup>224</sup>. Additional advantages of MRI include superior soft tissue contrast, no radiation is needed allowing for repeated scanning, and the ability to perform functional imaging. The prevalence of MRI in both the clinical and pre-clinical settings also facilitates transfer of experimental protocols from the bench to the hospital.

One of the drawbacks of magnetic cell tracking is the inability to determine cell viability. Cases where hypointensity losses are slower than the loss of injected cells over time suggest that magnetic particles remain at the injection site after cells have died<sup>225,226</sup>. Magnetic particles are also often taken up by macrophages<sup>227,228</sup> along with migration of extracellular particles<sup>229</sup> can lead to false positive signals, along with microhaemorrhages caused by stereotaxic injection into the brain. Despite this magnetic cell targeting is used frequently in the brain and can deliver single cell resolution with high field MRI.

MRI plays an integral role throughout this thesis. If magnetic particles are to be used as a minimally invasive cell manipulation technology, their location must be accurately determined. In chapter 5, *in*

*vivo* testing of mechanical stimulation of astrocytes using micron sized magnetic particles was performed by injecting particles into the rostroventrolateral medulla as it is known that the astrocytes in this area control sympathoexcitatory activity. In chapter 6, the MRI scanner itself is used as a means of propelling and tracking a single magnetic particle through the brain which can then be heated to cause cell death as shown in chapter 7. The next chapter therefore outlines the basic principles of MRI and how it can be used to not just image magnetic particles, but also to target them to a specific region of the body using magnetic force.

### 3 Magnetic Resonance Imaging and targeting

Magnetic resonance imaging (MRI) is an imaging technique based on the nuclear magnetic resonance phenomenon. Its popularity has risen in the last 20 years thanks to its ability to image living beings non-invasively with good tissue contrast and minimal energy deposition compared to modalities such as computed tomography, which relies on x-rays to acquire an image. These distinct advantages have led to MRI scanners being installed in most hospitals and are now routinely used for imaging important parts of the body including the brain, heart, lungs, liver, muscle, cartilage, ligaments and others<sup>230</sup>. It is also used for detecting a range of pathologies including cancer, multiple sclerosis, epilepsy and dementia. Arguably MRI has made the biggest impact on the field of neuroimaging, providing structural detail and functional information on cortical organisation never before possible.

Its promise as a diagnostic and research tool has already been fully realised, with hospitals and research centres utilising an ever improving imaging modality. And yet, there is a possibility that MRI could be used for more than just imaging. Using the principles of magnetic force outlined in the previous chapter, it is possible to move small magnetic objects from one location in the body to another, transforming MRI from a purely diagnostic device into a combined therapeutic and diagnostic, or theranostic platform<sup>231</sup>. Whether this be a targeted drug therapy, minimally invasive surgical technique or remote controlled biosensing, the potential impact of turning an MRI scanner into a theranostic device could be profound. To realise such a possibility it is essential to go back to basics. This chapter therefore outlines the basic principles of MRI, how it works and the challenges involved in both imaging and navigating magnetic particles inside the body.

## 3.1 Basic principles of MRI

### 3.1.1 Nuclear magnetic resonance

In a typical MRI scan, the source of the signal comes from the magnetic moment of hydrogen nuclei inside a sample which is picked up by a receiving coil. Hydrogen is the dominant source of MRI signal because of its abundance in living tissue, such as fat and water, and also has the highest gyromagnetic ratio. Water molecules have one oxygen and two hydrogen atoms. The hydrogen nucleus is comprised of a single unpaired charged proton which possesses a spin. This moving charge creates a magnetic moment, behaving as a small dipole magnet. When no magnetic field is present, these spins are randomly orientated, and as in a bulk material will cancel each other out. In the presence of a large magnetic field however, such as inside an MRI scanner, these spins will either align with or against the direction of the magnetic field ( $B_0$ ). A higher percentage will align with the field than oppose according to the Boltzmann distribution, which depends on the energy difference between states to give the sample a small net magnetisation in the direction of  $B_0$ .

While the net magnetisation aligns with the magnetic field, each individual magnetic moment actually rotates about the  $B_0$  axis. This rotation has a specific frequency, the Larmor frequency ( $\omega_0$ ), for a given  $B_0$ :

$$\omega_0 = \gamma B_0 \quad 3.1$$

Where  $\gamma$  is the gyromagnetic ratio of a specific nucleus. The Larmor frequency is also considered the resonant frequency as energy can be transferred to these moments when applied at that frequency. As this net magnetisation cannot be measured directly (it is much smaller than  $B_0$ ) a signal is acquired by first giving it energy using a radiofrequency (RF) pulse at the Larmor frequency to effectively flip the magnetisation towards a plane transverse to  $B_0$  where it can then be picked up by the receiver coil. It is only in this transverse plane where the receiver coil can measure the magnetisation. An RF pulse of a particular bandwidth that excites a range of frequencies about the Larmor frequency to flip the magnetisation from the  $B_0$  plane ( $M_z$ ) to the transverse plane ( $M_{xy}$ ) is called a  $90^\circ$  RF pulse. Immediately after a  $90^\circ$  pulse,  $M_z$  is zero and  $M_{xy}$  is at its maximum, the magnetisation then gradually returns or relaxes to the z axis resulting in a decay of signal over time. There are two distinct process which occur during relaxation, named  $T_1$  and  $T_2$ .

### 3.1.2 Relaxation

While  $T_1$  and  $T_2$  relaxation can be described as two processes they are very much intertwined, with one process effecting the other.  $T_1$  relaxation is the gradual increase in longitudinal magnetisation after the RF pulse. The time constant  $T_1$  of a particular tissue or sample is then taken as the time for 63% of the recovery to occur following a  $90^\circ$  RF pulse. The magnetisation  $M_z$  at a given time ( $t$ ) can be given as:

$$M_z(t) = M_{z,eq}(1 - e^{-\frac{t}{T_1}}) \quad 3.2$$

Where  $M_{z,eq}$  is the equilibrium magnetisation along the z axis.

$T_2$  relaxation is the decrease in magnetisation in the xy plane,  $M_{xy}$ . This process is often faster than  $T_1$  (apart from in water and other liquids where  $T_1 = T_2$ ) due to the added dependence of phase coherence of all the individual magnetic moments within a specific region. When an RF pulse is applied, all the magnetic moments will rotate in phase with each other. When the pulse is turned off, the moments are free to rotate at its Larmor frequency. This frequency is dependent on the magnetic field the moment is experiencing, which due to small local field inhomogeneities can be slightly different for each moment, causing them to lose phase coherence until they eventually cancel each other out ( $M_{xy}$  is zero). The time constant  $T_2$  is then given as the time taken for  $M_{xy}$  to reach 37% of its value after a  $90^\circ$  RF pulse ( $M_{xy,0}$ ):

$$M_{xy}(t) = M_{xy,0} \cdot e^{-\frac{t}{T_2}} \quad 3.3$$

These differences in the local field experienced by a magnetic moment are caused by three factors: spatial variations in  $B_0$  occurring either because of imperfections in the magnet itself or the presence of biological tissue, local magnetic sources within the tissue and interactions with neighbouring magnetic moments (often called spin-spin interactions). The effects of the second and third factors can be seen in different tissue types. A key parameter that effects the magnetic moment in different tissues is its correlation time. For instance, the correlation time in fat is longer than in liquids (e.g. CSF) and is largely affected by the fluctuating magnetic fields produced by the tumbling motion of magnetic dipoles in liquids, or molecular motion in solids.

It is these differences in  $T_1$  and  $T_2$  within tissue that provide contrast in the MR image. Imaging of magnetic particles is then possible because of factor two, local magnetic sources. Magnetic particles cause localised reductions in  $T_2$  to generate hypointense regions on an image allowing their position to be tracked throughout the body.

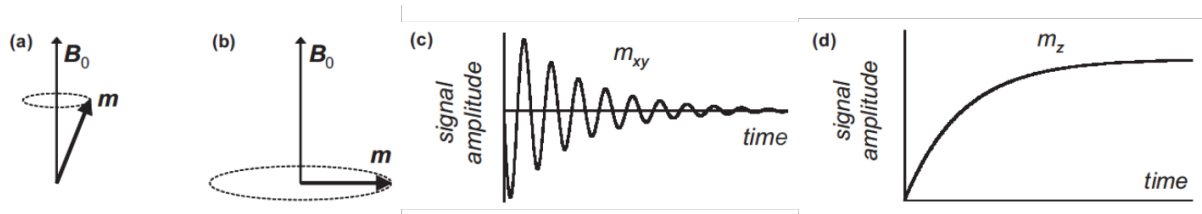


**Figure 3.1.** Taken from Pankhurst et al., 2003. **A)** In the presence of the MRI static magnetic field, the magnetic moment of the bulk signal from the protons will precess about  $B_0$  at the Larmor frequency,  $\omega_0$ . **B)** When an RF pulse is applied perpendicular to  $B_0$ , it resonantly excites the precession of the magnetic moment onto the perpendicular plane. **C-D)** Immediately after the RF pulse is applied, the magnetic moments perpendicular (**C**) and parallel (**D**) relax to their initial state.

### 3.1.3 Acquiring an image

The simplest MRI experiment that can be performed, called a free induction decay, consists of a single  $90^\circ$  pulse followed by detection of signal. The magnetisation oscillates at the Larmor frequency and the reduction in signal is driven by  $T_2^*$  relaxation. This  $T_2^*$  notation is used when all three factors mentioned above effect the decay in signal. A spin echo sequence can be used to recover some of the signal lost as a result of the local inhomogeneities in the magnetic field. After the initial  $90^\circ$  RF pulse is applied, a second  $180^\circ$  RF pulse is applied after a time interval  $\tau$ . The effect of this is the net magnetisation that has already begun dephasing is flipped back onto the xy plane but in the opposite direction. This effective re-phasing causes the moments to refocus to produce an increase in signal intensity or an echo at a second time interval equal to  $\tau$ . Multiple  $180^\circ$  RF pulses can be applied to measured multiple echoes.

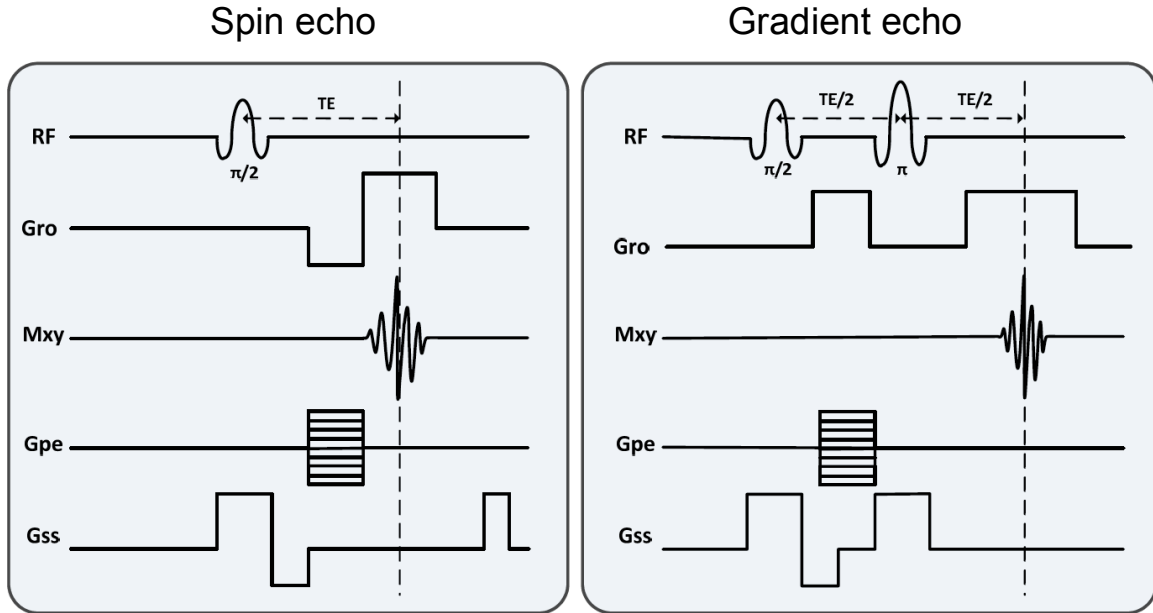


**Figure 3.2.** Simplified pulse sequence diagrams for Gradient echo and spin echo sequences.

To obtain 2D, or 3D information however, the signal from the magnetic moments at different locations need to be distinguishable from one another. To do this, equation 3.1 is manipulated so that the signal from a certain pixel or voxel experiences a different field strength by applying a linear magnetic field gradient using the gradient coils. Linear magnetic fields can be applied orthogonally in the x, y and z axes in Cartesian coordinates and spatially encoded by implementing frequency encoding, phase encoding and slice selection. For frequency encoding, a linear gradient is applied during signal acquisition so that the precession frequencies measured correspond to a particular magnetic field strength, which in turn is location dependent. The signal is then separated into discrete components, or locations depending on its frequency.

$$B_z(z, t) = B_0 + zG(t) \quad 3.4$$

$$\omega(z, t) = \omega_0 + \omega_G(z, t) = \omega_0 + \gamma zG(t) \quad 3.5$$

Phase encoding is then applied orthogonal to the frequency encoding axis. A linear gradient is applied before image acquisition for a set period of time where the magnetic moments will precess at different frequencies. After the gradient is switched off the frequencies return to the Larmor frequency but have accumulated additional phase which again is location dependent. For slice selection, the gradient is applied during the RF pulse, orthogonal to both the frequency and phase encoding axes. Due to the resonance effect at a particular field, the RF pulse must be centred around the precession frequency of the magnetic moments. If a gradient is applied across the whole imaging volume a slice can be selected by choosing a specific RF frequency and bandwidth. The thickness of the slice is then selected depending on the gradient strength. All of these spatial frequencies are put



into a data matrix commonly known as k space. In the case of a 2D image, axes  $k_x$  and  $k_y$  contain the signal intensity for each spatial frequency along the x and y axis respectively. This matrix is then converted into an image mathematically using a Fourier transform. The signal intensity  $S$  of one pixel within the image is then the average signal intensity originating from that region in space as defined by:

$$S = k\rho_p(1 - e^{-\frac{TR}{T_1}})e^{-\frac{TE}{T_2}} \quad 3.6$$

Where  $k$  is a hardware dependent parameter taking into account field strength, surface coil sensitivity and the nuclei specific constant,  $\rho_p$  is the proton density,  $TR$  is the relaxation time and  $TE$  is the echo time.

A gradient echo sequence generates an image slightly differently in that only one RF pulse is applied. As before, an RF pulse (typically  $90^\circ$ ) is applied at the same time as the slice select gradient. Phase and frequency encoding is performed in the same way except to generate an echo, an initial negative dephasing gradient is applied after the RF pulse followed by a positive rephasing gradient, typically in the frequency encoding direction. The echo then occurs when the positive gradient moment is equal to the negative gradient moment. The signal intensity of a gradient echo sequence is then:

$$S = k\rho_p(\sin \alpha e^{-\frac{TE}{T_2^*}}) \frac{(1 - e^{-\frac{TR}{T_1}})}{(1 - \cos \alpha e^{-\frac{TR}{T_1}})} \quad 3.7$$

Where  $\alpha$  is the flip angle of the RF pulse. In this case,  $T_2$  is replaced by  $T_2^*$  as any dephasing due to field inhomogeneities does not get rephased as they would after a  $180^\circ$  RF pulse. The benefit of not using a  $180^\circ$  pulse also means that shorter flip angles can be used ( $<90^\circ$ ), which can reduce the overall scan time. The optimum flip angle is then given by the Ernst angle  $\cos(\alpha) = e^{-\frac{TR}{T_1}}$ . The majority of fast imaging sequences are therefore based on a gradient echo imaging sequence.

As can be seen from equations 3.6 and 3.7, the contrast in a spin echo image can be controlled by varying  $TE$  and  $TR$ . In a gradient echo sequence the flip angle can also be changed. In cases where image contrast is still insufficient, contrast agents can be used which are chosen depending on whether their dominant effect is on  $T_1$  or  $T_2/T_2^*$ . The most common  $T_2$  contrast agents are magnetic nanoparticles, which as mentioned above, lead to increased dephasing due to field inhomogeneities caused by the magnetic field the particle creates when it is magnetised inside the MRI bore. When there is a particularly high concentration of magnetic particles, the degree of dephasing is so fast signal dropout can occur, whereby the signal is completely decayed before image acquisition takes

place. The next section therefore introduces ideas and concepts for imaging strongly magnetic material using MRI and how signal can either be recovered or exploited to identify the particles location.

## 3.2 Magnetic resonance targeting

### 3.3.1 Basic components of an MRI scanner

Before introducing the concept of magnetic targeting with MRI, it is useful to outline the essential components of an MRI scanner as understanding the role of each of them will allow for the adaptation of MRI from a purely diagnostic tool to a therapeutic device to create a theranostic interventional platform.

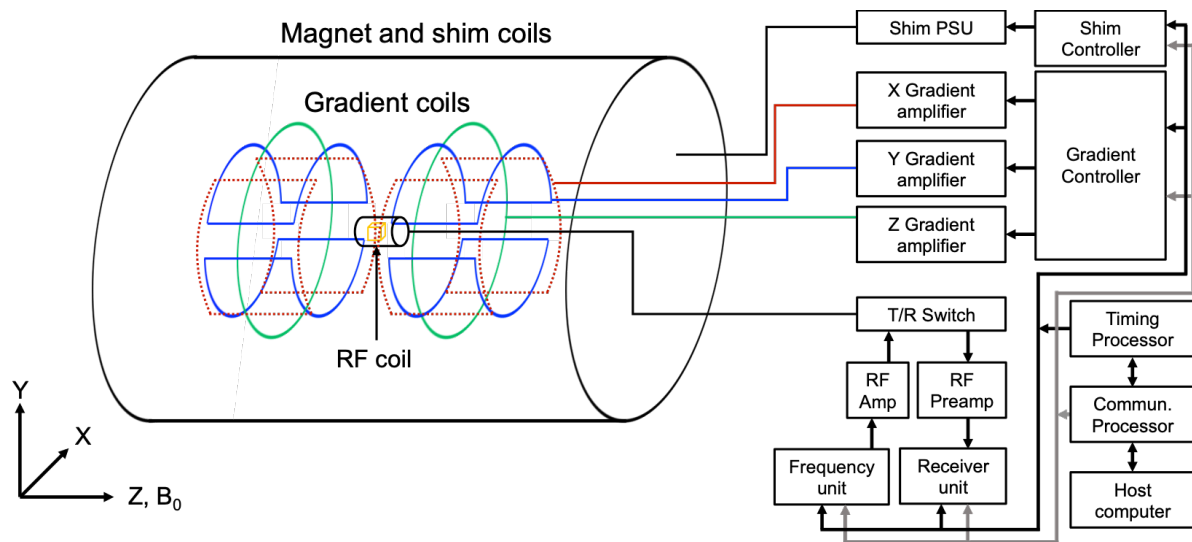


**Figure 3.3.** Schematic of an MRI scanner. The superconducting magnet and permanent shims are indicated by the outer cylinder. The z gradient is controlled by Maxwell pair coils while two Golay coils control the x and y gradients. A host computer provides the interface for preparing the imaging sequence. Gradient controllers generate the gradient waveforms which are sent to the gradient amplifiers. A frequency unit provides the frequency waveform which is sent to the RF amp. An RF coil then picks up currents induced by excited spins in the sample (orange box) which are amplified by the RF preamp and digitised in the receiver unit. The timing processor ensures all sub systems are accurately timed and synchronised. Following standard convention the z-axis is orientated parallel to  $B_0$ , with positive Z towards the front of the scanner.

First, the magnet itself provides a strong but more importantly homogenous magnetic field which aligns the spins of atomic nuclei in the direction of the field. The precession frequency (Larmor frequency) of these spins depends on the strength of the field. The proportion of spins that align with the field direction rather than oppose also increase with field strength, giving a higher signal to noise ratio. Typical clinical scanners use superconducting magnets generating field strengths of 1.5 T or 3 T, while Bruker™ provide preclinical MRI scanners up to 15.2 T. All magnets have a high uniformity requirement demanding at least <5ppm. The magnets are usually superconductors maintained in liquid helium in a cryostat.

The gradient coils sit inside the bore of the main magnet and generate linear magnetic field gradients over a central spherical space used for imaging where the field is most uniform. The concept of magnetic targeting with an MRI scanner stems from the manipulation of the gradient coils to generate strong directional magnetic field gradients for propulsion of magnetic particles as well as for imaging. This concept forms the basis of chapters 6 and 7.

A radio frequency coil is then placed inside the bore and the gradient coils. The sample or specimen is either placed in the centre of a volume coil, or adjacent to a surface coil. RF coils are used to both transmit the RF pulses to excite spins and to pick up any induced currents from the excited spins. Different RF coils can be used in combination (i.e. a volume coil to transmit and surface coil to receive) depending on the application.

When a specimen is placed inside the bore the material within it will perturb the homogeneous magnetic field. To ensure the magnetic field is as homogenous as possible before imaging shim coils are used, which are an extra set of gradient coils, to bring the field back to its highest uniformity.

Additional components are also needed to control the MRI scanner. A host computer is used as the user interface for selecting a particular imaging sequence and setting image parameters. Each sequence consists of a set of particular RF waves/pulses and controlled magnetic field gradients, the timing of each are incredibly important and are controlled via a timing processor. RF waves produced by the RF waveform generator are amplified by the RF amplifier bay and send to the RF coil via a transmit/receive switch. Commands for the gradients from the communications processor are translated into a particular gradient waveform, amplified then applied to the gradient coils. After a certain time after RF excitation, the current induced in the coil from the excited spins is amplified by the RF pre-amplifier and converted into a digital signal in a receiver unit. This data is then sent to an imaging processor which performs a Fourier transform to generate the final image.

### 3.3.2 Magnetic propulsion using MRI gradient coils

The static magnetic field generated by the magnet is governed by Maxwells equations:

$$\nabla \cdot \mathbf{B} = 0 \quad 3.8$$

$$\nabla \times \mathbf{B} = \mu_0 \epsilon_0 \frac{\partial \mathbf{E}}{\partial t} + \mu_0 \mathbf{J} = 0 \quad 3.9$$

Equation 3.9 equates to zero because the field inside the bore is considered a source free field in that there are no electric fields or currents present. Rewriting these two equations in their component forms gives:

$$\frac{\partial B_x}{\partial x} + \frac{\partial B_y}{\partial y} + \frac{\partial B_z}{\partial z} = 0 \quad 3.10$$

$$\left(\frac{\partial B_z}{\partial y} - \frac{\partial B_y}{\partial z}\right)i + \left(\frac{\partial B_z}{\partial x} - \frac{\partial B_x}{\partial z}\right)j + \left(\frac{\partial B_y}{\partial x} - \frac{\partial B_x}{\partial y}\right)k = 0 \quad 3.11$$

Each derivative inside the same bracket is therefore equivalent for equation 3.4 to equal zero. As the main magnetic field is along the z direction meaning magnetic particles are only magnetised along  $B_z$ ,  $B_y$  and  $B_x$  components can be neglected to give gradients in x, y and z with respect to  $B_z$ :

$$g_x \equiv \frac{\partial B_z}{\partial x} \quad g_y \equiv \frac{\partial B_z}{\partial y} \quad g_z \equiv \frac{\partial B_z}{\partial z} \quad 3.12$$

Assuming the gradients are linear and the z gradient  $g_z$  has cylindrical geometry,  $\partial B_x / \partial x$  and  $\partial B_y / \partial y$  are identical. In which case a symmetry parameter  $\alpha$  can be introduced:

$$\alpha \equiv -\frac{\frac{\partial B_x}{\partial x}}{g_z}; \quad 1 - \alpha \equiv -\frac{\frac{\partial B_y}{\partial y}}{g_z} \quad 3.13$$

And an independent variable:

$$\beta \equiv \frac{\partial B_y}{\partial x} = \frac{\partial B_x}{\partial y}$$

The magnetic field produced by the gradient coils can then be given as:

$$\begin{bmatrix} B_x \\ B_y \\ B_z \end{bmatrix} = \begin{bmatrix} \frac{\partial B_x}{\partial x} & \frac{\partial B_x}{\partial y} & \frac{\partial B_x}{\partial z} \\ \frac{\partial B_y}{\partial x} & \frac{\partial B_y}{\partial y} & \frac{\partial B_y}{\partial z} \\ \frac{\partial B_z}{\partial x} & \frac{\partial B_z}{\partial y} & \frac{\partial B_z}{\partial z} \end{bmatrix} \begin{bmatrix} x \\ y \\ z \end{bmatrix} = \begin{bmatrix} \alpha g_z & \beta & g_x \\ \beta & -(1 - \alpha)g_z & g_y \\ g_x & g_y & g_z \end{bmatrix} \begin{bmatrix} x \\ y \\ z \end{bmatrix} \quad 3.14$$

Due to cylindrical geometry,  $\alpha = 0.5$ , so equation 3.7 can be further simplified to:

$$\begin{bmatrix} B_x \\ B_y \\ B_z \end{bmatrix} = \begin{bmatrix} -0.5g_z x + g_x z \\ -0.5g_z y + g_y z \\ g_z x + g_y y + g_z z \end{bmatrix} \quad 3.15$$

Importantly, equation 3.15 shows that gradients along x and y are produced by the  $B_z$  field which allows force to be applied in these directions despite the magnetisation of the material being solely in the z axis.

Considering the magnetic force acting on a magnetic particle that is fully saturated, in the case of targeting using MRI gradients, the equation becomes:

$$\mathbf{F}_m = VD_c(\mathbf{M}_s \cdot \nabla)\mathbf{B} \quad 3.16$$

Where  $D_c$  is the duty cycle of the MRI gradients. The large currents needed to generate strong gradients (up to 500mT/m) for particle propulsion means the coils would over heat if applied continuously. To compensate for this, a duty cycle is used where strong gradients can be applied for a short period of time (tens of milliseconds) and then switched off to allow for cooling. This on/off cycle can then be looped or repeated to deliver pulsed forces over a sustained period of time.

As the particles magnetisation is predominantly in the z axis, the x and y components can be neglected to give:

$$\begin{bmatrix} F_{m,x} \\ F_{m,y} \\ F_{m,z} \end{bmatrix} = VM_z D_c \begin{bmatrix} \frac{\partial B_z}{\partial x} \\ \frac{\partial B_z}{\partial y} \\ \frac{\partial B_z}{\partial z} \end{bmatrix} \quad 3.17$$

### 3.3 Imaging magnetic particles using MRI

Originally, magnetic nanoparticles were used as contrast agents due to their magnetic properties and their effect on  $T_2$  relaxation. Several of these particles have been FDA approved including Feridex (Endorem) for liver and spleen imaging<sup>232</sup>, Lumiren for bowel imaging and Combidex for lymph node metastases imaging<sup>233</sup>, to name a few. In particular, superparamagnetic iron oxide nanoparticles (SPION) have accrued huge interest in research over the past decade because of their physico-chemical characteristics, biocompatibility and potential clinical applications<sup>234</sup>. Their small size and magnetic properties mean that they become magnetised when a magnetic field is applied but retain no magnetisation when the field is removed. Their use in cell tracking and labelling is particularly appealing for cellular based therapies. Magnetic particles can be internalised by cells either by endocytosis or magnetofection so that their location can be imaged non-invasively with MRI<sup>235</sup>. The ability to image them accurately relies on the concentration of particles within a particular location and the imaging method. This section will address a selection of these imaging methods.

### 3.3.1 Positive contrast imaging

In tissue with relatively low signal it can be hard to distinguish hypointense regions caused by magnetic particles to other sources of field inhomogeneity and artefacts in tissue. To isolate signal surrounding magnetic particles it is possible to use positive contrast imaging methods<sup>236,237</sup>. The simplest method for this is the GRASP sequence dubbed the ‘white marker’ method. Based on a standard gradient echo sequence, it has a lower rephasing gradient after the slice selection gradient. The result is the bulk signal from the image is reduced but the volume of signal surrounding the magnetic particles is enhanced due to the addition of the local field gradients they produce. An example of this gradient is shown in figure 3.4.

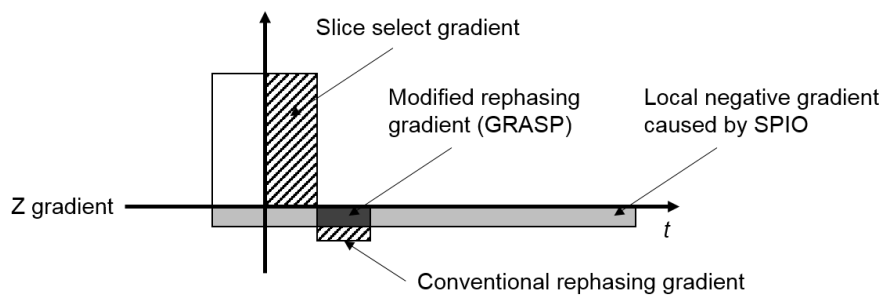


**Figure 3.4.** Diagram illustrating gradients on the slice select axis for conventional gradient echo and GRASP sequences for positive contrast imaging of magnetic nanoparticles as described by Mani et al.<sup>238</sup>.

Another method is to use off resonance techniques which actively suppress or excite a narrow bandwidth of signal around the magnetic particles. The magnetic field produced by a magnetic particle when inside an MRI scanner causes a well-defined anisotropic frequency distribution around it (Figure 3.3) which is dependent on its size, shape and magnetic content. An example of a method for selective signal suppression is IRON, Inversion Recovery with On Resonance water suppression, which simply adds a dual inversion prepulse for fat and water suppression centred at the larmor frequency and a bandwidth  $BW_{\text{water}}$ , leaving only the off resonance water signal (caused by the magnetic particles) unaffected<sup>239</sup>. It is also possible to localise and quantify the amount of magnetic



particles within the hypointense region by exciting a specific band of off resonant frequencies which are only caused by the magnetic particles<sup>240</sup>. The ratio of off resonant signal is then affected by the power of the off resonant pulse and particle concentration. Positive contrast imaging techniques such as these work well with relatively small concentrations or weakly paramagnetic or ferromagnetic material. Strongly magnetic material is much harder to image because of the considerable susceptibility artefacts they induce. These artefacts are briefly introduced in the next section.

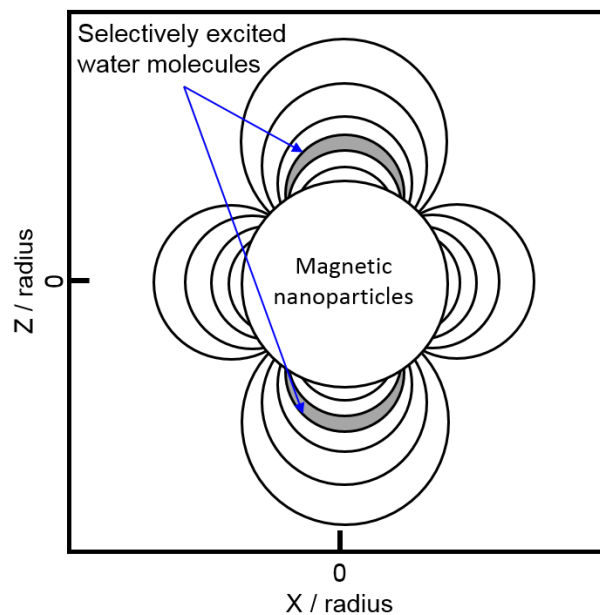


**Figure 3.5.** Bands of water molecules around magnetic particles can be selectively excited by a 90-180 pulse pair at a specific off resonant frequency and bandwidth.



**Figure 3.6.** Taken from Liu et al., 2008<sup>237</sup>. Examples of gradient echo (A), white marker (B) and IRON (C) images of a phantom containing 3 vials of iron oxide labelled glioma cells.

### 3.3.2 Susceptibility artefacts

Susceptibility is a measure of how strongly a material is magnetised when in the presence of an external magnetic field. Neighbouring materials with different susceptibilities interfere with each other to cause distortions in the local magnetic field. For materials with high susceptibility these distortions can interfere with the imaging gradients during acquisition to produce artefacts in the image, such as signal dropout, geometric distortions and signal pile up. Consider the case of imaging a millimetre sized steel ball, which becomes strongly magnetic when inside an MRI scanner. The magnetic field the ball creates causes large magnetic field gradients surrounding it causing the magnetisation of the signal surrounding the ball to lose coherence so quickly that it has fully decayed before image acquisition. These magnetic gradients will also affect the localisation of the signal when using frequency encoding. The gradients from the ball will add to the frequency encoding gradient causing the signal to precess at a different frequency which corresponds to an incorrect location in the image. When a fourier transform is performed the signal is positioned in the wrong voxel, creating geometric distortion. Distortions can also occur between slices. Any gradient added to the slice select gradient can result in the slice itself being warped, or moments outside of the slice can be excited, manifesting as signal pile up in the image.

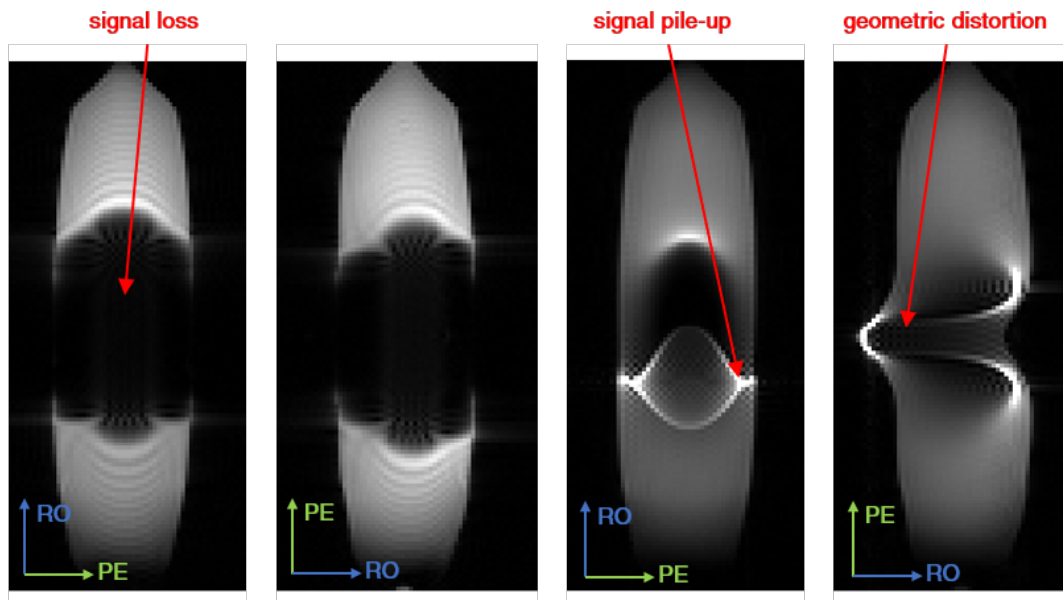


**Figure 3.7. MRI susceptibility artefacts of steel balls.** Two gradient echo (left) and two spin echo images (right) of a 2 mm chrome steel sphere in a 50 mL falcon tube filled with agar showing examples of signal loss, signal pile up and geometric distortion artefacts. The shape of the artefacts cause by the latter two are dependent on the direction of the read out (RO, blue) and phase encoding (PE, green) gradient direction.

Artefacts such as these are most commonly associated with the imaging of prosthetic joints or limbs as they are commonly made of metal. A number of methods have been adopted to compensate for these artefacts such as VAT (view angle tilting) where an additional slice select gradient is applied in combination with a frequency encoding gradient. The readout direction is then tilted towards the slice selection axis causing a shearing of the voxels to remove any in-plane geometric distortion. The disadvantage of VAT is any distortion in the slice select axis remains, while blurring is generated from the shearing. Alternative methods such as SEMAC, Slice Encoding for Metal Artefact Correction and MAVRIC, Multi Acquisition Variable Resonance Image Combination. SEMAC combines VAT with 3D imaging by applying phase encoding along two axes, differentiating the signals along the slice select axis to compensate for through plane distortions<sup>241</sup>. MAVRIC uses a non-selective RF pulse (without imaging gradients) to excite all the magnetic moments on resonance when performing 3D imaging. The sequence is then repeated with off resonance pulses to cover the full range of offset frequencies surrounding the steel ball<sup>242</sup>. Both methods use multiple 3D images to generate a composite image, which removes in and through plane distortions, however the repeated 3D imaging results in long scan times.

To obtain accurate images of metallic limb prostheses, which remain relatively static during the scan, long scan times are not an issue. However in the case of a dynamic or moving metallic implant, image acquisition must be quick to avoid motion distortions. This is especially important when moving magnetic particles through the vasculature where its position will be affected by fluid flow.

While this is less of an issue as the particle remains stationary, short imaging times will reduce the overall time of the intervention. This is discussed further in chapter 6. The earliest examples of magnetic resonance targeting (MRT), or magnetic resonance navigation (MRN) used MRI gradient coils to move steel spheres through liquid with the goal of creating a method for guiding untethered micro devices through blood vessels. Steel spheres were chosen over magnetic nanoparticles because greater forces could be applied to them, especially when gradients were limited to around 18mT/m. Movement of a single larger particle is also simpler to detect, with the earliest example showing that a 3 mm carbon steel could be held stationary against fluid flow using MRI gradients<sup>243</sup>. Considerable artefacts were observed however, determining that a robust imaging localisation method must be developed in order to determine an accurate location of the steel ball. The following section will therefore introduce two imaging techniques that have emerged that deliver fast and accurate localisation of steel spheres.

### 3.3.2 MRI tracking of steel spheres

#### 3.3.2.1 Magnetic Signature Selective Excitation (MS-SET)

As seen in figure 3.2, the magnetic field gradients generated by a magnetic sphere when inside an MRI scanner cause the signal surrounding it to precess at a frequency offset which is dependent on the position about the sphere. Knowing the size and magnetisation of the steel sphere, the spatial distribution of these frequencies can be solved analytically. Higher offset frequencies are found closer to the steel sphere where the gradient is strongest. If an off resonance RF pulse is applied with a narrow bandwidth, the excited signal appears as bands surrounding the sphere. While these bands are many times the actual diameter of the steel sphere, its centre of mass will always be at the centre of the bands. The strong gradients from the sphere also cause the signal to be excited at frequencies much further from the bulk signal from surrounding tissue or media, meaning that this signal is specific only to the sphere. The excited region therefore acts as a magnetic signature for the steel sphere<sup>244–246</sup>.

To obtain either a relative or absolute position of the sphere, the signature is projected onto three orthogonal axes x, y and z using a 1D spin or gradient echo sequence. Correlating 1D projections at two different times allows the relative displacement that occurred to be measured. Average errors were calculated for a static case (sphere is stationary during localisation) and a dynamic case (sphere

continuously moves) using a mechanical rotating arm with a sphere attached to the end. The average error for the dynamic case was 0.55 mm with a refresh rate of 20 positions per second<sup>247</sup>. Average errors in the static case were even lower at 0.064 mm, demonstrating that this technique not only delivers sub-millimetre precision, but relays near real time feedback of the spheres location.

Before taking this imaging technique in vivo, this localisation technique was incorporated into a software environment whereby propulsion gradients are applied automatically to guide the sphere along a pre-planned path<sup>248</sup>. With this automatic feedback system they demonstrated movement of a 1.5 mm steel ball along the artery of a living swine with average positional errors of 0.59 mm and a refresh rate of 24 Hz. To do this, waypoints were placed onto a pre acquired x-ray angiogram. The position of the steel ball was then superimposed onto the angiogram to locate its position within the artery.

### *3.3.2.2 Artefact recognition/Template matching*

This technique also exploits the consistent magnetic field gradients that a steel sphere produces when inside an MRI scanner. Because of this consistency, the shape of the artefact observed from a spin echo or gradient echo is also consistent. The actual shape of the artefact depends on both the magnetic object and the imaging sequence. The saturation magnetisation and volume of the magnetic object are of most importance, while the artefact shape will also depend on the echo type of the sequence (e.g. spin echo or gradient echo). In short, artefact recognition begins with image segmentation followed by feature based object recognition. Connected objects are then detected from the segmentation. Shape and pixel statistics are extracted from each object which are input to a support vector machine classifier, which is trained to recognise features associated with the artefact and rejects artefacts resulting from anatomical structures or cavities. The location of the sphere can then be detected from the position of the segmented susceptibility artefacts centroid<sup>249</sup>. Movement of the artefact is then tracked using a template matching procedure. To determine its 3D position, a correlation is applied to a template stack. Template stacks are generated by repeated imaging of different sphere sizes and imaging sequences. A number of correlation matrices are calculated based on the number of templates in the stack and the best matching slice is determined. This algorithm is then sped up by skipping image reconstruction by performing the correlation in k-

space. Full acquisitions of k-space delivered position uncertainties of  $<30\text{ }\mu\text{m}$ , while reduced k space acquisitions produced uncertainties comparable to the MS-SET technique of around  $0.156\text{ mm}$ . Using propulsion gradients up to  $20\text{mT/m}$  they were able to guide a  $0.75\text{ mm}$  steel ball around a maze<sup>249</sup>. The total time taken for the ball to navigate the maze was decreased from  $120\text{ s}$  to  $40\text{ s}$  using the reduced k space acquisition.

Adaptations of this technique has also been used for tracking other metal objects such as brachytherapy seeds and catheter tip placement<sup>250,251</sup>. The accuracy of post implant dosimetry for brachytherapy is strongly dependent on correct seed placement. Simulated seed artefacts at different orientations in the MRI scanner were used as the template libraries as they corresponded well with scanned seeds<sup>250,252</sup>. The biggest challenge in this case is not the speed of acquisition but to reduce the number of false positive detections as multiple seeds are implanted during a single treatment. When using MRI gradients to manoeuvre magnetic seeds, ideally only one is used as the gradients are applied across the whole volume. However, this technique was also used for real-time tracking of the position of a MRI compatible needle used for MR guided interventions<sup>251</sup>. The accuracy of this method was evaluated by tracking the position of multiple steel balls in an agar phantom. A CT image was taken of the same phantom as a ground truth so that, when the whole phantom was moved, the distances between each ball remains the same. The accuracy of detection of each ball was then evaluated by measuring the distances between each ball after each movement. With a 2D frame rate of  $10\text{ Hz}$  and 3D frame rate of  $5\text{ Hz}$ , the localisation error was  $0.3\text{ mm}$ , again consistent with the previous methods.

Out of these detection methods, the MS-SET technique was adopted in chapters 6 and 7 due to its relative simplicity and doesn't require prior knowledge in the way of template stacks. Experimentally, artefact recognition was not possible for steel balls of  $2\text{ mm}$  diameter or higher because of the restricted imaging volume of the  $9.4\text{T}$  pre-clinical MRI scanner used. In this case the artefact size is greater than the volume of the sample used and the segmentation would be incomplete.

### 3.4 Existing magnetic resonance targeting work

To date the majority of MRI based magnetic targeting work has been performed using steel balls due to the relatively large forces MRI gradients incur on them compared to magnetic nanoparticles. The application in mind was to develop a method for remote control of small magnetic devices through the body, in part inspired by the 1960's film *fantastic voyage*. With recent advancements in the miniaturisation of circuits and sensors, the demand for increasingly precise localisation methods along with the ability to actuate them remotely will increase alongside them. The imaging techniques above have been used to investigate movement of steel balls through various flow phantoms<sup>253,254</sup> and mazes<sup>249</sup>, optimising the frequency of imaging and propulsion for both maximum force and regular feedback on its location. A group led by Sylvian Martel has already demonstrated real-time guidance of a 1.5 mm steel ball *in vivo* through the artery of a living swine<sup>208</sup>. 3 way points were selected along the artery and the trajectory of the ball were superimposed over an x-ray angiography. Integrated real-time imaging software allowed the user to track the ball as it was navigated between each way point<sup>255</sup>.

Arguably just as important was their ability to insert and remove the steel ball safely from the MRI system. An introducer holding the ball in place was inserted into the femoral artery before the animal was placed inside the uniform region of the MRI scanner. A catheter is then used to push the ball into the carotid artery, while a balloon catheter was used to control blood flow and block the sphere to facilitate its retrieval using a magnetically tipped catheter<sup>256</sup>.

The same group also demonstrated *in vivo* targeting of smaller micrometer sized particles using a custom built dedicated gradient coil able to produce up to 400mT/m<sup>257,258</sup>. Therapeutic magnetic microcarriers consisting of iron-cobalt nanoparticles and doxorubicin encapsulated in a biodegradable poly-D L-lactic-co-glycolic acid (PLGA, diameter = 50  $\mu$ m) were injected directly into the hepatic artery and subsequently guided to either the left or right liver lobe for targeted chemoembolization. The dedicated coils were then removed to image the liver. This was the first example of MRT of magnetic particles for the delivery of therapeutic agents, and emphasises the need for gradient strengths an order of magnitude stronger than those currently available in the clinic for micron sized particles.

In light of this, magnetically labelled cells have also been targeted using preclinical MRI systems. Riegler et al<sup>259</sup> were able to guide human mononuclear cells loaded with iron oxide nanoparticles in the direction of the gradient (300 mT/m) in a simple bifurcation model. The same gradient strengths were then used to demonstrate targeting of magnetically labelled cells *in vivo*<sup>260</sup>. Applying a gradient across the whole animal, macrophages loaded with iron oxide particles were targeted to primary prostate tumours and pulmonary metastases. This was then taken further using oncolytic macrophages and demonstrated a reduction in tumour growth as a result of MRT. While there was concern that targeting or aggregation of magnetically labelled cells could cause blockages or embolization, they also show that targeting had no effect on the vasculature. These results show that not only can cells be targeted to anatomical locations using MRI, but targeting also has a therapeutic effect.

To deliver magnetic particles or cells in the micron size range along the vasculature, dedicated gradient coils would need to be installed to improve existing clinical MRI scanners. At present, typical scanners will generate gradients up to 80 mT/m, an order of magnitude lower than the 300 mT/m needed for the actuation of cells. The same can also be said if MRI is to be used to guide magnetic particles through tissue. Even with steel balls, an estimated minimum force of 0.07N has been quoted for moving a 3mm sphere through brain tissue at a rate of 1 cm / 15 seconds<sup>165</sup>, requiring magnetic field strengths between 0.5 – 1.5 T/m. With this apparent limitation in mind, elaborate contraptions such as the Gauss gun<sup>261</sup> and magnetic hammer<sup>262</sup> have been developed. The



latter contraption, magnetic actuation hammer, was composed of a steel ball inside a cylinder with a spring at one end and impact plate on the other with a pointed tip at the end. The MRI gradients are then used to push the ball back onto the spring, which is released when gradients are switched off to generate large, pulsed forces. A hammer 50 mm long, 7.5 mm in diameter with a 5 mm steel ball penetrated up to 9 mm into *ex vivo* goat brain using gradients of 23 mT/m.

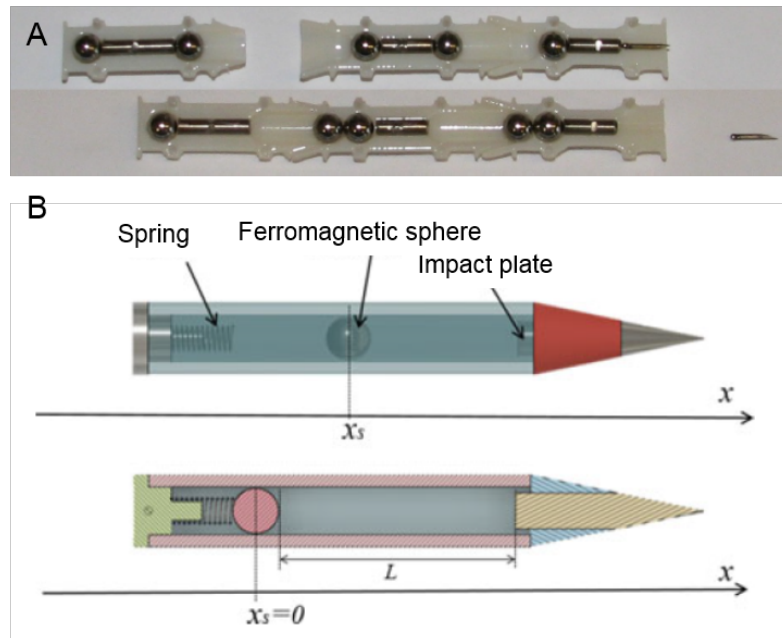


**Figure 3.8.** **A.** photo of the cross section of the gauss gun in Becker et al., 2015<sup>261</sup> showing the positions before and after firing. **B.** Schematic of the magnetic actuation hammer from Leclerc et al., 2018<sup>262</sup>.

To realise actuation of magnetic particles in the brain, whether that is the targeting of magnetic particles through the vasculature, mechanical stimulation of cells or manoeuvring millimetre sized magnetic seeds through tissue, the gradient strength is key to delivering the forces needed. With current clinical MRI gradients limited to a few 10's of mT/m, millimetre sized particles are needed if they're to be moved through the vasculature. To reduce the size of these particles, or to move them through tissue, gradient strength must be increased by at least an order of magnitude. High field pre-clinical MRI systems however, have gradient sets that can deliver up to 1 T/m albeit for very short times. In chapter 6 these increased gradient strengths are utilised to realise the potential of using MRI as a minimally invasive surgical tool.

To realise whether MRI could be used for cell stimulation, a minimum force threshold must first be established. This threshold will depend on a number of variables: gradient strength, particle volume, particle material, particle contact area to the cell and cell type. The following chapter investigates each of these variables in turn using custom built electromagnet which could sit atop an inverted

fluorescent microscope. Whether MRI gradients can be used for stimulation or not, MRI can still be used to verify the location and fate of magnetic particles after administration as shown in chapter 5.

## 4 Characterisation of forces for *in vitro* stimulation of astrocytes using magnetic particles

### 4.1 Introduction

To truly understand the remarkable complexity of the human brain, it is pertinent to have the ability to selectively control the activity of a specific cell type to achieve the goal of assembling an overall theory of the mind. The advent of optogenetics less than 20 years ago appeared to be that Holy Grail, allowing for spatial and temporal specificity of cellular control previously unattainable to facilitate investigations into specific functional neural circuits within the brain that could not be done before<sup>1,263</sup>. Optogenetics is not limited to neurons either. Astrocytes, the most abundant glial cell in the brain, have been revealed to play an important role in breathing and sleep through optogenetic control. However, this technology is not without its drawbacks. Delivery of light often requires insertion of an optical fibre and genetic modification of the cells alone may cause perturbations in their natural physiology and could prove to be a hindrance for clinical translation. While wireless untethered light delivery systems have been developed<sup>264</sup>, and in 2015 the FDA approved clinical trials of optogenetics for the treatment of advanced Retinitis Pigmentosa, there is scope for the development of less invasive methods that can utilise the intrinsic properties of a particular cell type without the need for genetic modification.

Magnetic nanoparticles hold huge promise in this regard. The use of magnetic fields allow for remote control actuation, while their surface can be coated with ligands that target specific cell types, attaching to certain proteins or channels on the cell surface<sup>81</sup>. A variety of methods have been explored for the control of cellular activity using magnetic nanoparticles. Rotational or translational forces can be applied to cells using a static field, while hyperthermia can be induced by heating particles with an alternating magnetic field. One method that has come to the fore is thermogenetics or magnetogenetics, whereby the target cell is genetically altered to express the heat sensitive ion channel TRPV-1<sup>59,63</sup>. Magnetic particles are then targeted to this channel, which when heated or force is applied causes the channel to open (Figure 1.3)<sup>265</sup>. While the actuation of these techniques can be considered non-invasive, they still require genetic modification of cells.

In this study I assessed the feasibility of using magnetic particles as a targeted mechanical stimulation technique for astrocytes. Astrocytes were chosen for their inherent mechano-sensitivity, and targeted using magnetic particles coated with ACSA-1, an antibody that binds to the GLAST

protein naturally expressed in the cell membrane. First the minimum force required to stimulate astrocytes *in vitro* was calculated using  $\text{Fe}_3\text{O}_4$  particles coated with collagen similar to an existing method<sup>64,66</sup> and I used a custom built electromagnet capable of generating a uniform magnetic force across the whole cell culture. Cells were exposed to successive bursts of magnetic force which were increased incrementally until stimulation was observed. The volume of particles attached to each stimulated cell was then estimated in respect to its base area from bright-field images by establishing the relationship between the two using 3D reconstructed SEM images of cell cultures that exhibit stimulation. Equipped with this force threshold, new particles were tested which could be coupled with an astrocyte specific antibody ACSA-1 to deliver targeted stimulation of astrocytes. Stimulation was then demonstrated using Biomag Maxi and SiMAG particles, the latter being of suitable size to take forward for *in vivo* applications.

## 4.2 Methods

### 4.2.1 Iron oxide particles used

Several types of particles were used in this study. A super conducting quantum interference device (SQUID) was used to measure the B-H curve for each particle. The slope about zero was taken as the mass susceptibility of the particle. All other properties were provided by the manufacturer.

### 4.2.2 Ligand coupling

#### 4.2.2.1 *Fe<sub>3</sub>O<sub>4</sub> particles with collagen*

20 mg of Fe<sub>3</sub>O<sub>4</sub> particles were incubated in a mixture of 50 µl of type I collagen solution (3.0mg/mL, Sigma Aldrich®,  $m_{\text{ligand}}/m_{\text{particle}} = 7.5 \times 10^{-3}$ ), 200 µl of PBS (Sigma Aldrich®) and 5 µl of 1 M NaOH (Fisher scientific) at 37°C for 1 hour. Particles were washed with 500 µl of PBS three times, re-suspended in 500 µl of PBS (concentration = 40mg/mL) and mixed in a rotator for 24 hours at room temperature before storing at 4°C.

#### 4.2.2.2 *Biomag Plus with ACSA-1*

50 µl of BioMag Plus suspension (20 mg/mL) was taken and washed with 500 µl of MES buffer (50 mM, pH 5.2) four times. 1.6 mg of EDAC was dissolved in 500 µl of MES buffer and added to the particle solution and mixed in a rotator for 30 minutes at room temperature. Particles were washed a further four times with 500 µl of MES buffer. 200 µl of ACSA-1 solution and 300 µl of MES buffer was added to the particles ( $m_{\text{ligand}}/m_{\text{particle}} = 20.0 \times 10^{-3}$ ) and incubated for 16 hours in a rotator at room temperature. Particles were then washed once with 500 µl of MES buffer solution 500 µl of quenching solution (distilled water with 1 M glycine, pH 8.0) was added to the particles and incubated for 30 minutes in a rotator at room temperature. Particles were then washed with 500 µl of storage solution (distilled water with 0.15 M NaCl, 0.01 M Tris, 0.001 M Ethylenediaminetetraacetic acid (EDTA), 1 mg/mL BSA and 1 mg/mL sodium azide, all from Sigma Aldrich®) four times. The particles are finally resuspended in 100 µl of storage solution and stored at 4°C.

#### 4.2.2.3 *SiMAG with ACSA-1*

20 µL of SiMAG suspension (50 mg/mL) was washed with 100 µL of MES buffer (100mM, pH 5.0) twice. Particles were then re-suspended in 120 µL of MES buffer and 0.5 mg of EDAC was added to

activate the particles for 10 minutes in a rotator at room temperature. Particles were then washed twice again with 100  $\mu$ L of MES buffer, re-suspended in a mixture of 50  $\mu$ L of ACSA-1 solution and 10  $\mu$ L of MES buffer ( $m_{\text{ligand}}/m_{\text{particle}} = 5.0 \times 10^{-3}$ ) and incubated for 2 hours in a rotator at room temperature. Particles were then washed with 100  $\mu$ L of PBS three times, re-suspended in 10  $\mu$ L of PBS (concentration: 10 mg/mL) and stored at 4°C.

#### 4.2.3 Astrocyte cell culture

This protocol was modified from Schildge et al.<sup>266</sup>. After rat pups were sacrificed (post-natal day 3-4) by decapitation, their brains were removed and placed in ice-cold Hanks Balanced Salt Solution (HBSS, Gibco). Cerebral cortices were dissected out, cut into small pieces and digested in HBSS containing 0.25% trypsin (Gibco) at 37°C for 10 minutes. Cells were pelleted via centrifugation, the supernatant was removed and astrocyte culture medium (Dulbecco's Modified Eagle Medium, DMEM, with high glucose Glutamax™ supplement with 10% heat inactivated fetal bovine serum (FBS) and 1% penicillin-streptomycin (10,000 U/mL), all from Gibco) was added. Cells were further dissociated by titration with a pipette tip and cell suspension was sieved through a 40  $\mu$ m cell strainer (Corning incorporated) to remove debris. Cells were then counted and diluted before plating onto T75 culture flasks (ThermoFisher scientific) coated with poly-D-lysine (Merck Millipore). Cultures were maintained at 37°C, 100% humidity and 5% CO<sub>2</sub>, changing the medium every 2-3 days. When cells were confluent, flasks were shaken on an orbital shaker at 180 rpm for 30 minutes then 210 rpm for 6 hours to remove microglia and oligodendrocyte precursor cells. The remaining cells were washed with HBSS twice, detached from the flask with 0.05% trypsin-EDTA (Gibco), centrifuged and resuspended in astrocyte culture medium. After counting and diluting a desired concentration, cells were re-plated onto 12mm circular coverglasses coated with poly-D-lysine (Gerhard Menzel GmbH, Germany) in 24 well plates (Corning incorporated). Approximately 70,000 cells were plated onto a single coverglass reaching 90% confluency after 3-4 days. All cell cultures were used within 1 week of plating.

#### 4.2.4 Calcium imaging

Cell cultures were washed twice with HBSS before being incubated in HBSS containing iron oxide particles for 1 hour at room temperature. Cells were washed twice again with HBSS and incubated in HBSS containing 4  $\mu$ M Fura-2 AM (Molecular Probes) and 0.04% Pluronic F-127 (Molecular Probes) for 0.5-1 hour at room temperature in the dark, followed by two further washes with HBSS before imaging. Changes in  $[Ca^{2+}]_i$  were monitored in individual cells using an Olympus IX71 inverted

microscope with an Andor CCD camera. Excitation light was provided by a xenon arc lamp with the beam passing through the monochromator at 340 and 380 nm (Cairn research, UK) and an emitted fluorescence at 515 nm was registered. The ratio of the Fura-2 fluorescence between the two wavelengths was measured, giving an accurate indication of changes in  $[Ca^{2+}]_i$ .

Cells were considered responsive when the maximum ratio during the 20 seconds post stimulation was at least 25% higher than the baseline signal taken as the average over the 20 seconds prior to stimulation<sup>267</sup>. The size of response was taken as the percentage increase from baseline to peak ratio.

#### 4.2.5 Yoke electromagnet design

This magnet, designed by Dr Ana Garcia Prieto, generates a uniform magnetic force over an area between two pole pieces. The shape of these pole pieces were designed according to a well-known faraday susceptibility method<sup>268</sup> and the report on the magnetic susceptibility balance by Garber et al<sup>269</sup>. The force exerted on magnetic particles by an external magnetic field is proportional to the sum of the magnetic field strength and field gradient  $(\mathbf{B} \cdot \nabla)\mathbf{B}$  (equation 2.11). The custom built Yoke magnet allowed for all cells within the field of view to experience the same  $(\mathbf{B} \cdot \nabla)\mathbf{B}$ . It also allows the force exerted on each cell to be increased incrementally until stimulation is observed to pinpoint the minimum force required to stimulate a particular cell. To do this, the two pole pieces were designed so that the magnetic field between them fulfilled the following condition:

$$-B_y \frac{dB_x}{dx} + B_x \frac{dB_x}{dy} = constant \quad 4.1$$

As an approximation, variation with respect to x can be ignored, simplifying the condition to:

$$B_x \frac{dB_x}{dy} = constant \quad 4.2$$

To yield:

$$B_x = \sqrt{ay + b} \quad 4.3$$

Where a and b are constants. The gap  $B_x$  is assumed inversely proportional to the gap width:

$$B_x \propto \frac{1}{\Delta x} \quad 4.4$$

If  $\Delta x$  is then half the gap width at a level y, then:

$$\Delta x = \sqrt{\frac{c}{ay+b}} \quad 4.5$$

Where  $c$  is a constant. This determines the shape of the pole pieces for positive  $y$  values. At negative  $y$  positions, the shape of each pole piece is given as:

$$x = -ycot60 + d_{min} \quad 4.6$$

Where  $d_{min}$  is the minimum separation gap at  $y=0$ .

$$d_{min} = \Delta x(y = 0) = \sqrt{c/b} \quad 4.7$$

To maximise magnetic field strength, but still provide a suitable gap between the poles to facilitate imaging with a microscope the values of the constants were chosen as:  $a = -0.25$ ,  $b = 1$ ,  $c = 25$  and  $2d_{min} = 10 \text{ mm}$ .

#### 4.2.6 Force Calculation

The minimum force threshold for astrocyte stimulation was determined using the Yoke electromagnet and collagen coated iron oxide particles. Cells were placed between the pole pieces at a height of 2mm above the base of the Yoke magnet for calcium imaging with the inverted microscope. Cells were incubated with an optimum particle concentration of 0.2 mg/ml which produce a sparse distribution of particle clusters so that each cluster could be associated to a single cell.  $[Ca^{2+}]_i$  responses were measured over 11 astrocyte cultures. Cells were exposed to increasing amounts of magnetic force by increasing the current passing through the magnet from 0.3 – 0.9A in 0.1A increments. All stimulated cells were identified and assigned the minimum current that caused the  $[Ca^{2+}]_i$  response. Particle clusters attached to each cell were identified on the brightfield micrographs and their base area measured using thresholding and the ‘analyse particles’ function in ImageJ (National Institute of Health, USA). The forces applied to each cell was then calculated using equation 2.11. The volumetric magnetic susceptibility of the iron oxide particles was measured from the B-H curve from the SQUID measurements and  $\Delta\chi$  was found by subtracting the value for water ( $-9.06 \times 10^6$ ).  $(\mathbf{B} \cdot \nabla)\mathbf{B}$  was determined by measuring the magnetic field along the midline of the pole gap at each current value. The  $(\mathbf{B} \cdot \nabla)\mathbf{B}$  at the position the cells were placed (14.5 – 26.5 mm) was uniform for currents up to 0.9A, deviating less than  $0.005T^2m^{-1}$  from the mean. 3D simulations of the Yoke magnet were performed using the magnetostatic module on Opera vector fields (version 16.1, Cobham plc, UK) using physical measurements of the finished product.

The volume of each cluster was estimated from its base area by finding the relationship between the two using scanning electron microscopy (SEM). Three cell cultures used for imaging were prepared for SEM. Cell cultures were fixed with a buffer containing 0.1 M sodium cacodylate, 2%



paraformaldehyde and 1.5% glutaraldehyde (pH 7.3, Sigma Aldrich®) overnight at 3°C and post fixed with a buffer containing 0.1 M sodium cacodylate and 1% osmium tetroxide (Sigma Aldrich®) at 3°C for 30 minutes. Cells were then washed in 0.1 M sodium cacodylate buffer, rinsed with distilled water, dehydrated with ethanol and dried using CO<sub>2</sub>. Specimens were then mounted on aluminium stubs using carbon adhesive tabs and coated with a thin layer of gold/palladium or carbon using Gatan ion beam coater. All cultures were scanned at x700 magnification with a JEOL JSM-7401F field emission scanning electron microscope (JEOL Ltd, UK) at four similar positions, one in each quadrant. Images were taken at a tilt angle of 10 and 20° respectively for each field of view. Stereoscopic 3D surface reconstruction was then performed on pairs of images followed by tilt correction using MountainsMap® SEM (Digital Surf, France) to produce a topographic map. An island map was generated after thresholding by height and regions of interest were drawn around each cluster to acquire values for base area and volume. From this data the relationship between base area and volume was found and used to estimate the volume of magnetic material associated with each stimulated cell. All volumes were weighted by a 95% purity given by the manufacturer.

To determine the force threshold, the distribution of thresholds obtained for each stimulated cell was modelled by a log normal curve by solving for the parameters A,  $\mu$  and  $\sigma$  of the function

$$f(x) = \frac{A}{x\sigma\sqrt{2\pi}} \exp\left(\frac{-(\ln x - \mu)^2}{2\sigma^2}\right) \quad 4.8$$

Using the nonlinear regression model fitting function “fitnlm” in Matlab. The force threshold was then taken as the median value from this distribution.

As the force applied by the magnet is predominantly coplanar with the coverglass, the cells will experience a sheer stress at their point of contact with the particles. This is equal to the force divided by the cross sectional area on which it acts. For calculating stresses for Biomag and SiMAG particles, the area was assumed to be the cross section through the centre of a sphere while for the Fe<sub>3</sub>O<sub>4</sub> particles, the area was taken as the base area of the cluster.

## 4.3 Results

### 4.3.1 Characterisation of electromagnet and magnetic particles used

Finding the ideal magnetic particle for astrocyte specific stimulation first requires an understanding of the minimum forces needed. To measure the minimum force threshold, collagen coated  $\text{Fe}_3\text{O}_4$  particles were used as they have been shown to stimulate astrocytes with a similar method<sup>66</sup>. From this, particles that could be coated with the astrocyte specific antibody ACSA-1 were chosen according to their size, shape, magnetic content and biocompatibility based on the assumption that they would produce enough force if they form a tightly packed monolayer on the astrocyte.

Equation 2.11 shows that the magnetic force acting on a particle depends on three variables: i) the magnetic susceptibility of the magnetic particles, ii) the volume of magnetic content attached to the cell, and iii) the vector dot product magnetic field gradient operator acting on the magnetic field  $(\mathbf{B} \cdot \nabla)\mathbf{B}$ . First the magnetic field produced by the magnet was assessed to ensure it produces a uniform  $(\mathbf{B} \cdot \nabla)\mathbf{B}$  across a region of cells that could be imaged. The magnet used was a custom built electromagnet designed for this purpose. Figure 4.1 shows the dimensions of the magnet (Figure 4.1A), simulations of the  $(\mathbf{B} \cdot \nabla)\mathbf{B}$  field it generates between its poles (figure 4.1B) and how the cells are positioned between them when positioned upon an inverted microscope (figure 4.1C). As the magnet was initially designed to be most uniform at the centre of the poles, simulations were carried out at two positions: 10 mm above its base and 2mm above where the cells are positioned during imaging, to ensure the forces are still uniform over the imaging plane. The simulated field across the cell culture shows minimal variation in force ( $0.29 \pm 0.002 \text{ T}^2\text{m}^{-1}$ ) over the area that can be imaged (pink dotted oval) at a height of 2 mm when driven at 0.9 A. This shows that a particle anywhere within the imaging region will experience the same magnetic force.

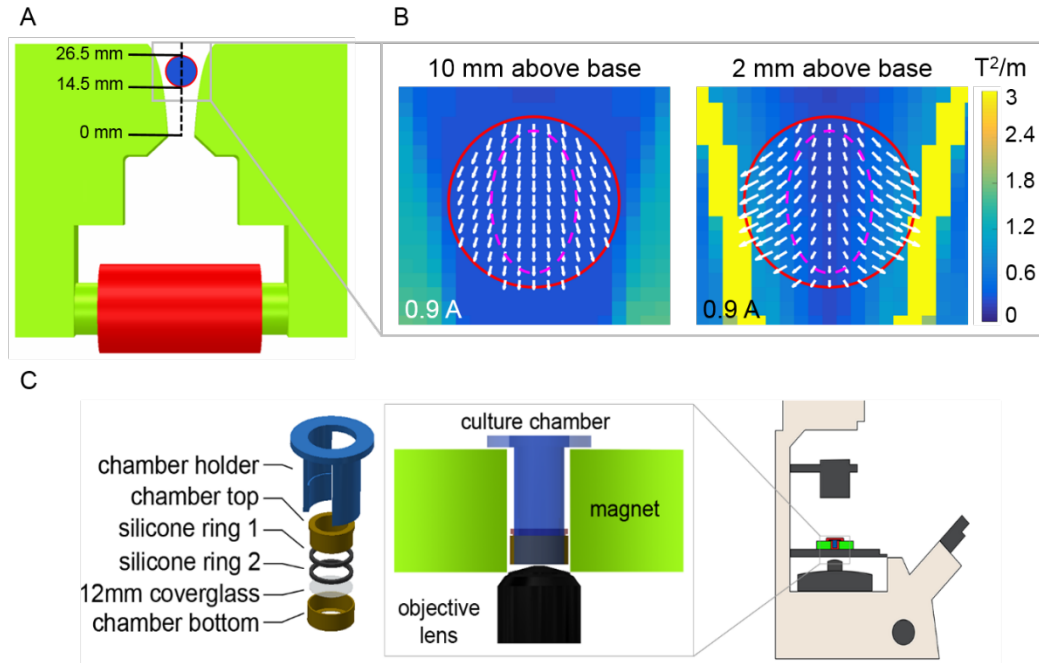


**Figure 4.1.** Yoke magnet simulations. **A.** Top-down view of simulated Yoke magnet. Soft steel is represented in green and coil windings in red. The position of the cell culture between the pole pieces is indicated by the blue circle. **B.** Simulated  $(\mathbf{B} \cdot \nabla)\mathbf{B}$  fields at the mid height (10mm above base) and the cell culture height (2mm above base) show minimal variation in force across the total imaging area (pink oval) when the magnet is driven at 0.9A. Red circle indicates position of whole cell culture, white arrows indicate force direction. **C.** Display of components of cell culture chamber and it's placement within the magnet during experiments.

To find the minimum force required for astrocyte stimulation, the magnet must be controllable, with the ability to be increase the force incrementally until a response is observed. The magnet was therefore tested at a range of input currents to determine the range of forces it can produce. Figure 4.2A shows that hall probe measurements match the simulated magnetic field along the midline of the two pole pieces for each current input value at 2 mm above the magnet base. This allowed the use of simulated data to measure the distribution of forces generated by the magnet. Figure 4.2B shows the  $(\mathbf{B} \cdot \nabla)\mathbf{B}$  values for each current input at both heights. The  $(\mathbf{B} \cdot \nabla)\mathbf{B}$  increases incrementally with increasing input current while the uniformity gradually decreases. While the spread of forces is less at the centre height of the magnet, at 1 A when the magnet is designed to run continuously without heating, the variation in  $(\mathbf{B} \cdot \nabla)\mathbf{B}$  is still small at  $0.36 \pm 0.07 \text{ T}^2\text{m}^{-1}$  within the available imaging area, showing that all cells in the imaging region

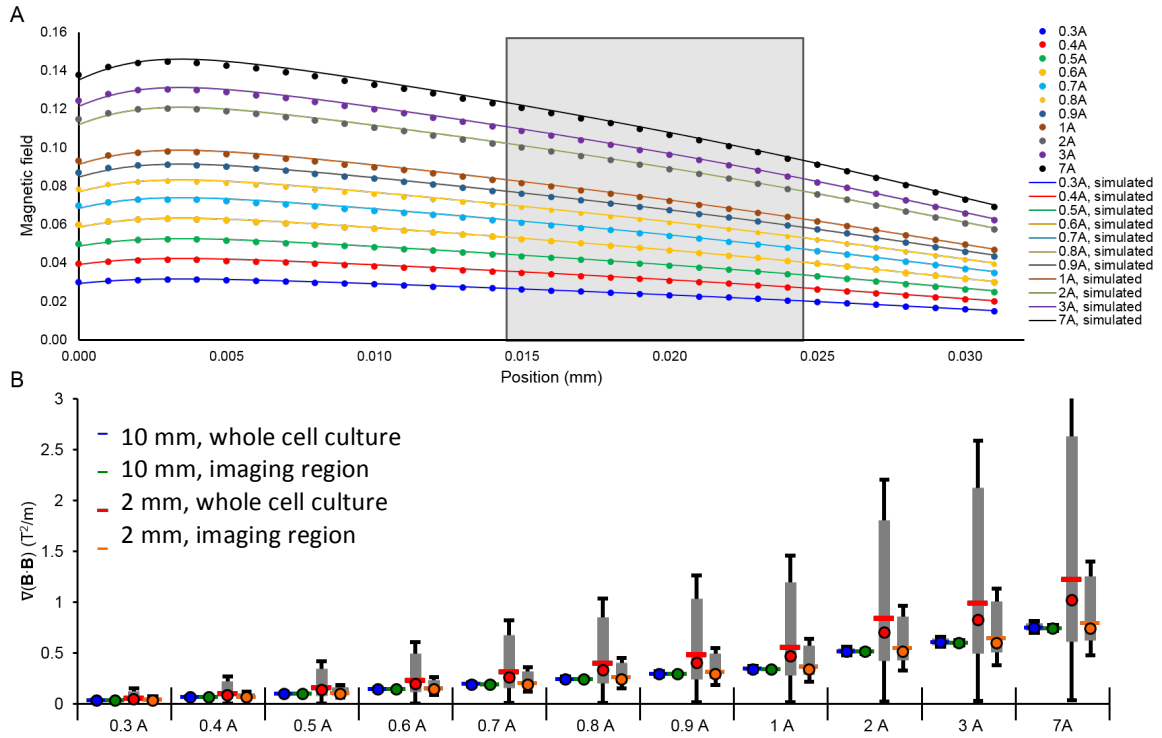


**Figure 4.2.** Yoke magnet simulation validation. **A.** Comparisons of the measured versus simulated field along the midline of the two pole pieces show good agreement. Grey region indicates position of cells. **B.** Graph showing increasing current input increases the  $(B \cdot \nabla)B$  field generated by the magnet. The mean (coloured line), median (coloured circle), upper and lower limit (black bars) and standard deviation (grey bars) of the  $(B \cdot \nabla)B$  field for both heights across the whole cell culture and within the imaging plane

Next the magnetic susceptibility of all the particles used in this study were measured. SQUID measurements of the magnetisation of the particles over a field sweep are shown in figure 4.3. The particles reaching the highest magnetisation, and highest susceptibility were the  $\text{Fe}_3\text{O}_4$  particles ( $\chi = 9.8 \times 10^{-4}$ ), followed by the two Biomag particles with the SiMAG particles having the smallest susceptibility. This is due to the decrease in size and magnetic content.

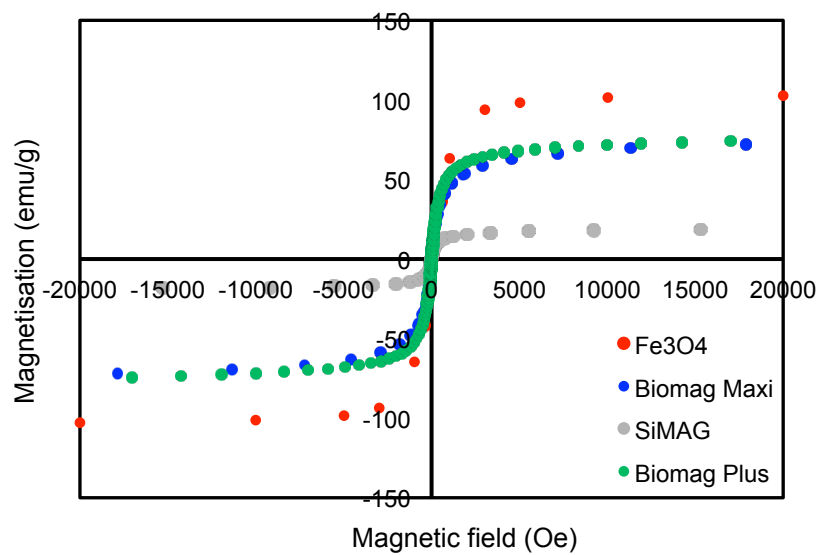


**Figure 4.3.** Magnetisation curves of the magnetic particles used

### 4.3.2 *In vitro* force threshold quantification

Having established that the magnet will generate the same field over all cells within the imaging region, and measured the magnetic properties of the particles, the volume of particles attached to each stimulated astrocyte now needs to be measured. To do this  $[Ca^{2+}]_i$  responses of individual astrocytes decorated with iron oxide particles were recorded while a magnetic field was applied for consecutive 10 second bursts, increasing the current each time by 0.1A (Figure 4.4A). The concentration of particles was optimised so that discrete particle clusters could be identified from brightfield images and matched with a single cell on an overlaid fluorescence image. In the first instance stimulation is observed in a particular cell, the current input is assigned to that cell which corresponds to a particular  $(\mathbf{B} \cdot \nabla) \mathbf{B}$  value (Figure 4.3B).  $[Ca^{2+}]_i$  responses were observed at input currents as low as 0.3A (Figure 4.4C) with the majority of the cells (>70%) being stimulated between 0.5 – 0.7A.

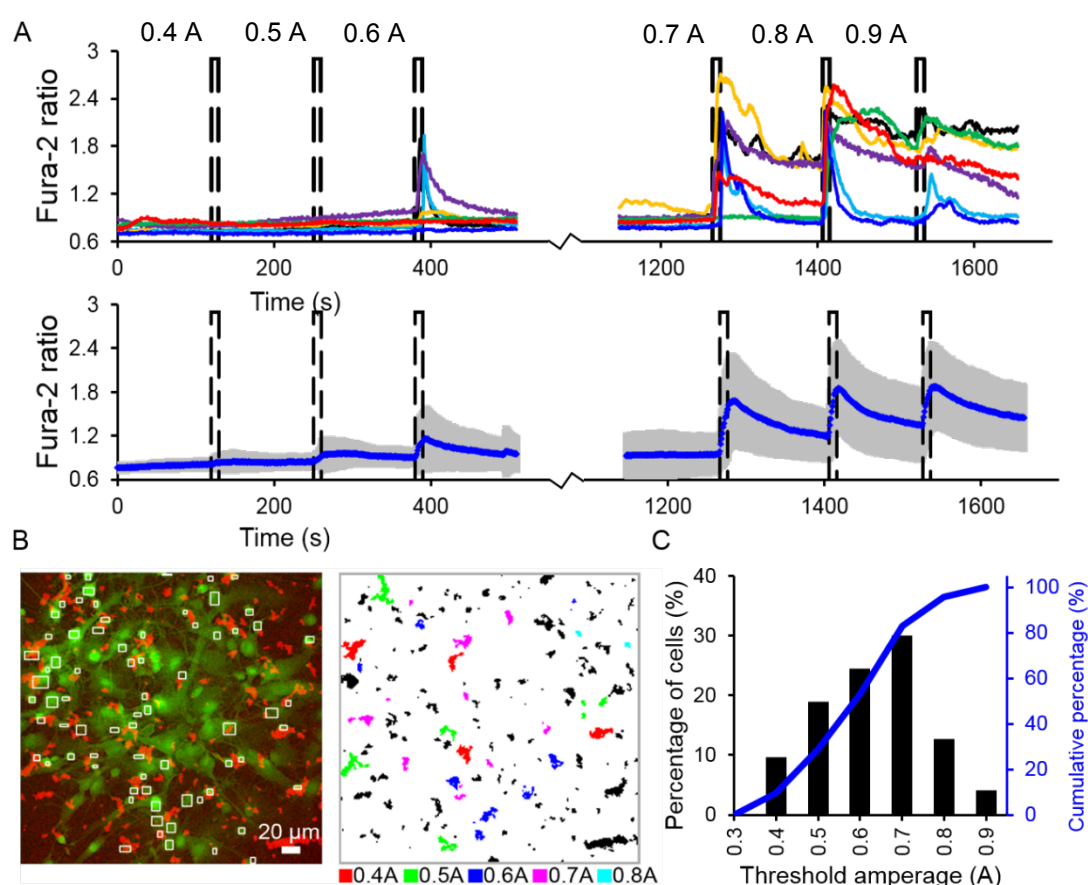


**Figure 4.4.** Astrocyte stimulation with collagen coated  $Fe_3O_4$  particles. **A.** Example Fura-2 ratios (above) and mean ratio (below) from ROI's drawn over stimulated astrocytes in B after successive incrementally increasing 10 second force applications. Grey indicates standard deviation. **B. Left.** Example FOV showing astrocytes (green) overlaid with the brightfield image of magnetic particles (red). **Right.** Brightfield image of magnetic particles colour coded according to the minimum current

for that cluster to stimulate its associated astrocyte. **C.** Graph showing percentage of cells stimulated at each current input.

As the base area of the cluster can be measured directly (figure 4.4B), the volume can be inferred by investigating the relationship between the two. This was done using 3D reconstructed SEM images of cell cultures where mechanical stimulation was observed. Figure 4.5A shows example SEM images of the two tilt angles with the topographical and island maps generated from the 3D reconstruction (Figure 4.5B-C). The SEM images also show that the clusters that form are not solid but porous. Figure 4.5D shows a linear correlation between the natural logarithm of the volume and base area of clusters. Figure 4.5E shows a log normal distribution of the volume over base area and figure 4.5F shows the average volume of clusters for cells stimulated at different current inputs, which decreases with increasing current.

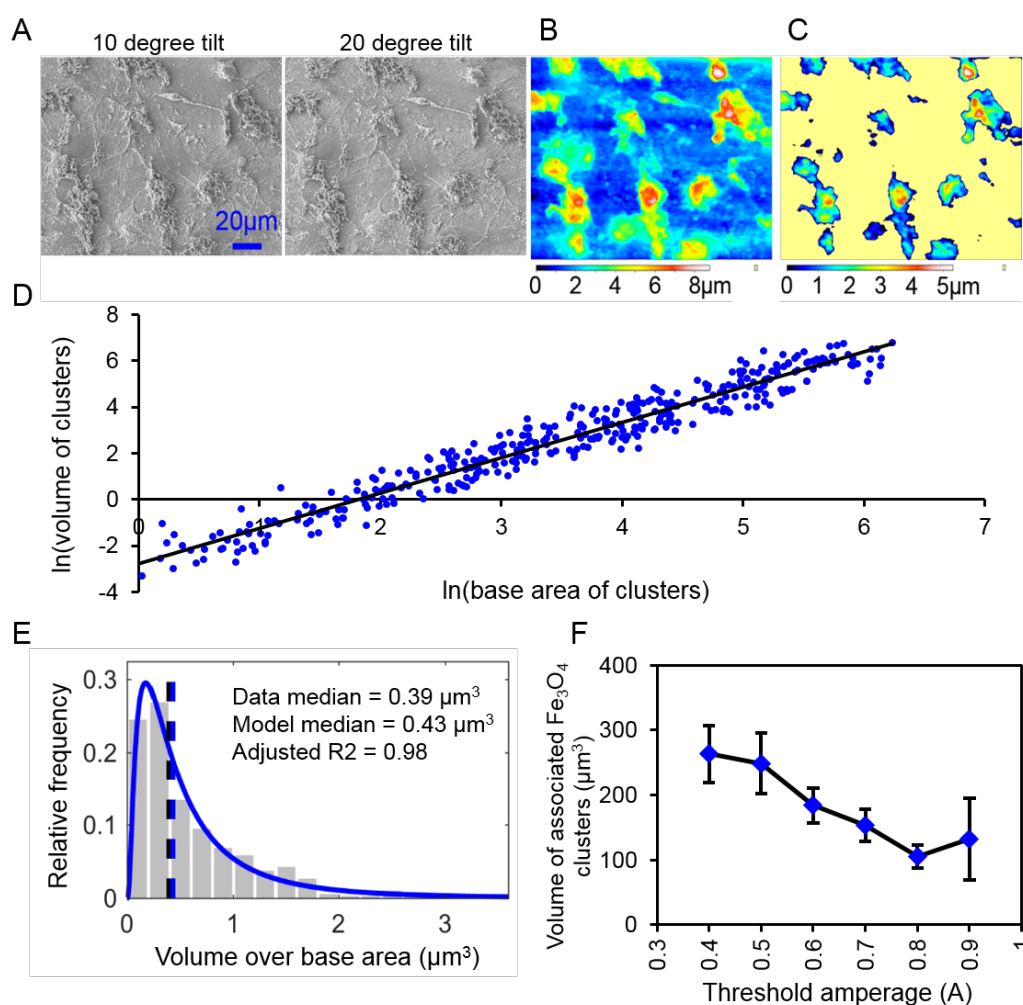


**Figure 4.5.** Particle cluster volume calculation. **A.** Example paired SEM images at different tilt angles used for 3D reconstruction with the resulting topographical and island map generated in **B** and **C**. **D.** Graph showing the natural logarithm of cluster volume over base area showing a linear relationship.

**E.** Graph showing the particle cluster volumes displayed a lognormal distribution. **F.** Graph showing the average cluster volume associated with each current input used for stimulation. With an established relationship between base area and volume, the forces applied to each stimulated astrocyte could be calculated. Over a total of 277 astrocytes the median force was found to be 25.37 pN, and a median stress of 0.2 Pa for mechanical stimulation of astrocytes using magnetic particles (Figure 4.6).

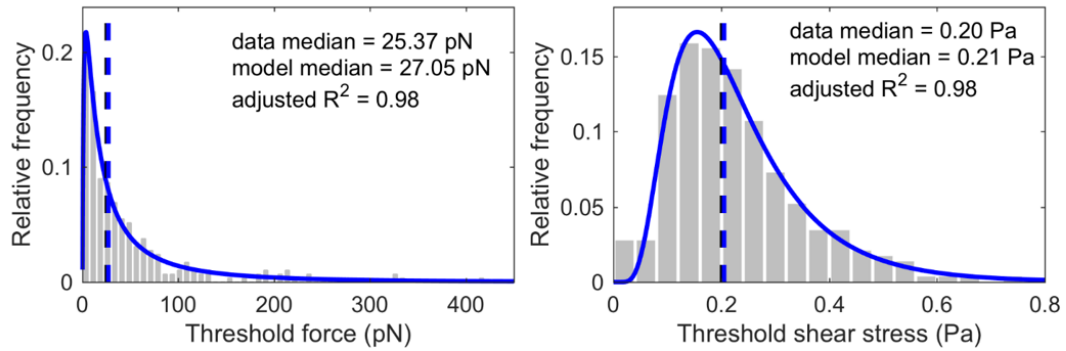


**Figure 4.6.** Force and stress threshold for astrocyte stimulation. Graphs displaying the median force (left) and median stress values (right) for the data and model fitting.



### 4.3.3 Targeted stimulation of astrocytes with ACSA-1 coupled magnetic particles

So far the magnetic particles used have been collagen coated  $\text{Fe}_3\text{O}_4$  particles which bind non-specifically to most cells. To deliver true cell specific targeted stimulation different particles are needed that can be ligand coupled to the astrocyte specific antibody ACSA-1. Two potential magnetic particles were identified: Biomag Plus particles were chosen for their high magnetic content (90% iron oxide) and were of a size comparable to the  $\text{Fe}_3\text{O}_4$  particles ( $1.5\ \mu\text{m}$  versus  $< 5\ \mu\text{m}$ ). The SiMAG particles were also chosen as they were smaller (500 nm) but still had a high magnetic content (80% iron oxide), as smaller particles are tolerated better in vivo and are less likely to block the syringe during administration.

First, when measuring their magnetic properties (figure 4.3), closer inspection of the M-H curves revealed that the magnetic susceptibility of the  $\text{Fe}_3\text{O}_4$  particles remains constant over the field values generated by the Yoke magnet (-0.1T to 0.1T) whereas the Biomag Plus and SiMAG particles begin to saturate within this range. This means that a different equation was needed to calculate the forces on these particles:

$$\mathbf{F}_m = V_m \nabla \left( \frac{1}{2} \mathbf{B} \cdot \mathbf{M} \right) \quad 4.9$$

Where  $\mathbf{V}_m$  is the particle volume and  $\mathbf{M}$  is the volumetric magnetisation.  $\mathbf{M}$  is then dependent on the magnetic field  $\mathbf{B}$  produced by the Yoke magnet, which is dependent on the input current. The magnitude of  $\mathbf{M}$  can then be obtained from the M-H curve at the  $\mathbf{B}$  value associated with the minimum input current for stimulation. Initial calculations of the stress applied by the Biomag plus particles suggested that stimulation should occur when the magnet was driven at 0.8A or higher (Figure 4.7A). However, even when driven at a maximum of 7A no stimulation was observed using these particles (data not shown). SEM images of the particles alone revealed the Biomag plus particles to be flake like and not spherical (Figure 4.7B) which reduces the volume of iron content assumed in the stress calculations. When this reduced volume was taken into account these particles were below the stress threshold for stimulation.

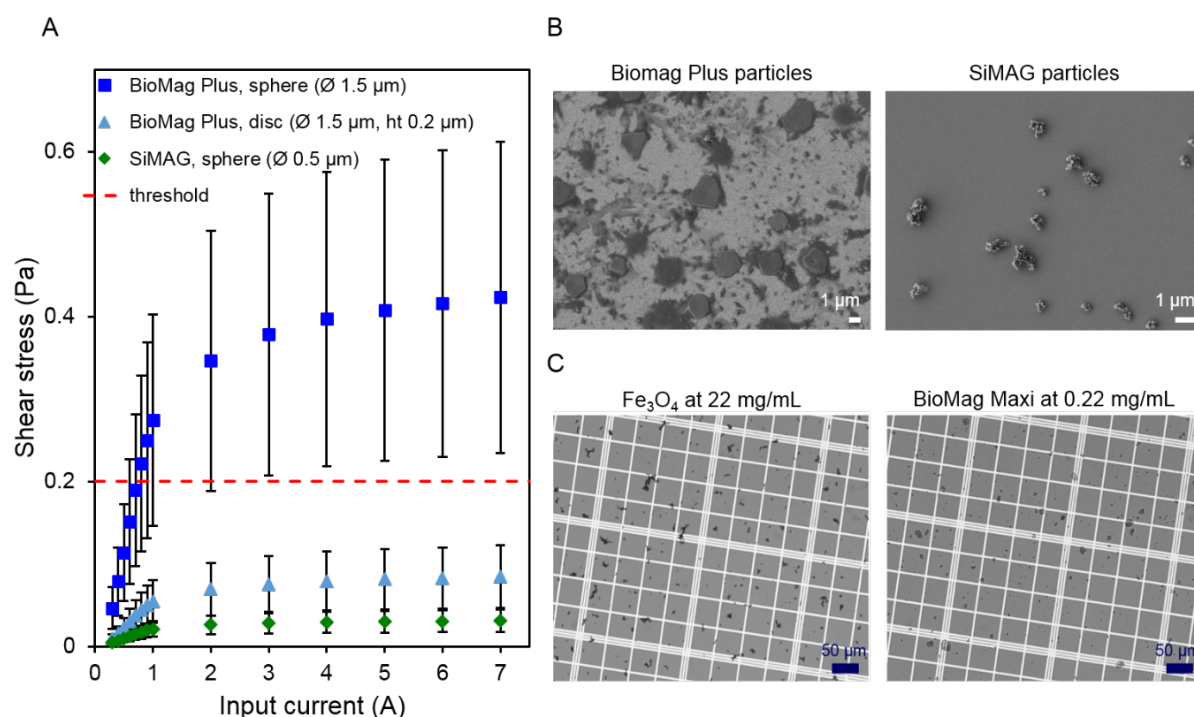


**Figure 4.7.** Stress calculations for biocompatible magnetic particles. **A.** Graph comparing the estimated stress of single particles at different current inputs showing that the non spherical Biomag Plus particles generate stresses below the stress threshold (red dotted line). **B.** SEM images of Bio Plus and SiMAG particles. **C.** Brightfield micrographs showing similar particle clusters for  $\text{Fe}_3\text{O}_4$  and Biomag Maxi particles at the same concentration.

To overcome this, larger Biomag Maxi particles were tested as they had larger particle diameters (3-12  $\mu$ m). Brightfield microscope images revealed these particles to produce similar particle distribution to the  $\text{Fe}_3\text{O}_4$  particles at 0.22 mg/mL (Figure 4.7C), however attempts to stimulate with the Biomag Maxi particles at this concentration were also unsuccessful even when the magnet was driven at 7A. Again, because of their flake like shape it is likely the volume to base area ratio of the Biomag Maxi particles were less than the  $\text{Fe}_3\text{O}_4$ .

Therefore to further increase the volume of magnetic particle attached to the cells, the particle concentration was increased. By increasing from 0.22 mg/mL to 0.44 mg/mL, stimulation was finally observed using the ACSA-1 coupled Biomag Maxi particles when the magnet was driven at 7A. Figure 4.8A shows example traces of stimulated cells using the Biomag Maxi particles, demonstrating that magnetic particles coupled with the astrocyte specific antibody ACSA-1 can be used for targeted cell mechanical stimulation.  $[\text{Ca}^{2+}]_i$  transients were recorded in a total of 10 astrocytes across 3 cell cultures. Due to the increase in concentration, individual clusters could not be identified so further analysis of the forces applied was not possible. While they facilitated the first example of astrocyte stimulation with antibody coupled particles, the large size of the Biomag Maxi particles make them impractical for *in vivo* applications.

The SiMAG particles were chosen with this size limitation in mind. As astrocyte stimulation depends on the concentration of particles, it was thought that despite their smaller size, SiMAG particles could produce enough force at sufficiently high concentrations. Increasing the concentration to 0.88 mg/mL,  $[Ca^{2+}]_i$  transients were observed using ACSA-1 coupled SiMAG particles when the magnet was driven at 7A ( $0.74 \text{ T}^2\text{m}^{-1}$ ) (Figure 4.8C-D), thus demonstrating mechanical stimulation using biocompatible magnetic particles of a size appropriate for *in vivo* application.

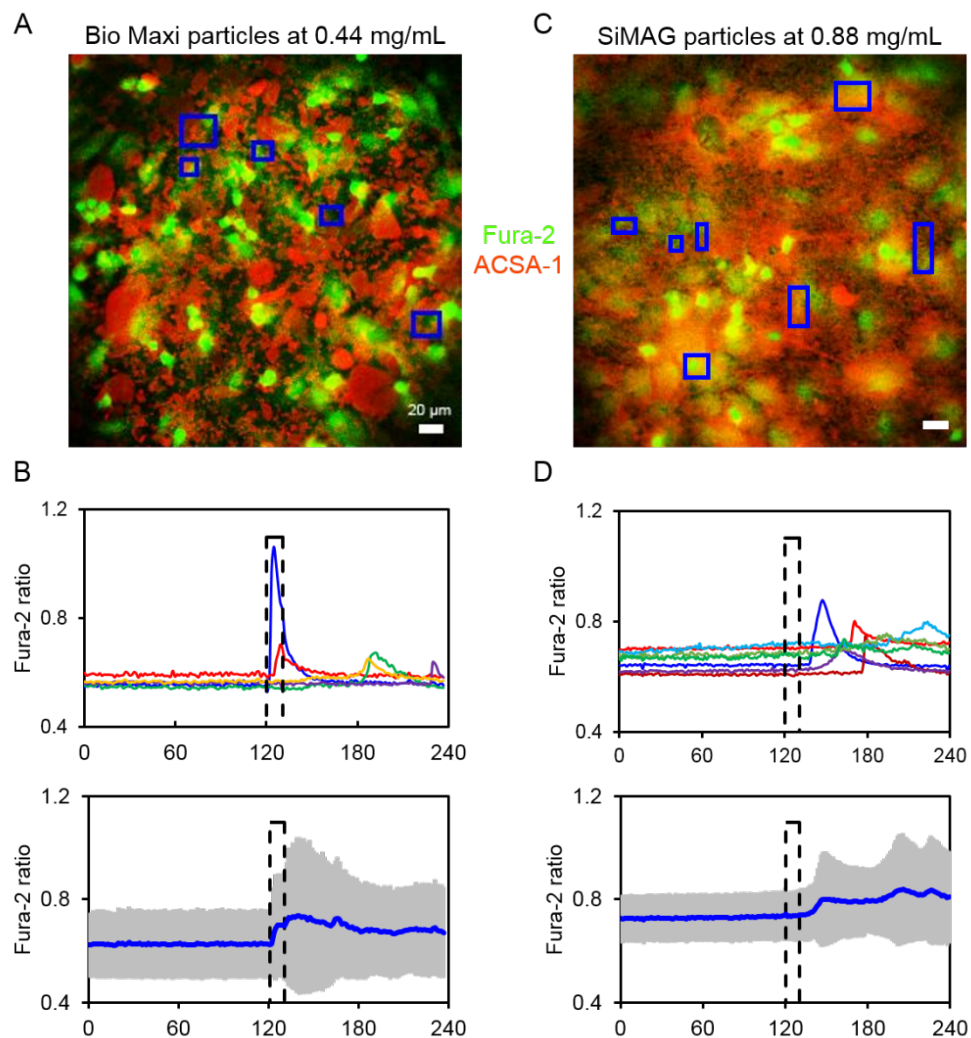


**Figure 4.8.** Targeted mechanical stimulation of astrocytes with antibody coated magnetic particles. Example FOV of astrocytes (green) coated with ACSA-1 coated Biomag Maxi (A) and SiMAG particles (C) (red). B and D. Example Fura-2 ratios and mean ratio taken from ROI's (blue) in A and C. Grey indicates standard deviation.

## 4.4 Discussion

In this study a novel brain cell stimulation technique was developed whereby antibody-coated magnetic particles bind to a specific cell type to provide mechanical stimulation when actuated by an external magnetic field. The aim of this study was to show that biocompatible iron oxide particles couple with ACSA-1, which binds to the GLAST protein naturally expressed by astrocytes, can induce a  $[Ca^{2+}]_i$  response in cultured astrocytes via mechanical stimulation when a magnetic field is applied. The minimum force needed to cause mechanical stimulation was first established using  $Fe_3O_4$  particles that have been used previously to stimulate various cell types including fibroblasts<sup>64,70,270</sup>, C6 glioma cells, bovine aortic endothelial cells and astrocytes<sup>66</sup>. Using a custom built electromagnet, the force applied to particle clusters attached to a specific cell could be quantified. As these particles are not biocompatible and cannot be coupled with ACSA-1, this force threshold was used as a guide to find alternative particles that can generate equivalent forces on a cell while also being suitable for *in vivo* applications.  $[Ca^{2+}]_i$  transients were then observed after mechanical stimulation of cultured cells using SiMAG particles, outlining them as ideal candidates for testing this technique *in vivo*.

Previous studies have used a variety of strategies using magnetic particles to assess the mechanical properties of cells. Some of the earliest experiments used magnetic particles inside cells to measure the viscoelastic properties of cytoplasm and other rheological properties<sup>271–273</sup>. Other studies targeted magnetic particles to specific cell surface receptors, such as integrin, to investigate how mechanical stress effects organisation of the cytoskeleton<sup>51,72,75,274–276</sup>. The majority of these studies used electromagnets with a sharp pole piece which creates a large magnetic field gradient close to the tip, enabling relatively large forces to be applied to single particles (up to thousands of piconewtons). The reduction in force with distance from the tip however is rapid, restricting this magnet design to single particle/single cell observations. The benefit of the Yoke magnet used in my study is the ability to apply force and image a whole population of cells within a typical field of view of  $320\ \mu m^2$ .

Glogeaur et al used both permanent<sup>70</sup> and electromagnets<sup>64</sup> to approximate the amount of force applied to whole populations of cells. However, rather than calculate the force applied to individual cells, they estimated the force for a given particle coverage at different current inputs or distances from the magnet, giving an average force for each combination. They also use the assumption that particles form a monolayer over the cells, which was not the case when analysing the SEM images of the  $Fe_3O_4$  particles. This assumption is also unlikely with the Biomag and SiMAG particles as from figure 4.8, their distribution is not even across the cells. If all the particles on a cell are not tightly

packed they are unlikely to act as a single cluster, reducing the force applied to the cell. The contact area could also play an important role, a smaller contact area would increase the amount of pressure applied to that part of the cell membrane causing a larger local deformation. Inaccuracies in the density and purity of the particles used, which were taken from the manufacturer and not measured directly could also be sources of error, as well as the indirect measurement of volume. Nonetheless, an underestimate of the force is preferable to an over estimate when considering the design of a suitable magnet for *in vivo* applications.

$[Ca^{2+}]_i$  transients in response to mechanical stimulation have been reported in a wide range of cell types including fibroblasts<sup>64,270</sup>, astrocytes<sup>66,277–279</sup>, neurons<sup>280,281</sup>, bone cells<sup>282,283</sup>, inner ear hair cells<sup>284,285</sup>, endothelial cells<sup>78,286</sup>, aortic smooth muscle cells<sup>287,288</sup>, red blood cells<sup>289</sup> and others. A number of different mechanisms have been employed to investigate the relationship between the magnitude of force applied and the degree of  $[Ca^{2+}]_i$  response. Such mechanisms include using a glass pipette to depress the cell membrane<sup>282</sup>, magnetic particles actuated by a magnet<sup>64,66,72</sup> or using a flow chamber to apply shear stress to cells<sup>279,287,290</sup>. A larger  $[Ca^{2+}]_i$  response was observed when more force was applied in all studies. The fluid flow chamber studies demonstrated a plateau in response at large forces, with both aortic smooth muscle cells<sup>287</sup> and endothelial cells<sup>290</sup> exhibiting a large proportion of cells responding at sheer stresses above 0.2Pa. This is in agreement with our findings, with over 80% of cells undergoing stimulation at 0.2Pa. Our minimum force and stress data also exhibited a log normal distribution, which is in keeping with the literature on mechanical stimulation of cells using magnetic beads<sup>274,291,292</sup>. Using either translational<sup>276</sup> or rotational forces these studies found that bead displacement varied from cell to cell of the same type when the same force was applied, displaying an overall log normal distribution. As we observed this distribution in the forces applied, this implies that the minimum displacement of a particle cluster (indicating cell membrane deformation) required to trigger a  $[Ca^{2+}]_i$  response is relatively uniform across all astrocytes.

There are however a few discrepancies between our force/stress threshold and other studies. Shear stresses of at least 2 Pa were reportedly needed to stimulate over 50% of meniscal cells<sup>267</sup> and chondrocytes<sup>293</sup> in oscillatory fluid flow studies. While this could be a result of different cell types having different thresholds, Maneshi et al. reports that the rise time in force applied is also a factor, stating that changes in the duration and rise time could lead to stimulation with sub threshold stimuli. They state a threshold of 1.15 Pa where no  $[Ca^{2+}]_i$  transients were observed for a 10 ms pulse but robust responses occurred using a 1000 ms pulse. However, a  $[Ca^{2+}]_i$  response was observed at 1.15 Pa when the rise time was shortened from 200 ms to 2 ms. The rise time for the Yoke magnet is unknown but is likely to increase with input current due to increased resistivity and heating of the

coil and core. The pulses we used are also much longer at 10 s, which could account for a lower threshold value. Another factor could also be due to the shear stresses using oscillatory fluid flow are applied to the whole apical surface of the cell, whereas the forces exerted by particle clusters would only occur at the contact points between particle and cell, delivering a more focal deformation to lower the threshold.

## 4.5 Conclusion

In this study a novel magnetic particle technique for mechanical stimulation of astrocytes has been developed. Using a custom built electromagnet, the minimum force threshold needed to stimulate astrocytes was evaluated using collagen coated iron oxide particles. This in turn guided the search for magnetic particles capable of delivering the same forces but coupled with the astrocyte specific antibody ACSA-1 to provide cell specific stimulation. *In vitro* astrocyte stimulation was then demonstrated using both Biomag Maxi particles and SiMAG particles. The smaller size of the SiMAG particles make them prime candidates for taking this technique forward into *in vivo* applications.

## 5 In vivo stimulation of astrocytes using magnetic nanoparticles

### 5.1 Introduction

Optogenetics has provided neuroscientists with the ability to control the activity of specific cell types with high spatial and temporal specificity, unlocking knowledge of brain function and connectivity that were previously unattainable. As a minimum requirement for our novel magnetic particle based technique to be considered a valuable alternative, it must be able to deliver an equivalent level of control to elicit the same *in vivo* responses. In this study, astrocytes in the rostral ventrolateral medulla were targeted due to their ability to activate sympathoexcitatory C1 neurons within the region when they release ATP<sup>294</sup>. For this purpose a novel magnetic device was developed called the magnetic mangle, whereby the head of a small rat is placed between four rotatable magnets that could apply changeable, above threshold forces on ACSA-1 coupled SiMAG particles to elicit a sympathoexcitatory response.

This study outlines the design and testing of the magnetic mangle, with comparisons to the Yoke electromagnet used in the previous chapter to establish the shear stress threshold. As the release of ATP activates C1 neurons in the RVLM, the magnetic mangle and Yoke magnet were assessed by measuring increases in extracellular ATP in response to mechanical stimulation. This was performed initially using the collagen coated Fe<sub>3</sub>O<sub>4</sub> particles followed by ACSA-1 coupled SiMAG particles which were identified as ideal particles for *in vivo* stimulation from chapter 4. Immunohistochemistry and MRI were then used to identify the distribution and fate of the particles post injection. Examples of *in vivo* stimulation using our technique were finally demonstrated using the combination of magnetic mangle and SiMAG particles.



## 5.2 Methods

### 5.2.1 Mixed cortical cell cultures

Protocol was modified from Kivell et al. Pups were culled by decapitation and their cerebral cortices isolated in ice cold Hibernate®-A medium (Hib-A, Gibco). Cortical tissue was cut into small pieces and digested in Hib-A containing 0.25 % trypsin for 10 minutes at 37°C. Tissue pieces were then centrifuged, supernatant removed, and pellet re-suspended in Hib-A containing 10% HBS. Cells were then dissociated via trituration, washed once with Neurobasal®-A medium (NB-A, Gibco), then re-suspended in neural cell medium (NB-A, 2% B-27® supplement [50X], 1% GlutaMAX™ supplement [100X] and 1% penicillin-streptomycin [10,000 U/mL], all Gibco). The suspension was sieved through a 40 µm cell strainer and diluted before quantifying cell concentration. The suspension could then be further diluted until at the desired concentration before plating onto poly-D-lysine coated 12 mm coverglasses in a 24 well plate. Cultures were stored at 37°C, 100% humidity and 5% CO<sub>2</sub>. After 24 hours half the medium was replaced to reduce cell debris followed by whole medium changes every 2-3 days. Cells were used between 7-14 days *in vitro*.

### 5.2.2 Design and simulation of a magnetic mangle

One of the difficulties of designing a magnetic device suitable for *in vivo* applications is to generate suitable magnetic forces over a volume whereby the head of a small animal can be placed. The final design chosen for this purpose, dubbed the 'magnetic mangle' was based on the designs proposed by Cugat et al<sup>295</sup>. A variety of rectangular and cylindrical permanent magnets of varying sizes were screened based on magnetic field simulations using Opera vector fields (version 16.1, Cobham plc, UK). The final magnetic mangle design consisted of four diametrically magnetized ring shaped N42 grade NdFeB magnets (20 mm outer diameter, 6 mm inner diameter, 20 mm height, First4Magnets, UK). Mounted on a base plate on a rectangular grid so that the head of a small rat could be positioned between the magnets, each driven by a stepper motor (SY28STH51-0674B, Changzhou Songyang Machinery & Electronics Co., Ltd., China) through a 40:1 worm gear connected to a central box housing an Arduino UNO microcontroller board (Arduino AG, Italy) with a 4-axis stepper driver CNC shield (Protoneer.co.nz) installed with four stepper motor driver carriers (A4988, Pololu Corporation, USA) to enable simultaneous rotation of the four magnets. Connected to the central control box is an interface unit that allows the user to switch between programmable preset magnetic configurations. The magnitude and direction of force applied to magnetic particles are controlled depending on the orientation of each magnet. The magnetic fields produced by the

magnetic mangle were simulated using Opera Vector fields to find configurations that produce the maximum and minimum magnetic force over the central region with the requirement that the maximum force produced by the mangle is greater than the Yoke electromagnet used in chapter 4.

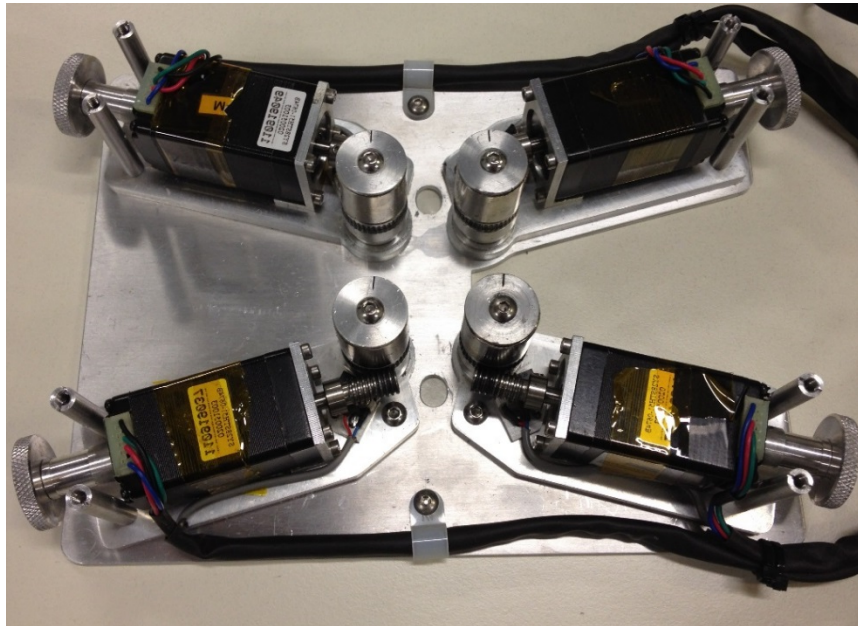


**Figure 5.1.** Photo of the magnetic mangle

### 5.2.3 Detection of ATP release

Due to the inability to fit the magnetic mangle on a microscope stage another means of measuring responses to mechanical stimulation was essential. To establish whether ATP release can be induced by mechanical stimulation, cell medium samples were collected before and after force application. The ATP concentration in the samples were then measured for comparison. This measurement gives an indication of the excitability of a whole population of cells compared to fluorescence imaging which measures changes on a cell by cell basis. This method also allowed for direct comparison to the Yoke magnet to establish global differences in astrocyte stimulation. The procedure was carried out as follows:

Cultures were grown on 12 mm coverslips which were transferred to 3D printed cups (13 mm inner diameter, 0.5 mm wall thickness) and allowed to rest in culture medium in an incubator for 1 hour. Cells were then washed twice with HBSS and incubated with 265  $\mu\text{L}$  of HBSS containing iron oxide particles for 1 hour at room temperature. The cup was then placed in the magnet and an 80  $\mu\text{L}$  pre-stimulation medium sample was collected immediately and frozen on dry ice. Cells were then subjected to stimulation before another 80  $\mu\text{L}$  post stimulation sample was collected and frozen on dry ice.

The concentration of ATP, [ATP], in the medium samples was measured using an assay based on the luciferin-luciferase reaction (CellTiter-Glo®, Promega Corporation, USA). 20 µL of each collected sample were added to an opaque 384 well plate (Greiner Bio One International GmbH) along with a series of ATP standard solutions (0-80 nM of ATP in HBSS) and mixed with 20 µL of luciferin-luciferase reagent. The bioluminescence of the samples were read using an IVIS Lumina imaging system (PerkinElmer Inc., USA) and the photon count was converted to [ATP] using the standard curve. To evaluate whether extracellular concentrations of ATP were significantly different to zero a student's *t* test was performed. A multiple linear regression was used to evaluate the factors of particle concentration and shear stress applied to the cells.

#### 5.2.4 Stereotaxic injection of magnetic particles

Male Sprague-Dawley rats were used. Rats were anaesthetised using an intraperitoneal (IP) injection of a mixture of ketamine (Vetalar™ V, Pfizer, 75 mg/kg) and medetomidine (Domitor®, Orion Corporation, Finland, 0.5 mg/kg) and their fur was shaved from the neck to the line between the eyes before being placed in a stereotactic frame (David Kopf Instruments, USA). Once the rat was in place a midline incision in the scalp was made and small intracranial holes were drilled where SiMAG particles could be injected into the rostro-ventrolateral medulla (RVLM) using a glass pipette. Coordinates for injection in rats > 270 g were based on a histological atlas of the rat brain and a previous study. Coordinates used for rats < 270 g were experimentally determined. First MRI images were taken of large rats with SiMAG particles injected into the RVLM as a reference (n = 2). Particles were then injected into the brainstem of small rats using tentative coordinates, MRI was performed and images registered with the reference images until there was a good match between the location of the particles (n = 9). After injection the wound was sutured and buprenorphine (Vetergesic®, Ceva Sante Animale, 0.03 mg/kg, IP) was given to the animal for pain relief and atipamezole (Antisedan®, Orion Corporation, Finland, 1 mg/kg, IP) to reverse anaesthesia.

#### 5.2.5 MRI for particle retention

MRI was used to determine the location of the magnetic particles after injection into the rostroventrolateral medulla of rats. MRI was performed on a 9.4 T horizontal bore system (Agilent Technologies, USA) using a 72 mm diameter volume coil for RF transmission (RAPID Biomedical GmbH, Germany) and a 4 channel array head coil as a receiver (RAPID Biomedical GmbH, Germany). Body temperature was maintained with a heated water bed and anaesthesia induced initially with 4 % isoflurane and maintained with 1.5 % isoflurane. Physiological monitoring was provided using

respiratory bellows and rectal thermometer (SA Instruments, USA). A T2\*-weighted gradient echo was used with parameters: TE = 6.5 ms, TR = 2230 ms, flip angle = 56°, averages = 5, FOV = 28.8 mm × 28.8 mm, matrix = 192 × 192, slice thickness = 0.15 mm, interslice distance = 0 mm, total scan time = 35 minutes 40 s. Affine registration of the images was performed using a block-matching algorithm. To evaluate the fate of the particles up to 8 days post injection, the volume of the hypointense region caused by the particles was estimated using Amira (FEI).

### 5.2.6 Immunofluorescence

Cell cultures were immunostained to determine the affinity of ACSA-1 coupled magnetic particles to astrocytes. Cell cultures on 12 mm coverglasses placed in a 24 well plate were washed with 400 µL twice and fixed with buffered 4% Paraformaldehyde (PFA) solution (VWR chemicals) for 10 minutes at room temperature. Cells were then washed twice with PBS and incubated with 300 µL of blocking buffer (PBS with 5% donkey serum, 0.3% Triton™ X-100, all Sigma-Aldrich Co. LCC) for 45 minutes at room temperature. After blocking buffer was removed, 300 µL of dilution buffer (PBS with 10 mg/mL BSA, 1% donkey serum, 0.3% Triton™ X-100) with the primary antibody was added and incubated for 1 hour at room temperature. After two further washes with PBS cells were incubated with dilution buffer containing the secondary antibody for 1 hour in the dark at room temperature. This process was repeated if additional antibodies were used. When antibody staining was complete cells were washed twice with PBS and incubated with 300 µL of DAPI solution (PBS plus 2.86 mM DAPI, Sigma-Aldrich) for 5 minutes, washed once again with PBS and once with distilled water. Coverglasses were then taken out of their wells, dried with tissue paper and mounted onto microscope slides dispensed with histology mounting medium (Fluoroshield™, Sigma-Aldrich). To finish the edges of the coverglass was sealed with clear nail varnish.

Alongside MRI, rat brainstem sections were also immunostained to evaluate the localised distribution of SiMAG particles after injection with greater detail. Animals were anaesthetised terminally using pentobarbitone sodium (Pentoject®, Animalcare Ltd, UK, 60mg/kg) and transcardially perfused with a flow rate 5 mL/min with 100 mL of saline followed by 50 mL of buffered 4% PFA solution. Brains were then removed and post-fixed in 4% PFA solution at 4°C. The brains were then immersed in PBS containing 30% sucrose at 4°C for a minimum of 2 days for cryoprotection. Brain stems were then dissected and sectioned into 10-15 µm slices using a cryostat (Leica CM3050 S, Leica Biosystems, Germany) and mounted onto gelatin coated 12 mm coverglasses. Coverglasses were prepared by dissolving 5 g of gelatin (Sigma-Aldrich) in 1 L of deionised water and heated to approximately 45°C. Once dissolved, 0.5 g of chromium (III) potassium sulphate (Sigma-

Aldrich) was added to positively charge the coverglass to help negatively charged brain stem sections to adhere to it. The solution was then filtered before coverglasses were immersed in solution for 5 minutes and dried overnight. Immunostaining on the brainstem sections was then performed identically to the cell cultures with the exception of a 24 to 48 hour incubation period of the primary antibody at 4°C.

#### 5.2.7 In vivo stimulation

Magnetic stimulation was performed on small rats (80-120 g) so that their head would fit in the inter-magnet gap of the magnetic mangle. Up to 2 days post injection of magnetic particles, the animal was anaesthetised with an IP injection of urethane (Sigma-Aldrich, 1.3 g/kg body weight) before being positioned into the magnetic mangle. The animals head was adjusted so that the RVLM was positioned in the central mid-height region of the inter-magnet space where the magnetic field is characterised. The mangle was fitted with a water bed similar to the MRI setup to keep the animal warm. The femoral artery was cannulated to record arterial blood pressure and femoral vein cannulated should additional urethane need to be administered. The left renal nerve was dissected retroperitoneally to record its activity using implanted bipolar silver electrodes. Magnetic stimulation was only performed once blood pressure and renal activity had stabilised.

## 5.3 Results

### 5.3.1 Magnetic Mangle simulations and validation

Figure 5.1A shows a birdseye view of the position of the animal during in vivo stimulation in the custom built magnetic mangle. The dimensions of the mangle were chosen so that the head of a small rat could fit in the inter-magnet space to maximise the magnetic field strength, and in turn the force applied to magnetic particles. Figure 5.1B shows minimum variation in field within a region of 10 mm about the mid height of the magnets when in the OFF position ( $84 \text{ mT} \pm 2 \text{ mT}$ ); the RVLM of the animal was therefore positioned within this region. Four magnetic configurations were assessed; the first three named OFF, ON1 and ON2 were based on the positions identified by Cugat et al<sup>295</sup>. The fourth position (ON3) was a new position that generates a steep gradient about the centre space to provide around 60% more force than the maximum of the yoke magnet used in chapter 4. The field maps and  $(\mathbf{B} \cdot \nabla)\mathbf{B}$  maps are displayed in figure 5.1 C-D, showing the spatial distribution of the forces over where the rats head is placed. All configurations exhibited a minimum force at the exact centre of the inter-magnet space, indicating that the brain region selected for stimulation should be positioned slightly off centre by 3 mm.

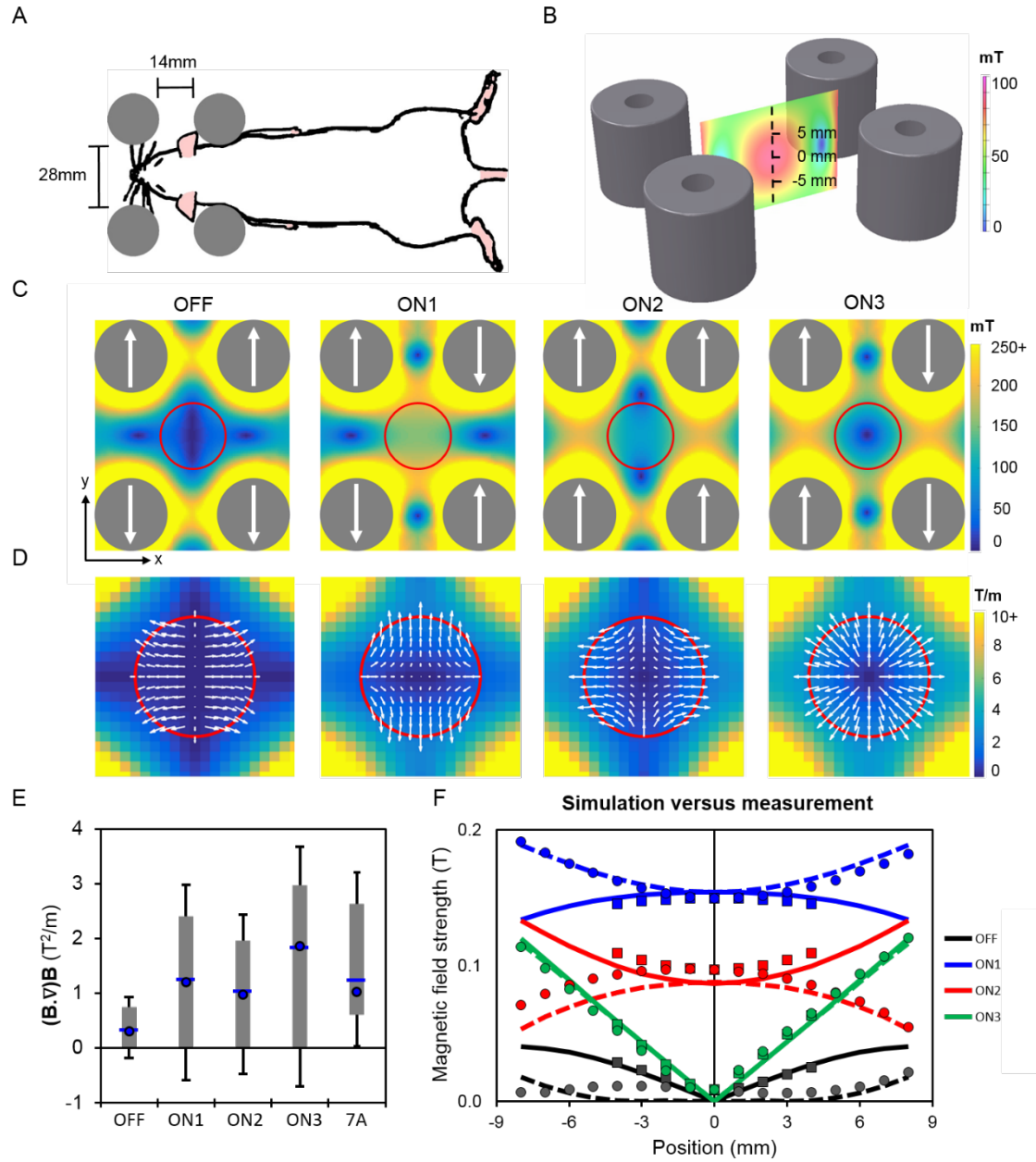


**Figure 5.2.** Design and characterisation of the magnetic mangle. **A.** Schematic showing four cylindrical diametrically magnetised permanent magnets placed at coordinates as close to a rats head as possible. **B.** Simulation of the field of the intermagnet space shows minimal variation in the field  $\pm 5$  mm from the centre point. **C.** Simulated magnetic field maps for four configurations. Red circle diameter = 12 mm. **D.**  $(\mathbf{B} \cdot \nabla) \mathbf{B}$  maps for each configuration. White arrows indicate direction of force. **E.**  $(\mathbf{B} \cdot \nabla) \mathbf{B}$  values of the magnetic mangle compared to the Yoke magnet driven at 7A over 12 mm diameter area. line = mean, circle = median, range = grey bar, error bars = S.D. **F.** Graph showing measured and simulated field along the x and y axes ( $z = 0$  mm) of the magnetic mangle for the four configurations. Solid and dotted lines are the simulated fields along x and y axes respectively. Squares and circles are measured fields along x and y axes respectively.

Measurements of the magnetic field along the x and y axis at the mid height of the magnetic mangle were performed to validate the field simulations (Figure 5.2F). The measurements matched reasonably well with the simulated fields for all four positions, showing that the simulations are sound for evaluating the forces on the magnetic particles. Small deviations between the measured and simulated values at positions OFF and ON2 are likely due to slight inaccuracies on hall probe placement and magnet orientation. The average  $(\mathbf{B} \cdot \nabla) \mathbf{B}$  for each position was compared against the Yoke magnet used in chapter 4 which is known to generate enough force to stimulate astrocytes with ACSA-1 coupled SiMAG particles when driven at 7A. While the OFF position cannot be considered a true off in that there is still a magnetic field present, the forces it generates is below that of the Yoke magnet at 7A so would be below the threshold for stimulation with the SiMAG particles. Position ON3, designed to provide the maximum force has a higher average  $(\mathbf{B} \cdot \nabla) \mathbf{B}$  of 1.8 T<sup>2</sup>/m compared to 1.2 T<sup>2</sup>/m generated by the Yoke magnet. Positions ON1 and ON2 generate  $(\mathbf{B} \cdot \nabla) \mathbf{B}$  values comparable to the Yoke magnet at 7A. Transitioning from the OFF to the ON3 position therefore generates a force greater than the maximum force generated by the Yoke magnet, meaning that the mangle should be effective for *in vivo* stimulation.



### 5.3.2 ATP release using Fe<sub>3</sub>O<sub>4</sub> particles

As the magnetic mangle was not compatible with the fluorescent microscope used for calcium imaging in chapter 4, an alternative method for measuring stimulation was required. As ATP is the main transmitter by which astrocytes communicate to other cells, I instead measured the changes in ATP concentration as a result of mechanical stimulation.

The release of ATP from astrocytes in response to magnetic stimulation was first performed using the yoke electromagnet. Like in chapter 4, the stimulation threshold was first established using the same Fe<sub>3</sub>O<sub>4</sub> particles. However, rather than turning the magnet on in successive 10 second bursts, the yoke magnet was switched on once for 10 seconds, taking media samples before and after. This was then repeated for each input current and the threshold was determined when the extracellular ATP concentration was significantly different to zero. Figure 5.3A shows that the threshold for stimulation of ATP release occurs at a current input greater than 0.7 A, which matched the threshold observed with [Ca<sup>2+</sup>] imaging. As the ratio of volume to base area had already been established using SEM (Figure 4.5), the theoretical shear stress at 0.8 A was calculated to be slightly above 0.2 Pa, showing that the threshold for stimulation is the same for astrocytes when measuring whole cell populations and on a cell by cell basis. Further investigation into the effect of cumulative stimulation was also performed by stimulating cells at 0.6 A, allowed to time to settle, then at 0.8 A and vice versa. Regardless of the order, a significance increase in ATP release was observed at 0.8 A but not at 0.6 A. These results demonstrate that the release of ATP and calcium are robust and equivalent responses as a result of mechanical stimulation using magnetic particles.

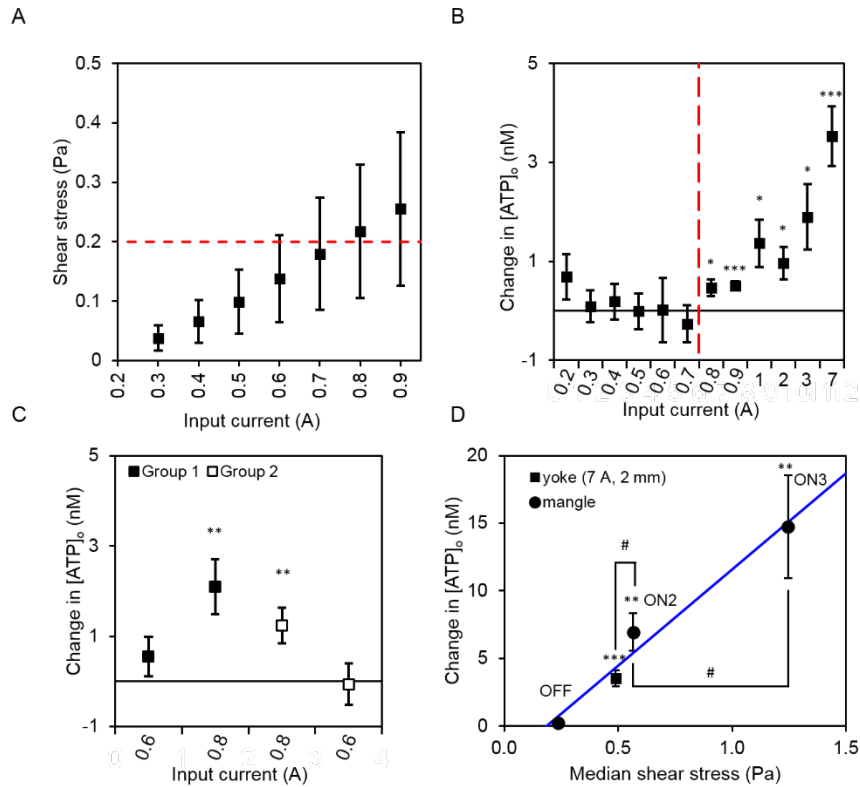


**Figure 5.3. Measuring ATP release of astrocytes using collagen coated  $Fe_3O_4$  particles.** The sensitivity of measuring ATP release after stimulation of astrocytes was comparable to measuring increases in  $[Ca^{2+}]$ . **A.** Graph showing estimated median shear stress threshold lies between 0.7-0.8 A. Threshold was calculated by multiplying force per unit particle volume by the median cluster volume over base area value ( $0.39 \mu m^3$ , Figure 4.5E) **B.** A significant increase in ATP concentration was observed when the Yoke magnet was driven at 0.8 A and above ( $n = 8$  for all conditions). **C.** Regardless of the order of stimulation, an increase in ATP was observed at 0.8 A but not at 0.6 A. ( $n = 16$  for all conditions) **D.** Stimulation with the magnetic mangle using ON2 and ON3 configurations caused greater release of ATP than the Yoke magnet at 7A, showing a linear increase in ATP release with shear stress. Data shown as mean  $\pm$  Standard error. \*,  $p < 0.05$  for two-tailed  $t$  test of null hypothesis that mean change in ATP equals zero. \*\*,  $p < 0.01$  and \*\*\*,  $p < 0.001$  for same test. #,  $p < 0.05$  for two sample two-tailed  $t$  test.

Stimulation of astrocytes was then demonstrated using the mangle and  $Fe_3O_4$  particles. First, no significant change in ATP was observed when the mangle remained in the OFF position, while significant changes in ATP were measured when the mangle was placed in the ON2 (7 nM,  $p < 0.01$ ) and ON3 positions (15 nM,  $p < 0.01$ ). There was a strong linear relationship between the estimated shear stress and the measured ATP changes ( $p < 0.0001$ , Figure 5.3D), with ON3 producing a larger change than ON2 ( $p < 0.05$ ), demonstrating that the mangle can not only be used to stimulate astrocytes *in vitro*, but elicits a stronger response than the Yoke magnet.

### 5.3.3 ATP release using SiMAG particles

While stimulation using ACSA-1 coupled SiMAG particles was demonstrated in chapter 4, there was no evidence to suggest that the particles were targeted to astrocytes. Immunostaining was therefore performed on mixed cortical cell cultures decorated with ACSA-1 coupled SiMAG particles to assess their affinity to astrocytes. Figure 5.4 shows increased amounts of SiMAG particles (red) concentrated around astrocytes (green) while their distribution appeared unaffected by the presence of neurons. The concern of increasing the concentration in the previous chapter was that, if high amounts of SiMAG particles cover all cells then they would stimulate non-selectively. However figure 5.4 shows that even at the higher concentration of 0.88 mg/mL, preferential binding to astrocytes still occurs.

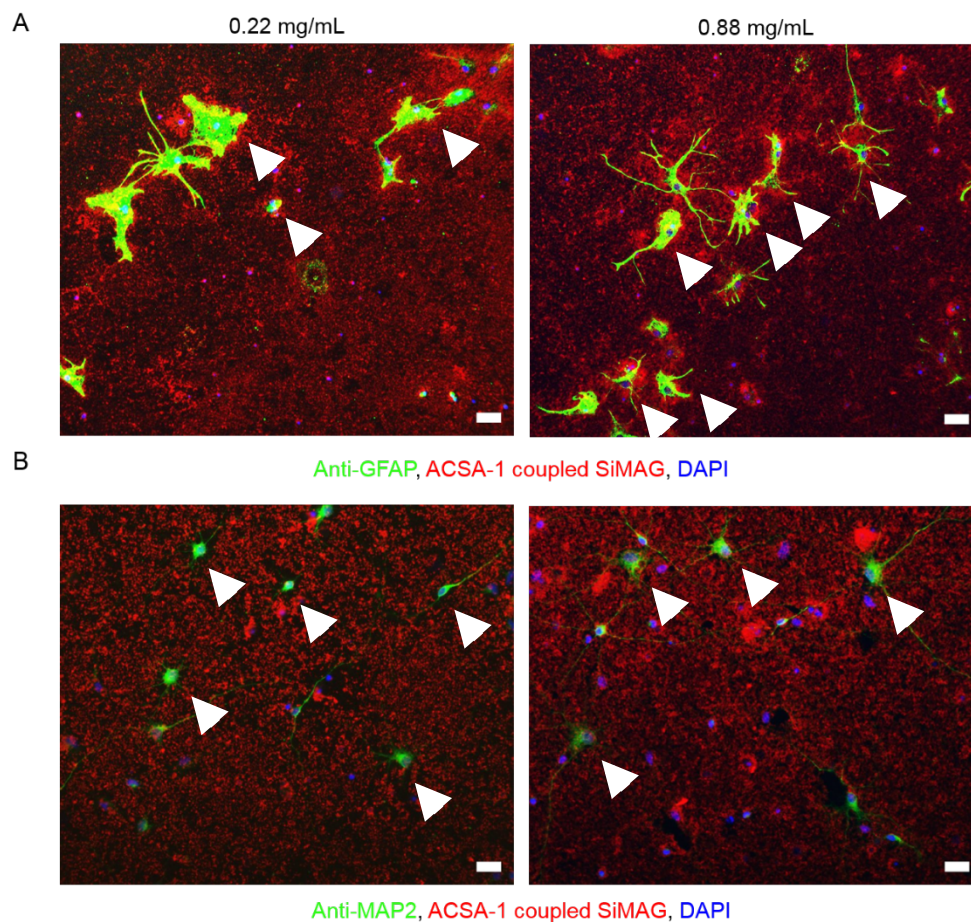


**Figure 5.4. ACSA-1 coupled SiMAG particles selectively bind to astrocytes.** Immunohistostaining revealed SiMAG particles attached to GFAP positive astrocytes (A) in preference to MAP2 positive neurons (B). White arrows indicate increased amounts of SiMAG particles (red) around astrocytes in A but no changes in concentration around neurons in B.

Now that the targeting of SiMAG particles has been established, they were tested to see whether ATP release could be measured when stimulated with the magnetic mangle. The estimated sheer stress of a single SiMAG particle and  $\text{Fe}_3\text{O}_4$  particle is shown for each mangle configuration in figure 5.5A. The highest sheer stress was produced by position ON3 (0.095 Pa), almost 3 times higher than the yoke magnet at 7A (0.036 Pa). The fact that this value sits below the stress threshold for stimulation means that multiple particles are needed to form a larger cluster on the cell. The concentration of particles is therefore crucial for increasing the number of particles attached to the cell to achieve stimulation.

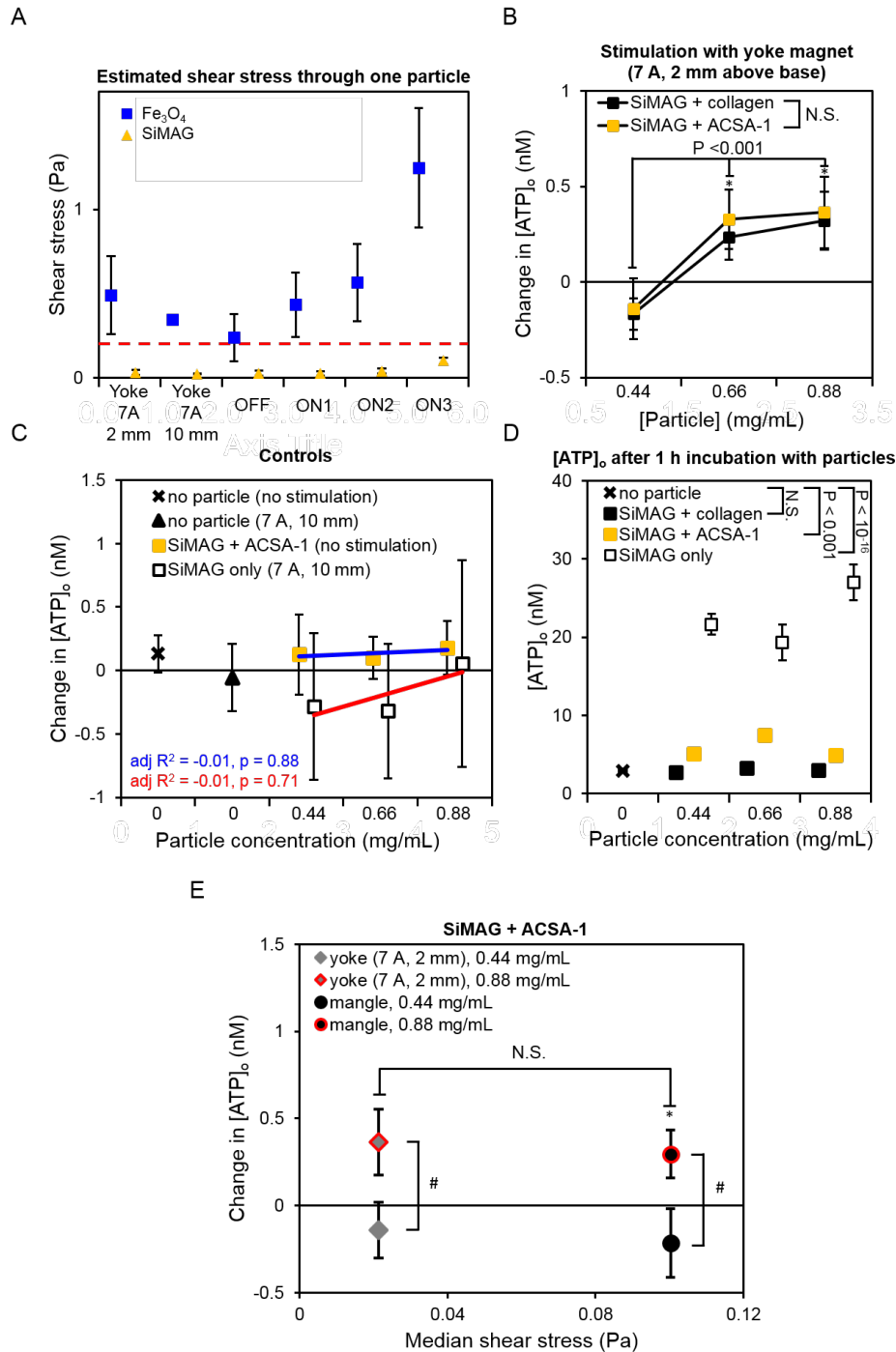


**Figure 5.5. Measuring ATP release of astrocytes using SiMAG particles.** **A.** Comparison of estimated shear stress for Fe<sub>3</sub>O<sub>4</sub> and SiMAG particles for each mangle configuration. **B.** Increasing concentration of SiMAG particles to 0.66 mg/mL caused significant release of ATP was observed ( $p < 0.001$ ,  $n = 24$  for all conditions). No difference was observed between collagen coated and ACSA-1 coupled SiMAG particles (N.S.  $p = 0.641$ ). **C.** No significant changes in ATP was observed for the following conditions: no particles no stimulation, no particles and yoke driven at 7A, ACSA-1 coupled SiMAG particles no stimulation, SiMAG only and yoke driven at 7A ( $n = 24$  for all conditions). **D.** Graph showing ATP concentration after 1 hour incubation (from left to right  $n = 48, 16, 24, 24, 32, 16, 32, 16, 16$ ). **E.** Stimulation of astrocytes using the magnetic mangle at ON3 caused significant release of ATP at 0.88 mg/mL ( $n = 24$  for all conditions). \*,  $< 0.05$  for two-tailed  $t$  test of null hypothesis that mean change in ATP equals zero. #,  $p < 0.05$  for two sample two-tailed  $t$  test.

To investigate this thoroughly, the yoke magnet was first used running at 7A to see whether ATP release occurs at the same concentrations used for calcium imaging in chapter 4. Significant changes in ATP were observed when the concentration was increased from 0.22 mg/mL to 0.66 mg/mL (0.32 nM,  $p < 0.001$ ) and 0.88 mg/mL (0.36 nM,  $p < 0.001$ ) led to a significant change in ATP (Figure 5.5B). The same test was performed with SiMAG particles coated with collagen to assess the effect of the binding agent (Figure 5.5B). Increasing particle concentration again led to significant changes in ATP but were not significantly different to ACSA-1 coupled particles, showing they are equally effective. A variety of control experiments were also performed (Figure 5.5C). No changes in ATP occurred when a magnetic field was applied in the absence of particles or with uncoated SiMAG particles, and when no field was applied but ACSA-1 coupled particles were present, regardless of particle concentration. However the presence of particles did have an effect on the overall starting extracellular ATP concentration (Figure 5.5D). While no difference was observed for collagen coated particles, both ACSA-1 coupled (5-7 nM,  $p < 0.001$ ) and naked SiMAG particles (19-27 nM,  $p < 10^{-16}$ ) caused marked increases in ATP concentration.

Finally, stimulation using SiMAG particles with the magnetic mangle was assessed (Figure 5.5E). Like the Yoke magnet, increasing the concentration from 0.44 mg/mL to 0.88 mg/mL resulted in an increase in ATP concentration when the mangle transitioned from the OFF to the ON3 position. Interestingly, whereas there was a significant change in ATP between the mangle and yoke magnet for the  $\text{Fe}_3\text{O}_4$  particles (figure 5.3D), there was no significant difference between them for the SiMAG particles. Nonetheless, stimulation of astrocytes using a magnetic device suitable for *in vivo* applications was demonstrated.

### 5.3.4 MRI and immunofluorescence of particle fate in vivo

Knowing that the magnetic mangle can elicit a release of ATP in culture astrocytes using the biocompatible SiMAG particles, their location and fate after injection into the brain were investigated. MRI was used to assess particle retention at the injection site up to 8 days post injection. Representative axial and sagittal MRI images are shown in figure 5.6A-B displaying the hypo intense region caused by the particles (red arrow) compared to a sham saline injection in the opposite hemisphere. The variability in volume (figure 5.6C) is likely due to the high concentration of particles (1 mg/mL) injected with a glass pipette which often led to blockages and variable amount of particles eventually being delivered. Nonetheless the volume of the hypo intense regions remained constant up to 8 days post injection (figure 5.6D), decreasing by only 8.5% at day 8, indicating that the majority of particles remain at the injection site.

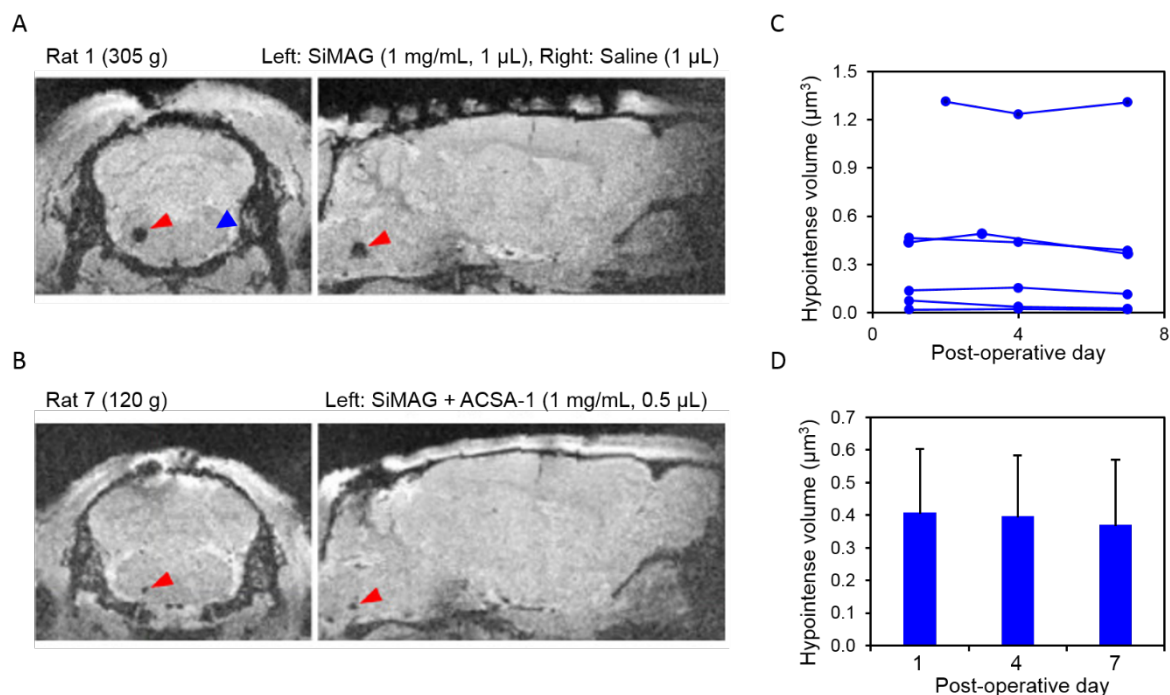


**Figure 5.6. MRI for location and fate of SiMAG particle after injection into rat brainstem. A.** Axial and sagittal images showing location unmodified SiMAG particles in RVLm post injection in normal sized rat. **B.** Images of small rat were affinely registered to images in panel A. Red arrows indicate magnetic particle injection sites, blue arrow indicates saline injection. **C.** Graph showing variation of hypointense volumes caused by particles in 6 rats over 7 days. **D.** The mean hypointense volume decreased slightly over 7 days. Error bars = Standard error.



For better visualisation of whether the injected particles were in the correct anatomical location, and whether they had targeted specifically to astrocytes, immunohistochemistry was performed. Figure 5.7 shows the location of particles after injection in 3 rats. For rat 1, immunohistochemistry was performed at day 8, and shows an abundance of astrocytes (green) surrounding the injected particles (red). In rats 8 and 9, immunohistochemistry was performed at day 2. In these two slices, the presence of TH-positive C1 neurons (pink) which are only present in the RVLM, indicates the particles are in the correct anatomical location. While they do not appear to have bound specifically to astrocytes, but have remained as a single cluster, this is advantageous for stimulation as a greater volume of particles will impart larger stresses on the cells. Despite difficulties with the initial injection (particles would often block the needle), a concentration of 1mg/mL appeared to deliver a good amount of particles to the RVLM (visible with both MRI and immunofluorescence) and was used for initial demonstrations of *in vivo* stimulation.

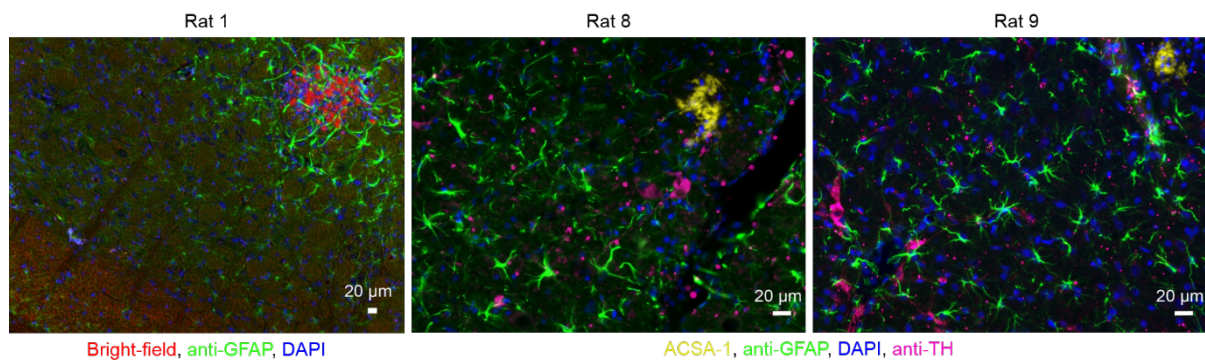


**Figure 5.7.** Immunofluorescent images of the brainstem shows particles clustered at the injection site. Particles appear as red (rat 1) and yellow (rat 8 and 9), astrocytes as green, other cell nuclei as blue and C1 neurons as pink.



### 5.3.5 In vivo magnetic stimulation

Sympathoexcitation was observed as a result of mechanical stimulation using ACSA-1 coupled SiMAG particles and the magnetic mangle in anaesthetised rats. 1  $\mu$ L of particles (1 mg/mL) were injected into the RVLM at four sites before the head of the animal was placed into the inter-magnet space of the magnetic mangle. Once ABP and RSNA had stabilised, the mangle was operated using the sequence: OFF – ON3 – ON1 – ON3 – OFF; to create an ‘on and off’ effect. Increased ABP and RSNA was observed after magnetic force was applied (Figure 5.8A), with figure 5.8 showing that repeated stimulation was also possible. The large RSNA peaks in figure 7A that occurring during magnetic mangle operation are a result of electrical interference from the motors during rotation of the magnets. An increase in RSNA was induced in a further two animals (figure 5.8C).

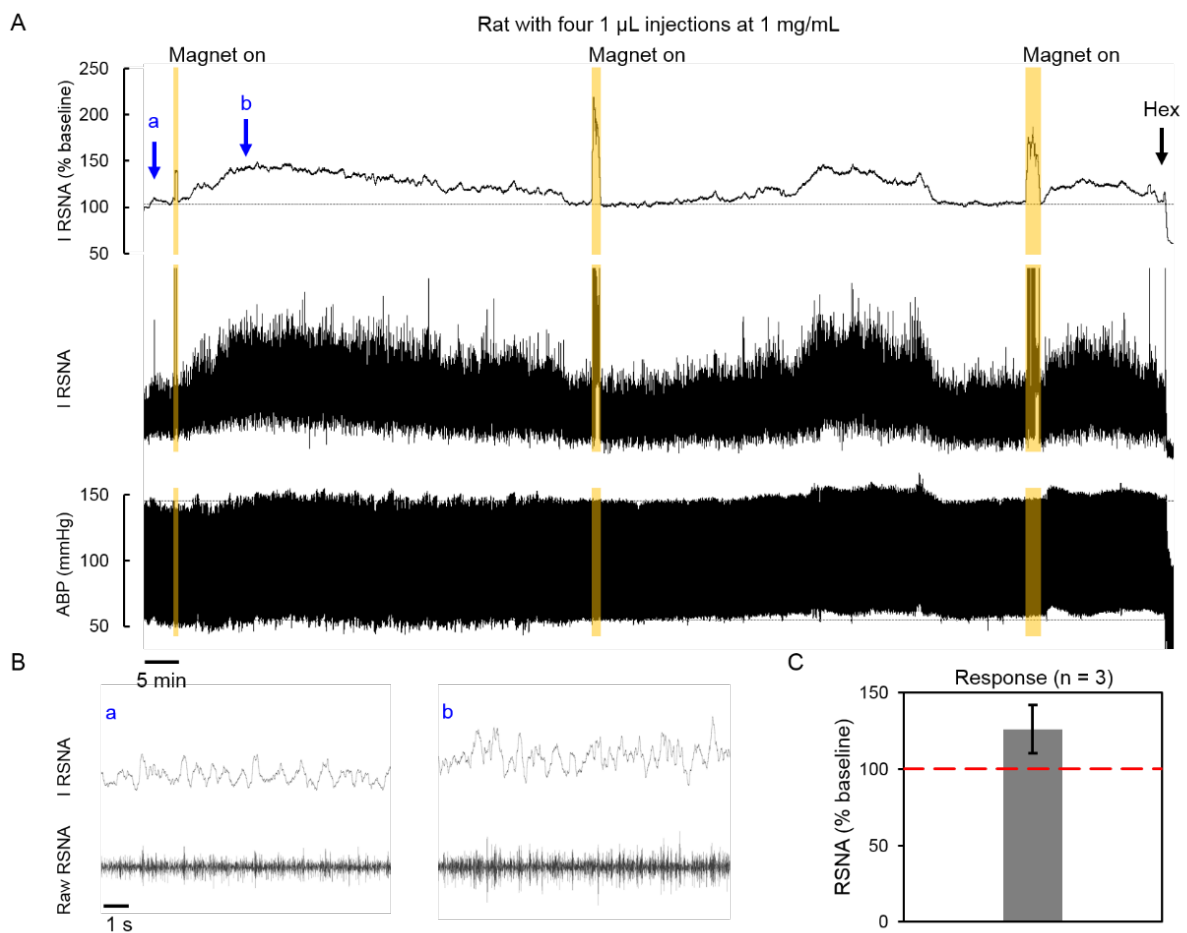


**Figure 5.8.** Measured sympathoexcitation response after stimulation using ACSA-1 coupled SiMAG particles and the magnetic mangle. **A.** Increased renal synaptic nerve activity (RSNA) and arterial blood pressure (ABP) were observed in anaesthetised rats after stimulation using the following mangle transitions: OFF > ON3 > ON1 > ON3 > OFF which was repeated up to 3 times. Orange area indicates duration of mangle transitions. Hex = administration of hexamethonium. **B.** Blow up of I RSNA traces at points a and b with corresponding raw RSNA traces. **C.** Mean RSNA recordings in 3 rats (Error bars = S.D).

Having established *in vivo* stimulation was possible using this technique it was decided that a reduced concentration should be tested as figure 5.7 indicates that particles remain as a single cluster and was unclear as to whether particles had bound specifically to astrocytes. A lower concentration of 0.25 mg/mL was subsequently injected at the same four sites except instead of a single 1  $\mu$ L injection, three 0.33  $\mu$ L particle injections were delivered, one at the intended height and two 0.1 mm above and below each injection site to encourage spreading of the particles. A spike in ABP was again observed after magnetic mangle operation (Figure 5.9A) with comparable magnitude but shorter duration than the response when a larger concentration was used. In light of this, the concentration was lowered further to 0.1 mg/mL which was injected at two sites. In this case 1  $\mu$ L of particles was spread across 5 mm about the injection site with five 0.2  $\mu$ L injections at 0.1 mm intervals. With this concentration and distribution of particles no response was observed after magnetic mangle operation (Figure 5.9B) indicating a preliminary minimum concentration 0.25 mg/mL of ACSA-1 coupled SiMAG particles for *in vivo* sympathoexcitation using the magnetic mangle.

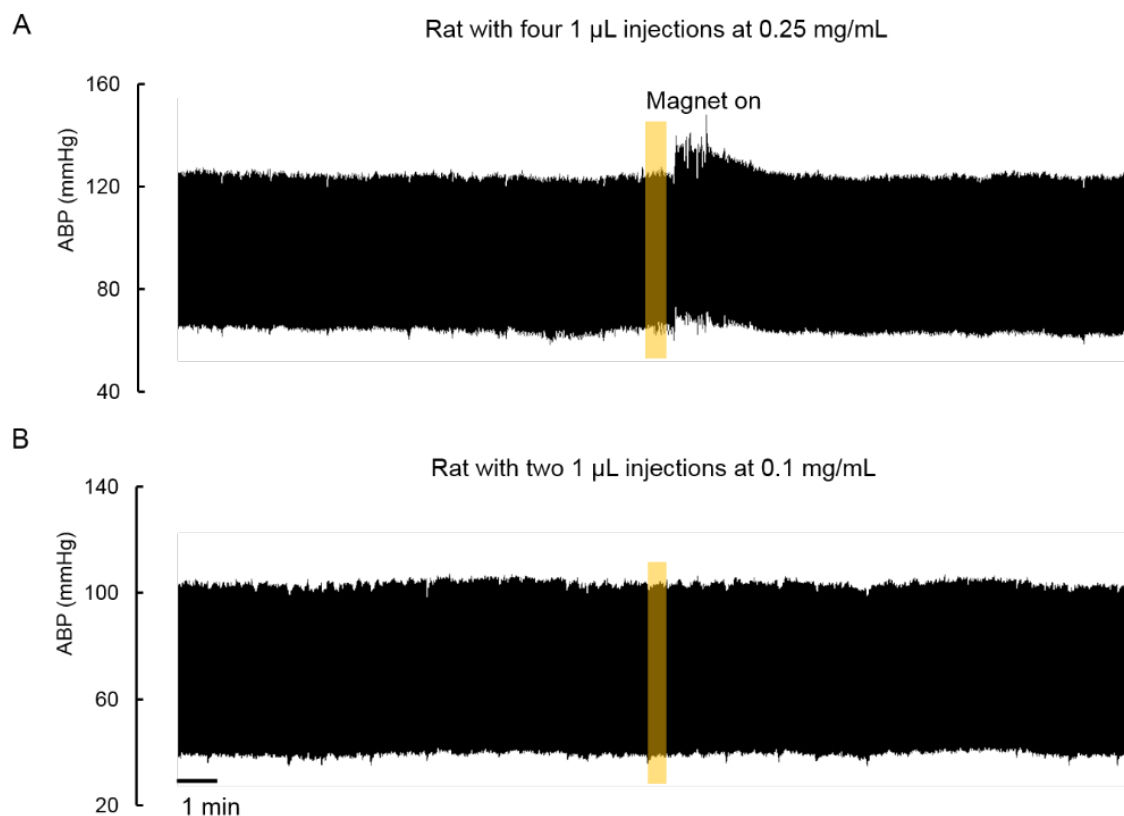


**Figure 5.9.** *In vivo* stimulation using lower concentrations of ACSA-1 coupled SiMAG particles. An elevation in ABP was observed in 1 rat after stimulation with four 1  $\mu$ L injections of ACSA-1 coupled

SiMAG particles at 0.25 mg/mL into the RVLM (A) while no elevation was observed after two injections at 0.1 mg/mL (B).

## 5.4 Discussion

This study demonstrated the proof of concept of a novel magnetic particle based technique for mechanically stimulating astrocytes *in vivo* using magnetic force. To generate the magnetic forces identified in chapter 4 over the head of a small rat, the magnetic mangle was designed. Measureable ATP release was observed using ACSA-1 coupled SiMAG particles with the magnetic mangle and the Yoke magnet, while the shear stress threshold for ATP release matched the threshold for calcium release using collagen coated Fe<sub>3</sub>O<sub>4</sub> particles. Finally, stimulation using the combination of magnetic mangle and ACSA-1 couple SiMAG particles injected into the RVLM caused a measurable increase in sympathoexcitation in rats.

A novel magnetic device was designed and manufactured based on the work by Cugat et al<sup>295</sup> that could produce magnetic forces greater than the Yoke magnet used for *in vitro* stimulation. The challenge of this design, as is the case for all *in vivo* magnetic actuation studies, is the ability to generate a magnetic field and field gradient strong enough to provide adequate forces over distances greater than a few millimetres. Permanent magnets were therefore chosen for their strong magnetic fields which were positioned as close to the animals head as possible. The ability to rotate each magnet allowed for the magnetic field to change so that force could be applied once the animal was in position. While a magnetic field is always present between the magnets, an orientation for the minimum and maximum force was established to generate an effective on and off period for force application.

While *in vivo* stimulation was demonstrated using the magnetic mangle, there is room for further optimisation of the magnet design. The cylindrical diametrically magnetised magnets were chosen to maximise the amount of force applied in the inter magnet space. While increasing the size of the magnets would increase the strength of the field they produce, they would have to be positioned further from each other, resulting in a decrease in force. The balance between magnet size and position in this case can be considered optimal for our application. However, considering the dependency of the ramp times of magnetic force on cellular response<sup>279</sup>, the quickest the magnets could rotate from one position to another was approximately 1 second. Rotation faster than this would cause the rotors to slip and malfunction. The OFF position also cannot be considered a true off as there is still a small force acting on the particles when a non homogenous field is applied. To remove the field would involve either removing the magnets from about the animals head, or

removing the animal. Considering the intricacy of the physiological recording of the animal during experiments, adapting the design so that the magnets can be removed should be considered.

Further assessment of the shear stress threshold was carried out by investigating changes in extracellular ATP in whole cell culture in response to mechanical stimulation. Using the Yoke electromagnet and collagen coated  $\text{Fe}_3\text{O}_4$  particles a minimum input current of 0.8 A was needed to elicit a significant release of ATP, indicating the same force threshold for both ATP and Calcium release. The same dependency on concentration of SiMAG particles was also observed with a minimum concentration of 0.66 mg/mL needed for significant ATP release. While the increase in shear stress produced by the mangle resulted in an increased release of ATP when the  $\text{Fe}_3\text{O}_4$  particles were used, there was no significant difference in ATP release between the mangle and Yoke magnet with the SiMAG particles. This is likely due to the change in shear stress being relatively small for the SiMAG particles (+0.079 Pa for a single particle) compared to the  $\text{Fe}_3\text{O}_4$  particles (+0.76 Pa) as shown in figure 5.5A. Measuring the release of ATP in whole cell populations, added to the single cell calcium excitability using magnetic force gives robust evidence that astrocytes can be stimulated readily using this technique. ATP release can also be considered a more reliable measure for predicting *in vivo* responses to stimulation as a whole region of cells would need stimulation to elicit any physiological or behavioural changes.

The application of our magnetic nanoparticle based technique was demonstrated *in vivo* by measuring an increase in sympathoexcitation in rats when astrocytes in the RVLM were mechanically stimulated using iron oxide nanoparticles and a novel magnet design. The response observed was comparable to the optogenetic study on which our experimental design was based<sup>294</sup>. Injection of 1  $\mu\text{L}$  of SiMAG particles at a concentration of 1 mg/mL resulted in the formation of a single particle cluster at the injection site, with no evidence to suggest astrocyte specific binding. A lower concentration of 0.25 mg/mL was subsequently used and injected over a larger volume to encourage a greater spread of particles to allow for astrocyte binding. A response was also observed when magnetic force was applied, while no response was observed when a lower concentration of 0.1 mg/mL was used, indicating a preliminary minimum dose of particles for stimulation.

MRI revealed that particles remain at the injection site up to 8 days post injection with only a small decrease in particle volume (8.5%) as a result of clearance, concurrent with previous thermogenetic studies showing particles are retained for up to 1 month<sup>60</sup>. Immunostaining also revealed that the particles remained as a single agglomeration at the injection site, with no clear affinity or targeting to astrocytes. While an *in vivo* response was observed after stimulation it is unclear whether the stimulation was astrocyte specific, with previous studies showing that calcium influx can be induced

in neural networks via mechanical stimulation<sup>79</sup>. This led to injection of a lower concentration of particles spread over a larger region of the RVLM. A response was observed once more with the lower concentration however, additional immunostaining is needed to assess the post injection location of the particles to identify whether this approach aided astrocyte specific binding of the ACSA-1 coupled SiMAG particles. While increasing the number of particles attached to an astrocyte will increase the chance of stimulation, this must be balanced with an even distribution of particles about the injection site. Nonetheless, the target of demonstrating *in vivo* stimulation using our novel magnetic particle technique was achieved.

While the magnetic mangle allowed for the observation of a physiological response to stimulation it is not without its drawbacks. While the mangle has an 'OFF' position (minimum magnetic force), there is still a field present. The rotation of the magnets are also slower than the ramp times of the electromagnet, which as explained in the previous chapter can affect the force threshold for stimulation<sup>279</sup>. Future iterations of the magnetic mangle could include retractable magnets, so that when the magnets are removed no field is present. Orientation of the magnets could also be changed to increase the amount of magnetic force available. Initially the magnets were positioned to allow for *in vivo* two photon imaging except the vibrations caused by the motors during rotation made this unfeasible. Changing the orientation of the magnets therefore to a vertical configuration would allow the magnets to be positioned closer to the animal to generate a higher magnetic force on the particles. Such changes to magnet design should be considered for further studies of *in vivo* stimulation using this magnetic particle stimulation technique.

## 5.5 Conclusion

This chapter demonstrates the feasibility of using magnetic particles for *in vivo* mechanical stimulation of cells using an external magnetic field. A novel magnet design called the magnetic mangle was devised which generated the forces needed to stimulate the release of ATP in cultured astrocytes. ACSA-1 coupled SiMAG particles were injected into the RVLM of small rats, which upon stimulation elicited a sympathoexcitatory response with an increase in arterial blood pressure and increased renal sympathetic nerve activity. MRI showed particles remain in the RVLM for up to 8 days, indicating the potential for time courses of repeated stimulation. Immunostaining however revealed that particles remain as a single cluster, necessitating a re-evaluation of the administration of particles into the RVLM in order to achieve astrocyte specific *in vivo* stimulation. While further optimisation of the magnet design and particle targeting is still needed, this magnetic particle based technique shows promise for being a viable, less invasive alternative to optogenetic stimulation.

## 6 Navigation of magnetic beads through the brain using MRI

### 6.1 Introduction

The ability to manipulate the position of medical devices remotely inside the body would equip surgeons with a minimally invasive tool for both diagnosis and treatment of cancer<sup>296,297</sup>. With the interest in micro robotic devices ever increasing, the ability to control their location in the body with precision would enable their potential for localised sensing<sup>298,299</sup>, drug deposition<sup>257</sup> and ablation<sup>165</sup>. Such minimally invasive approaches would be of most benefit in the brain, where preservation of surrounding healthy tissue is paramount and essential for improving patient prognosis and outcome. MRI is routinely used for cancer diagnosis, but can also be used to image ferromagnetic particles as they appear as hypo intense or cause signal dropout on an image. In addition to diagnosis and localisation, the magnetic field gradients inherent in all MRI scanners can be used to generate translational forces onto the device to guide it to a target location. The ability to both move and image an untethered device through the brain using MRI would negate image registration issues associated with other image guided techniques, delivering a minimally invasive alternative to conventional surgical operations.

To date, the field of magnetic resonance targeting (MRT), a concept whereby the magnetic field gradients of an MRI scanner are used to direct magnetic particles inside the body, has focused on steering magnetic micro or nanoparticles through vasculature for the enhancement of drug delivery. Magnetically labelled cells<sup>259</sup> or magnetic microcapsules can be guided towards a target site and has been shown to have a therapeutic effect<sup>207</sup>. At the millimetre scale it has been shown that a clinical MRI scanner can be modified to navigate a small steel ball around a maze filled with liquid and vessel simulator<sup>249</sup>. Martel et al have demonstrated that a 1.5mm ferromagnetic ball can be guided along a swine artery with a real-time feedback loop<sup>208</sup>, while another group have shown that superconducting magnets can give added control to a magnetic tipped catheter<sup>300</sup>. The magnetic forces needed to guide magnetic particles through tissue, however, is far greater than that needed to move through the vasculature<sup>231</sup>. While gradients of up to 400mT/m have been used on clinical MRI systems<sup>257</sup>, it has been suggested that typical clinical gradient strengths (< 80 mT/m) are insufficient to move particles through tissue<sup>261</sup>. As such contraptions such as the gauss gun<sup>261</sup> and magnetic hammer<sup>262</sup> have been introduced which can be used with existing MRI gradients. However these technologies lack the precision in movement for them to become viable medical devices. We

hypothesise that, with increased gradient strengths of up to 500mT/m, enough force can be generated on a millimetre sized magnetic particle or to move it through brain tissue.

In this study the manoeuvrability of millimetre sized magnetic beads through brain tissue using MRI was established. The effect of seed size and gradient strength on distance moved was investigated in both viscous and viscoelastic media. An established method for detecting ferromagnetic implants was modified and adopted, assessing its accuracy in detecting the seeds position with a multi-seed phantom. This imaging technique was then employed to show that a 2 mm diameter chrome steel seed can be moved through ex vivo brain tissue in submillimetre increments using standard pre-clinical imaging gradients. To improve manoeuvrability of the magnetic bead, a dedicated propulsion/imaging gradient set was developed capable of generating continuous gradients up to 400 mT/m, enabling movement of magnetic beads up to 5 cm within a typical surgical time scale. Observations on the movement are then discussed along with suggestions for future investigations and optimisation.



## 6.2 Methods

### 6.2.1 Propulsion gradients

Images were acquired using a pre-clinical 9.4T Varian MRI scanner. Phantoms were positioned in a 35mm Rapid RF volume coil. An edited gradient echo acquisition was used with added propulsion gradients before image acquisition. The gradient strength, direction, on/off time (duty cycle) and loops were controllable variables for the propulsion gradients. For consistency and due to restrictions on the gradients, a duty cycle of 2/7ms was used and loops kept at 500, delivering an effective on time of 1 second. In brain tissue the duty cycle was increased to 20/70ms. The gradient strength varied between 1-500mT/m.

### 6.2.2 Movement measurements in 0.125% agar

A 0.5 mm and 1 mm chrome steel sphere (aisi 52100) was placed in a 22x25x25 mm container filled with 0.125% agar (sigma Aldrich®). Agar was prepared by adding 0.5 g to 100 ml of distilled water, heated until boiling, diluted to 0.125% with 300 mL of distilled water, poured into phantom and left at room temperature to set. The gradient echo imaging parameters were: FOV = 25.6x25.6x2 mm, data matrix = 64 x 64, TR = 15.428 ms, TE = 0.69 ms. Movement was always measured in the phase encoding direction (perpendicular to B<sub>0</sub>). The distance between each movement was measured manually using imageJ. Unpaired t tests were performed at 400, 300 and 200 mT/m for the two sizes.

### 6.2.3 Localisation using signature selective excitation and validation

A phantom was prepared containing 1 × 0.5 mm chrome steel sphere and 3 × 2 mm plastic spheres. 3 g of agar (sigma Aldrich®) was added to 100 mL of distilled water, heated until boiling and poured into a 50 mL Falcon tube. The spheres were positioned at different heights within the Falcon tube, with two plastic spheres below and one plastic spheres above the chrome steel sphere. This was achieved by cooling a layer of agar until set, laying a sphere on the surface and pouring hot agar over the top to create the next layer.

CT images were acquired using a nanoScan PET/CT scanner (Mediso). The FOV covered the entire agar phantom volume and the images were reconstructed using the vendor software to a resolution of 251 µm. The coordinates of the plastic and chrome steel spheres were determined using ImageJ. The in-plane coordinates for each sphere was determined from a circular region of interest, drawn

over the slice in which the circle was largest. The through plane coordinate was taken as the centre of the slice.

MR Images were acquired using a pre-clinical 9.4 T Bruker Biospec 94/20 MRI scanner. The coordinates of the plastic spheres were determined using a multislice fast spin-echo pulse sequence; with an in-plane resolution = 176  $\mu\text{m}$ , slice thickness = 729  $\mu\text{m}$ , TE = 3.89 ms, TR = 2 s. With 4 averages the total scan time was 8 min 32 sec. Images were acquired in three orthogonal planes. The centre of mass (CM) for each sphere was determined from a circular region of interest, drawn over the slice in which the circular signal void was largest. Each image gave two in-plane coordinates which were averaged across the three images, to give the final coordinates of the three plastic spheres. The analysis was performed using Analyze tools available in ImageJ.

The projections used to determine the coordinates of the chrome steel sphere were acquired using a non-selective spin-echo sequence. An RF pulse with an offset frequency = 3 kHz, bandwidth = 1 kHz and duration = 1.28 s was used. TR was 1 s, 1024 data points were acquired with a resolution of 107  $\mu\text{m}$ , with a total of 8 averages. This was repeated twice along each orthogonal axis (x,y,z); once with a positive readout gradient and once with a negative readout gradient. The total scan time for the 6 projections was 48 s. A cross correlation was performed between the positive and negative gradient projections for each axis; the position of the maximum in the resulting correlation directly relates to the coordinates of the sphere, with respect to the isocentre of the magnet. This analysis was performed using a custom script in Matlab. The difference between each measured distance was calculated from the MRI and CT data.

#### 6.2.4 Movement detection of 2mm seeds

All samples were placed in a 35 mm Rapid RF volume coil. The movement was then detected using one of two methods, both adapted from an established method<sup>246</sup>. A 1D projection was obtained by summing each line of pixels in the readout and phase encoding directions from a 2D non-slice selective spin echo image to obtain two 1D projections. Parameters for the spin echo sequence were: FOV = 50x35 mm, data matrix = 128x128, Bandwidth = 1994 Hz, TR = 0.5 s, TE = 13.8 ms, Offset frequency = -30000 Hz. For movement in viscous medium (Golden syrup) the duty cycle was kept at 2/7 ms. The gradient strength was kept at 500 mT/m and loops were varied between 500 – 2000. A layer of water was added above the viscous medium to provide MR signal. Displacement between two consecutive positions were then calculated using either a cross correlation method or a signal detection method. The cross correlation method (a cross correlation is performed between two consecutive 1D projections) was only used for movement in golden syrup where the all signal

from the bead could be obtained. In *ex vivo* pig brain, the signal detection method was used. This method finds either the first or last position along the projection (depending on direction of movement) that reaches a certain signal intensity. This signal intensity was chosen manually by analysing the first projection along each axis. The duty cycle was changed to 20/70 ms to allow the seed to achieve greater acceleration. Gradient strengths were varied between 300-500 mT/m and loops 500-5000.

#### 6.2.5 *Ex vivo* brain tissue movement detection

The method for detecting movement in *ex vivo* brain tissue was altered again due to the incomplete signature signal from the seed near the edge of the sample and would therefore provide an underestimate of the distance moved. Instead the relative movement was taken as the first (or last depending on movement direction) point that reached half the maximum signal intensity in each projection. These position were then placed on a 22x25 mm grid and overlaid onto the pre acquired anatomical MR image. The edges of the grid were manually adjusted to fit the edges of the box on the MR image. Whole pig brains were acquired from Meat16, London and were used within 5 days post mortem.

#### 6.2.6 Navigation of magnetic seeds through brain tissue using bespoke propulsion gradient set

To improve navigation and manoeuvrability of magnetic seeds through tissue, a custom built, dedicated propulsion gradient set was developed (Tesla Engineering®, UK) capable of generating up to 500 mT/m continuously (without a duty cycle) as well as operating as a standard imaging gradient set. To evaluate improvement in total distance and total time taken during navigation a vertical sample was used. A burr hole was made at the top of a 60 x 35 x 15 mm container filled with a brain slice taken from the inner most section of either the left or right hemisphere. Before placing a 3 mm bead into the burr hole, a small puncture was made to the brain and the burr hole was filled with margarine to hold the bead in place when the sample was inserted into the MRI scanner. The sample was then maintained at 37°C for 1 hour before the first movement, allowing the margarine to melt and release the bead.

## 6.3 Results

### 6.3.1 Characterisation of distance moved by magnetic beads in viscoelastic medium

First, it was important to understand the level of control that could be obtained in terms of the direction and distance moved by magnetic beads using MRI imaging gradients. Initially, an agar phantom was used (0.125%) as this provided a medium of homogenous density and allowed us to characterise movement in a viscoelastic medium similar to brain tissue. The direction and distance moved by the seed could be controlled by changing the direction and strength of the magnetic field gradient. To maximise the force that could be applied to the seeds, chrome steel balls were used as they become strongly magnetic when inside an MRI scanner (more so than rare earth Neodymium magnets<sup>261</sup>). The gradients were applied with a duty cycle with the ratio 2/7 ms as this allowed the gradients to be applied over a longer period of time without overheating<sup>259</sup>.

Figure 6.1 shows examples of movement of a 0.5 mm seed (indicated by white dot) in all three dimensions in water (blue arrows mark the hypointensity from the bead). The seed could be moved from left to right (Figure 6.1B), up and down (Figure 6.1C), and moved up against gravity to bring the seed out of the imaging field of view (Figure 6.1D). The blue arrows indicate the changes in position of the characteristic susceptibility artefact generated by the seed in the MR image.

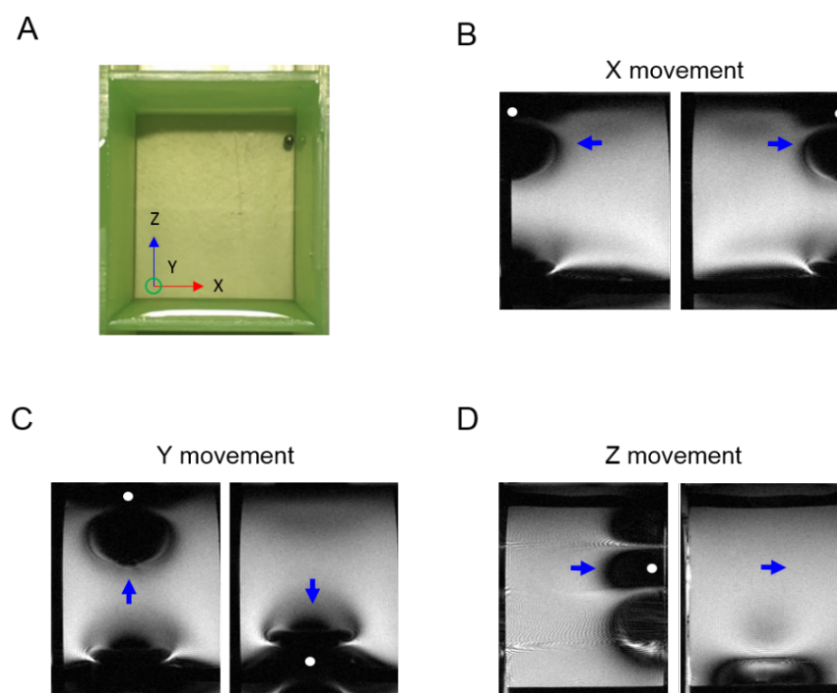
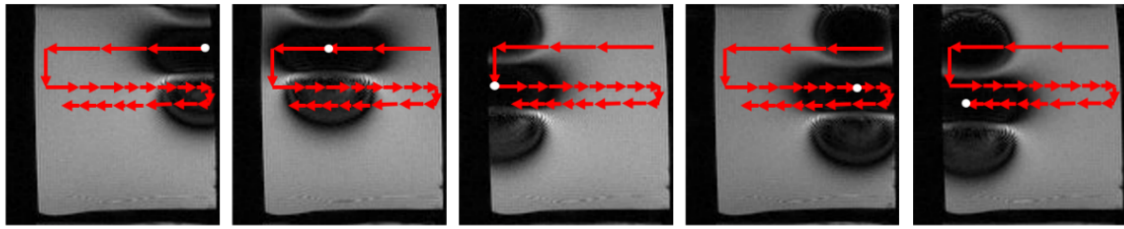


**Figure 6.1. Demonstration of movement in 3 dimensions. A.** Photo of agar phantom with seed placed in the top right corner. **B-D)** Coronal MRI images show the position of a 0.5mm seed

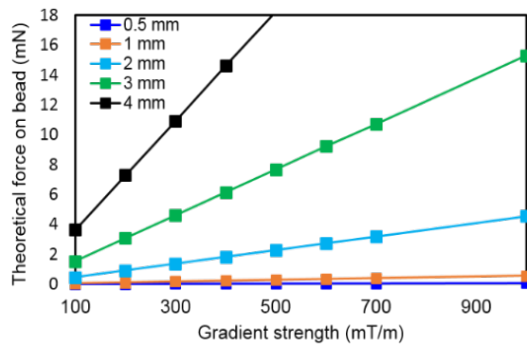
(indicated by white dot) after being moved from left to right (**B**), up and down (**C**) and in and out of plane (**D**). Blue arrows indicate the position of the susceptibility artefact produced by the seed. Knowing that the seeds movement could be controlled in 3 dimensions, the next step was to assess its movement in a viscoelastic medium to observe its behaviour in a medium more similar to biological tissue. For this agar (0.125%) was used in the same 22 x 22 x 25 mm container. Figure 6.2A shows how the seed could be rastered through the agar phantom, with each movement from left to right (phase encoding direction) calculated by measuring the difference between the two positions. Figure 6.2B shows the effect of increasing the gradient strength over the distance the seed moves when the duty cycle and duration is kept constant (DC = 2/7 ms, loops = 500, total time = 4.5 s). Increasing both the gradient strength and seed size increased the distance the seed moved. For example at 400mT/m, a 1mm bead will moved nearly 20 times further than a 0.5mm bead (8.55 mm vs 0.46 mm,  $p < 0.0001$ ). Perhaps more importantly, this data indicates a minimum force threshold for observable movements. At gradient strengths below 300 mT/m, no movement was observed for the 0.5 mm seed, while no movement was seen below 150 mT/m for a 1 mm seed, with significant differences in movement seen at 200 and 300 mT/m (0.34 mm vs 0, 5.42 mm vs 0.04 mm,  $p < 0.001$ ). This underlines the importance of maximising the amount of magnetic force applied to the seeds, as biological tissue with a higher Young's or elastic modulus than this agar will require greater force for movement to be possible.

The absolute distances moved by a seed also depends on either the viscosity of the liquid, or the youngs modulus of the tissue. Increasing both these properties will reduce the distance moved by the seed, therefore to move the same distances in denser media, or through biological tissue, the force applied to the seed must be increased. The theoretical forces applied to seeds of different size are shown in figure 6.2C, indicating the considerable increase in force as seed size is increased. Maximising both seed size and gradient strength is therefore critical for generating enough force on a seed to move it through tissue.

A



B



C

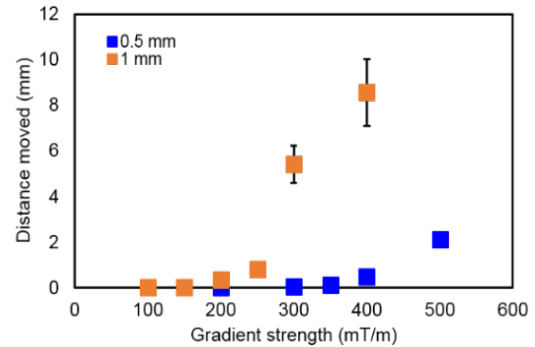


**Figure 6.2. Distance moved can be controlled with gradient strength and seed size. A)** MRI images showing the characteristic susceptibility artefact produced by the seed at different points as it is rastered through agar. Red arrows indicate each individual movement. White circle indicates position of seed. **B.** Graph showing the distance moved for a 0.5mm and 1mm seed for a given gradient strength. (Error bars = SD.  $N > 3$  for all conditions) **C.** Theoretical magnetic force applied to seeds of different sizes at different gradient strengths.

### 6.3.2 Initial movements in *ex vivo* brain tissue

With an understanding of the impact increasing seed size and gradient strength has on the forces applied, it was decided that the seed diameter be increased to 2 mm for testing movement in brain tissue. On first observation, preparation of the tissue appeared critical to whether movement occurred. Figure 6.3 shows two examples of movement of a brain that had been stored as frozen (A), and kept refrigerated (B). A white dot is placed in the centre of the considerably large susceptibility artefact that the larger 2 mm seed creates to indicate the actual position of the seed. The difference in the amount of movement observed was stark, with the seed moving relatively freely in the unfrozen brain while movement was restricted in the refrigerated sample. This is likely due to damage of the microstructure of the tissue during the thawing process. Both cases were repeated twice, and resulted in similar observations. For detectable movements in the thawed brain, 500 loops at 500 mT/m with a 2/7 ms duty cycle was used. The distance and direction then appeared dependent on the part of the brain it was in. In figure 6.3A a total of 85 movements were performed at 5000 loops along the path indicated by the red arrows, taking 64 minutes for the bead to traverse

approximately several centimetres. The total amount of movement in figure 6.3B was after 66 repeats of 5000 loops at the same strength and duty cycle, taking a combined total of 49.5 minutes to achieve only millimetres of movement.

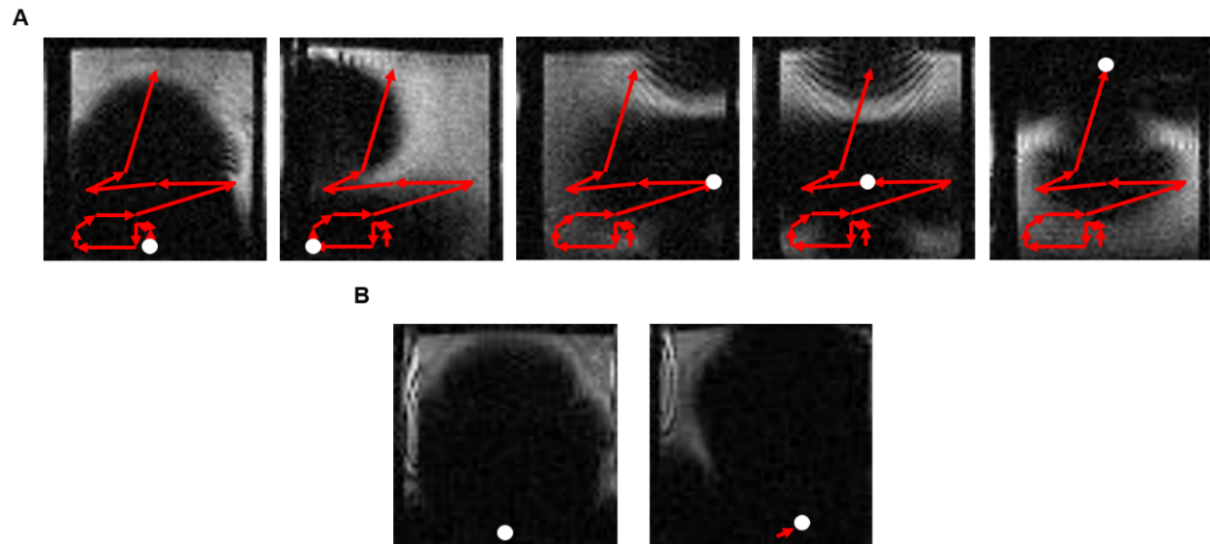


**Figure 6.3. Movement of 2 mm seed in *ex vivo* brain tissue.** Coronal MRI images show the position of a 2mm seed at different positions in *ex vivo* brain tissue that had been stored as frozen (A) and refrigerated (B). Red arrows indicate path taken by seed. White circle = approximate position of seed.

The temperature at which the tissue was kept during experiments was also a factor. Heating the tissue to body temperature allowed for movement to occur in the refrigerated sample (Figure 6.3B) while no movement was observed at room temperature (data not shown). While the movements observed here are small, it nonetheless demonstrates that magnetic seeds can be guided through brain tissue using the imaging gradients of an MRI system. However, obtaining any quantitative measurements with the current imaging parameters was not possible due to the large susceptibility artefacts the 2 mm seeds produce. To better measure the effect different tissue structures have on the movement of the seeds, an alternative localisation method was needed.

### 6.3.3 Development of localisation method and validation

To be able to accurately detect and locate the magnetic bead when inside tissue, an alternative localisation method was adopted. This new technique was based on a previous method for monitoring the location of similarly sized magnetic beads in the artery of a living swine<sup>208,256</sup>. This selective excitation method detects signal at a designated offset frequency to the bulk signal which is specific only to the magnetic bead. Figure 6.4A shows the simulated change in Larmor frequency caused by a 2mm diameter chrome steel bead in the XZ plane. The greatest change in frequency occurs closest to the beads surface where the field produced by the bead is strongest. When a particular bandwidth of offset frequencies are chosen, bands of signal are seen on the MRI image occurring each side of the bead. The centre of mass of the bead can then be inferred from these bands of signal. Figure 6.4B shows examples of 2D SEMS images of a 1 mm bead at two positions within a 0.125% agar phantom (offset frequency = + 30 kHz). The white dotted line indicates the side of the container.

To establish the difference in position after each movement, the 2D SEMS images were converted into 1D projections along x and z (figure 6.4C). The relative movement between the two positions could then be calculated via two methods: a cross correlation method and a signal detection method. The first performs a cross correlation between two consecutive 1D projections positions along each axis to determine the displacement, similar to that used by Martel et al<sup>208,244</sup>. However, when the bead is positioned close to the phantom edge not all of the signal is acquired, resulting in two 1D projections of two different profiles and causing inaccurate detection. In this case the signal detection method was used, where the first point that reaches a chosen signal intensity along the x and z projections is detected. For the example in figure 6.4C, a signal intensity of  $5 \times 10^4$  was chosen (black dashed line). When movement occurs this point will shift either left or right, depending on the direction of movement. Figure 6.4D shows the movement path of a 1 mm bead plotted on a 2D grid using the signal detection method. The bead was taken from the bottom right corner up 15 mm, and then iteratively moved left into the agar using a gradient strength of 200 mT/m, each time moving an average distance of  $0.38 \pm 0.14$  mm, consistent with figure 6.2C. The green circle indicate the position of the bead after each movement and the blue line shows the path taken.



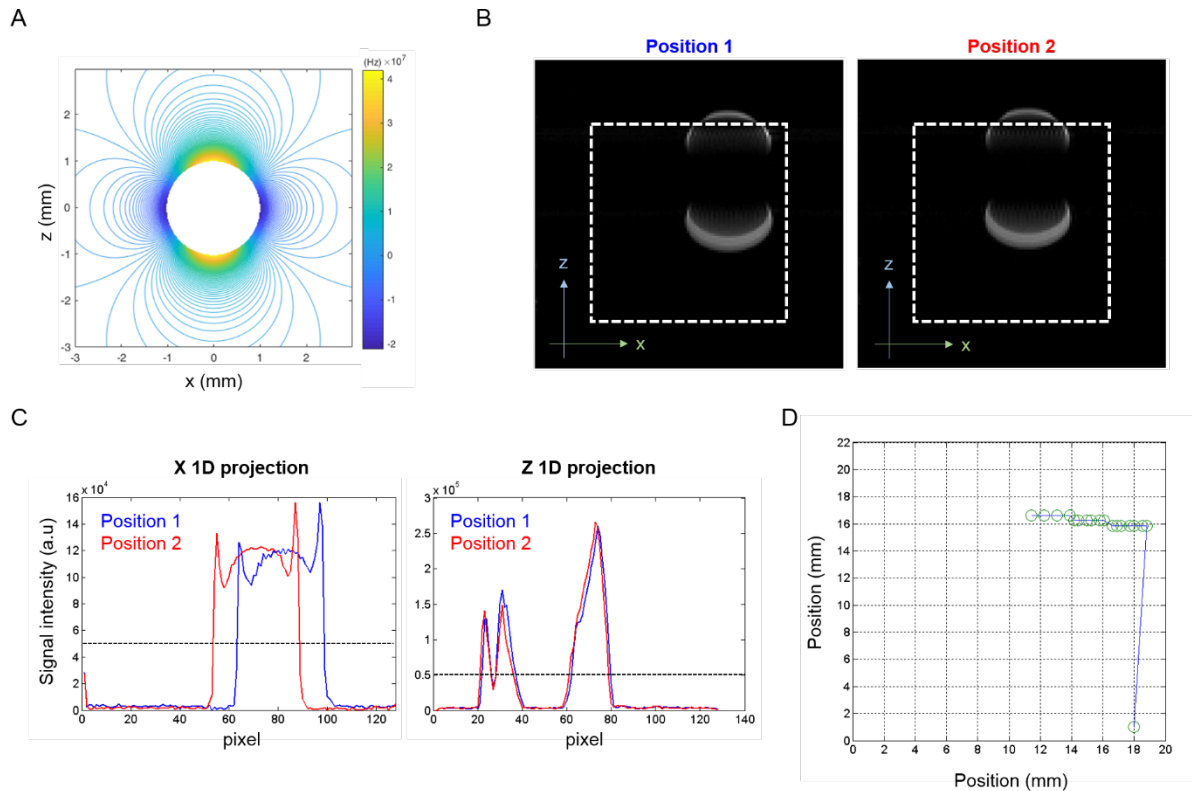


**Figure 6.4. Localisation of ferromagnetic beads using a modified signature excitation method.** **A** Shows the simulated change in frequency of an MRI signal around a 2 mm bead in a 9.4T scanner. **B** shows two examples of a 2D SEM images at +30 kHz off resonance showing the signature bands of signal around the bead at two positions. White dotted square indicates position of phantom. **C.** 2D SEM images are converted to 1D projections of the signal to measure differences in position along each orthogonal axis. Black dotted line indicates threshold for signal detection method. **D.** The path taken by the bead (blue line) can be plotted onto a 2D grid showing each individual position (green circle).

With this new localisation technique in place, beads larger than 1 mm could now be detected. However, for this technique to be a viable, minimally invasive option for patients the precision of this detection method must be assessed. To do so, a multibead phantom was developed containing 1 magnetic and 3 plastic beads in 2% agar positioned according to figure 6.5A. MR images were used to measure the location of the plastic beads (Figure 6.5B) while orthogonal 1D projections were obtained to locate the magnetic bead (Figure 6.5C). As a ground truth measurement between each of the beads, CT images of the phantom were also acquired (Figure 6.5D) as these images do not undergo the same geometric distortions that can result from the presence of the magnetic bead. The measurements using the two imaging modalities are compared in table 2. The maximum error between the MRI and CT measurements was 0.274mm, which is in agreement with existing work<sup>244,246</sup>, demonstrating submillimetre precision of seed localisation with MRI. The total time

taken to acquire the projections was 48 seconds, which can be reduced to 6 seconds by only taking one average, allowing for real-time updates on the seeds location after each movement.

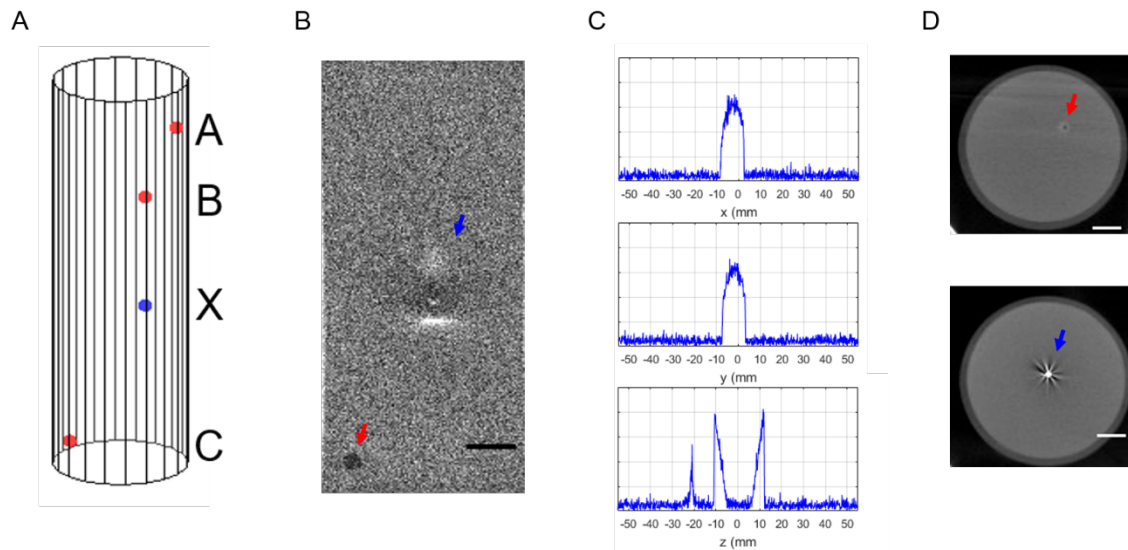


**Figure 6.5. Localisation validation phantom.** **A.** schematic of the positions of a magnetic seed (blue) and three plastic seeds (red) within an agar filled cylinder. **B.** MRI image of plastic seed (red arrow) and in plane susceptibility artefact of magnetic seed (blue arrow). **C.** example 1D projections along the three orthogonal axes used to locate the magnetic seed. **D.** CT images of plastic (above) and magnetic (below) seed. Scale bars indicate 5mm.

	AB (mm)	AC (mm)	BC (mm)	AX (mm)	BX (mm)	CX (mm)
CT	9.590	41.383	33.221	23.170	16.134	18.786
MRI	9.496	41.187	33.014	23.205	16.096	18.512
Difference	-0.094	-0.196	-0.207	0.035	-0.038	-0.274

**Table 2.** Comparisons of measurements between magnetic seed (X) and 3 plastic seeds (A, B and C) using CT and a selective excitation MRI imaging method.

#### 6.3.4 Assessment of movement control using 2 mm magnetic beads

With a new, precise method for detecting the beads location, the accuracy of the movement of beads larger than 1 mm could be characterised. However, while movement of a 1 mm bead moved consistently both in distance and direction (figure 6.4D), figure 6.6A-B shows how the path taken by a 2 mm bead deviates greatly from the intended path. This deviation is most likely due to small inhomogeneities in density of the agar phantom. Similarly to figure 6.4D, the intended path of the bead was to move it up along the wall of the phantom, and then left into the agar (orange arrow). Instead the 2 mm seeds appear to follow a diagonal path, which slowly curves towards the intended direction. To establish whether this effect is caused by the agar itself, and not errors in the gradient direction or anisotropic magnetisation of the beads, movement was performed in golden syrup, chosen because it is a purely Newtonian fluid with a high viscosity.

Figure 6.6D-E shows how a 2 mm seed could be moved exactly in line with gradient direction, concluding that it was the agar itself causing deflections in movement direction. As golden syrup has relatively low water content, a layer of water was placed on top so that an MRI signal could be detected. As a result, all the signal at +30 kHz off resonance could be acquired and was not cut off at the edges of the phantom. Figure 6.6D and E therefore show the movement detection using the cross correlation and signal detection method respectively, with the goal of moving the bead to the position of 7 mm in x, and then 12 mm in z. The cross correlation method recorded consistent distances when the bead was moved right initially using 500 mT/m and 1000 loops. The bead then moved further when loops were increased from 2000 to 4000. Loops were then reduced to 2000 until the seed had traversed a total distance of 5.47 mm. All movements upwards were using 1000 loops, each time traveling the same distance per gradient application (0.39 mm) reaching a total distance of 7.42 mm in z. The signal detection method measured the same total distance of 5.47 mm in x and 7.42 mm in z, performing as well as the cross correlation method. The differences in each individual movement are likely a result of an increased sensitivity to the reduced SNR compared to the movement example in figure 6.4D. Nonetheless both detection methods showed the bead had moved to a position of 7.02 mm in x and 11.55 mm in z.

Figure 6.6F shows the distance moved by beads ranging from 0.5 – 3 mm diameters for different gradient strengths (duty cycle = 2/7 ms, loops = 500). Here the distance moved by the bead increases linearly with gradient strength ( $R^2$  values for 3, 2, 1 and 0.5 mm beads are 0.99, 0.99, 0.84 and 0.25 respectively), whereas in agar, a minimum gradient strength is needed before movement is observed. The benefit of using larger beads is clear, with a 4 fold increase in distance moved with a 2 mm bead versus a 1 mm bead at 500 mT/m.

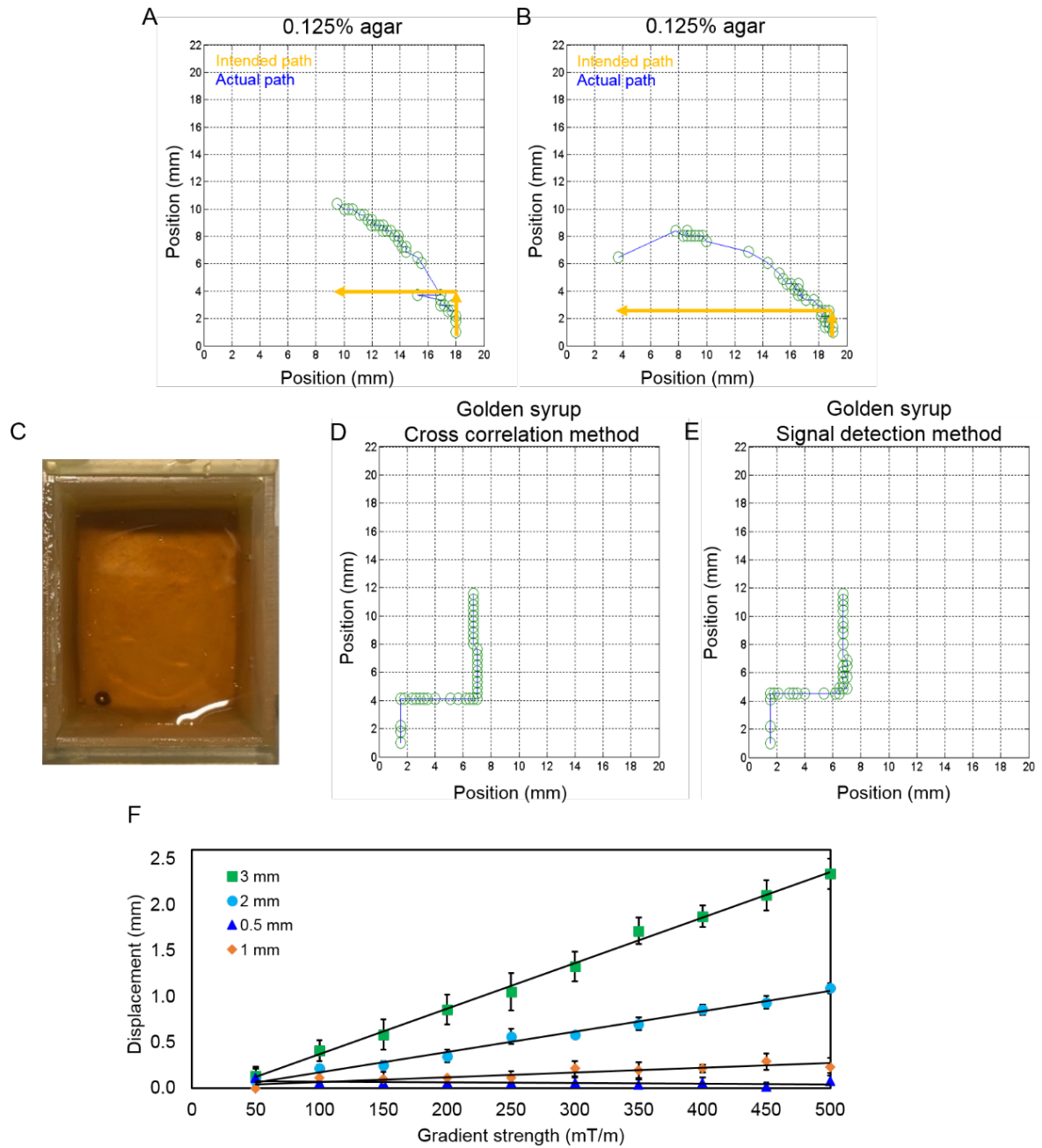


**Figure 6.6. Movement characterisation of 2 mm beads with two new localisation methods.** A-B show how the direction of a 2 mm bead was affected by small inhomogeneities in 0.125% agar, deflecting it from the intended path (yellow). C shows a 2 mm bead placed in phantom filled with golden syrup. D-E demonstrate that two different localisation methods show that a 2 mm bead can be accurately guided set distances in line with gradient direction. F shows the displacement of different sized beads in golden syrup for different gradient strengths.

### 6.3.5 Movement of 2 mm beads through ex vivo brain tissue using preclinical imaging gradients

With an established localisation method in place, movement of 2 mm bead through *ex vivo* brain tissue was re-investigated in greater detail. Figure 6.7 shows three examples of the path taken of a 2 mm bead through ex vivo pig brain. T2 weighted anatomical images were taken of the brain sample before the bead was inserted into the posterior corner of the sample. As the signal from the bead is only partially visible at the sides of the sample, the signal detection method was used for measuring bead displacement. The bead was then moved from the corner into the centre of the sample with the path overlaid onto the anatomical image.

The total distance travelled by the bead in sample 1 and 2 was 8.17 mm and 15.22 mm taking a total time of 266 and 102 minutes respectively (Initial movements in z along the side of the container were not included). Considering a typical brain surgery will take several hours, and assuming the beads pre planned path to span several centimetres, the speeds achieved in sample 1 would not be feasible for clinical translation. Were it not for the single large movement in sample 2, the total distance would have been 8.27 mm in 99 minutes. This variation in speed and direction as a result of different tissue types within the brain emphasises the need for real time imaging and control so that if an impenetrable obstacle is encountered, a new path can be calculated around it. Different average distances were also observed depending on the location within the sample. Movements in direction x at 2000 loops had a higher average distance than the later movements in zx and 4000 loops (0.24 vs 0.11 mm), despite the duration being twice as long.

The direction of bead movement was largely dictated by the properties of the tissue, with the blue arrows in figure 6.7A-B indicating areas of tissue that needed navigating around. Movements were detectable when a duty cycle of 20/70 ms was used (20 ms on, 70 ms off), whereas the bead remained stationary when 2/7 ms was used, suggesting that the amount of 'on' time is a crucial factor in addition to gradient strength. Gradient strength was kept at 500 mT/m for A and B. As C had a longer storage time and showed signs of degradation, movement was observed at 300 mT/m.

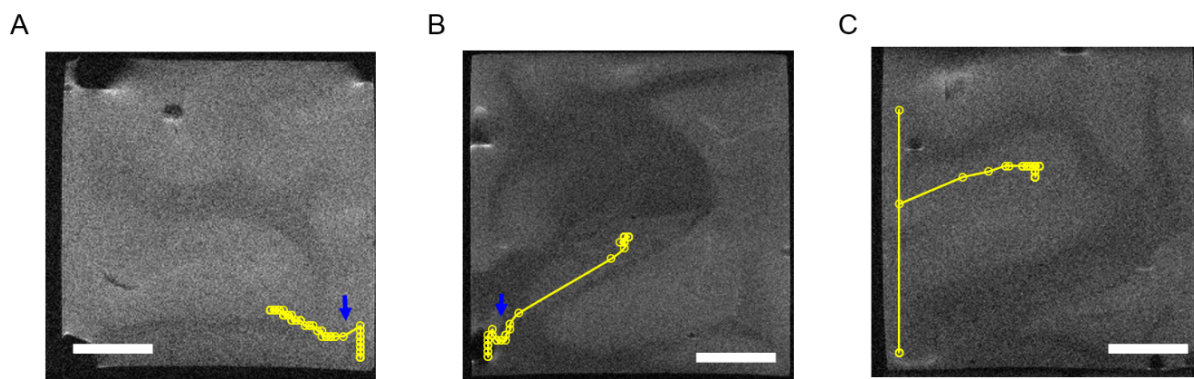


**Figure 6.7. A-C.** Examples of movement of a 2mm seed through *ex vivo* brain tissue. The relative movement of the seed (Yellow) was overlaid onto the in plane slice of a pre acquired anatomical image. Gradient strengths of 500 mT/m were used for samples A and B. As sample C was used the following day and tissue had started to degrade, movement was observed at gradient strengths of 300 mT/m. Blue arrows indicate intervening brain structure the seed needed to move around. Scale bar = 5mm.

Due to the different tissue types, densities and anisotropy within the brain tissue, characterising expected distances depending on gradient strength or loops was difficult. As such a 0.4% agarose phantom was adopted that had the same elastic modulus as brain tissue<sup>301</sup>, in the hope that having a homogenous density throughout the phantom would allow for characterisation results similar to figures 6.2 and 6.6. Unfortunately, at this concentration the agarose behaved in a more plastic manner than brain tissue and appeared more rigid. Figure 6.8 shows four examples of the movement observed using this phantom where we attempted to raster the bead across the phantom using different gradient strengths. Figure 6.8B in particular shows how initial small incremental movements were observed until a single large movement occurred (using the same parameters). This is the result of a crack forming in the direction of movement. Any attempts to move in a direction that was not parallel to the crack were unsuccessful as the bead always moved along the path of least resistance.

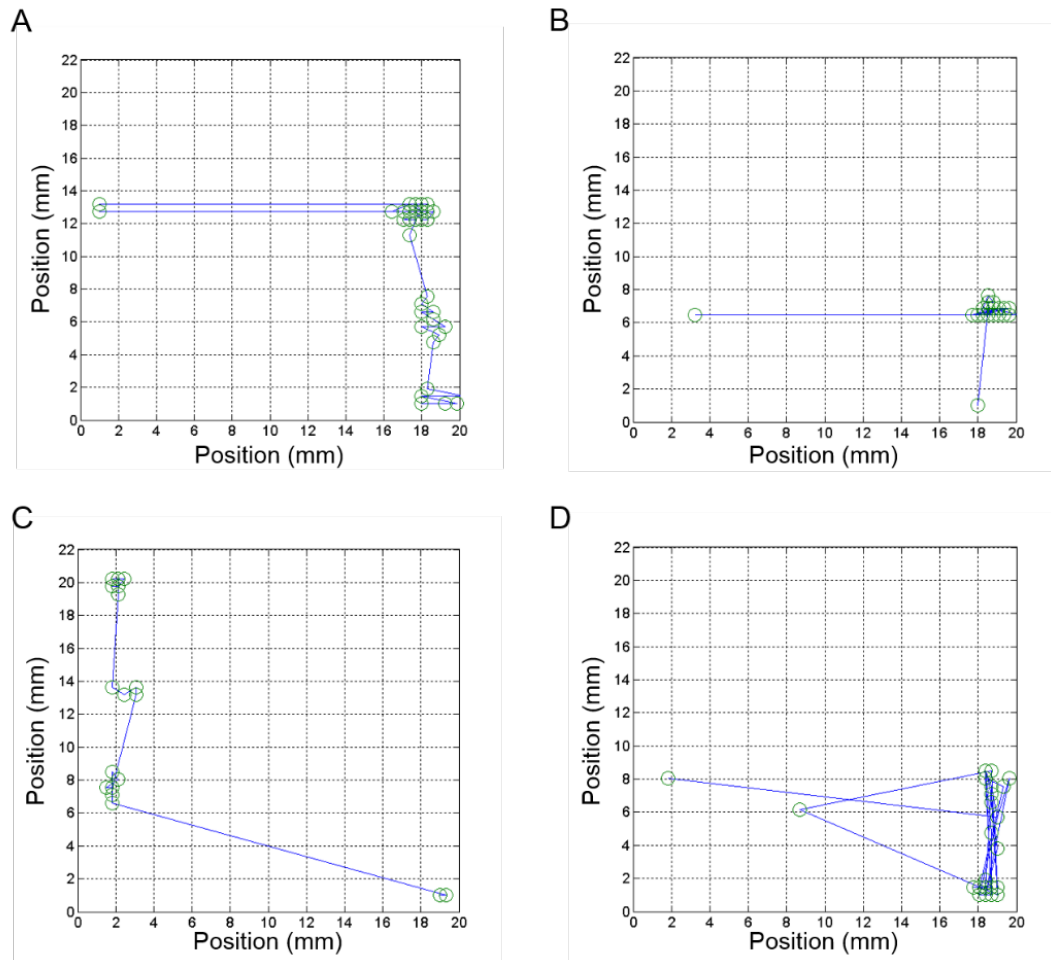


**Figure 6.8.** Examples of the path taken by a 2 mm bead through 0.4% agarose phantom. The position of the bead after each movement is plotted onto a 2D grid. Green circles indicate position of taken by the bead after each movement. Blue line indicates path taken.

### 6.3.6 Ex vivo navigation of magnetic beads using dedicated imaging/propulsion gradient coil

When imparting a magnetic force on a particle, while the distance moved is affected by the magnitude of the force, it is also dependent on the duration of force application. Despite the gradient strengths being used here are an order of magnitude higher than that of clinical MRI systems, the duty cycle still limits the total distance the bead can be moved within an appropriate surgical timescale. As increasing the gradient strength of clinical MRI systems is technically challenging due to the larger bore size, we developed a bespoke dedicated gradient/propulsion coil, capable of producing similar gradient strengths continuously.

To test this new coil, I created a 3D brain slice holder to assess the movement. This 60 x 38 x 10 mm container was positioned parallel to the  $B_0$  field (figure 6.9A). A burr hole was made at the top of the container to hold the bead in place when the phantom was inserted into the scanner. The pre-planned path for the bead was then simply to reach the bottom of the brain sample, using a gradient strength of 400 mT/m which could be applied continuously for durations of up to 2 minutes. 3 mm beads were also used as this should provide a 3 fold increase in the amount of force at this gradient strength. Each brain slice was taken from the same section of brain (figure 6.9B). The path taken by the bead for samples 1, 2, 3 and 4 are shown in figure 6.9D-G. In sample 1, the bead moved to the top right corner of the sample after placing the sample into the scanner due to the  $B_0$  fringe field. For the other three samples the bead remained inside the dedicated burr hole.

In samples 1 and 4, the bead was moved iteratively through the brain slice reaching the bottom. In sample 4 (Fig 6.9G), the bead was moved left once the bead was close to the bottom. The total distance traversed in samples 1 and 4 were 24.31 mm and 41.18 mm taking a total time of 13.3 and 12.2 minutes. Not only was it possible to move a greater distance using the new gradient coil, but the time taken was drastically reduced when continuous gradients were applied. In samples 2 and 3, the bead encountered a barrier mid route and could not be moved further despite increasing the duration of gradient application to 100 seconds. From the anatomical images, in sample 2 (Fig 6.9E) it appears the obstacle occurs at a grey/white matter boundary while in sample 3 it is unclear what impeded the beads movement. It was apparent in later tests that the samples would sink slightly during each experiment (Figure 6.10). If this occurred in sample 3 then the obstacle could have also aligned with a grey/white matter boundary. Nonetheless the distances travelled in samples 2 and 3 were 17.32 mm and 11.48 mm in 25.8 and 31.3 minutes, traversing similar distances to figure 6.7 but over a much reduced time scale.



The displacements of the bead in each of these four samples were collated according to the duration of gradient application in figure 6.9C. The majority of the displacements were less than 1 mm as before, and like sample 3 in figure 6.7, sample 4's apparent degradation due to its increased storage time resulted in an increase in average displacement at shorter durations. These result show that increasing bead size and having a dedicated gradient set that can generate propulsive forces without a duty cycle increases the total traversable distance within a much reduced timescale.

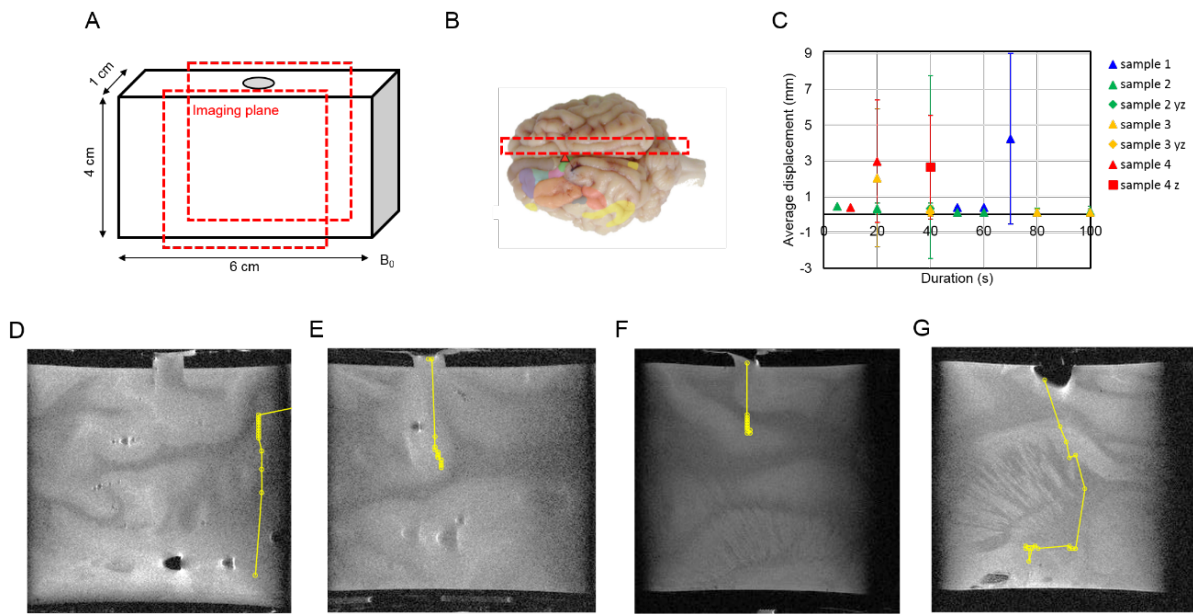


**Figure 6.9. Navigation of a 3 mm bead through brain tissue using bespoke propulsion gradient coil.** **A.** dimensions of brain sample with burr hole positioned above for bead insertion. **B.** Red dotted outline indicates the slice excised from an intact pig brain. **C** shows the average displacement of the bead depending on the duration of force application for four tissue samples. Error bars = SD. **D-G** show the path taken by the bead as it was navigated through samples 1 – 4 respectively.

For clinical translation of this technique, existing MRI scanners would have to be modified, or be made compatible with a dedicated propulsion gradient insert. While Martel et al have designed an insert capable of  $400 \text{ mT/m}^{302}$ , the gradient is unidirectional and would not deliver the 360 degree control needed. At present, the strongest clinical gradient set is  $300 \text{ mT/m}$  used for increasing sensitivity and contrast for diffusion MRI imaging as part of the human connectome project<sup>303</sup>. With this in mind two further options were investigated to determine the best approach for the design of a dedicated clinical gradient set: 1) increasing gradient strength to  $400 \text{ mT/m}$  while still operating with a duty cycle (15/85 ms), and 2) keeping gradient strength at  $300 \text{ mT/m}$  but operating continuously.

At 400 mT/m with a 15/85 ms duty cycle (figure 6.10A), movement was restricted to 7.58 mm taking 45 minutes. However, pre and post anatomical images revealed that the brain tissue had sunk downwards during the procedure, reducing the effective total distance. Figure 6.10 B-C on the other hand shows two examples of the path taken using a gradient strength of 300 mT/m without a duty cycle travelling a total of 53.15 mm and 44.82 mm in 8.3 and 66.3 minutes respectively. This difference in duration (8.3 and 66.3 mins) was largely due to the bead travelled mostly in grey matter in sample 1 (figure 6.10B) and white matter in sample 2 (figure 6.10C), which has a higher density, and again highlights the importance of the need for imaging feedback. In addition, figure 6.10 C shows that the bead can be navigated back along its pre made path back to its initial position for retrieval. While it took 58.8 minutes to navigate the bead 25.57 mm downwards through white matter, only five 90 second movements were required to move the bead 19.25 mm back along the path it came with the largest displacement occurring on the last movement. The path taken by the seed was visible on the post anatomical image (figure 6.10C) indicating that care should be taken to avoid large, fast movements to minimise tissue damage. Figure 6.10D shows the difference in average displacements between movement in grey matter and white matter. As grey matter has a lower elastic modulus than white matter, the bead could be moved further in a shorter space of time. The total average displacement for samples 1 and 2 were significantly different ( $5.6 \pm 1.42$  mm vs  $0.24 \pm 0.20$  mm,  $P < 0.0001$ , unpaired t test with Welch's correction).

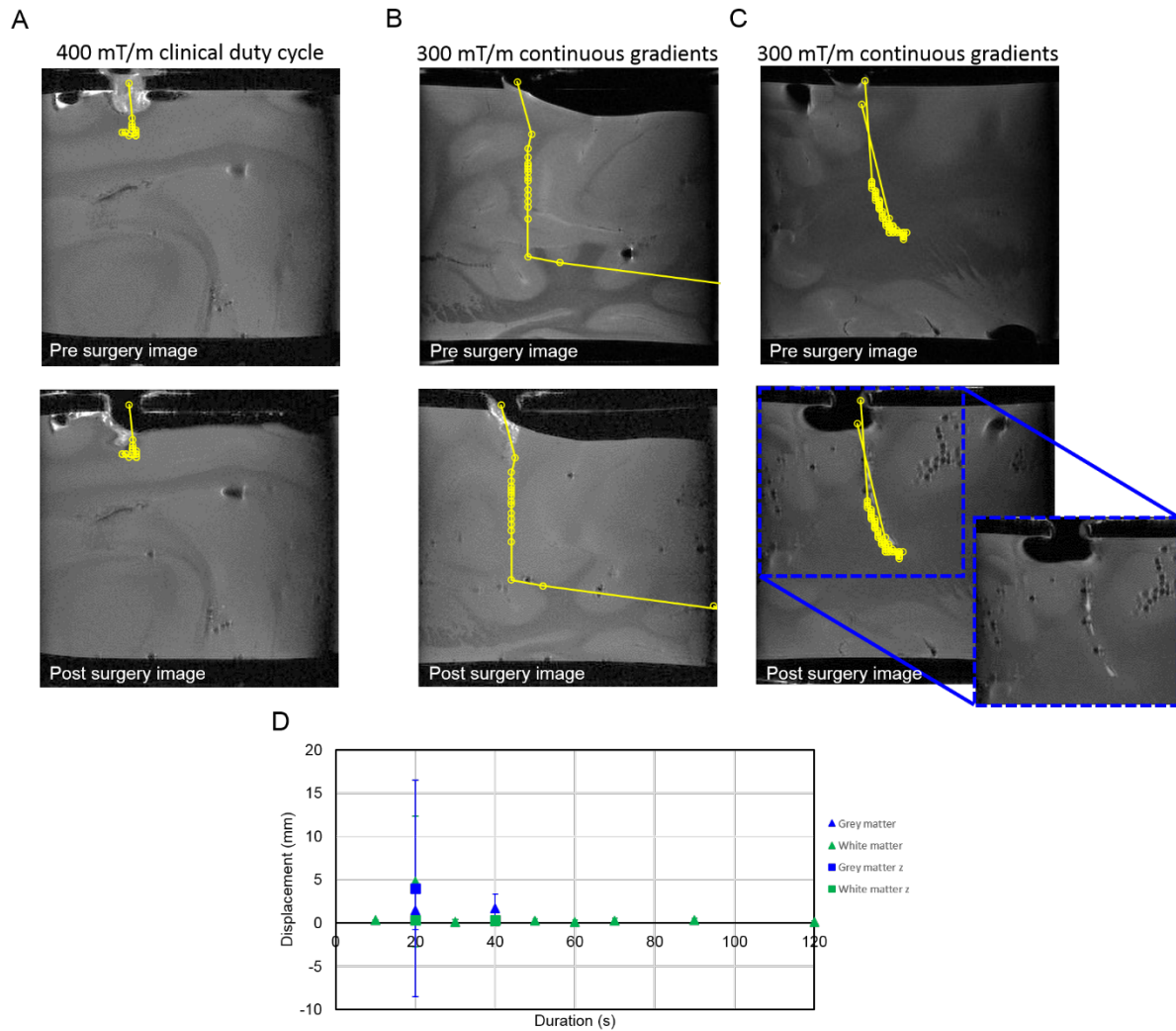


**Figure 6.10. A-C.** The path of a 3 mm bead navigated through brain tissue using overlaid onto pre and post acquired anatomical images. A gradient strength of 400 mT/m with a duty cycle of 15/85 ms was used in **A** and at 300 mT/m with no duty cycle in **B** and **C**. Blue blow up in **C** shows the path taken by the bead as it was manoeuvred back to the starting position. **D** shows the average displacement of the bead for the samples 1 (**B**) and 2 (**C**).

## 6.4 Discussion

In this study the concept of moving an untethered magnetic bead through brain tissue using an MRI scanner has been demonstrated. Using the magnetic field imaging gradients inherent in all scanners, magnetic forces applied to a 2mm chrome steel sphere were enough to deliver movement through *ex vivo* brain tissue. Not only was tissue penetration possible, but by modifying an existing imaging technique for locating ferromagnetic beads *in vivo*<sup>244</sup>, the position of the sphere could be manipulated with submillimetre precision towards a target location. In addition, a dedicated propulsion/imaging gradient set was developed, showing that magnetic beads can be navigated several centimetres within a clinically relevant time scale and manoeuvred back to its starting point for its removal. The use of magnetic field gradients to manipulate the beads position means this technique is minimally invasive while still providing the surgeon with a high degree of precision and control over the bead. Once in the desired location the bead can either be used to ablate, sense or deposit a therapeutic agent.

This study provides the first example of movement of a magnetic bead through brain tissue using MRI. Previous work using rotatable electromagnets and millimetre sized neodymium magnets have shown how the magnets could be manoeuvred in a dog brain *in vivo* and imaged with fluoroscopy as a hyperthermia treatment<sup>165</sup>. Once in position, a separate coil would generate an alternating magnetic field to heat the magnets to induce localised hyperthermia. An electromagnet capable of generating magnetic gradients of 400mT/m was capable of moving a 4.8mm steel ball through dog brain<sup>166</sup> with later editions updated to 2T/m to move 5mm x 4.5mm NdFeB cylinders<sup>304</sup>. They also state an average force to move a 3mm spherical seed through brain tissue at a speed of <1cm/15s was  $0.07 \pm 0.03\text{N}$ <sup>305,306</sup>. For a minimum detectable movement of 0.27mm at 2000 loops and 20/70ms duty cycle, force is applied for a total of 40 seconds (including rise time) giving an effective velocity of 0.006mm/s compared to their 0.66mm/s. This is to be expected with a much lower theoretical force of 0.002N for a 2mm seed and pulsed gradients.

Average speeds when using a gradient strength of 300 mT/m continuously and a 3 mm bead were 0.041 mm/s and 0.007 mm/s in grey and white matter respectively. While there is a clear improvement in speeds in grey matter, the dependence of tissue type on speed iterates the need for real time imaging and careful route planning to give the surgeon the best indication of the length of time needed. Increasing either gradient strength or bead size would further increase the forces available and therefore speed, however the restricted volume with our current pre-clinical MRI

setup limits bead size to 3mm as the susceptibility artefact becomes larger than the total imaging volume.

The ability to navigate the magnetic bead along a pre-determined path is critical to the success of this technique. Through a purely viscous medium it was possible to manoeuvre the bead a set distance exactly in line with gradient direction (Figure 6.6). However, movement through viscoelastic media such as agar and brain tissue was affected even by small differences in density. In brain tissue, anisotropy such as the orientation of white matter tracts may also affect the direction of movement, with the bead always following a path of least resistance. This can be seen in figure 6.10 C, where the path taken by the bead curves to the right slightly despite force only being applied downwards. This emphasises the need for real-time monitoring of the beads location, so that adjustments can be made either to the direction of force or change the expected path the bead will take. With the current forces available, navigating the bead across tissue boundaries is a challenge. As such either a path must be chosen which does not encounter tissue boundaries, or the amount of forces that can be applied to the bead must be increased.

To increase the forces available there are two options: optimise the bead and/or optimise the gradients. In regards to bead optimisation, the most effective option is to increase the size as force is proportional to bead volume. While the chrome steel used in this study has a high magnetic saturation point, there are a few metal alloys that can achieve higher values. Iron-Cobalt alloys can reach saturation magnetisations of around  $1.72 \times 10^6 \text{ Am}^{-1}$  (2.45 T)<sup>307</sup>, however it is more brittle and prone to cracking, so the therapeutic application of the bead should also be considered when selecting a material. For hyperthermia seeds the magnetic and electrical properties of the material should both be considered. Changing the shape of the bead could also reduce the amount of force needed move it through tissue. However, any non-spherical shape will align with the static field inside the MRI bore which would restrict the range of movement. For gradient optimisation we have shown that the ability to generate gradients continuously without a duty cycle increases the distance moved within an appropriate surgical time scale. Purpose built unidirectional propulsion gradients are already in use capable of  $400 \text{ mT/m}$ <sup>302</sup>, while a gradient insert capable of operating at  $200 \text{ mT/m}$  continuously has also been built specifically for UTE imaging<sup>308</sup>. Developing a dedicated propulsion/imaging gradient set for clinical MRI systems capable of generating continuous gradients upwards of  $300 \text{ mT/m}$  still remains a technological challenge.

For this technique to be a viable alternative treatment option, not only must the surgeon have absolute control over the position of the bead, but its position within the brain must be determined with a high degree of precision. By modifying an existing localisation technique we demonstrate that

the absolute position of a magnetic bead can be detected with an accuracy of 0.27 mm, similar to existing methods ( $< 0.3 \text{ mm}$ )<sup>244,246</sup>. The total acquisition time could be reduced from 48s to 3s by measuring only the relative positioning of the seed (only one readout direction for x, y and z projections) and reducing the number of averages, however this in turn could increase the measurement errors. Translation of our technique from pre-clinical to clinical MRI systems will also affect the precision of localisation with pixel size, number of data points and SNR all contributing to the accuracy of detection. Nonetheless, previous studies have optimised localisation of ferromagnetic beads in the vasculature so that both propulsion and tracking could be performed within a repetition time of 41.6ms by acquiring 1D projections along each orthogonal axes with a single RF pulse<sup>208</sup>. Such constraints would not be needed for our technique, as our bead would be considered stationary when propulsion gradients are not applied.

Other groups have used an alternative template based method, whereby the distinctive susceptibility artefact shape of the device is save in a template library and used for artefact recognition<sup>249</sup>. The position is then determined with a template matching procedure. After optimisation and reduction in the number of k-space lines, the total acquisition time with this method can be reduced to approximately 1 second with dynamic errors of  $< 0.5\text{mm}$ . The limited working volume of the MRI scanner used in this study means template matching would not be possible with the current setup for 2mm seeds. Future work should therefore focus on delivering similar detection accuracies on a clinical MRI system. As time is the primary constraint for the precision of localisation, the time taken to navigate the bead to the target location, deposit the therapeutic payload, and its retrieval, along with the beads proximity to eloquent brain areas should all be taken into account when incorporating our detection method.

Careful consideration must be taken when inserting and removing the seed from the patient. Due to the considerable field gradients caused by fringe fields surrounding the scanner bore, the bead cannot be inserted beforehand unless adequate shielding can be provided. Martel's group inserted an 'introducer' into the femoral artery of a pig before moving into the MRI scanner<sup>208</sup>. A steel ball fixed into a catheter tip was inserted into the introducer by an interventional radiologist and then moved into the scanner, arguing that the forces on a 1.5mm seed do not exceed the stresses generated on vessel walls during normal catheter placements<sup>245</sup>. An MRI compatible stereotactic frame, similar to those used for MRI guided interventions<sup>309–311</sup> and biopsies<sup>312</sup> could also be adopted. Both solutions would allow for the seed to be inserted once the patient is inside the bore of the scanner, where the seed can then be navigated along its predetermined path. Movement back along the path also requires much less force, meaning that the seed can be moved back to the

insertion site where it can be recaptured and safely removed. These options will be explored in future investigations.

## 6.5 Conclusion

This study demonstrated the feasibility of navigating a millimetre sized magnetic particle through brain tissue using MRI. Real-time imaging allows for accurate localisation of a magnetic bead in respect to pre-acquired anatomical images of the brain. Controlling the strength and direction of the magnetic field gradients allows for the bead to be guided around intervening structures towards a target location. This study also demonstrates that with a dedicated propulsion/imaging gradient set capable of generating continuous gradients up to 400 mT/m, magnetic beads can be navigated several centimetres through brain tissue within a typical surgical timescale. For clinical translation of this technique, existing MRI systems would require a dedicated gradient insert to generate the same forces available in this study.

Inspired by the magnetic stereotaxis hyperthermia study, whereby millimetre sized neodymium magnets can be guided through the brain and deliver hyperthermia<sup>165</sup>, the next chapter investigates whether an MRI scanner can be converted into a combined navigation and ablation device. Using the same magnetic beads, their ability to ablate localised regions of cells is assessed, allowing MRI to be used as a minimally invasive, image-guided ablation therapy named MINIMA.



## 7 Thermal ablation using magnetic beads for MINIMA, an MRI based minimally invasive, image-guided ablation technique

### 7.1 Introduction

Hyperthermia as a cancer treatment is appealing because it has fewer side effects than chemotherapy and radiotherapy. It can also be used in combination with these therapies for a more effective treatment<sup>313,314</sup>. Sustained hyperthermia (42-46°C) is thought to alter proteins within cells which can alter cell growth, differentiation and induce apoptosis<sup>315,316</sup>. Elevate temperatures to above 46 °C and thermal ablation occurs, with irreversible cell damage dependent on the duration. Thermal ablation of tumours can enhance immunotherapy<sup>317</sup> with one study showing that an antigen source for anti-tumour immunity is generated after radiofrequency ablation<sup>318</sup>. If a selected area of tissue reaches 60 °C, cell death will occur after 1 second<sup>319</sup>. In recent years a variety of focal ablation and radiation therapies have emerged including HIFU, Gamma Knife®, radiofrequency ablation (RFA), Interstitial laser ablation, photodynamic therapy and interstitial implant hyperthermia amongst others. The advantages these therapies have are: Minimal side effects to limit postoperative morbidities and mortality, non-surgical patients can benefit from these treatments, real-time image guidance is possible, most procedures only need local anaesthesia leading to faster recovery times, they can be performed as an outpatient procedure to reduce hospital time and shorten time to daily function.

While these therapies have led to clinical trials, only Gamma Knife and the interstitial laser therapy Visualase® have been introduced into hospitals in the UK. Even so, surgical complications, along with inaccuracies in ablation or imprecision of applicator placement have all been reported for the Visualase system<sup>135,320</sup>. The precision of Gamma Knife is impressive (0.3mm spherical ablation volume) but restricted to small spherical lesion volumes and at present can only be used in the brain. Other ablation techniques such as cryoablation and brachytherapy are more suited to larger lesion areas due to their ablation volumes (cryoablation typically 20x20x20mm) and implantation of multiple seeds. The majority of thermoseed or rod studies have focused on arrays of seeds as these deliver more uniform temperatures within the array<sup>321</sup>, however this in turn increases the invasiveness of the technique. Following on from the previous chapter, showing that a single magnetic bead can be manoeuvred through tissue towards a desired location, this chapter

investigates the potential for a remote controlled, minimally invasive, image-guided ablative therapy (MINIMA) using a single millimetre sized bead.

The main advantage of MINIMA is the ability to move a single bead remotely into the desired position iteratively with image guidance, using the magnetic field gradients of the MRI scanner. As a cancer therapy, the bead should only be heated when inside the tumour boundaries. The beads must heat rapidly above 60°C to minimise ablation time and maximise the number of ablation positions available within an acceptable surgical time scale. We hypothesise that using an external alternating magnetic field (AMF) at radiofrequency, a ferromagnetic bead can be heated readily to induce controllable and precise regions of cell death while leaving distant healthy tissue unaffected.

In this study, the heating characteristics of ferromagnetic beads are assessed. Initially, heating of beads of different size and surrounding medium were investigated using a thermal imaging camera and temperature probe, assessing the time taken for the bead to reach ablative temperatures. A novel 3D cell culture staining method was then developed using TTC as an indicator of cell viability, which is typically used as an indicator of cell viability on tissue slices<sup>322,323</sup>. Once a protocol was established that provided good spatial contrast between live and dead cells, the volume of cell death was investigated as a result of heating the bead. From this a novel, MRI compatible coil that could generate similar alternating magnetic fields was built, showing that thermoseeds reach ablative temperatures rapidly inside an MRI scanner. Finally, in vivo ablation was performed using this coil, demonstrating localised cell death in the brain after only 1 minute of heating.

## 7.2 Materials and Methods

### 7.2.1 Initial heating attempts with MRI radiofrequency coil

A 33mm diameter Rapid volume RF coil was used to generate radiofrequency pulses in a 9.4T Varian MRI scanner. Consecutive RF pulses were applied using custom sequence with parameters: pulse length = 1.5 s, power = 62 dB, repetitions = 40, frequency = 400 MHz. A 50 ml falcon tube was filled with 2% agar (Sigma Aldrich®) with a temperature probe position in the centre. Temperature was then measured with and without a 2 mm chrome steel sphere (aisi 52100) adjacent to the temperature probe.

### 7.2.2 Heating coil specification

The magnetic alternating current hyperthermia system (MACH) provided by Resonant Circuit Limited (London, UK) was deployed to generate the AMF in this study. A magnetic field was generated at the split pair of double-turn coils when an alternating current was running through the coil (Figure 7.1A). The adjustable range of field strength was between 2 kA/m and 15 kA/m, while the frequency of the field was between 850 - 1000 kHz. To stabilise the temperature of the coil, temperature-controlled water was circulated through the inside of the coil by a chiller.

An MRI compatible MACH coil was also developed consisting of 5 litz wires wound helically into a 5 turn coil that can generate 700 kHz at 7 kA/m (Figure 7.1B). Miniature ceramic capacitors soldered to copper housing allowed the coil to be placed inside the bore of a 9.4T preclinical Varian MRI scanner. 2 m extension cables were added for connection to the non MRI safe power supplies outside the 5 gauss line. As the coil was not water cooled, the coil was limited to 1 minute AMF applications to avoid overheating.

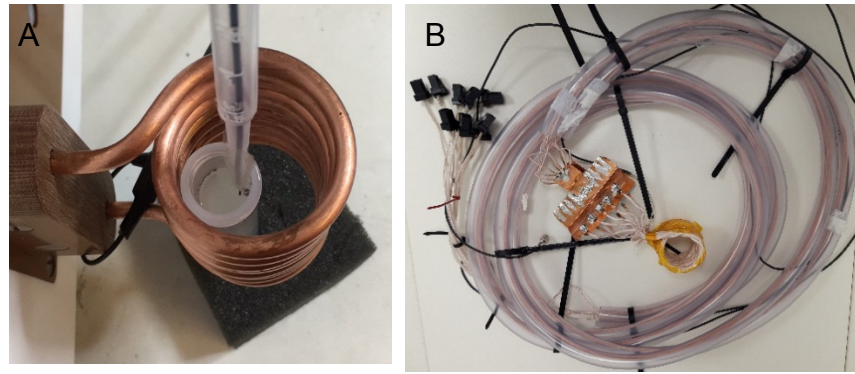


**Figure 7.1.** Hyperthermia coils. A. Photo of experimental setup using MACH system for in vitro ablation showing a 2 mm bead embedded in agar phantom positioned inside the coil. A fibre optic temperature probe is positioned adjacent to the bead. B. Photo of the MRI compatible coil and connecting cables.

### 7.2.3 Heating of bead in air and water

Initial experiments investigating the heating abilities of chrome steel beads used a thermal imaging camera (VarioCAMhr InfraTec GmbH, Dresden, Germany) placed above the heating coil. Beads of different sizes were placed inside a small glass vial which would sit in a 3D printed holder which held the bead in the middle of the coil when inserted. To measure the surface temperature of the bead a thermometer was tapped to the bead. This was performed in both air and water.

### 7.2.4 Temperature distribution in agar phantom

To better indicate heat dissipation from the bead through biological tissue an agar phantom was used. This consisted of a 15ml Falcon tube filled with 12 ml of 1% agar (Sigma Aldrich®). A 10mm coverslip was placed on top and 1ml of 0.5% agar was added. The bead was placed in the centre of the agar before setting. The agar was prepared by adding 0.5 g of agar to 100ml of distilled water and heated in a microwave oven until the agar was dissolved. A temperature probe was placed either on the surface of the bead or at 1, 2 and 3mm away while the bead was heated for 10 minutes. Measurement at each position was repeated three times using fresh phantoms samples.

### 7.2.5 Development of TTC staining of 3D cell culture

A TTC staining technique was developed to assess macroscopic cell death as a result of heating the beads. To assess staining visibility of two cell types, mouse mesenchymal stem cells (MSC D1 cell line (CRL-12424), acquired from ATCC) and mouse mammary gland tumour cells (4T1, ATCC) were cultured in a T75 flask (Thermo Scientific®) until confluent in DMEM media (Gibco) supplemented

with 10% FBS (Gibco). 13ml of cells were transferred to a 15ml falcon tube and centrifuged to form a pellet. Media was removed and 1ml of 1%TTC (Sigma Aldrich®) in PBS (Gibco) was added to the cell pellet, and incubated at 37°C for 1 hour, when TTC was removed. To optimise staining in 3D cell culture, MSC's were added to 1ml of unset 1% agar in a 24 well plate. All cells were extracted from a confluent T75 flask initially, where 1ml of cells in PBS was added to the agar and stirred using a pipette before setting. This was then increased to a T175 flask. A confluent T175 flask containing approximately 30 million cells provided good staining contrast. To assess cell viability, a well containing the 3D cell culture was placed above a heat plate for 5 minutes at 100°C. For the 3D cell culture to fit inside the MACH coil, a 15ml falcon tube was first filled with 12ml of 1% agar. Initially 500µl of 1% agar and 500µl of 30 million MSC's were added on top and stirred with a pipette. To aid stirring to ensure cells were spread homogenously about the agar, a 10mm diameter coverslip was placed between the agar and 3D cell culture. The media was also kept in incubator at 37°C and only taken out immediately before stirring.

#### 7.2.6 Cell death via heating of bead

2mm beads were placed in the 3D cell culture as described above after cells had been stirred but hadn't set. The field strength and frequency of the MACH system was set at 6kA/m and 895kHz. Cells were maintained at 37°C before placing them inside the MACH coil. An AMF was then applied for 0, 1, 5 and 10 minutes. 1 ml of 1% TTC in PBS was added to the cell culture and incubated for 1 hour. TTC was then removed and photographs were taken of the cells immediately after. A 3D cell culture without a bead was also placed in the AMF for 10 minutes. 3 replicates were taken for each time duration. The area of cell death was then measured using ImageJ by manually drawing a circle over the cell death perimeter. The surface temperatures of the cell cultures were also recorded using a thermal imaging camera (Infratec GmbH, Dresden, Germany). Minimum, maximum and mean temperatures of the cell culture were taken from an ROI over the cell culture using Irbis 3 plus thermal imaging software (Infratec).

#### 7.2.7 In vivo ablation

All animal work was performed in accordance with the United Kingdom's Animals (Scientific Procedures) Act of 1986 and was previously approved by UCL's internal Animal Welfare and Ethical Review Body. Male Wistar rats (8±1 weeks-of-age) were bred by Charles River (UK) and delivered to UCL's Centre for Advanced Biomedical Imaging one week prior to experiments. Rats (300±25 g) were anaesthetised with 3.5 % isoflurane vaporised in oxygen at a flow rate of 1 L/min. The head was

shaved, and the animal positioned in a stereotaxic frame in the horizontal skull position, where 2.5 % isoflurane (delivered in 1 L/min oxygen) was delivered via a nose cone. A midline incision was made in the scalp, and a cranial window made by removing a ~6 mm disc of skull above the left striatum (3 mm lateral and 0.2 mm anterior to bregma). A 27 gauge needle was inserted into the striatum (6 mm ventral to the brain surface) and removed. This process was subsequently repeated at the same position with a 21 and 18 gauge needle. A 2 mm diameter chrome steel sphere (AISI 52100, grade 100, Simply Bearings, UK) was positioned on the surface of the brain, above the needle tract. The sphere was inserted into the striatum using a blunt 18 gauge needle, prior to the needle being retracted, and the skin sutured closed to cover the skull.

The rat was transferred to the MRI compatible MACH system, with the head positioning in the centre of the coil, and anaesthetic delivered via a nose cone (2.5 % isoflurane delivered in 1 L/min oxygen). An alternating magnetic field was applied for 1 minute. Following heating, the animal was sacrificed with an overdose of pentobarbital administered via intraperitoneal injection. The animal was decapitated, sutures removed and the chrome sphere extracted through the original needle tract, using a permanent magnet. The brain was removed from the skull and sectioned into 1 mm thick slices using a McIlwain tissue chopper (Mickle Laboratory Engineering Co. Ltd., UK). Each slice was placed into freshly prepared 1% 2,3,5-Triphenyltetrazolium chloride (TTC) (Sigma Aldrich, USA) solution and incubated at 37°C for 10 minutes. The slices were removed from solution, excess liquid removed and placed on a petri dish. The samples were photographed immediately. Images were loaded into ImageJ and a region of interest (ROI) was manually drawn around the area of cell death on each slice.

## 7.3 Results

### 7.3.1 Temperature of spherical beads dependent on bead diameter

As an initial test to investigate the range of temperatures achievable with chrome steel spherical beads when exposed to an alternating magnetic field (895 kHz, 6kA/m) a thermal imaging camera was used to detect the surface temperature of the bead when placed inside the MACH heating coil. Beads 1, 2, 2.5 and 3 mm in diameter were placed in a small glass vial with the camera positioned directly above ( $N = 1$ ). Figure 7.2A shows that increasing the size of the bead substantially increases the temperatures that can be achieved. After 1 minute of heating the 1mm bead heated from room temperature to 32°C, 2mm to 66.9°C, 2.5mm to 99.1°C, while the 3mm bead reached above 100°C in less than 17 seconds. Clearly at this field strength and frequency, beads above 2mm in diameter will heat to temperatures above the hyperthermia threshold of 42°C. As movement through brain tissue is possible with a 2 mm bead (from the previous chapter), it was decided that 2 mm beads would be the focus for heating characterisation.

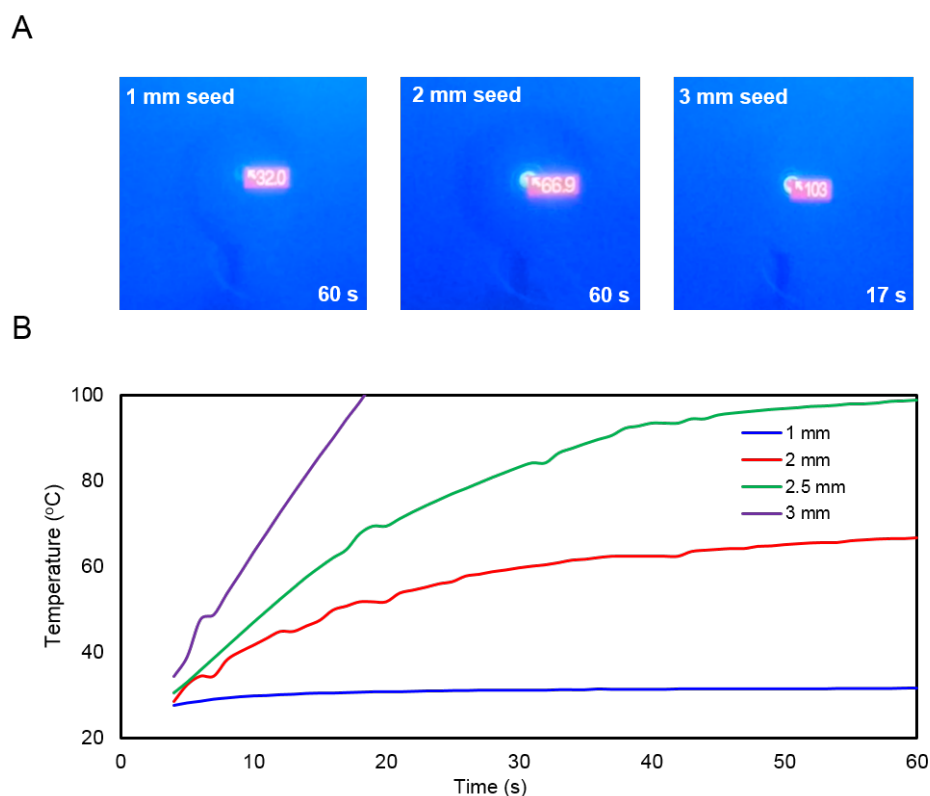


**Figure 7.2.** **A.** Images taken from the thermal imaging camera indicating the maximum temperature at 60 seconds for a 1 mm and 2 mm bead and after 17 seconds for a 3 mm bead. **B.** Graph showing the increase in temperature over time for different sized beads in air ( $n = 1$  for each size).

### 7.3.2 Characterisation of 2 mm bead heating in different media

To investigate the effect of surrounding media on the maximum temperatures achievable, and for a more precise measurement of bead temperature, a fibre optic probe was attached to the surface of 2 mm beads suspended in air, water and agar phantoms. Figure 7.3A shows the surface temperature of a 2 mm bead in air when heated in 4 consecutive short bursts of AMF application. A sharp rise in surface temperature was observed when the AMF was applied, followed by a sharp decrease when the field was switched off. The rate of temperature increase measured with the fibre optic probe was much more rapid than that recorded by the thermal imaging camera (8.33 vs 1.96 °C/s) and as such the AMF was switched off before the bead reached its maximum temperature to avoid damaging the probe. Nonetheless, after only 12 seconds a 2 mm bead can reach over 80 °C in air.

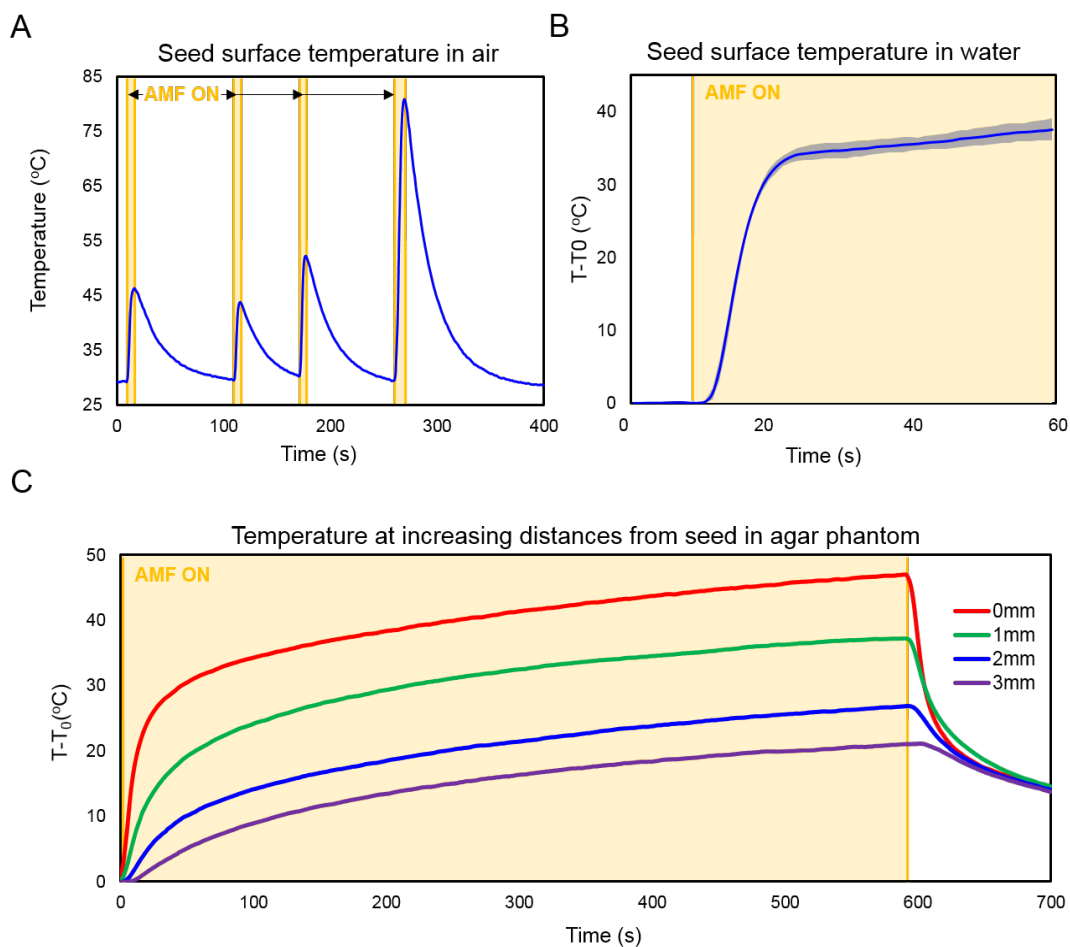


**Figure 7.3.** Fibre optic temperature probe measurements of the surface of 2 mm beads in air, water and agar phantoms. **A.** Graph showing the rapid heating and cooling of a bead after consecutive short bursts of AMF application (yellow areas). **B.** Graph showing the average temperature increase of a 2 mm bead immersed in water. Grey area indicates S.D. ( $n = 3$ ). **C.** Graph showing the average temperature at increasing distances away from a bead after 10 minutes of AMF application. ( $n = 3$  for all distances)



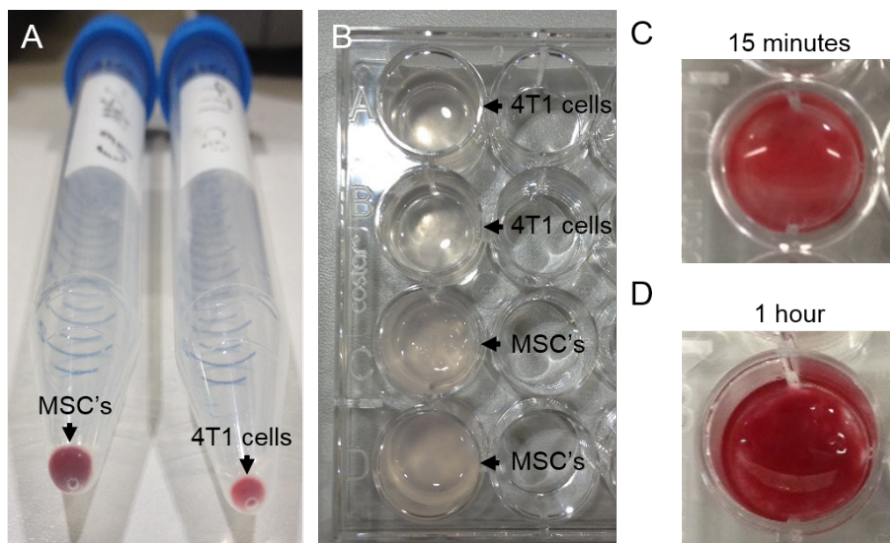
For 2 mm beads submersed in water (Figure 7.3B), their surface temperature would increase by more than 30 °C within the first 10 seconds of AMF application (n=3) at which point the temperature plateaus, increasing at a much slower rate (3.65 °C/s). The initial temperature increase is at a slower rate than in air as water is a more efficient heat sink. These results show that, if the bead is surrounded by liquid inside the body, and assuming a starting temperature of 37 °C, the beads will reach above 60 °C which should deliver rapid cell death.

To understand the temperature distribution expected inside biological tissue, 2 mm beads were positioned inside an agar phantom and the temperature was recorded at distances up to 3 mm from the bead when an AMF was applied for 10 minutes (Figure 7.3C). The temperature of the bead surface (0 mm) increases by 30 °C within one minute meaning that, *in vivo*, cell death should be expected as the bead will reach above 60 °C within this time. At a distance 1 mm from the bead the temperature increased by around 20 °C, meaning that the kill zone around the bead should be within this distance. After 10 minutes, the bead increases in temperature by 46 °C and at 3 mm away, the temperature increase was above 18 °C for 4 minutes, meaning that cell death should be expected to reach up to this distance from the bead over this time.

### 7.3.3 Development of TTC staining of 3D cell culture

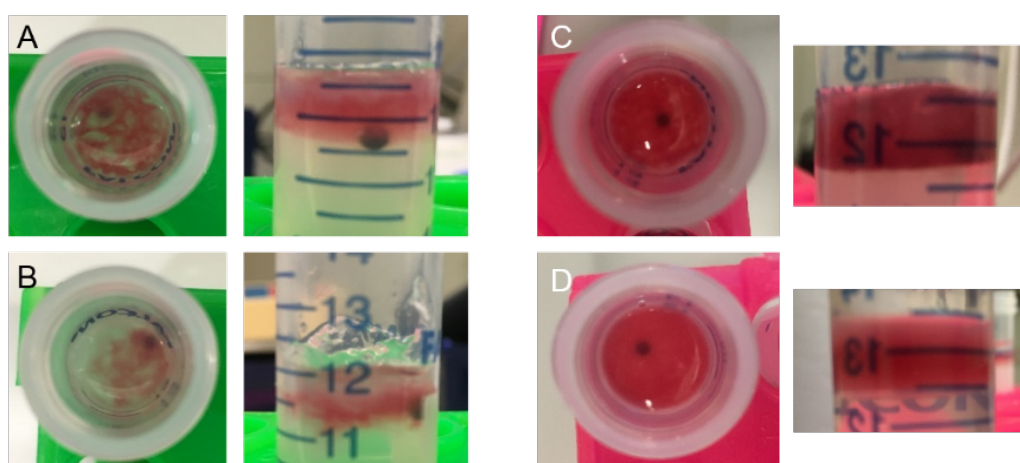
To measure cell death as a result of heating the beads, a 3D cell culture and staining technique was developed. By using a tissue mimicking medium (agar) with homogenous density, the extent of cell death could be compared against the predicted kill zones from the temperature measurements (reaching < 1mm after 1 minute, < 3 mm after 10 minutes). TTC was chosen as a cell viability indicator as it has been shown to provide clear contrast between live (red) and dead cells (clear) and is regularly used in tissue slices of damaged brain areas from MCA occlusion<sup>322</sup> and HIFU ablation<sup>323</sup>, cell viability assays<sup>324</sup> and has been shown to be more suitable than MTT, NR and LDH to analyse toxic effects in human skin<sup>325</sup>.

Figure 7.4A shows that the staining works for multiple cell types with cell pellets of mouse mesenchymal stem cells and 4T1 tumour cells appearing vivid red after 1 hour of staining. To visualise cell death as a result of heating the bead, the staining must show sufficient contrast in a container of a size of at least 10 mm in diameter. Figure 7.4B shows a 24 well plate with wells containing 5 mL of 1% agar plus approximately 5 million MSC's (bottom two) and 4T1 cells (top two) after 1 hour of TTC staining. The MSC's appeared slightly pink whereas the staining was not visible for the 4T1 cells. It was therefore decided that increasing the number of MSC cells would provide adequate contrast from TTC staining. Figure 7.4C and D show wells containing approximately 30 million MSC's appear bright red after 15 minutes of staining and deep red after 1 hour.



**Figure 7.4.** A. Cell pellets of mouse mesenchymal stem (MSC) cells (left) and 4T1 tumour cells (right) stained with TTC. B. 3D cell cultures after TTC staining (4T1 = top two, MSC = bottom two). C-D. Increased cell concentration provided vivid red TTC staining after 15 minutes and 1 hour respectively.

Now that good homogenous staining is possible with this 3D cell culture, the next step was to use a vessel that could be placed inside the MACH. Figure 7.5 shows 3D cell cultures in a 15 mL falcon tube filled with 12 mL of 2% agar which positioned the cells in the middle of the MACH coil. Initial the staining of the cell cultures appeared patchy (A and B). This was rectified by placing a coverslip between the agar and the cell culture and keeping culture media warm during the mixing process. Figure 7.5 C and D show two examples homogenous red staining of cells with no visible effects of the bead being present. These cell cultures were stored at room temperature for 2 hours before staining, showing that cells are viable over a typical experimental time period.



**Figure 7.5.** A-B. TTC staining of 3D cell culture in 15ml falcon tube with 2mm bead present displaying inhomogeneous cell distribution. C-D. 3D cell cultures with homogenous cell distribution displaying no visible effect on cell viability when bead is immersed.

### 7.3.4 *In vitro* cell death via bead heating

To assess cell death, 3D cell cultures were placed inside the MACH coil and heated for 1, 5 and 10 minutes. Clear perimeters of cell death were observed for all conditions (Figure 7.6A), with the cross sectional cell death area increasing from  $8.5 \pm 0.39 \text{ mm}^2$  to  $27.1 \pm 0.86 \text{ mm}^2$  and  $44.9 \pm 3.35 \text{ mm}^2$  for 1, 5 and 10 minutes respectively (Figure 7.6B). One way ANOVA revealed cell death area means are statically different ( $P < 0.0001$ ). The areas give an average reach of 0.64 mm, 1.94 mm and 2.78 mm from the bead corresponding to the predictions of  $< 1 \text{ mm}$  after 1 minute and  $< 3 \text{ mm}$  after 10 minutes made from figure 7.3C. No cell death was observed when an AMF was applied for 10 minutes without a bead present, or when cells + bead were placed in the coil for 10 minutes but no AMF was applied ( $n = 3$  for all conditions).

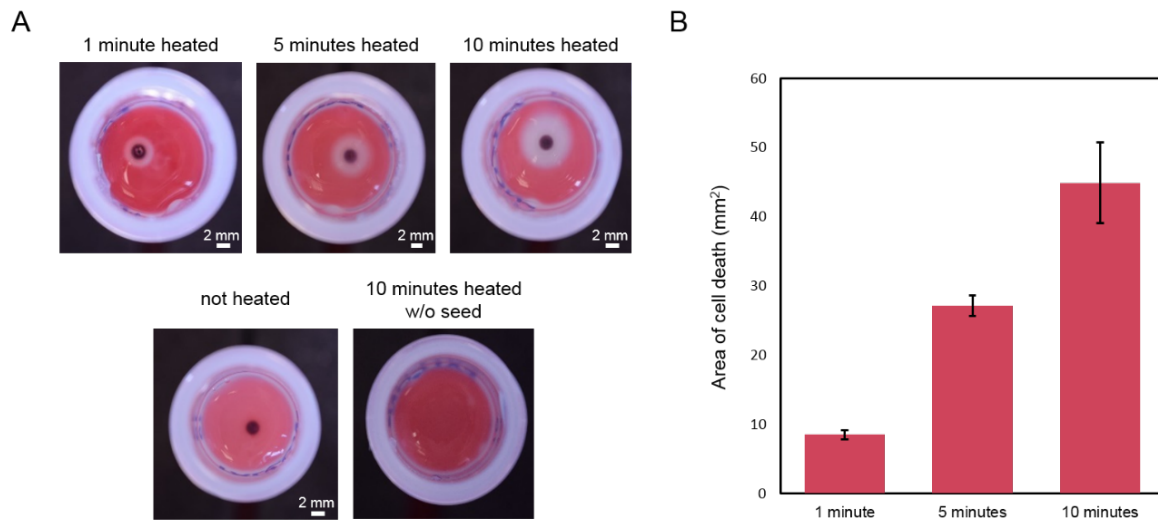


**Figure 7.6. A)** TTC staining of 3D cell culture indicates clear perimeter of cell death after AMF application for 1, 5 and 10 minutes (Red = live, clear = dead). No visible cell death was observed for cell cultures without bead and AMF was applied for 10 minutes, and when a bead was present but no AMF was applied ( $N = 3$  for all conditions). **B)** Graph showing the cross sectional area of cell death around a 2mm bead after heating for 1, 5 and 10 minutes. Error bars = SD.

The temperature of the top of the cell cultures were also monitored. Figure 7.7A-C show the minimum, mean and maximum temperature within an ROI placed around the cells. The minimum temperature in each condition decreases to room temperature where it remains constant, showing that there is no non-specific heating of the cells. The maximum temperatures recorded show similar trends to figure 7.3C. An initial sharp increase in temperature can be seen each time, followed by a plateauing to a slower rate of temperature change. The top of the cell cultures heated for 1 minute reached  $56.755 \pm 0.5 \text{ }^{\circ}\text{C}$ , making this an effective minimum threshold for cell death. The top of the

cell cultures heated for 5 minutes reached  $77.223 \pm 4.7$  °C while  $90.52 \pm 3.8$  °C was reached for 10 minutes. The average temperatures of the cell cultures were well below the maximum temperatures ( $37.2 \pm 0.4$  °C,  $42.71 \pm 1$  °C and  $44.83 \pm 0.02$  °C for 1, 5 and 10 minutes of heating) further showing that the ablative temperatures are localised around the bead which can also be seen in the final images in figure 7.7D.

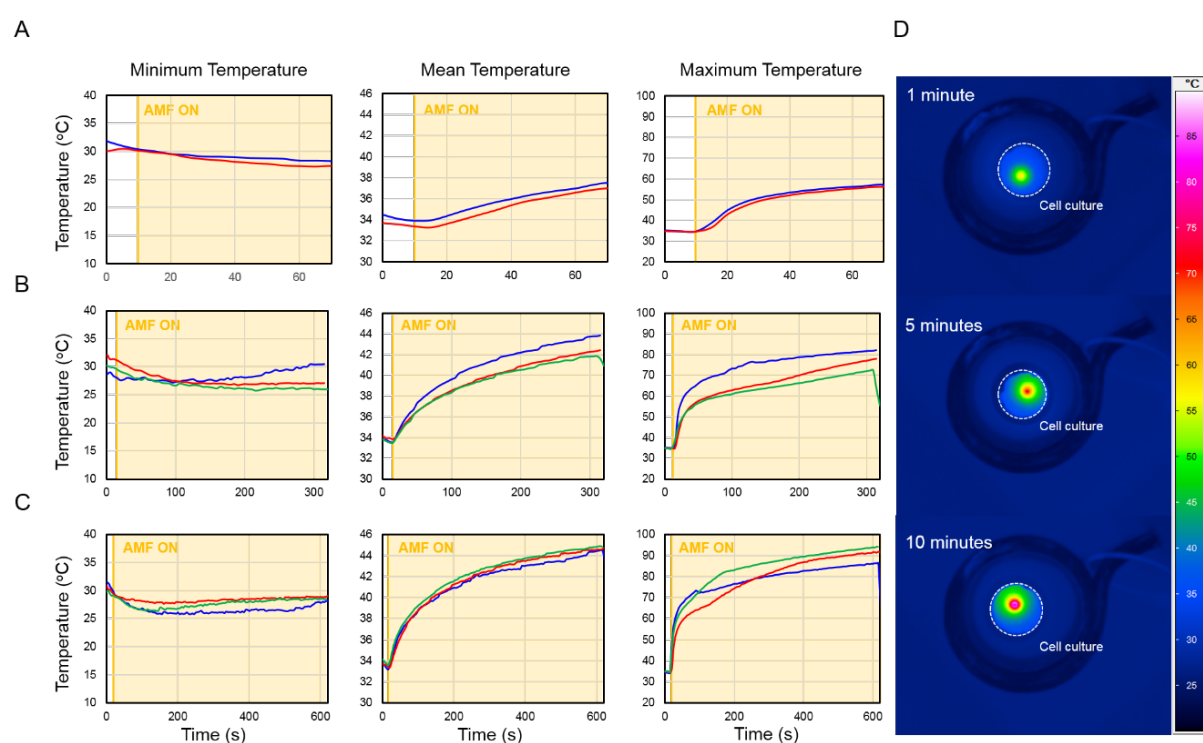


**Figure 7.7.** Thermal camera temperature readings of beads in 3D cell culture. **A**, **B** and **C** show the minimum, mean and maximum temperatures across the cell culture surface after heating for 1, 5 and 10 minutes respectively. **D**) Screenshots of the final temperatures after heating for 1, 5 and 10 minutes.

### 7.3.5 *In vivo* ablation with MRI compatible hyperthermia coil

In order to combine the heating abilities of magnetic beads with the manoeuvrability demonstrated in chapter 6, it was essential to investigate the heating characteristics of the beads when inside the bore of an MRI scanner, as the heating mechanisms within the bead will be effected by the presence of the large static magnetic field. For this, an MRI compatible coil was developed consisting of non-magnetic components that could generate an AMF with frequency of 700 kHz at a strength of 7 kA/m (Figure 7.1B). Figure 7.8A and B show the temperature of the bead after 30 seconds of AMF application outside and inside an MRI scanner. At this stronger field, the rate of temperature increase was higher than at 6kA/m, reaching temperatures above 80 degrees in 30 seconds when outside the scanner. When placed inside, the rate of temperature increase was similar to figure 7.3C, with a temperature increase of around 30 degrees after 30 seconds, demonstrating that beads can be heated to ablate cells when inside an MRI scanner.

Finally, *in vivo* ablation was demonstrated using the MRI compatible coil. A 2 mm bead was placed into the left Striatum of a live rat before placing the head inside the coil. As a suitable insertion/removal procedure has yet to be developed, ablation was performed outside the MRI scanner. Figure 7.8. C-G show TTC stained brain slices showing the extent of cell death around the bead after 1 minute of heating. The largest area of 12.3 mm<sup>2</sup> was in slice 3 where the bead was placed. The area then decreases with each slice creating a spheroid of cell death around the bead. While the areas cell death observed in figure 7.6 were circular, the shape of *in vivo* was affected by different surrounding tissue structures. The in slice area of 12.3 mm<sup>2</sup> was higher than the 8.5 mm<sup>2</sup> measured for the 3D cell culture, which is likely a result of increasing the AMF from 6 to 7 kA/m, which delivers around a 35% increase in power from the H<sup>2</sup> relationship in equation 2.15 .

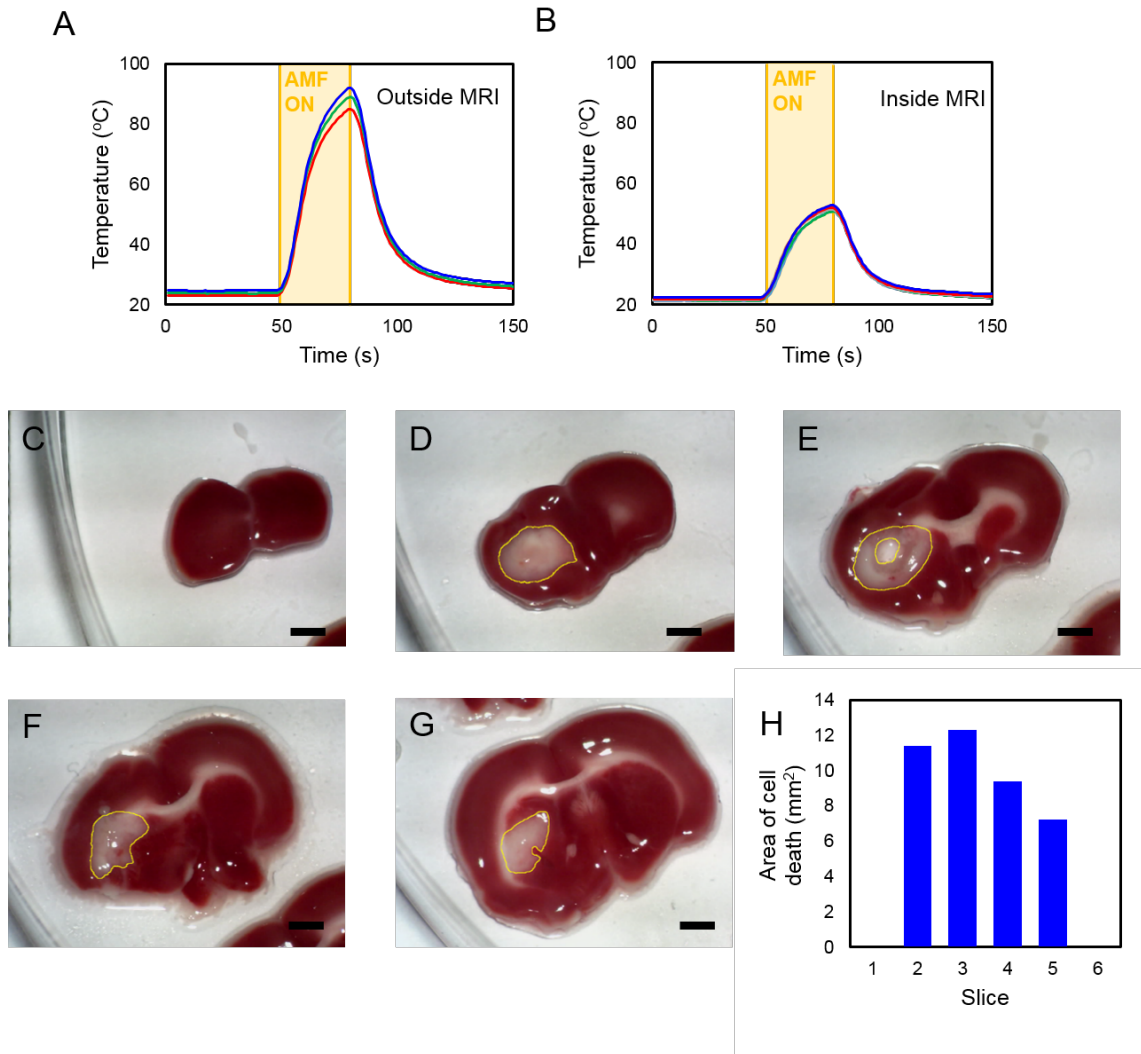


**Figure 7.8. MRI compatible heating coil.** **A-B.** Bead temperature measurements in agar phantom positioned outside (**A**,  $n = 5$ ) and inside an MRI scanner (**B**,  $n = 4$ ). **C-G.** TTC stained brain slices after 1 minute of heating using the MRI compatible coil outside the MRI scanner. Yellow ROI indicates area of ablated cells. **H.** Graph showing the area of cell death in each slice.

## 7.4 Discussion

In this study we demonstrated that spherical magnetic beads can be heated using an externally applied alternating magnetic field to cause well defined, localised regions of cell death. The extent of cell death around the bead can be controlled by changing the duration and strength of the AMF applied as shown in figures 7.3C and 7.8A. The size of the bead also effects the heating, however as chapter 6 demonstrated movement is possible using a 2 mm bead, this size was chosen as the focus for this study.

In a scenario where multiple locations require ablation, it is desirable for the bead to heat quickly to temperatures above 60°C so that immediate cell death occurs via coagulative necrosis, reducing the overall treatment time. Whether in air, water, or a tissue mimicking agar phantom, the beads used in this study increase in temperature by over 30 °C within 1 minute, reaching above 60 °C when starting at body temperature. Attempts to heat the bead using a standard preclinical radiofrequency coil (35 mm volume coil, Rapid MR international®) were unsuccessful (data not shown), causing non-specific heating throughout the whole sample, which is in agreement with a stated threshold of 10MHz for direct heating of tissue due to eddy currents<sup>211</sup>. Even at 1.5 T, the larmour frequency of protons is 42 MHz, indicating that a purpose built MRI compatible heating device would be necessary for specific heating of the bead alone. As such, an MRI compatible heating coil was developed capable of generating an AMF of strength and frequency for specific heating of the bead alone.

Using the MRI compatible coil, we demonstrated the first example of heating inside the bore of an MRI scanner. The reduction in temperature increase when inside the scanner indicates that the bead heats via both eddy current heating and hysteresis losses (explained in chapter 2) when outside the scanner<sup>326,327</sup>, but solely from eddy current heating when inside. This is a result of the bead becoming magnetically saturated when inside the scanner, meaning that the area of its hysteresis loop is reduced to zero. As such the use of magnetic nanoparticles for hyperthermia treatment using MRI is discouraged as the static field can cancel their heating properties<sup>328–330</sup>. Coating the bead with a biocompatible conducting material would increase the surface area for eddy currents to be generated to improve heating without compromising its movement capabilities<sup>331</sup>. In past studies the focus on the material of thermoseeds have been on thermoregulatory alloys that when their curie temperature is reached, do not heat further<sup>153,154</sup>. MRI guided therapies can use MR thermometry, however this would not be an option due to the large susceptibility artefact surrounding the bead. While our beads are not thermoregulatory, their heating is rapid, meaning



that AMF application can be reduced to avoid excessive heating. Both modelling and direct measurements of heat transfer in different tissues would determine these timings.

Our dynamic thermoseed approach has distinct advantages over existing static treatments. Currently arrays of rods are implanted into the target region as this generates a more homogenous temperature throughout the region and are normally left in situ after treatment<sup>332</sup>. However, issues of seed migration and chemical toxicity from seed degradation has been reported<sup>333</sup>. Due to the presence of large magnetic field gradients immediately outside the MRI scanner, our seed must be inserted and removed while the patient is inside the scanner, unless adequate shielding can be designed. Having to safely insert the seed, guide it along a pre-planned route which could include multiple ablation positions, and then safely removing the seed all during a single surgery overcomes the issue of seed migration and positioning inaccuracies. The ability to ablate at multiple locations allows for larger total ablation volumes to be achieved of an irregular shape, negating the need for seed arrays and reducing the invasiveness of the technique.

The majority of studies on magnetic thermoseeds have focused on rod or needle shaped seeds rather than spherical<sup>334</sup>. While rods have shown to heat more efficiently, their orientation in respect to the AMF is important, with more effective heating when the rod is parallel to the field rather than perpendicular<sup>153,334</sup>. The static field inside the bore of the MRI scanner would help keep a rods orientation constantly aligned with the field, however this would restrict its range of movement. As our spherical seeds heat readily, their shape should remain spherical to ensure that their range of movement remains unrestricted. However, the use of static rods implanted under MR guidance could be explored in the future.

Both *in vitro* and *in vivo* ablation results show localised, spheroid volumes of cell death surrounding the seed. The increased area of cell death observed *in vivo* is a result of using a stronger AMF (7 vs 6 kA/m) and a higher starting temperature (37 vs 34 °C). The ability to change the ablation volume by changing either the strength of the field or the duration opens the possibility of ablating larger irregularly shaped tumours ( $> 2 \text{ cm}^3$ ) without the need for inserting multiple probes as would be the case for interstitial laser ablation or RF ablation probes. The range of volumes that can be ablated with our thermoseeds are comparable to existing techniques. Focal cryotherapy typically delivers a volume of 10x10x20 mm at  $-40^\circ\text{C}$ <sup>148</sup>. The precision of photodynamic therapy is still being investigated<sup>335</sup>, but an estimated precision of 2 mm can be achieved<sup>336</sup>, however a photodynamic agent still needs to be administered along with a detailed analysis of the optical properties of the effected tissue. Interstitial laser ablation delivers thermal ablation to an ellipsoid with a radius of 1 - 2.5 cm<sup>320</sup>. Preclinical HIFU systems have ablation regions that vary from centimetres to millimetres,

with one study stating a focal spot of  $0.5 \times 0.5 \times 2 \text{ mm}^{337}$ , however this system was limited to a depth of 30 mm. Transcranial HIFU systems<sup>137,338</sup> typically have an initial focal spot of around  $2 \text{ mm}^2$  that reaches around  $44^\circ\text{C}$ , but then increases considerably as the temperature increases after consecutive applications. Rectal HIFU probes can ablate regions of around  $3 \times 3 \times 10\text{-}12 \text{ mm}$ , and can reach temperatures  $>80^\circ\text{C}$  near instantaneously but are reduced to focal depths of  $40\text{-}50 \text{ mm}^{339}$ . At present we have demonstrated variable ablation volumes with a radius between  $8.5\text{-}45 \text{ mm}^2$ , which can be further reduced by applying the AMF for less than 1 minute. The depth of this technique is limited by the estimated time taken for the seed to traverse along the entirety of its path from insertion to removal. This estimated depth is dependent on the tissue or organ into which the seed is placed and is to be investigated in future studies.

Current limitations of this study include the inability to image and move the seeds when the heating coil is positioned inside the scanner. Future efforts should go into adapting the coil to provide either an imaging window between the windings of the coil, or modify it so that RF can pass through without effecting image quality. There is also potential for investigating different surface coatings and different shapes, which could also improve movement speeds and reduce imaging artefacts. For example, adding cutting faces would allow for the seed to cut through tissue while the added surface area would increase eddy current heating. However, considering the effect of simply increasing seed size and gradient or AMF strength, the benefits of changing shape are less obvious and beyond the scope of this study.

## 7.5 Conclusion

In this study we have demonstrated that a 2mm ferromagnetic seed heats rapidly when subjected to an AMF to cause controllable, well defined regions of cell death *in vitro* and *in vivo*. Development of a 3D cell culture staining method allowed for clear visualisation of the extent of cell death around the seed. Clear cell death was observed after only 1 minute of heating, delivering fast ablation to open up the possibility of multiple ablation sites during one surgical procedure. The development of an MRI compatible heating coil has shown that a similar level of heating can be expected when magnetic seeds are placed inside an MRI scanner. Further investigations into the mechanisms of cell death several days after ablation would be worthwhile as previous thermoseed studies have shown a rim of coagulative necrosis along with signs of inflammation and surrounding fibrosis 7 days after treatment<sup>158,340</sup>. Nonetheless, with such rapid and controlled ablation, combined with the results from chapter 6 this work has demonstrated the three essential components for transforming an MRI scanner into a theranostic tool: precise localisation, controlled movement through tissue, and now accurate ablation using magnetic thermoseeds.

## 8 General conclusions and future direction

This thesis has utilised magnetic particles to develop two different minimally invasive technologies: one for the precise stimulation of a discrete region of cells (in this case astrocytes) and other as a minimally invasive ablation therapy. In each case, both the external magnetic source and the magnetic particles have been carefully chosen to fulfil the specific requirements for that application. For astrocyte stimulation, the particles needed to be in the nanometre to micron range so that individual astrocytes could be targeted. At this size range, commercially available particles were identified that had the highest magnetic content to maximise the amount of magnetic force that could be applied to them. While chapter 4 uses a magnet designed to generate a uniform magnetic force across a whole population of cells (for an accurate measure of the stimulation threshold), the magnet designed in chapter 5 was designed to maximise the magnetic force across a volume that would cover the head of a small animal. This ability to generate the forces required over distances of centimetres still remains the greatest challenge for magnetic particle applications.

With this in mind, an MRI scanner was chosen for the development of the ablation therapy MINIMA for two main reasons: the magnetic field gradients span across the whole body and allows for real time localisation of the particle. With preclinical MRI scanners limited to gradients of  $< 500$  mT/m (clinical MRI scanners  $< 80$  mT/m), the size of the particle needed to be far larger and contain a great deal more magnetic content than the nanoparticles used for stimulation. With chrome steel having one of the highest magnetic saturation points of any known material (apart from a few rare earth metal compounds such as samarium cobalt<sup>327</sup>) the only option for increasing the force is to increase particle size. However with the limited imaging volume in preclinical MRI scanners, the particle was limited to a diameter of 3 mm in order to obtain images as the particle would cause magnetic field distortions greater than the imaging volume. Moving to clinical MRI scanners would allow for the use of larger particles, but would require custom built gradient coils to reach the same strengths, which in itself is an engineering challenge.

Both applications are limited by the forces available. For small animal stimulation, the magnetic mangle should be re-evaluated. For there to be no field, a permanent magnet arrangement would need to be retractable. While the fields from electromagnets can be turned off and on, they struggle to generate the same field strengths as permanent magnets. There is also the option of using the fringe field of an MRI scanner where the field gradients are steepest. Practically speaking, the 500 nm particles used in chapter 5 are the largest particles that should be considered, at this size the particles were prone to blockages in the syringe during injection. While *In vivo* stimulation was

observed with the SiMAG particles, it would be worth investigating alternative particles that allow for the maximum number of particles to attach to each astrocyte and spread evenly within the injection site region. Determination of whether the particles are binding specifically to astrocytes in the brain could also be identified with extensive immunostaining studies. Along with an improved magnet design, such optimisation would increase the chances and reliability of the stimulation of discrete brain regions using this magnetic particle technique.

Limitations that arose from the restricted imaging volume of the current MINIMA setup would be overcome via translation of the technique to a clinical MRI scanner. The increased imaging volume would allow for the cross correlation detection technique to be used, much like the detection method used by Martel et al<sup>208,244</sup>. The increased imaging volume would also facilitate the ability to both navigate and ablate during the same scan; currently it is not possible to fit the heating coil inside the 39 mm RF volume coil used for imaging. Again however, generating the same magnetic field gradients over a larger volume would be technically challenging. Moreover, integrating both the bespoke propulsion gradients and heating coil with an existing MRI setup poses another challenge, though integrated MRI-HIFU systems such as Sonalleve (Philips®) gives promise that an “all-in-one” system could be designed.

Another limitation of the current study is the use of healthy brain tissue for both navigation and ablation. For MINIMA to be used as a cancer therapy, both navigation and ablation should be tested in appropriate tumour models as the difference in macro and microenvironment are likely to impact the performance of both movement and heating. Investigations using subcutaneous tumour mouse models are currently underway to investigate reduction in tumour volume after ablation, while glioma animal models would also be worthwhile. As brain tissue has the lowest elastic modulus of biological tissue, using MINIMA in any other tissue would require more force. For further work in the brain, it would be useful to apply diffusion tensor imaging (DTI) to *ex vivo* tissue samples to understand whether the orientation of white matter tracts affects the direction and distance moved by the particle.

Safe insertion and removal of the magnetic bead also poses a serious challenge. Once the bead is within the imaging region where the field is homogenous it experiences no net force, but when moving from outside the scanner to this region the large changes in magnetic field generate forces on the bead far greater than that used for navigation. To avoid a potential calamity, one option is to use a form of introducer that can be positioned by a surgeon outside the scanner which holds the bead in place when the patient goes in such as that used by Martels group<sup>208</sup>. The alternative option is to bring the magnetic field down to only a few millitesla when the patient is brought into and out of

the scanner. Cryogen free MRI machines such as those produced by MR solutions® not only have this ability but are able to change between effectively zero field to 3 tesla in under 10 minutes, making this a genuinely viable option. Unfortunately the only cryogen free scanners commercially available are for pre-clinical use, but with worldwide Helium resources depleting and a universal push for greater energy efficiency there may just be a gap in the market for a rampable MINIMA dedicated MRI machine.

For any promising new therapy or technology, without a “clinical pull” or a clear throughput strategy from benchtop to hospital bed, clinical translation is incredibly difficult. While the nanoparticle mediated mechanical stimulation technology developed in chapters 4 and 5 has advantages over existing technologies such as optogenetics, in that cells are not genetically altered, the lack of clinical pull will likely limit this technique to being a pure investigative scientific tool. While there is a clear clinical need for improving the treatment of brain tumours, the difficulties of taking MINIMA into the clinic are clear to see. Considering the lengths that went into developing the Connectome™ scanner, which has the strongest clinical gradients at present; the time, effort and costs that would be needed to develop a bespoke propulsion gradient set and ablation coil would be considerable. An increased focus on interdisciplinary practice should help make the clinical translation mountain a little easier to climb. If future work shows the same promise as the results shown in this thesis; clinicians, engineers, scientists, technology companies and the general public may feel it’s worth the effort.

## References

1. Deisseroth, K. Optogenetics. *Nat. Methods* **8**, 26–29 (2011).
2. Broca, P. Sur le siège de la faculté du langage articulé. *Bull. Mém. Société Anthropol. Paris* **6**, 377–393 (1865).
3. Munk, H. Of the visual area of the cerebral cortex, and its relation to eye movements. *Brain* **13**, 45–70 (1890).
4. Penfield, W. & Boldrey, E. Somatic motor and sensory representation in the cerebral cortex of man as studied by electrical stimulation. *Brain* **60**, 389–443 (1937).
5. Thomas, R. K. & Young, C. D. A Note on the Early History of Electrical Stimulation of the Human Brain. *J. Gen. Psychol.* **120**, 73–81 (1993).
6. Bartholow, R. ART. I.—Experimental Investigations into the Functions of the Human Brain. *Am. J. Med. Sci. 1827-1924* 305 (1874).
7. Pogliano, C. Penfield’s homunculus and other grotesque creatures from the Land of If. *Nuncius* **27**, 141–162 (2012).
8. Broca, P. Comparative anatomy of the cerebral convolutions: The great limbic lobe and the limbic fissure in the mammalian series. *J. Comp. Neurol.* **523**, 2501–2554 (2015).
9. Brindley, G. S. & Lewin, W. S. The sensations produced by electrical stimulation of the visual cortex. *J. Physiol.* **196**, 479–493 (1968).
10. Salzman, C. D., Murasugi, C. M., Britten, K. H. & Newsome, W. T. Microstimulation in visual area MT: effects on direction discrimination performance. *J. Neurosci. Off. J. Soc. Neurosci.* **12**, 2331–2355 (1992).
11. Histed, M. H., Ni, A. M. & Maunsell, J. H. R. Insights into cortical mechanisms of behavior from microstimulation experiments. *Prog. Neurobiol.* **103**, 115–130 (2013).
12. Pahwa, R., Wilkinson, S. B., Overman, J. & Lyons, K. E. Bilateral subthalamic stimulation in patients with Parkinson disease: long-term follow up. *J. Neurosurg.* **99**, 71–77 (2003).
13. Rehnborn, S. *et al.* Long-term efficacy of thalamic deep brain stimulation for tremor: Double-blind assessments. *Mov. Disord.* **18**, 163–170 (2003).

14. Abelson, J. L. *et al.* Deep brain stimulation for refractory obsessive-compulsive disorder. *Biol. Psychiatry* **57**, 510–516 (2005).
15. Loher, T. J. *et al.* Deep brain stimulation for dystonia: outcome at long-term follow-up. *J. Neurol.* **255**, 881–884 (2008).
16. Vonck, K. *et al.* A decade of experience with deep brain stimulation for patients with refractory medial temporal lobe epilepsy. *Int. J. Neural Syst.* **23**, 1250034 (2012).
17. Abreu, V. *et al.* Thalamic Deep Brain Stimulation for Neuropathic Pain: Efficacy at Three Years' Follow-Up. *Neuromodulation J. Int. Neuromodulation Soc.* **20**, 504–513 (2017).
18. Aum, D. J. & Tierney, T. S. Deep brain stimulation: foundations and future trends. *Front. Biosci. Landmark Ed.* **23**, 162–182 (2018).
19. Oh, M. Y., Abosch, A., Kim, S. H., Lang, A. E. & Lozano, A. M. Long-term hardware-related complications of deep brain stimulation. *Neurosurgery* **50**, 1268–1274; discussion 1274–1276 (2002).
20. Pepper, J. *et al.* The Risk of Hardware Infection in Deep Brain Stimulation Surgery Is Greater at Impulse Generator Replacement than at the Primary Procedure. *Stereotact. Funct. Neurosurg.* **91**, 56–65 (2013).
21. Zrinzo, L., Foltynie, T., Limousin, P. & Hariz, M. I. Reducing hemorrhagic complications in functional neurosurgery: a large case series and systematic literature review: Clinical article. *J. Neurosurg.* **116**, 84–94 (2012).
22. Method of the Year 2010. *Nat. Methods* **8**, 1 (2011).
23. Zemelman, B. V., Lee, G. A., Ng, M. & Miesenböck, G. Selective Photostimulation of Genetically ChARGed Neurons. *Neuron* **33**, 15–22 (2002).
24. Boyden, E. S., Zhang, F., Bamberg, E., Nagel, G. & Deisseroth, K. Millisecond-timescale, genetically targeted optical control of neural activity. *Nat. Neurosci.* **8**, 1263–1268 (2005).
25. Gradinaru, V., Thompson, K. R. & Deisseroth, K. eNpHR: a *Natronomonas* halorhodopsin enhanced for optogenetic applications. *Brain Cell Biol.* **36**, 129–139 (2008).
26. Zhang, F. *et al.* Optogenetic interrogation of neural circuits: technology for probing mammalian brain structures. *Nat. Protoc.* **5**, 439–456 (2010).
27. Arenkiel, B. R. *et al.* In vivo light-induced activation of neural circuitry in transgenic mice expressing channelrhodopsin-2. *Neuron* **54**, 205–218 (2007).



28. Hägglund, M., Borgius, L., Dougherty, K. J. & Kiehn, O. Activation of groups of excitatory neurons in the mammalian spinal cord or hindbrain evokes locomotion. *Nat. Neurosci.* **13**, 246–252 (2010).
29. Kätzel, D., Zemelman, B. V., Buetfering, C., Wölfel, M. & Miesenböck, G. The columnar and laminar organization of inhibitory connections to neocortical excitatory cells. *Nat. Neurosci.* **14**, 100–107 (2011).
30. Fenno, L., Yizhar, O. & Deisseroth, K. The Development and Application of Optogenetics. *Annu. Rev. Neurosci.* **34**, 389–412 (2011).
31. Iwai, Y., Honda, S., Ozeki, H., Hashimoto, M. & Hirase, H. A simple head-mountable LED device for chronic stimulation of optogenetic molecules in freely moving mice. *Neurosci. Res.* **70**, 124–127 (2011).
32. Wentz, C. T. *et al.* A wirelessly powered and controlled device for optical neural control of freely-behaving animals. *J. Neural Eng.* **8**, 046021 (2011).
33. Shin, G. *et al.* Flexible Near-Field Wireless Optoelectronics as Subdermal Implants for Broad Applications in Optogenetics. *Neuron* **93**, 509-521.e3 (2017).
34. Cardin, J. A. Dissecting local circuits in vivo: integrated optogenetic and electrophysiology approaches for exploring inhibitory regulation of cortical activity. *J. Physiol. Paris* **106**, 104–111 (2012).
35. Masamoto, K. *et al.* Unveiling astrocytic control of cerebral blood flow with optogenetics. *Sci. Rep.* **5**, 11455 (2015).
36. Gourine, A. V. *et al.* Astrocytes Control Breathing Through pH-Dependent Release of ATP. *Science* **329**, 571–575 (2010).
37. Halassa, M. M. *et al.* Astrocytic Modulation of Sleep Homeostasis and Cognitive Consequences of Sleep Loss. *Neuron* **61**, 213–219 (2009).
38. Pelluru, D., Konadhode, R. R., Bhat, N. R. & Shiromani, P. J. Optogenetic stimulation of astrocytes in the posterior hypothalamus increases sleep at night in C57BL/6J mice. *Eur. J. Neurosci.* **43**, 1298–1306 (2016).
39. Nam, Y. *et al.* Reversible Induction of Pain Hypersensitivity following Optogenetic Stimulation of Spinal Astrocytes. *Cell Rep.* **17**, 3049–3061 (2016).

40. Sweeney, P., Qi, Y., Xu, Z. & Yang, Y. Activation of hypothalamic astrocytes suppresses feeding without altering emotional states. *Glia* **64**, 2263–2273 (2016).
41. Busskamp, V., Picaud, S., Sahel, J. A. & Roska, B. Optogenetic therapy for retinitis pigmentosa. *Gene Ther.* **19**, 169–175 (2012).
42. Swiersy, A., Klapper, S. D. & Busskamp, V. [Optogenetics: A Therapeutic Option for Advanced Retinal Dystrophies]. *Klin. Monatsbl. Augenheilkd.* **234**, 335–342 (2017).
43. Jiang, C. *et al.* Cardiac optogenetics: a novel approach to cardiovascular disease therapy. *Eur. Pacing Arrhythm. Card. Electrophysiol. J. Work. Groups Card. Pacing Arrhythm. Card. Cell. Electrophysiol. Eur. Soc. Cardiol.* **20**, 1741–1749 (2018).
44. Nussinovitch, U. & Gepstein, L. Optogenetics for in vivo cardiac pacing and resynchronization therapies. *Nat. Biotechnol.* **33**, 750–754 (2015).
45. Yu, L. *et al.* Optogenetic Modulation of Cardiac Sympathetic Nerve Activity to Prevent Ventricular Arrhythmias. *J. Am. Coll. Cardiol.* **70**, 2778–2790 (2017).
46. Machhada, A. *et al.* Vagal determinants of exercise capacity. *Nat. Commun.* **8**, 15097 (2017).
47. Tønnesen, J. & Kokaia, M. Epilepsy and optogenetics: can seizures be controlled by light? *Clin. Sci. Lond. Engl. 1979* **131**, 1605–1616 (2017).
48. Richardson, R. T., Thompson, A. C., Wise, A. K. & Needham, K. Challenges for the application of optical stimulation in the cochlea for the study and treatment of hearing loss. *Expert Opin. Biol. Ther.* **17**, 213–223 (2017).
49. Wahl, A. S. *et al.* Optogenetically stimulating intact rat corticospinal tract post-stroke restores motor control through regionalized functional circuit formation. *Nat. Commun.* **8**, 1187 (2017).
50. Chuong, A. S. *et al.* Noninvasive optical inhibition with a red-shifted microbial rhodopsin. *Nat. Neurosci.* **17**, 1123–1129 (2014).
51. Wang, N., Butler, J. P. & Ingber, D. E. Mechanotransduction across the cell surface and through the cytoskeleton. *Science* **260**, 1124–1127 (1993).
52. Dhaka, A., Viswanath, V. & Patapoutian, A. Trp ion channels and temperature sensation. *Annu. Rev. Neurosci.* **29**, 135–161 (2006).

53. Kohatsu, S., Koganezawa, M. & Yamamoto, D. Female contact activates male-specific interneurons that trigger stereotypic courtship behavior in *Drosophila*. *Neuron* **69**, 498–508 (2011).
54. von Philipsborn, A. C. *et al.* Neuronal control of *Drosophila* courtship song. *Neuron* **69**, 509–522 (2011).
55. Ermakova, Y. G. *et al.* Thermogenetic neurostimulation with single-cell resolution. *Nat. Commun.* **8**, 15362 (2017).
56. Hirsch, S. M. *et al.* FLIRT: fast local infrared thermogenetics for subcellular control of protein function. *Nat. Methods* **15**, 921 (2018).
57. Huang, H., Delikanli, S., Zeng, H., Ferkey, D. M. & Pralle, A. Remote control of ion channels and neurons through magnetic-field heating of nanoparticles. *Nat. Nanotechnol.* **5**, 602 (2010).
58. Stanley, S. A. *et al.* Radio-wave heating of iron oxide nanoparticles can regulate plasma glucose in mice. *Science* **336**, 604–608 (2012).
59. Stanley, S. A. *et al.* Bidirectional electromagnetic control of the hypothalamus regulates feeding and metabolism. *Nature* **531**, 647–650 (2016).
60. Chen, R., Romero, G., Christiansen, M. G., Mohr, A. & Anikeeva, P. Wireless magnetothermal deep brain stimulation. *Science* **347**, 1477–1480 (2015).
61. Liang, Z. *et al.* Mapping the functional network of medial prefrontal cortex by combining optogenetics and fMRI in awake rats. *NeuroImage* **117**, 114–123 (2015).
62. Christie, I. N. *et al.* fMRI response to blue light delivery in the naïve brain: implications for combined optogenetic fMRI studies. *NeuroImage* **66**, 634–641 (2013).
63. Nimpf, S. & Keays, D. A. Is magnetogenetics the new optogenetics? *EMBO J.* **36**, 1643–1646 (2017).
64. Glogauer, M., Ferrier, J. & McCulloch, C. A. Magnetic fields applied to collagen-coated ferric oxide beads induce stretch-activated Ca<sup>2+</sup> flux in fibroblasts. *Am. J. Physiol.-Cell Physiol.* **269**, C1093–C1104 (1995).
65. Kirkham, G. R. *et al.* Hyperpolarization of Human Mesenchymal Stem Cells in Response to Magnetic Force. *IEEE Trans. NanoBioscience* **9**, 71–74 (2010).
66. Niggel, J., Sigurdson, W. & Sachs, F. Mechanically Induced Calcium Movements in Astrocytes, Bovine Aortic Endothelial Cells and C6 Glioma Cells. *J. Membr. Biol.* **174**, 121–134 (2000).

67. Chen, J., Fabry, B., Schiffrin, E. L. & Wang, N. Twisting integrin receptors increases endothelin-1 gene expression in endothelial cells. *Am. J. Physiol. Cell Physiol.* **280**, C1475-1484 (2001).
68. Goldschmidt, M. E., McLeod, K. J. & Taylor, W. R. Integrin-Mediated Mechanotransduction in Vascular Smooth Muscle Cells: Frequency and Force Response Characteristics. *Circ. Res.* **88**, 674–680 (2001).
69. Oliet, S. H. R. & Bourque, C. Mechanosensitive channels transduce osmosensitivity in supraoptic neurons. *Nature* **364**, 341 (1993).
70. Glogauer, M. & Ferrier, J. A new method for application of force to cells via ferric oxide beads. *Pflüg. Arch.* **435**, 320–327 (1997).
71. Hughes, S., El Haj, A. J. & Dobson, J. Magnetic micro- and nanoparticle mediated activation of mechanosensitive ion channels. *Med. Eng. Phys.* **27**, 754–762 (2005).
72. Fass, J. N. & Odde, D. J. Tensile Force-Dependent Neurite Elicitation via Anti- $\beta$ 1 Integrin Antibody-Coated Magnetic Beads. *Biophys. J.* **85**, 623–636 (2003).
73. Hynes, R. O. Integrins: bidirectional, allosteric signaling machines. *Cell* **110**, 673–687 (2002).
74. Hughes, S., Dobson, J. & El Haj, A. J. Magnetic targeting of mechanosensors in bone cells for tissue engineering applications. *J. Biomech.* **40 Suppl 1**, S96-104 (2007).
75. Pommerenke, H. *et al.* Stimulation of integrin receptors using a magnetic drag force device induces an intracellular free calcium response. *Eur. J. Cell Biol.* **70**, 157–164 (1996).
76. Meyer, C. J. *et al.* Mechanical control of cyclic AMP signalling and gene transcription through integrins. *Nat. Cell Biol.* **2**, 666–668 (2000).
77. Na, S. *et al.* Rapid signal transduction in living cells is a unique feature of mechanotransduction. *Proc. Natl. Acad. Sci. U. S. A.* **105**, 6626–6631 (2008).
78. Matthews, B. D., Overby, D. R., Mannix, R. & Ingber, D. E. Cellular adaptation to mechanical stress: role of integrins, Rho, cytoskeletal tension and mechanosensitive ion channels. *J. Cell Sci.* **119**, 508–518 (2006).
79. Tay, A., Kunze, A., Murray, C. & Di Carlo, D. Induction of Calcium Influx in Cortical Neural Networks by Nanomagnetic Forces. *ACS Nano* **10**, 2331–2341 (2016).

80. Tay, A. & Di Carlo, D. Magnetic Nanoparticle-Based Mechanical Stimulation for Restoration of Mechano-Sensitive Ion Channel Equilibrium in Neural Networks. *Nano Lett.* **17**, 886–892 (2017).
81. Dobson, J. Remote control of cellular behaviour with magnetic nanoparticles. *Nat. Nanotechnol.* **3**, 139–143 (2008).
82. Hughes, S., McBain, S., Dobson, J. & El Haj, A. J. Selective activation of mechanosensitive ion channels using magnetic particles. *J. R. Soc. Interface* **5**, 855–863 (2008).
83. Kanczler, J. M. *et al.* Controlled differentiation of human bone marrow stromal cells using magnetic nanoparticle technology. *Tissue Eng. Part A* **16**, 3241–3250 (2010).
84. Stanley, S. A., Sauer, J., Kane, R. S., Dordick, J. S. & Friedman, J. M. Remote regulation of glucose homeostasis in mice using genetically encoded nanoparticles. *Nat. Med.* **21**, 92–98 (2015).
85. Qin, S. *et al.* A magnetic protein biocompass. *Nat. Mater.* **15**, 217–226 (2016).
86. Long, X., Ye, J., Zhao, D. & Zhang, S.-J. Magnetogenetics: remote non-invasive magnetic activation of neuronal activity with a magnetoreceptor. *Sci. Bull.* **60**, 2107–2119 (2015).
87. Cyranoski, D. Chinese scientists row over long-sought protein that senses magnetism. *Nat. News* (2015) doi:10.1038/nature.2015.18397.
88. Pang, K. *et al.* MagR Alone Is Insufficient to Confer Cellular Calcium Responses to Magnetic Stimulation. *Front. Neural Circuits* **11**, 11 (2017).
89. Meister, M. Physical limits to magnetogenetics. *eLife* **5**, (2016).
90. Cao, E., Cordero-Morales, J. F., Liu, B., Qin, F. & Julius, D. TRPV1 Channels Are Intrinsically Heat Sensitive and Negatively Regulated by Phosphoinositide Lipids. *Neuron* **77**, 667–679 (2013).
91. Brain, other CNS and intracranial tumours statistics. *Cancer Research UK* <https://www.cancerresearchuk.org/health-professional/cancer-statistics/statistics-by-cancer-type/brain-other-cns-and-intracranial-tumours> (2015).
92. Quaresma, M., Coleman, M. P. & Rachet, B. 40-year trends in an index of survival for all cancers combined and survival adjusted for age and sex for each cancer in England and Wales, 1971-2011: a population-based study. *Lancet Lond. Engl.* **385**, 1206–1218 (2015).
93. Cortnum, S. & Laursen, R. J. Fluorescence-guided resection of gliomas. *Dan. Med. J.* **59**, A4460 (2012).

94. Díez Valle, R. *et al.* Observational, retrospective study of the effectiveness of 5-aminolevulinic acid in malignant glioma surgery in Spain (The VISIONA study). *Neurol. Barc. Spain* **29**, 131–138 (2014).
95. Stupp, R. *et al.* Radiotherapy plus concomitant and adjuvant temozolomide for glioblastoma. *N. Engl. J. Med.* **352**, 987–996 (2005).
96. Fernandes, C. *et al.* Current Standards of Care in Glioblastoma Therapy. in *Glioblastoma* (ed. De Vleeschouwer, S.) (Codon Publications, 2017).
97. Nabors, L. B. *et al.* Central Nervous System Cancers, Version 1.2015. *J. Natl. Compr. Canc. Netw.* **13**, 1191–1202 (2015).
98. Ferrer, V. P., Moura Neto, V. & Mentlein, R. Glioma infiltration and extracellular matrix: key players and modulators. *Glia* **66**, 1542–1565 (2018).
99. D’Amico, R. S., Englander, Z. K., Canoll, P. & Bruce, J. N. Extent of Resection in Glioma—A Review of the Cutting Edge. *World Neurosurg.* **103**, 538–549 (2017).
100. Oppenlander, M. E. *et al.* An extent of resection threshold for recurrent glioblastoma and its risk for neurological morbidity: Clinical article. *J. Neurosurg.* **120**, 846–853 (2014).
101. Pope, W. B. *et al.* MR Imaging Correlates of Survival in Patients with High-Grade Gliomas. *Am. J. Neuroradiol.* **26**, 2466–2474 (2005).
102. Bianco, J. *et al.* On glioblastoma and the search for a cure: where do we stand? *Cell. Mol. Life Sci. CMLS* **74**, 2451–2466 (2017).
103. Mahvash, M., Boettcher, I., Petridis, A. K. & Besharati Tabrizi, L. Image guided surgery versus conventional brain tumor and craniotomy localization. *J. Neurosurg. Sci.* **61**, 8–13 (2017).
104. Saito, T. *et al.* Neurophysiological Monitoring and Awake Craniotomy for Resection of Intracranial Gliomas. *Prog. Neurol. Surg.* **30**, 117–158 (2018).
105. Minniti, G. *et al.* Fractionated stereotactic conformal radiotherapy for large benign skull base meningiomas. *Radiat. Oncol.* **6**, 36 (2011).
106. Gilbert, M. R. *et al.* Dose-Dense Temozolomide for Newly Diagnosed Glioblastoma: A Randomized Phase III Clinical Trial. *J. Clin. Oncol.* **31**, 4085–4091 (2013).
107. Patel, M. M. & Patel, B. M. Crossing the Blood-Brain Barrier: Recent Advances in Drug Delivery to the Brain. *CNS Drugs* **31**, 109–133 (2017).

108. Lu, C.-Y., Chen, X.-L., Chen, X.-L., Fang, X.-J. & Zhao, Y.-L. Clinical application of 3.0 T intraoperative magnetic resonance combined with multimodal neuronavigation in resection of cerebral eloquent area glioma. *Medicine (Baltimore)* **97**, (2018).
109. Fahlbusch, R. & Samii, A. Editorial: Intraoperative MRI. *Neurosurg. Focus* **40**, E3 (2016).
110. Nimsy, C., Fujita, A., Ganslandt, O., Von Keller, B. & Fahlbusch, R. Volumetric assessment of glioma removal by intraoperative high-field magnetic resonance imaging. *Neurosurgery* **55**, 358–370; discussion 370-371 (2004).
111. Dewhirst, M. W., Viglianti, B. L., Lora-Michiels, M., Hanson, M. & Hoopes, P. J. Basic principles of thermal dosimetry and thermal thresholds for tissue damage from hyperthermia. *Int. J. Hyperth. Off. J. Eur. Soc. Hyperthermic Oncol. North Am. Hyperth. Group* **19**, 267–294 (2003).
112. Rhoon, G. C. van. Is CEM43 still a relevant thermal dose parameter for hyperthermia treatment monitoring? *Int. J. Hyperthermia* **32**, 50–62 (2016).
113. Lindquist, C. Gamma Knife Surgery: Evolution and Long-Term Results. in *Radiosurgery* (ed. Kondziolka, D.) vol. 3 1–12 (KARGER, 1999).
114. Asgari, S., Banaee, N. & Nedaie, H. A. Comparison of full width at half maximum and penumbra of different Gamma Knife models. *J. Cancer Res. Ther.* **14**, 260–266 (2018).
115. Chang, S. D., Main, W., Martin, D. P., Gibbs, I. C. & Heilbrun, M. P. An analysis of the accuracy of the CyberKnife: a robotic frameless stereotactic radiosurgical system. *Neurosurgery* **52**, 140–146; discussion 146-147 (2003).
116. Feygelman, V., Lohr, F. & Orton, C. G. The future of MRI in radiation therapy belongs to integrated MRI-linac systems, not the standalone MRI-Sim. *Med. Phys.* **44**, 791–794 (2017).
117. Whelan, B. *et al.* A novel electron accelerator for MRI-Linac radiotherapy. *Med. Phys.* **43**, 1285–1294 (2016).
118. Sinclair, G. *et al.* Adaptive hypofractionated gamma knife radiosurgery in the acute management of large thymic carcinoma brain metastases. *Surg. Neurol. Int.* **8**, 95 (2017).
119. Hasegawa, T. *et al.* Multisession gamma knife surgery for large brain metastases. *J. Neurooncol.* **131**, 517–524 (2017).
120. Brezovich, I. A. *et al.* End-to-end test of spatial accuracy in Gamma Knife treatments for trigeminal neuralgia. *Med. Phys.* **41**, 111703 (2014).

121. Arslan, I. *et al.* Gamma Knife Radiosurgery for Arteriovenous Malformations: Clinical Series of 199 Patients. *Turk. Neurosurg.* **27**, 301–308 (2017).
122. Dmytriw, A. A. *et al.* Gamma Knife radiosurgery for the treatment of intracranial dural arteriovenous fistulas. *Interv. Neuroradiol. J. Peritherapeutic Neuroradiol. Surg. Proced. Relat. Neurosci.* **23**, 211–220 (2017).
123. McGonigal, A. *et al.* Radiosurgery for epilepsy: Systematic review and International Stereotactic Radiosurgery Society (ISRS) practice guideline. *Epilepsy Res.* **137**, 123–131 (2017).
124. Higuchi, Y., Matsuda, S. & Serizawa, T. Gamma knife radiosurgery in movement disorders: Indications and limitations. *Mov. Disord. Off. J. Mov. Disord. Soc.* **32**, 28–35 (2017).
125. Hatiboglu, M. A., Tuzgen, S., Akdur, K. & Chang, E. L. Treatment of high numbers of brain metastases with Gamma Knife radiosurgery: a review. *Acta Neurochir. (Wien)* **158**, 625–634 (2016).
126. Brain stereotactic radiosurgery - Mayo Clinic. <https://www.mayoclinic.org/tests-procedures/brain-stereotactic-radiosurgery/about/pac-20384679>.
127. Ashkan, K., Lavrador, J. P. & Bhangoo, R. Visualase - An alternative approach to both old and new problems in Neuro-Oncology. *Semin. Oncol.* (2018) doi:10.1053/j.seminoncol.2018.12.001.
128. Hoppe, C. *et al.* Laser interstitial thermotherapy (LiTT) in epilepsy surgery. *Seizure* **48**, 45–52 (2017).
129. Patel, N. V. *et al.* Laser Interstitial Thermal Therapy Technology, Physics of Magnetic Resonance Imaging Thermometry, and Technical Considerations for Proper Catheter Placement During Magnetic Resonance Imaging-Guided Laser Interstitial Thermal Therapy. *Neurosurgery* **79 Suppl 1**, S8–S16 (2016).
130. Attaar, S. J., Patel, N. V., Hargreaves, E., Keller, I. A. & Danish, S. F. Accuracy of Laser Placement With Frameless Stereotaxy in Magnetic Resonance-Guided Laser-Induced Thermal Therapy. *Oper. Neurosurg. Hagerstown Md* **11**, 554–563 (2015).
131. Medvid, R. *et al.* Current Applications of MRI-Guided Laser Interstitial Thermal Therapy in the Treatment of Brain Neoplasms and Epilepsy: A Radiologic and Neurosurgical Overview. *Am. J. Neuroradiol.* **36**, 1998–2006 (2015).
132. Tovar-Spinoza, Z., Carter, D., Ferrone, D., Eksioglu, Y. & Huckins, S. The use of MRI-guided laser-induced thermal ablation for epilepsy. *Childs Nerv. Syst.* **29**, 2089–2094 (2013).



133. Bandt, S. K. & Leuthardt, E. C. Minimally Invasive Neurosurgery for Epilepsy Using Stereotactic MRI Guidance. *Neurosurg. Clin.* **27**, 51–58 (2016).
134. LaRiviere, M. J. & Gross, R. E. Stereotactic Laser Ablation for Medically Intractable Epilepsy: The Next Generation of Minimally Invasive Epilepsy Surgery. *Front. Surg.* **3**, 64 (2016).
135. Pruitt, R., Gamble, A., Black, K., Schulder, M. & Mehta, A. D. Complication avoidance in laser interstitial thermal therapy: lessons learned. *J. Neurosurg.* **126**, 1238–1245 (2017).
136. Jenne, J. W. Non-invasive transcranial brain ablation with high-intensity focused ultrasound. *Front. Neurol. Neurosci.* **36**, 94–105 (2015).
137. Lipsman, N. *et al.* MR-guided focused ultrasound thalamotomy for essential tremor: a proof-of-concept study. *Lancet Neurol.* **12**, 462–468 (2013).
138. Martínez-Fernández, R. *et al.* Focused ultrasound subthalamotomy in patients with asymmetric Parkinson's disease: a pilot study. *Lancet Neurol.* **17**, 54–63 (2018).
139. Kim, M., Kim, C.-H., Jung, H. H., Kim, S. J. & Chang, J. W. Treatment of Major Depressive Disorder via Magnetic Resonance-Guided Focused Ultrasound Surgery. *Biol. Psychiatry* **83**, e17–e18 (2018).
140. Hersh, D. S. & Eisenberg, H. M. Current and future uses of transcranial focused ultrasound in neurosurgery. *J. Neurosurg. Sci.* **62**, 203–213 (2018).
141. Moser, D., Zadicario, E., Schiff, G. & Jeanmonod, D. Measurement of targeting accuracy in focused ultrasound functional neurosurgery. *Neurosurg. Focus* **32**, E2 (2012).
142. Martin, E. & Werner, B. Focused Ultrasound Surgery of the Brain. *Curr. Radiol. Rep.* **1**, 126–135 (2013).
143. Hong, K. & Georgiades, C. Radiofrequency ablation: mechanism of action and devices. *J. Vasc. Interv. Radiol. JVIR* **21**, S179–186 (2010).
144. Voges, J., Buntjen, L. & Schmitt, F. C. Radiofrequency-thermoablation: General principle, historical overview and modern applications for epilepsy. *Epilepsy Res.* **142**, 113–116 (2018).
145. Meijerink, M. R. *et al.* Radiofrequency ablation of large size liver tumours using novel plan-parallel expandable bipolar electrodes: initial clinical experience. *Eur. J. Radiol.* **77**, 167–171 (2011).
146. Yi, B., Somasundar, P. & Espat, N. J. Novel laparoscopic bipolar radiofrequency energy technology for expedited hepatic tumour ablation. *HPB* **11**, 135–139 (2009).

147. LEVEEN, RF. Laser hyperthermia and radiofrequency ablation of hepatic lesions. *Sem Interv. Radiol* **14**, 313–324 (1997).
148. Shah, T. T. *et al.* Focal cryotherapy of localized prostate cancer: a systematic review of the literature. *Expert Rev. Anticancer Ther.* **14**, 1337–1347 (2014).
149. Gage, A. A. & Baust, J. Mechanisms of tissue injury in cryosurgery. *Cryobiology* **37**, 171–186 (1998).
150. Gage, A. A., Guest, K., Montes, M., Caruana, J. A. & Whalen, D. A. Effect of varying freezing and thawing rates in experimental cryosurgery. *Cryobiology* **22**, 175–182 (1985).
151. Cowan, B. D., Sewell, P. E., Howard, J. C., Arriola, R. M. & Robinette, L. G. Interventional magnetic resonance imaging cryotherapy of uterine fibroid tumors: Preliminary observation. *Am. J. Obstet. Gynecol.* **186**, 1183–1187 (2002).
152. Baeza, A., Arcos, D. & Vallet-Regí, M. Thermoseeds for interstitial magnetic hyperthermia: from bioceramics to nanoparticles. *J. Phys. Condens. Matter* **25**, 484003 (2013).
153. Tompkins, D. T., Partington, B. P., Steeves, R. A., Bartholow, S. D. & Paliwal, B. R. Effect of implant variables on temperatures achieved during ferromagnetic hyperthermia. *Int. J. Hyperth. Off. J. Eur. Soc. Hyperthermic Oncol. North Am. Hyperth. Group* **8**, 241–251 (1992).
154. Brezovich, I. A. & Meredith, R. F. Practical aspects of ferromagnetic thermoseed hyperthermia. *Radiol. Clin. North Am.* **27**, 589–602 (1989).
155. Brezovich, I. A. *et al.* Hyperthermia of pet animal tumours with self-regulating ferromagnetic thermoseeds. *Int. J. Hyperth. Off. J. Eur. Soc. Hyperthermic Oncol. North Am. Hyperth. Group* **6**, 117–130 (1990).
156. Burton, C., Hill, M. & Walker, A. E. The RF Thermoseed-A Thermally Self-Regulating Implant for the Production of Brain Lesions. *IEEE Trans. Biomed. Eng.* **BME-18**, 104–109 (1971).
157. Tucker, R. D. Use of Interstitial Temperature Self-Regulating Thermal Rods in the Treatment of Prostate Cancer. *J. Endourol.* **17**, 601–607 (2003).
158. Park, B. H., Koo, B. S., Kim, Y. K. & Kim, M. K. The Induction of Hyperthermia in Rabbit Liver by means of Duplex Stainless Steel Thermoseeds. in *Korean journal of radiology* (2002).
159. Geng, Y.-C., Wang, X.-X., Ma, Y., Hu, Y. & Zhang, R.-L. Orientated thermotherapy of ferromagnetic thermoseed in hepatic tumors. *World J. Gastroenterol.* **4**, 326–328 (1998).

160. Ouyang, W. *et al.* Thermoseed hyperthermia treatment of mammary orthotopic transplantation tumors in rats and impact on immune function. *Oncol. Rep.* **24**, 973–979 (2010).
161. Abe, K., Shiozawa, N. & Makikawa, M. Hyperthermia system with thermoseed set in abdominal cavity and AC-magnetic-field. *Conf. Proc. Annu. Int. Conf. IEEE Eng. Med. Biol. Soc. IEEE Eng. Med. Biol. Soc. Annu. Conf.* **2007**, 1483–1486 (2007).
162. Matsumoto, M., Yoshimura, N., Honda, Y., Hiraoka, M. & Ohura, K. Ferromagnetic hyperthermia in rabbit eyes using a new glass-ceramic thermoseed. *Graefes Arch. Clin. Exp. Ophthalmol. Albrecht Von Graefes Arch. Klin. Exp. Ophthalmol.* **232**, 176–181 (1994).
163. Deger, S. *et al.* Thermoradiotherapy using interstitial self-regulating thermoseeds: an intermediate analysis of a phase II trial. *Eur. Urol.* **45**, 574–579; discussion 580 (2004).
164. Kida, Y., Ishiguri, H., Ichimi, K. & Kobayashi, T. [Hyperthermia of metastatic brain tumor with implant heating system: a preliminary clinical results]. *No Shinkei Geka.* **18**, 521–526 (1990).
165. Grady, S. M. *et al.* Magnetic Stereotaxis: A Technique to Deliver Stereotactic Hyperthermia. *Neurosurgery* **27**, 1010–1016 (1990).
166. Grady, M. S. *et al.* Nonlinear magnetic stereotaxis: Three-dimensional, in vivo remote magnetic manipulation of a small object in canine brain. *Med. Phys.* **17**, 405–415 (1990).
167. Lim, P. C. Y. *et al.* Remote magnetic catheter navigation versus conventional ablation in atrial fibrillation ablation: Fluoroscopy reduction. *J. Arrhythmia* **33**, 167–171 (2017).
168. Pankhurst, Q. A., Connolly, J., Jones, S. K. & Dobson, J. Applications of magnetic nanoparticles in biomedicine. *J. Phys. Appl. Phys.* **36**, R167 (2003).
169. Riegler, J., Allain, B., Cook, R. J., Lythgoe, M. F. & Pankhurst, Q. A. Magnetically assisted delivery of cells using a magnetic resonance imaging system. *J. Phys. Appl. Phys.* **44**, 055001 (2011).
170. Yu, W. *et al.* Occurrence of Bruise, Hematoma, and Pain in Upper Blepharoplasty Using Blunt-Needle vs Sharp-Needle Anesthetic Injection in Upper Blepharoplasty: A Randomized Clinical Trial. *JAMA Facial Plast. Surg.* **19**, 128–132 (2017).
171. Pankhurst, Q. A., Thanh, N. T. K., Jones, S. K. & Dobson, J. Progress in applications of magnetic nanoparticles in biomedicine. *J. Phys. Appl. Phys.* **42**, 224001 (2009).
172. Patrick, P. S., Pankhurst, Q. A., Payne, C., Kalber, T. L. & Lythgoe, M. F. Magnet-targeted delivery and imaging. in *Design and Applications of Nanoparticles in Biomedical Imaging* 123–152 (Springer, 2017).

173. Connell, J. J., Patrick, P. S., Yu, Y., Lythgoe, M. F. & Kalber, T. L. Advanced cell therapies: targeting, tracking and actuation of cells with magnetic particles. *Regen. Med.* **10**, 757–772 (2015).
174. Colombo, M. *et al.* Biological applications of magnetic nanoparticles. *Chem. Soc. Rev.* **41**, 4306–4334 (2012).
175. Lu, A.-H., Salabas, E. L. & Schüth, F. Magnetic Nanoparticles: Synthesis, Protection, Functionalization, and Application. *Angew. Chem. Int. Ed.* **46**, 1222–1244 (2007).
176. Grüttner, C. *et al.* Synthesis and antibody conjugation of magnetic nanoparticles with improved specific power absorption rates for alternating magnetic field cancer therapy. *J. Magn. Magn. Mater.* **311**, 181–186 (2007).
177. Veisheh, O., Gunn, J. W. & Zhang, M. Design and fabrication of magnetic nanoparticles for targeted drug delivery and imaging. *Adv. Drug Deliv. Rev.* **62**, 284–304 (2010).
178. He, J., Huang, M., Wang, D., Zhang, Z. & Li, G. Magnetic separation techniques in sample preparation for biological analysis: a review. *J. Pharm. Biomed. Anal.* **101**, 84–101 (2014).
179. Frodsham, G. & Pankhurst, Q. A. Biomedical applications of high gradient magnetic separation: progress towards therapeutic haemofiltration. *Biomed. Eng. Biomed. Tech.* **60**, 393–404 (2015).
180. Melville, D., Paul, F. & Roath, S. Direct magnetic separation of red cells from whole blood. *Nature* **255**, 706 (1975).
181. Frankel, R. B., Papaefthymiou, G. C., Blakemore, R. P. & O'Brien, W. Fe<sub>3</sub>O<sub>4</sub> precipitation in magnetotactic bacteria. *Biochim. Biophys. Acta BBA - Mol. Cell Res.* **763**, 147–159 (1983).
182. Mosayebi, J., Kiyasatfar, M. & Laurent, S. Synthesis, Functionalization, and Design of Magnetic Nanoparticles for Theranostic Applications. *Adv. Healthc. Mater.* **6**, (2017).
183. Kuhara, M., Takeyama, H., Tanaka, T. & Matsunaga, T. Magnetic Cell Separation Using Antibody Binding with Protein A Expressed on Bacterial Magnetic Particles. *Anal. Chem.* **76**, 6207–6213 (2004).
184. Bohmer, N. *et al.* Removal of Cells from Body Fluids by Magnetic Separation in Batch and Continuous Mode: Influence of Bead Size, Concentration, and Contact Time. *ACS Appl. Mater. Interfaces* **9**, 29571–29579 (2017).
185. Shields, C. W., Reyes, C. D. & López, G. P. Microfluidic cell sorting: a review of the advances in the separation of cells from debulking to rare cell isolation. *Lab. Chip* **15**, 1230–1249 (2015).

186. Zhao, M., Xie, Y., Deng, C. & Zhang, X. Recent advances in the application of core-shell structured magnetic materials for the separation and enrichment of proteins and peptides. *J. Chromatogr. A* **1357**, 182–193 (2014).
187. Berensmeier, S. Magnetic particles for the separation and purification of nucleic acids. *Appl. Microbiol. Biotechnol.* **73**, 495–504 (2006).
188. Ye, L., Wang, Q., Xu, J., Shi, Z. & Xu, L. Restricted-access nanoparticles for magnetic solid-phase extraction of steroid hormones from environmental and biological samples. *J. Chromatogr. A* **1244**, 46–54 (2012).
189. Ding, J. *et al.* Magnetic solid-phase extraction based on magnetic carbon nanotube for the determination of estrogens in milk. *J. Sep. Sci.* **34**, 2498–2504 (2011).
190. Hoyos, M., Moore, L., Williams, P. S. & Zborowski, M. The use of a linear Halbach array combined with a step-SPLITT channel for continuous sorting of magnetic species. *J. Magn. Magn. Mater.* **323**, 1384–1388 (2011).
191. Murray, C. *et al.* Quantitative Magnetic Separation of Particles and Cells Using Gradient Magnetic Ratcheting. *Small Wein. Bergstr. Ger.* **12**, 1891–1899 (2016).
192. Karande, P., Trasatti, J. P. & Chandra, D. Chapter 4 - Novel Approaches for the Delivery of Biologics to the Central Nervous System. in *Novel Approaches and Strategies for Biologics, Vaccines and Cancer Therapies* (eds. Singh, M. & Salnikova, M.) 59–88 (Academic Press, 2015). doi:10.1016/B978-0-12-416603-5.00004-3.
193. Riegler, J. *et al.* Superparamagnetic iron oxide nanoparticle targeting of MSCs in vascular injury. *Biomaterials* **34**, 1987–1994 (2013).
194. Kyrtatos, P. G. *et al.* Magnetic Tagging Increases Delivery of Circulating Progenitors in Vascular Injury. *JACC Cardiovasc. Interv.* **2**, 794–802 (2009).
195. Chertok, B. *et al.* Iron oxide nanoparticles as a drug delivery vehicle for MRI monitored magnetic targeting of brain tumors. *Biomaterials* **29**, 487–496 (2008).
196. Chertok, B., David, A. E. & Yang, V. C. Brain tumor targeting of magnetic nanoparticles for potential drug delivery: effect of administration route and magnetic field topography. *J. Control. Release Off. J. Control. Release Soc.* **155**, 393–399 (2011).
197. Al-Jamal, K. T. *et al.* Magnetic Drug Targeting: Preclinical in Vivo Studies, Mathematical Modeling, and Extrapolation to Humans. *Nano Lett.* **16**, 5652–5660 (2016).

198. Nacev, A., Beni, C., Bruno, O. & Shapiro, B. Magnetic nanoparticle transport within flowing blood and into surrounding tissue. *Nanomed.* **5**, 1459–1466 (2010).
199. Nacev, A., Beni, C., Bruno, O. & Shapiro, B. The behaviors of ferromagnetic nano-particles in and around blood vessels under applied magnetic fields. *J. Magn. Magn. Mater.* **323**, 651–668 (2011).
200. Lübke, A. S. *et al.* Clinical experiences with magnetic drug targeting: a phase I study with 4'-epidoxorubicin in 14 patients with advanced solid tumors. *Cancer Res.* **56**, 4686–4693 (1996).
201. Thomsen, L. B., Thomsen, M. S. & Moos, T. Targeted drug delivery to the brain using magnetic nanoparticles. *Ther. Deliv.* **6**, 1145–1155 (2015).
202. Barnsley, L. C., Carugo, D., Owen, J. & Stride, E. Halbach arrays consisting of cubic elements optimised for high field gradients in magnetic drug targeting applications. *Phys. Med. Biol.* **60**, 8303–8327 (2015).
203. Riegler, J. *et al.* Magnetic cell delivery for peripheral arterial disease: A theoretical framework. *Med. Phys.* **38**, 3932–3943 (2011).
204. Polyak, B. *et al.* High field gradient targeting of magnetic nanoparticle-loaded endothelial cells to the surfaces of steel stents. *Proc. Natl. Acad. Sci. U. S. A.* **105**, 698–703 (2008).
205. Forbes, Z. G. *et al.* Validation of high gradient magnetic field based drug delivery to magnetizable implants under flow. *IEEE Trans. Biomed. Eng.* **55**, 643–649 (2008).
206. Le, T.-A., Zhang, X., Hoshier, A. K. & Yoon, J. Real-Time Two-Dimensional Magnetic Particle Imaging for Electromagnetic Navigation in Targeted Drug Delivery. *Sensors* **17**, (2017).
207. Muthana, M. *et al.* Directing cell therapy to anatomic target sites in vivo with magnetic resonance targeting. *Nat. Commun.* **6**, 8009 (2015).
208. Martel, S. *et al.* Automatic navigation of an untethered device in the artery of a living animal using a conventional clinical magnetic resonance imaging system. *Appl. Phys. Lett.* **90**, 114105 (2007).
209. Jordan, A., Scholz, R., Wust, P., Fähling, H. & Roland Felix. Magnetic fluid hyperthermia (MFH): Cancer treatment with AC magnetic field induced excitation of biocompatible superparamagnetic nanoparticles. *J. Magn. Magn. Mater.* **201**, 413–419 (1999).
210. Kumar, C. S. S. R. & Mohammad, F. Magnetic nanomaterials for hyperthermia-based therapy and controlled drug delivery. *Adv. Drug Deliv. Rev.* **63**, 789–808 (2011).

211. Stauffer, P. R., Cetas, T. C. & Jones, R. C. Magnetic Induction Heating of Ferromagnetic Implants for Inducing Localized Hyperthermia in Deep-Seated Tumors. *IEEE Trans. Biomed. Eng. BME-31*, 235–251 (1984).
212. Coey, J. M. D. Magnetism and Magnetic Materials by J. M. D. Coey. *Cambridge Core* /core/books/magnetism-and-magnetic-materials/AD3557E2D4538CAA8488A8C1057313BC (2010) doi:10.1017/CBO9780511845000.
213. Rosensweig, R. E. Heating magnetic fluid with alternating magnetic field. *J. Magn. Magn. Mater.* **252**, 370–374 (2002).
214. Maier-Hauff, K. *et al.* Intracranial Thermotherapy using Magnetic Nanoparticles Combined with External Beam Radiotherapy: Results of a Feasibility Study on Patients with Glioblastoma Multiforme. *J. Neurooncol.* **81**, 53–60 (2007).
215. Thiesen, B. & Jordan, A. Clinical applications of magnetic nanoparticles for hyperthermia. *Int. J. Hyperthermia* **24**, 467–474 (2008).
216. Kalber, T. L. *et al.* Hyperthermia treatment of tumors by mesenchymal stem cell-delivered superparamagnetic iron oxide nanoparticles. *Int. J. Nanomedicine* **11**, 1973–1983 (2016).
217. Chang, D. *et al.* Biologically Targeted Magnetic Hyperthermia: Potential and Limitations. *Front. Pharmacol.* **9**, 831 (2018).
218. Gavins, F. N. E. & Smith, H. K. Cell tracking technologies for acute ischemic brain injury. *J. Cereb. Blood Flow Metab. Off. J. Int. Soc. Cereb. Blood Flow Metab.* **35**, 1090–1099 (2015).
219. Zheng, Y. *et al.* Stem Cell Tracking Technologies for Neurological Regenerative Medicine Purposes. *Stem Cells Int.* **2017**, 2934149 (2017).
220. Srinivas, M., Melero, I., Kaempgen, E., Figdor, C. G. & de Vries, I. J. M. Cell tracking using multimodal imaging. *Contrast Media Mol. Imaging* **8**, 432–438 (2013).
221. Comenge, J. *et al.* Multimodal cell tracking from systemic administration to tumour growth by combining gold nanorods and reporter genes. *eLife* **7**, (2018).
222. Hembury, M. *et al.* Gold–silica quantum rattles for multimodal imaging and therapy. *Proc. Natl. Acad. Sci.* **112**, 1959–1964 (2015).
223. Bulte, J. W. M. & Kraitchman, D. L. Iron oxide MR contrast agents for molecular and cellular imaging. *NMR Biomed.* **17**, 484–499 (2004).

224. Korchinski, D. J., Taha, M., Yang, R., Nathoo, N. & Dunn, J. F. Iron Oxide as an MRI Contrast Agent for Cell Tracking. *Magn. Reson. Insights* **8**, 15–29 (2015).
225. Winter, E. M. *et al.* Cell tracking using iron oxide fails to distinguish dead from living transplanted cells in the infarcted heart. *Magn. Reson. Med.* **63**, 817–821 (2010).
226. Namestnikova, D. *et al.* Methodological aspects of MRI of transplanted superparamagnetic iron oxide-labeled mesenchymal stem cells in live rat brain. *PloS One* **12**, e0186717 (2017).
227. Jasmin *et al.* Tracking stem cells with superparamagnetic iron oxide nanoparticles: perspectives and considerations. *Int. J. Nanomedicine* **12**, 779–793 (2017).
228. Gubert, F. *et al.* Intraspinal bone-marrow cell therapy at pre- and symptomatic phases in a mouse model of amyotrophic lateral sclerosis. *Stem Cell Res. Ther.* **7**, 41 (2016).
229. Huang, Z. *et al.* Magnetic resonance hypointensive signal primarily originates from extracellular iron particles in the long-term tracking of mesenchymal stem cells transplanted in the infarcted myocardium. *Int. J. Nanomedicine* **10**, 1679–1690 (2015).
230. Chang, Y. C., Huang, K. M., Chen, J. H. & Su, C. T. Impact of magnetic resonance imaging on the advancement of medicine. *J. Formos. Med. Assoc. Taiwan Yi Zhi* **98**, 740–748 (1999).
231. Hovet, S. *et al.* MRI-powered biomedical devices. *Minim. Invasive Ther. Allied Technol.* **27**, 191–202 (2018).
232. Hundt, W., Petsch, R., Helmberger, T. & Reiser, M. Signal changes in liver and spleen after Endorem administration in patients with and without liver cirrhosis. *Eur. Radiol.* **10**, 409–416 (2000).
233. Harisinghani, M. G. *et al.* Noninvasive detection of clinically occult lymph-node metastases in prostate cancer. *N. Engl. J. Med.* **348**, 2491–2499 (2003).
234. Bonnemain, B. Superparamagnetic agents in magnetic resonance imaging: physicochemical characteristics and clinical applications. A review. *J. Drug Target.* **6**, 167–174 (1998).
235. Bernsen, M. R., Guenoun, J., van Tiel, S. T. & Krestin, G. P. Nanoparticles and clinically applicable cell tracking. *Br. J. Radiol.* **88**, 20150375 (2015).
236. Lin, C., Cai, S. & Feng, J. Positive Contrast Imaging of SPIO Nanoparticles. *Journal of Nanomaterials* <https://www.hindawi.com/journals/jnm/2012/734842/> (2012) doi:10.1155/2012/734842.



237. Liu, W., Dahnke, H., Jordan, E. K., Schaeffter, T. & Frank, J. A. In vivo MRI using positive-contrast techniques in detection of cells labeled with superparamagnetic iron oxide nanoparticles. *NMR Biomed.* **21**, 242–250 (2008).
238. Mani, V., Briley-Saebo, K. C., Itskovich, V. V., Samber, D. D. & Fayad, Z. A. Gradient echo acquisition for superparamagnetic particles with positive contrast (GRASP): Sequence characterization in membrane and glass superparamagnetic iron oxide phantoms at 1.5T and 3T. *Magn. Reson. Med.* **55**, 126–135 (2006).
239. Stuber, M. *et al.* Positive contrast visualization of iron oxide-labeled stem cells using inversion-recovery with ON-resonant water suppression (IRON). *Magn. Reson. Med.* **58**, 1072–1077 (2007).
240. Zurkiya, O. & Hu, X. Off-resonance saturation as a means of generating contrast with superparamagnetic nanoparticles. *Magn. Reson. Med.* **56**, 726–732 (2006).
241. Lu, W., Pauly, K. B., Gold, G. E., Pauly, J. M. & Hargreaves, B. A. SEMAC: Slice Encoding for Metal Artifact Correction in MRI. *Magn. Reson. Med.* **62**, 66–76 (2009).
242. Koch, K. M., Lorbiecki, J. E., Hinks, R. S. & King, K. F. A multispectral three-dimensional acquisition technique for imaging near metal implants. *Magn. Reson. Med.* **61**, 381–390 (2009).
243. Mathieu, J.-, Martel, S., Yahia, L. ', Soulez, G. & Beaudoin, G. MRI systems as a mean of propulsion for a microdevice in blood vessels. in *Proceedings of the 25th Annual International Conference of the IEEE Engineering in Medicine and Biology Society (IEEE Cat. No.03CH37439)* vol. 4 3419-3422 Vol.4 (2003).
244. Aboussouan, E. & Martel, S. High-Precision Absolute Positioning of Medical Instruments in MRI Systems. in *2006 International Conference of the IEEE Engineering in Medicine and Biology Society* 743–746 (2006). doi:10.1109/IEMBS.2006.259265.
245. Felfoul, O., Mathieu, J., Beaudoin, G. & Martel, S. In Vivo MR-Tracking Based on Magnetic Signature Selective Excitation. *IEEE Trans. Med. Imaging* **27**, 28–35 (2008).
246. Aboussouan, E., Felfoul, O., Mathieu, J.-B., Beaudoin, G. & Martel, S. Real-Time Projection Based Technique for Tracking Ferromagnetic Devices. 1.
247. Felfoul, O., Aboussouan, E., Chanu, A. & Martel, S. Real-time positioning and tracking technique for endovascular untethered microrobots propelled by MRI gradients. in *2009 IEEE International Conference on Robotics and Automation* 2693–2698 (2009). doi:10.1109/ROBOT.2009.5152567.

248. Chanu, A., Martel, S. & Beaudoin, G. Real-time Magnetic Resonance Gradient-based Propulsion of a Wireless Microdevice Using Pre-Acquired Roadmap and Dedicated Software Architecture. in *2005 IEEE Engineering in Medicine and Biology 27th Annual Conference* 5190–5193 (2005). doi:10.1109/IEMBS.2005.1615647.
249. Dahmen, C., Belharet, K., Folio, D., Ferreira, A. & Fatikow, S. MRI-based dynamic tracking of an untethered ferromagnetic microcapsule navigating in liquid. *Int. J. Optomechatronics* **10**, 73–96 (2016).
250. Zijlstra, F. *et al.* Challenges in MR-only seed localization for postimplant dosimetry in permanent prostate brachytherapy. *Med. Phys.* **44**, 5051–5060 (2017).
251. Zijlstra, F. Knowledge-based acceleration of MRI for metal object localization. <http://dspace.library.uu.nl/handle/1874/356155> (2017).
252. Wachowicz, K., Thomas, S. D. & Fallone, B. G. Characterization of the susceptibility artifact around a prostate brachytherapy seed in MRI. *Med. Phys.* **33**, 4459–4467 (2006).
253. Mathieu, J.-B., Beaudoin, G. & Martel, S. Method of propulsion of a ferromagnetic core in the cardiovascular system through magnetic gradients generated by an MRI system. *IEEE Trans. Biomed. Eng.* **53**, 292–299 (2006).
254. Felfoul, O., Becker, A. T., Fagogenis, G. & Dupont, P. E. Simultaneous steering and imaging of magnetic particles using MRI toward delivery of therapeutics. *Sci. Rep.* **6**, 33567 (2016).
255. Martel, S. *et al.* A computer-assisted protocol for endovascular target interventions using a clinical MRI system for controlling untethered microdevices and future nanorobots. *Comput. Aided Surg.* **13**, 340–352 (2008).
256. Chanu, A. & Martel, S. Real-time Software Platform Design for In-Vivo Navigation of a Small Ferromagnetic Device in a Swine Carotid Artery Using a Magnetic Resonance Imaging System. in *2007 29th Annual International Conference of the IEEE Engineering in Medicine and Biology Society* 6584–6587 (2007). doi:10.1109/IEMBS.2007.4353868.
257. Pouponneau, P., Leroux, J.-C., Soulez, G., Gaboury, L. & Martel, S. Co-encapsulation of magnetic nanoparticles and doxorubicin into biodegradable microcarriers for deep tissue targeting by vascular MRI navigation. *Biomaterials* **32**, 3481–3486 (2011).
258. Pouponneau, P., Soulez, G., Beaudoin, G., Leroux, J.-C. & Martel, S. MR imaging of therapeutic magnetic microcarriers guided by magnetic resonance navigation for targeted liver chemoembolization. *Cardiovasc. Intervent. Radiol.* **37**, 784–790 (2014).

259. Riegler, J. *et al.* Targeted magnetic delivery and tracking of cells using a magnetic resonance imaging system. *Biomaterials* **31**, 5366–5371 (2010).
260. Muthana, M. *et al.* Directing cell therapy to anatomic target sites *in vivo* with magnetic resonance targeting. *Nat. Commun.* **6**, 8009 (2015).
261. Becker, A. T., Felfoul, O. & Dupont, P. E. Toward tissue penetration by MRI-powered millirobots using a self-assembled Gauss gun. in *2015 IEEE International Conference on Robotics and Automation (ICRA)* 1184–1189 (2015). doi:10.1109/ICRA.2015.7139341.
262. Leclerc, J., Ramakrishnan, A., Tsekos, N. V. & Becker, A. T. Magnetic Hammer Actuation for Tissue Penetration Using a Millirobot. *IEEE Robot. Autom. Lett.* **3**, 403–410 (2018).
263. Deisseroth, K. Optogenetics: 10 years of microbial opsins in neuroscience. *Nat. Neurosci.* **18**, 1213–1225 (2015).
264. Montgomery, K. L. *et al.* Wirelessly powered, fully internal optogenetics for brain, spinal and peripheral circuits in mice. *Nat. Methods* **12**, 969–974 (2015).
265. Wheeler, M. A. *et al.* Genetically targeted magnetic control of the nervous system. *Nat. Neurosci.* **19**, 756–761 (2016).
266. Schildge, S., Bohrer, C., Beck, K. & Schachtrup, C. Isolation and Culture of Mouse Cortical Astrocytes. *J. Vis. Exp. JoVE* (2013) doi:10.3791/50079.
267. Eifler, R. L., Blough, E. R., Dehlin, J. M. & Haut Donahue, T. L. Oscillatory fluid flow regulates glycosaminoglycan production via an intracellular calcium pathway in meniscal cells. *J. Orthop. Res. Off. Publ. Orthop. Res. Soc.* **24**, 375–384 (2006).
268. Cullity, B. D. & Graham, C. D. *Introduction to magnetic materials*. (IEEE/Wiley, 2009).
269. Garber, M., Henry, W. G. & Hoeve, H. G. A MAGNETIC SUSCEPTIBILITY BALANCE AND THE TEMPERATURE DEPENDENCE OF THE MAGNETIC SUSCEPTIBILITY OF COPPER, SILVER, AND GOLD, 295°–975 °K. *Can. J. Phys.* **38**, 1595–1613 (1960).
270. Ko, K. S., Arora, P. D. & McCulloch, C. A. G. Cadherins Mediate Intercellular Mechanical Signaling in Fibroblasts by Activation of Stretch-sensitive Calcium-permeable Channels. *J. Biol. Chem.* **276**, 35967–35977 (2001).
271. Crick, F. H. C. & Hughes, A. F. W. The physical properties of cytoplasm: A study by means of the magnetic particle method Part I. Experimental. *Exp. Cell Res.* **1**, 37–80 (1950).

272. Seifriz, W. An Elastic Value of Protoplasm, with Further Observations on the Viscosity of Protoplasm. *J. Exp. Biol.* **2**, 1–11 (1924).
273. Valberg, P. A. & Albertini, D. F. Cytoplasmic motions, rheology, and structure probed by a novel magnetic particle method. *J. Cell Biol.* **101**, 130–140 (1985).
274. Fabry, B. *et al.* Selected Contribution: Time course and heterogeneity of contractile responses in cultured human airway smooth muscle cells. *J. Appl. Physiol.* **91**, 986–994 (2001).
275. Goldmann, W. H. *et al.* Differences in Elasticity of Vinculin-Deficient F9 Cells Measured by Magnetometry and Atomic Force Microscopy. *Exp. Cell Res.* **239**, 235–242 (1998).
276. Alenghat, F. J., Fabry, B., Tsai, K. Y., Goldmann, W. H. & Ingber, D. E. Analysis of cell mechanics in single vinculin-deficient cells using a magnetic tweezer. *Biochem. Biophys. Res. Commun.* **277**, 93–99 (2000).
277. Charles, A. C., Merrill, J. E., Dirksen, E. R. & Sandersont, M. J. Intercellular signaling in glial cells: Calcium waves and oscillations in response to mechanical stimulation and glutamate. *Neuron* **6**, 983–992 (1991).
278. Bowser, D. N. & Khakh, B. S. Vesicular ATP Is the Predominant Cause of Intercellular Calcium Waves in Astrocytes. *J. Gen. Physiol.* **129**, 485–491 (2007).
279. Maneshi, M. M., Sachs, F. & Hua, S. Z. A Threshold Shear Force for Calcium Influx in an Astrocyte Model of Traumatic Brain Injury. *J. Neurotrauma* **32**, 1020–1029 (2015).
280. Li, W., Feng, Z., Sternberg, P. W. & Xu, X. Z. S. A *C. elegans* stretch receptor neuron revealed by a mechanosensitive TRP channel homologue. *Nature* **440**, 684 (2006).
281. Jacques-Fricke, B. T., Seow, Y., Gottlieb, P. A., Sachs, F. & Gomez, T. M. Ca<sup>2+</sup> Influx through Mechanosensitive Channels Inhibits Neurite Outgrowth in Opposition to Other Influx Pathways and Release from Intracellular Stores. *J. Neurosci.* **26**, 5656–5664 (2006).
282. Adachi, T., Sato, K. & Tomita, Y. Directional dependence of osteoblastic calcium response to mechanical stimuli. *Biomech. Model. Mechanobiol.* **2**, 73–82 (2003).
283. Malone, A. M. D. *et al.* Primary cilia mediate mechanosensing in bone cells by a calcium-independent mechanism. *Proc. Natl. Acad. Sci.* **104**, 13325–13330 (2007).
284. Lumpkin, E. A. & Hudspeth, A. J. Detection of Ca<sup>2+</sup> entry through mechanosensitive channels localizes the site of mechanoelectrical transduction in hair cells. *Proc. Natl. Acad. Sci.* **92**, 10297–10301 (1995).

285. Ohmori, H. Mechanical stimulation and Fura-2 fluorescence in the hair bundle of dissociated hair cells of the chick. *J. Physiol.* **399**, 115–137 (1988).
286. Sasamoto, A. *et al.* Mechanotransduction by integrin is essential for IL-6 secretion from endothelial cells in response to uniaxial continuous stretch. *Am. J. Physiol.-Cell Physiol.* **288**, C1012–C1022 (2005).
287. Sharma, R. *et al.* Intracellular Calcium Changes in Rat Aortic Smooth Muscle Cells in Response to Fluid Flow. *Ann. Biomed. Eng.* **30**, 371–378 (2002).
288. Tada, S. & Okazaki, K. A Novel Single-Photon Counting Technique Applied to Highly Sensitive Measurement of  $[Ca^{2+}]_i$  Transient in Human Aortic Smooth Muscle Cells. *J. Biomech. Eng.* **128**, 777–781 (2006).
289. Brain, M. C., Pihl, C., Robertson, L. & Brown, C. B. Evidence for a mechanosensitive calcium influx into red cells. *Blood Cells. Mol. Dis.* **32**, 349–352 (2004).
290. Baratchi, S. *et al.* Examination of the role of transient receptor potential vanilloid type 4 in endothelial responses to shear forces. *Biomicrofluidics* **8**, 044117 (2014).
291. Roberts, S. R., Knight, M. M., Lee, D. A. & Bader, D. L. Mechanical compression influences intracellular  $Ca^{2+}$  signaling in chondrocytes seeded in agarose constructs. *J. Appl. Physiol. Bethesda Md* **1985** **90**, 1385–1391 (2001).
292. Puig-de-Morales, M. *et al.* Cytoskeletal mechanics in adherent human airway smooth muscle cells: probe specificity and scaling of protein-protein dynamics. *Am. J. Physiol. Cell Physiol.* **287**, C643-654 (2004).
293. Edlich, M., Yellowley, C. E., Jacobs, C. R. & Donahue, H. J. Oscillating fluid flow regulates cytosolic calcium concentration in bovine articular chondrocytes. *J. Biomech.* **34**, 59–65 (2001).
294. Marina, N. *et al.* Purinergic signalling in the rostral ventro-lateral medulla controls sympathetic drive and contributes to the progression of heart failure following myocardial infarction in rats. *Basic Res. Cardiol.* **108**, 317 (2013).
295. Cugat, O., Hansson, P. & Coey, J. M. D. Permanent magnet variable flux sources. *IEEE Trans. Magn.* **30**, 4602–4604 (1994).
296. Sitti, M. *et al.* Biomedical Applications of Untethered Mobile Milli/Microrobots. *Proc. IEEE* **103**, 205–224 (2015).

297. Nelson, B. J., Kaliakatsos, I. K. & Abbott, J. J. Microrobots for Minimally Invasive Medicine. *Annu. Rev. Biomed. Eng.* **12**, 55–85 (2010).
298. Ergeneman, O. *et al.* A Magnetically Controlled Wireless Optical Oxygen Sensor for Intraocular Measurements. *IEEE Sens. J.* **8**, 29–37 (2008).
299. Alivisatos, A. P. *et al.* Nanotools for neuroscience and brain activity mapping. *ACS Nano* **7**, 1850–1866 (2013).
300. Matthew A. Howard, I. I. I. *et al.* Magnetic Neurosurgery. *Stereotact. Funct. Neurosurg.* **66**, 102–107 (1996).
301. Madsen, E. L., Hobson, M. A., Shi, H., Varghese, T. & Frank, G. R. Tissue-mimicking agar/gelatin materials for use in heterogeneous elastography phantoms. *Phys. Med. Biol.* **50**, 5597 (2005).
302. Mathieu, J.-B. & Martel, S. Steering of aggregating magnetic microparticles using propulsion gradients coils in an MRI Scanner. *Magn. Reson. Med.* **63**, 1336–1345 (2010).
303. Setsompop, K. *et al.* Pushing the limits of in vivo diffusion MRI for the Human Connectome Project. *NeuroImage* **80**, 220–233 (2013).
304. Quate, E. G. The Video Tumor Fighter magnetic manipulation system. (University of Virginia, 1989). doi:10.18130/V3PN8XD8H.
305. Howard, M. A. *et al.* Magnetic Movement of a Brain Thermoceptor. *Neurosurgery* **24**, 444–448 (1989).
306. Molloy, J. A. *et al.* Experimental determination of the force required for insertion of a thermoseed into deep brain tissues. *Ann. Biomed. Eng.* **18**, 299–313 (1990).
307. Jakubovics, J. P. *Magnetism and Magnetic Materials*. (Maney Publishing, 1994).
308. Weiger, M. *et al.* A high-performance gradient insert for rapid and short-T2 imaging at full duty cycle. *Magn. Reson. Med.* **79**, 3256–3266 (2018).
309. Carpentier, A. *et al.* Laser thermal therapy: Real-time MRI-guided and computer-controlled procedures for metastatic brain tumors. *Lasers Surg. Med.* **43**, 943–950 (2011).
310. Larson, B. T. *et al.* Design of an MRI-Compatible Robotic Stereotactic Device for Minimally Invasive Interventions in the Breast†. *J. Biomech. Eng.* **126**, 458–465 (2004).

311. Masamune, K. *et al.* Development of an MRI-compatible needle insertion manipulator for stereotactic neurosurgery. *J. Image Guid. Surg.* **1**, 242–248 (1995).
312. Krieger, A. *et al.* An MRI-Compatible Robotic System With Hybrid Tracking for MRI-Guided Prostate Intervention. *IEEE Trans. Biomed. Eng.* **58**, 3049–3060 (2011).
313. Robinson, J. E., Wizenberg, M. J. & McCreedy, W. A. Combined hyperthermia and radiation suggest an alternative to heavy particle therapy for reduced oxygen enhancement ratios. *Nature* **251**, 521–522 (1974).
314. Wust, P. *et al.* Hyperthermia in combined treatment of cancer. *Lancet Oncol.* **3**, 487–497 (2002).
315. Cavaliere, R. *et al.* Selective heat sensitivity of cancer cells. Biochemical and clinical studies. *Cancer* **20**, 1351–1381 (1967).
316. Harmon, B. V., Takano, Y. S., Winterford, C. M. & Gobé, G. C. The role of apoptosis in the response of cells and tumours to mild hyperthermia. *Int. J. Radiat. Biol.* **59**, 489–501 (1991).
317. Kennedy, J. E. High-intensity focused ultrasound in the treatment of solid tumours. *Nat. Rev. Cancer* **5**, 321–327 (2005).
318. den Brok, M. H. M. G. M. *et al.* In situ tumor ablation creates an antigen source for the generation of antitumor immunity. *Cancer Res.* **64**, 4024–4029 (2004).
319. Shinohara, K. Thermal ablation of prostate diseases: advantages and limitations. *Int. J. Hyperthermia* **20**, 679–697 (2004).
320. Patel, N. V. *et al.* Laser Interstitial Thermal Therapy Technology, Physics of Magnetic Resonance Imaging Thermometry, and Technical Considerations for Proper Catheter Placement During Magnetic Resonance Imaging–Guided Laser Interstitial Thermal Therapy. *Neurosurgery* **79**, S8–S16 (2016).
321. Moroz, P., Jones, S. K. & Gray, B. N. Magnetically mediated hyperthermia: current status and future directions. *Int. J. Hyperthermia* **18**, 267–284 (2002).
322. Kramer, M. *et al.* TTC staining of damaged brain areas after MCA occlusion in the rat does not constrict quantitative gene and protein analyses. *J. Neurosci. Methods* **187**, 84–89 (2010).
323. Chen, L., Bouley, D. M., Harris, B. T. & Butts, K. MRI study of immediate cell viability in focused ultrasound lesions in the rabbit brain. *J. Magn. Reson. Imaging* **13**, 23–30 (2001).

324. Wu, M.-T. & Wallner, S. J. Heat Stress Responses in Cultured Plant Cells: Development and Comparison of Viability Tests. *Plant Physiol.* **72**, 817–820 (1983).
325. Vostálová, J. *et al.* Comparison of various methods to analyse toxic effects in human skin explants: Rediscovery of TTC assay. *J. Photochem. Photobiol. B* **178**, 530–536 (2018).
326. Moidel, R. A., Wolfson, S. K., Selker, R. G. & Weiner, S. B. Materials for selective tissue heating in a radiofrequency electromagnetic field for the combined chemothermal treatment of brain tumors. *J. Biomed. Mater. Res.* **10**, 327–334 (1976).
327. Chikazumi, S. *Physics of Ferromagnetism 2e.* (Oxford University Press, 2009).
328. Mehdaoui, B. *et al.* Influence of a transverse static magnetic field on the magnetic hyperthermia properties and high-frequency hysteresis loops of ferromagnetic FeCo nanoparticles. *Appl. Phys. Lett.* **100**, 052403 (2012).
329. Ma, M. *et al.* Targeted inductive heating of nanomagnets by a combination of alternating current (AC) and static magnetic fields. *Nano Res.* **8**, 600–610 (2015).
330. Cantillon-Murphy, P., Wald, L. L., Adalsteinsson, E. & Zahn, M. Heating in the MRI environment due to superparamagnetic fluid suspensions in a rotating magnetic field. *J. Magn. Magn. Mater.* **322**, 727–733 (2010).
331. Cetas, T. C., Gross, E. J. & Contractor, Y. A ferrite core/metallic sheath thermoseed for interstitial thermal therapies. *IEEE Trans. Biomed. Eng.* **45**, 68–77 (1998).
332. Master, V. A., Shinohara, K. & Carroll, P. R. FERROMAGNETIC THERMAL ABLATION OF LOCALLY RECURRENT PROSTATE CANCER: PROSTATE SPECIFIC ANTIGEN RESULTS AND IMMEDIATE/INTERMEDIATE MORBIDITIES. *J. Urol.* **172**, 2197–2202 (2004).
333. Meredith, R. F. *et al.* Ferromagnetic thermoseeds: Suitable for an afterloading interstitial implant. *Int. J. Radiat. Oncol.* **17**, 1341–1346 (1989).
334. Haider, S. A., Cetas, T. C., Wait, J. R. & Chen, J.-. Power absorption in ferromagnetic implants from radiofrequency magnetic fields and the problem of optimization. *IEEE Trans. Microw. Theory Tech.* **39**, 1817–1827 (1991).
335. Bozzini, G. *et al.* Focal therapy of prostate cancer: energies and procedures. *Urol. Oncol. Semin. Orig. Investig.* **31**, 155–167 (2013).



336. Jankun, J., Keck, R. W., Skrzypczak-Jankun, E., Lilge, L. & Selman, S. H. Diverse optical characteristic of the prostate and light delivery system: implications for computer modelling of prostatic photodynamic therapy. *BJU Int.* **95**, 1237–1244 (2005).
337. Hoogenboom, M. *et al.* Development of a high-field MR-guided HIFU setup for thermal and mechanical ablation methods in small animals. *J. Ther. Ultrasound* **3**, 14 (2015).
338. Alkins, R. D. & Mainprize, T. G. High-Intensity Focused Ultrasound Ablation Therapy of Gliomas. *Intracranial Gliomas Part III - Innov. Treat. Modalities* **32**, 39–47 (2018).
339. Illing, R. & Emberton, M. Sonablate®-500: transrectal high-intensity focused ultrasound for the treatment of prostate cancer. *Expert Rev. Med. Devices* **3**, 717–729 (2006).
340. Kobayashi, T. *et al.* Magnetic induction hyperthermia for brain tumor using ferromagnetic implant with low Curie temperature. *J. Neurooncol.* **4**, 175–181 (1986).